Munemasa Mori, MD, PhD
Columbia Center for Human Development
Department of Medicine
Columbia University Medical Center
650 West 168th Street, BB8-812
New York, NY 10032
201.856.8451 Tel
mm4452@columbia.edu

July 12, 2023

Chicago, IL

Re: Tenure-tracked Faculty Position in The University of Chicago, Biological Sciences Division, Department of Pediatrics, Section of Neonatology

Dear Faculty Search Committee members,

I am writing to apply for the Faculty Position (Assistant professor or Associate Professor) at the University of Chicago, Biological Sciences Division, Department of Pediatrics, Section of Neonatology. I am currently an Assistant Professor of Medicine at the Columbia Center for Human Development (CCHD), Columbia University Irving Medical Center. I am currently exploring new faculty positions that will allow for more active collaborations, and I'm very excited about the possibility of joining your esteemed teams.

I have extensive training in developmental biology, molecular imaging with specialized microscopies, gene manipulation, and pluripotent stem cell biology. My career began as a pulmonologist in Japan, treating patients with refractory lung diseases. Seeking a better understanding of disease processes, I secured a Ph.D. in molecular biology and biochemistry. My postdoctoral training in lung development occurred under the mentorship of Dr. Wellington V. Cardoso, an expert in the field. My initial research focused on analyzing regulatory mechanisms involving the transition of undifferentiated progenitors and commitment during airway differentiation.

This work showed that Notch3 signaling controls undifferentiated progenitor pool expansion, such as p63+ basal and parabasal cells ***(Mori et al., Development, 2015***). I discovered how airway progenitors initiate large-scale centriole multiplication during lung development and in adult lung progenitors through genome-wide analyses and state-of-the-art technology, super-resolution microscopy (***Mori et al., Nature Commun., 2017***). My stem cell research using mouse Nkx2-1 ES cells resulted in collaborative work with Dr. Darrell Kotton (CReM, Boston Univ.) for generating ball-like structures consisting of thyroid progenitors (Kurmann, Serra, Mori, et al., Cell Stem Cell, 2015) as well as oesophageal organoids with Dr. Jianwen Que (CCHD, Columbia Univ.) (Zhang et al., Cell Stem Cell, 2018), respectively. I have expertise using cutting-edge imaging technologies that allow analyses of subcellular localization of cilia-related microstructures such as centrioles or pericentriolar materials by super-resolution microscopy and whole-mount three-dimensional tissue structures via confocal microscopies that honored me to be a confocal microscopy manager in the CCHD. I oversee the CCHD's confocal microscopy, am responsible for maintenance, and have trained more than 60 users.

In 2017, I received funding as the Principal Investigator for a US Department of Defense Discovery Award to pursue Blastocyst Complementation (BC) technology to regenerate functional lungs from pluripotent stem cells in vivo as an experimental basis for future regenerative medicine modalities. We developed a state-of-the-art bioengineering technology, conditional blastocyst complementation (CBC), and established a novel culture condition for pluripotent stem cells, allowing fully functional lung generation. Remarkably, the mice survived until adulthood with regenerated lungs ***(Mori et al., Nature Medicine, 2019).*** In this paper, I also showed my ability the whole mount confocal imaging using tissue clear (transparent) reagent.

Based on this accomplishment, I recently received an **RO1 (NHLBI, PI: Mori)** to study the mechanisms that control lung bioengineering. In addition, I received two funding from the Department of Defense, an **Expansion Award** and an **Investigator-Initiated Award (both funded, PI: Mori)**. These awards distilled further technological advancements in my ongoing research in rodents and swine toward human lung generation by owning my new lab in CCHD.

The primary objective of my laboratory is to generate human lungs in vivo, such as mice and swine, using human iPSC. This innovative approach aims to provide therapeutic options for patients suffering from refractory lung diseases and can also offer modeling of human lung development in vivo. Our research involves comprehensive studies on chimeric lung generation to reach this goal. Our pioneering work of studying swine lung development, compatible organ size with humans, can also model human lung development (Shimamura et al., 2023, Bioarchive), which provides fundamental knowledge of human development. Our most recent accomplishment is the successful generation of entire lungs in mice. These lungs, composed of epithelial, mesenchymal, and endothelial cells, were derived from donor pluripotent stem cells. We utilized the conditional blastocyst complementation method in this research (Miura et al., 2023, currently under revision). Additionally, we have generated interspecific lungs in mice using rat pluripotent stem cells, a study that is yet to be published. I'm especially eager to foster active collaborations with faculty members and clinicians. I firmly believe that such partnerships will enhance our understanding of human development and push the boundaries of scientific research across various fields. I can join your institution this summer or autumn if it works for you after the interviews. Furthermore, we are excited about discovering the regulatory mechanism of initiating interspecific barrier, the major hurdle of human organ generation in early embryogenesis in mice and swine (R01, pending).

In addition, I also have the successful experience of having been awarded the S10 instrument grant for Stellaris multiplex confocal microscopy in the CCHD and have been a committee member. I am pursuing a position and environment that can further extend my scientific knowledge and background.

I believe that our systematic approach towards intra- and interspecific lung generation harnessing developmental biology, stem cell biology, material science, and genome editing can overcome the significant handle of the xenogeneic barrier. We primarily focus on human lung generation by utilizing a unique pluripotent stem cell culture condition we established in my lab, cellular interaction mechanism by a customizable synthetic molecule approach, and mouse and swine genetic animal models. I hope we can offer scientific enthusiasm and extend the animal models in your division to advance the measurement of developmental biology. I envision a synergistic collaboration, particularly with clinicians and developmental biology, genetics, material science, and stem cell biology groups at your university, to empower the research analysis using various animal models and your exciting research programs. We are also more than welcome to collaborate for organ generation and share the precious resources of mouse and swine embryonic tissues genetically modified specimens to strengthen individual projects through seamless accessibility. I would be inspired to pursue cutting-edge technology for lung bioengineering through blastocyst and embryo manipulations in a highly advanced scientific-educational environment supporting minorities. I hope my dedication can encourage the underrepresented racial and sexual minority undergraduate and graduate students, and we can enjoy exciting research programs with more diverse backgrounds and active collaboration.

Enclosed, please find my curriculum vitae, research statement, and references. I look forward to hearing from you to discuss how I can contribute to the growth and reputation of your institute. Thank you for your time.

Sincerely,

Munemasa Mori, MD PhD

Assistant Professor of Medicine,
Columbia Center for Human Development (CCHD),
Pulmonary Allergy & Critical Care Medicine,
Department of Medicine,
Columbia University Irving Medical Center

Mori Lab,
https://www.morilab.org/
Email: mm4452@cumc.columbia.edu
Tel: 201-856-8451

Research plans:

I. CURRENT ONGOING RESEARCH AS A PRINCIPAL INVESTIGATOR AT COLUMBIA UNIVERSITY

Project 1. Studying the Molecular mechanism of interspecies cell competition for the generation of bioengineered lungs (1~3 years):

My lab is currently exploring the molecular mechanism of interspecies cell competition for generating bioengineered lungs. We discovered the essential genes crucial to outcompete host animals. Using this knowledge, we examine how human pluripotent stem cells (PSCs) can efficiently be targeted exclusively to the pulmonary organ niche and how to generate the lung endodermal and mesodermal lineages simultaneously into the defective lung organ niche. We are systematically analyzing the genes involved in cell competition, as reported by other biological systems, to enhance the efficiency of lung generation.

- *This project is funded by R01(NHLBI-1R01HL148223-01) and the DoD expansion award.*
- *This project will be submitted to the ALPHA-H program.*

Project 2: Generating a humanized lung mouse via CBC to model refractory lung diseases (2~5 years)

Our lab's primary goal is to generate humanized organs, as they can serve as a highly effective experimental platform for modeling refractory human lung diseases using our conditional blastocyst complementation (CBC) model mice. The developmental pattern of the mouse lung is spatially and temporally different from that of humans in terms of progenitor distribution and size. Hence, understanding how chimeric human-mouse lungs form is exceptionally insightful in revealing the hidden evolutionary differences in signaling pathways and cellular dynamics during interspecies development. Myc has been known to function as a central and intraspecies super competition factor (SCF) during early development. However, our preliminary studies indicate that Myc does not act as an SCF (unpublished data). It remains to be determined which molecule could serve as an interspecific super competition factor (iSCF). Employing interspecific cell culture techniques and the analysis of chimeric mice during early embryogenesis, we have discovered three genes that serve as iSCF, which are crucial in regulating human iPSC chimerism during mouse early embryogenesis (manuscript in preparation). Using the iSCF, we aim to enhance our understanding of niche-specific chimerism control for generating human lungs in mice. This will significantly advance our knowledge in the field and take us one step closer to the goal of human organ bioengineering in mice.

- *This project is funded by R01(NHLBI) and the DoD expansion award.*

Project 3: Optimization of pluripotent stem cell (PSC) culture and identification of functional PSCs for interspecies CBC (1~3 years)

We dedicated our effort to advancing the reprogramming of somatic cells to large animal-induced pluripotent stem cells (iPSC). Our dedicated effort allowed us to establish a novel medium, Medium C, which allows highly efficient reprogramming and maintenance of iPSC from the somatic cells of large animal species, such as no-human primates and swine. Using those iPSC lines, we validate how efficiently those iPSC form chimeras in vivo for interspecific lung generation (manuscript in preparation).

- *This project is funded by R01 (NHLBI) and the DoD investigator-initiated award.*

Project 4: Explore swine lung development for generating human bioengineered lungs in swine (1~5 years):

This project aims to apply the CBC technology to large animals. We systematically analyze swine lung development across the time points by morphological, histological, and transcriptome (bulk and at a single-cell level). We found that the essential genetic program regulating pig lung development common in mice and humans. We further elucidated the diversity of cell types and identified critical signaling pathways regulating progenitor expansion and differentiation during swine lung development. Those analyses revealed that the pig lung progenitor transcriptome and the protein marker expressions showed proximity with humans but far from mice (*Shimamura et al., 2023, Bioarchive*).

- *A DoD investigator-initiated award currently funds this project.*
- *I am currently planning to apply for the R01 next year.*

Project 5: Establishment of the artificial thorax by bio-printer:

The primary objective of this project is to develop an artificial thorax using parietal pleural mesothelial cells (PPMC), in collaboration with AspectBio. We aim to facilitate the long-term cultivation of human iPSC-derived lung organoids within this bioprinted artificial thorax. PPMC plays an instrumental role in lung organ size regulation and the differentiation of smooth muscle cells during lung development. Yet, the successful in vitro culture of PPMC has been a long-standing challenge, mainly due to the lack of clarity regarding the critical signaling pathways that influence their expansion and differentiation. We have managed to isolate porcine PPMC and subsequently establish a protocol that enables efficient PPMC expansion and differentiation into smooth muscle cells (manuscript under review). This

achievement paves the way for us to develop a method for the directed differentiation of lung mesothelial cells from human iPSC, which can be co-cultured with lung branching organoids. Our work can provide the unique aspect of the previously unveiled mechanism regulating lung development and homeostasis, ultimately applicable to diagnosing and treating mesothelial-related diseases, such as mesothelioma.

- *Funded by the Aspect-Bio company (collaborative work)*
- *This project will be submitted in R21(NHLBI) next year.*

II. FUTURE RESEARCH PLANS (funding pending)

Project 1. Studying the molecular and cellular mechanism of interspecies cell competition in early swine embryogenesis to produce human lungs in swine

To produce humanized lungs in pigs, overcoming human-pig interspecies barriers is necessary (See review, *Sarmah et al., Frontiers, Cell, and Dev. Bio.*). We have established an interspecies iPSC culture system using Medium C. In this culture system, human iPSC cells are the losers, and porcine iPSC cells are the winners. Since these cells have primed-type PSC characteristics, we hypothesized that they mimic the timing of epiblast formation in the pig. In this culture system, we found that introducing three genes into human PSC cells caused these cells to become Winners. We analyze how human cells change their cell fate from losers to winners, focusing on mitochondrial biology and cell behavior in vitro and in vivo chimerism analysis. We also discovered the molecular mechanism of how interspecific cell competition is initiated by a refined synthetic molecular switch (iSwitch) that responds exclusively to interspecific iPSC coupled with single-cell RNAseq (manuscript in preparation). Those approaches promise to pioneer human organ generation in swine.

- *This project is now pending a new R01 review.*

Project 2: Disease-modeling of human refractory lung diseases via lung bud complementation or CBC in mice or swine using human iPSC

Using human iPSC, we recently established the directed differentiation protocol for human lung co-development of lung epithelium and mesenchyme (Miura et al., 2023, under review). In this directed differentiation protocol, we can efficiently differentiate and expand both lung epithelium and mesenchyme simultaneously or separately from various hiPSC lines (unpublished). We also optimized the hiPSC reprogramming protocol from blood (PBMC), airway progenitors (basal cells), and skin using a Sendai virus-mediated reprogramming kit (CytoTune 2.1). We propose to model human neonatal diseases in vivo via lung bud complementation (LBC) in swine. We will inject hiPSC-derived lung bud cells expressing NKX2-1, CPM, and SOX9 (distal lung bud marker) with the pseudoglandular stage-specific of lung bud epithelial marker to complement the genetically defective niche of porcine (or mouse) lungs. We will analyze how those patients' derived iPSC initiate and cause the diseases in vivo. Our primary focus of the disease will be cystic fibrosis, surfactant proteinosis, and ChiLD syndrome. Alternatively, we will use the CBC approach to model diseases. This will provide critical knowledge of modeling refractory lung disease in vivo using patient's-specific iPSC lines.

- *This project will be submitted to the Cystic fibrosis foundation (under negotiation)*
- *This project will be submitted in R21(NHLBI)*

Project 3: Explore the molecular and cellular mechanism of the humanized lung generation in swine (1~4 years):

Lung transplantation is the only practical option for terminally ill patients with these diseases. Despite the technological development in the bioengineering and regenerative fields, none of the technology achieved humanized lung production. Elucidating the lineage critical for controlling the cell traits and composition can contribute to organ bioengineering and development. We have identified the Foxa2 lineage as a lung precursor lineage (LPL) that gives rise to all lung cell types, including lung epithelial, endothelial, and mesenchymal cells, in vivo lineage tracing, and flow cytometry analysis (**Miura et al., 2023, in revision, see Figure 1**). The induction of a mitotic signaling defect in LPL (a new

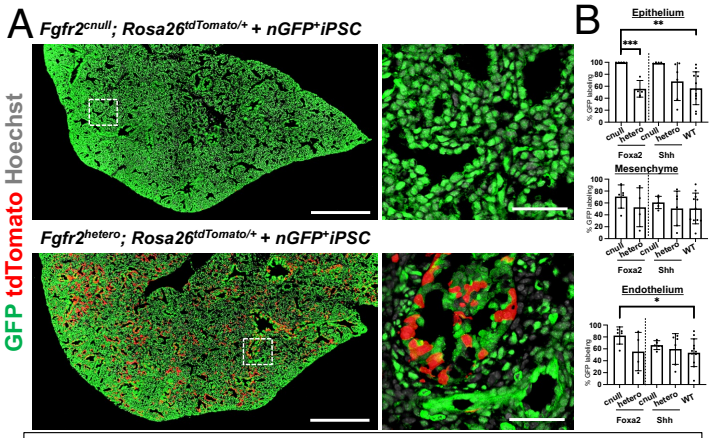

Fig. 1. Entire lung generation solely by donor-induced pluripotent stem cells (iPSC). (A) Top: Fully complemented lungs by injecting nGFP+iPSC, while host-derived cells (tdTomato) have substantially remained in the chimeric lungs of Fgfr2 ^{hetero} mice. (B) FACS chimerism analyses: Foxa2-driven Fgfr2^{cnull} mice showed the constant epithelial, mesenchymal, and endothelial cell complementation. (A dot in the graph indicates the biological replicates). Statistical significance: 1-way ANOVA (P*<0.05, P**<0.01, P***<0.001)

model mouse) resulted in defects in organ niches and showed lung agenesis phenotype. Significantly, entire lungs were produced solely from donor iPSCs by injecting induced pluripotent stem cells (iPSCs) into the host blastocysts. Almost 100% of the lung epithelial, mesenchymal, and endothelial cells were significantly complemented with donor iPSCs alone. We also recently established an interspecific molecular switch (iSwitch) that can respond to interspecific cell-cell contact-dependently, allowing us to control and trace specifically host developmental niches responding to human iPSCs. We are currently extending the research direction using the LPL-iSwitch-based human lung generation strategies for the humanized lung generation in swine.

- *This project is currently pending a DoD investigator-initiated award.*

Project 4: Elucidate the critical determinant of prominent organ size regulators in swine lung development (1~5 years):

Pigs are evolutionarily more distant from humans than mice, while it has similar physiological organs to humans, exemplified by porcine xenograft organs. Despite the importance of bioengineering human organs, it is unclear what molecular program defines the enormous human-compatible lung organ size phenotype in pig lung development, distinct from mice. Unlike mice, our cross-species transcriptome analyses revealed that swine lung development is closer to humans. Through collaborative work with Dr. Kazuhiko Yamada, a Professor in the Department of Surgery at Johns Hopkins University, Dr. James Cai at A&M Texas, expertise in bioinformatics, we discovered the core of the organ size regulator program (COSRP) that may define the large lung organ size, along with animal organismal size (*Shimamura et al., 2023, Bioarchive*). Studying the mechanism of swine lung organ size is an essential step toward creating vacant organ niches for CBC and for generating chimeric and, ultimately, transplantable autologous human lungs. Our study will contribute to a better understanding of the mechanism of human-compatible organ size regulations, which will establish a solid base for future lung bioengineering through organoids and CBC-based respiratory organ generation in regenerative medicine.

- *This project is currently pending an R01 (NHLBI) award.*

Project 5: Determine the effect of PlasmaClusterIons on airway differentiation (1~5 years):

Ions, one of the exogenous reactive oxygen species (ROS), are an unavoidable environmental stimulus generated by various devices such as TVs, PCs, hair dryers, air conditioners, and various electrical appliances. However, the association of ion stimuli with airway remodeling and COVID-19 has been unclear. We hypothesized that ion stimulation would not influence the cellular differentiation of human airway epithelial cells. To test this hypothesis, differentiated human tracheal epithelial cells (hTECs) cultured *in vitro* by air-liquid-interface (ALI) condition were exposed to ions with an ion generator (IG) as a collaborative work with the SHARP company (see CV the details of funding). We found the potential effect of ions in airway remodeling.

- *SHARP currently supports this project and will support it the following year.*

As part of the research plans, undergraduates and master's students will be integrated into these projects. They will participate hands-on in laboratory experiments, data collection, and analysis and will also receive mentoring in scientific writing and presentation skills. They will be encouraged to take ownership of their sub-projects, fostering a deeper understanding and engagement in scientific research.

For the successful execution of these research projects, significant equipment needs include state-of-the-art cell culture facilities, advanced microscopy tools (multiplexed confocal microscopy, inverted microscopy for microinjections), and high-throughput sequencing technologies. We also require molecular biology, protein biochemistry, histology, and animal facilities for rodents and large animals.

As described above, we are actively seeking external funding sources to sustain and expand our research endeavors. I will pursue opportunities for funding from the National Institutes of Health (NIH), the Department of Defense (DoD), and other relevant federal agencies. Collaborative program funding, such as P01, PPG, or U01, with your colleagues, particularly with clinicians, is more than welcome for me. I also plan to apply for grants from private foundations that support biomedical research, such as the Cystic Fibrosis Foundation and the Howard Hughes Medical Institute. Moreover, we currently have partnerships with three companies, SHARP (for the COVID-19 project), Aspects-Bio (for the bioprinter project), and United Therapeutics (for the organ generation project, under negotiation).

Date of preparation: July 10th, 2023

Munemasa Mori, MD PhD

Preferred nickname: Mooney

Columbia Center for Human Development
Department of Medicine
Columbia University Irving Medical Center
650 West 168th Street, BB 8-810
New York, NY 10032
mm4452@columbia.edu

Birthplace: Osaka, Japan
Citizenship: U.S.A. green card holder

ACADEMIC APPOINTMENTS, HOSPITAL APPOINTMENTS

07/2021 – Present	Assistant Professor, Department of Medicine, Pulmonary Division, Columbia Center for Human Development, Columbia University Irving Medical Center, (New York, NY)
03/2020 - 06/2021	Instructor of Medicine, Department of Medicine, Pulmonary Division, Columbia Center for Human Development, Columbia University Irving Medical Center, (New York, NY)
08/2021 - 02/2020	Associate Research Scientist, Department of Medicine, Pulmonary Division, Columbia Center for Human Development, Columbia University Irving Medical Center, (New York, NY)
09/2013 - 07/2016	Postdoctoral Research Scientist, Department of Medicine, Pulmonary Division, Columbia Center for Human Development, Columbia University Irving Medical Center, (New York, NY)
09/2011 - 08/2013	Postdoctoral Fellow, Boston University School of Medicine, Pulmonary Center
04/2010 - 08/2011	Research Fellow, Institute for Molecular and Cellular Regulation, **Advisor**: Prof. Takashi Matozaki, MD, PhD
2010-2011	Staff Physician, Department of Medicine and Molecular Science, Gunma University School of Medicine, Gunma (Japan)
04/2007-03/2010	PhD student, Institute for Molecular and Cellular Regulation, Gunma University (Japan) **Advisor**: Prof. Takashi Matozaki, MD, PhD **Project**: Understanding the molecular regulatory mechanism by vascular endothelial protein tyrosine phosphatase (VE-PTP)
04/2005-03/2006	Staff Physician, National Numata Hospital (Japan)
04/2004-03/2005	Staff Physician, Internal Medicine, Ashikaga Red Cross Hospital (Japan)
04/2003-03/2004	Medical Residency at Gunma University School of Medicine, (Japan)

EDUCATION

04/2007- 03/2010	**Ph.D.** in Molecular Biology, Institute for Molecular and Cellular Regulation, Gunma University (Japan) **Thesis**: Promotion of cell spreading and migration by vascular endothelial-protein tyrosine phosphatase (VE-PTP) in cooperation with integrins, J Cell Physiol. 2010 Jul;224(1):195-204. doi: 10.1002/jcp.22122. **Advisor**: Prof. Takashi Matozaki, MD, PhD
04/1997- 03/2003	**M.D.** Hamamatsu Medical University, Japan (Medicine)

TRAINING

09/2013-08/2015	Postdoctoral Research Scientist, Department of Medicine, Pulmonary Division, Columbia Center for Human Development, Columbia University Irving Medical Center, (New York, NY) **Advisor**: Wellington Cardoso, MD, PhD
09/2011-08/2013	Postdoctoral Fellow, Boston University School of Medicine, Pulmonary Center **Advisor**: Wellington Cardoso, MD, PhD

Project (i) Understanding the molecular mechanism regulating initiation of motile ciliogenesis
Project (ii) Elucidation of the molecular mechanism governing airway progenitor cell expansion and differentiation.

04/2010-08/2011 Research Fellow (Part time), Institute for Molecular and Cellular Regulation,
Advisor: Prof. Takashi Matozaki, MD, PhD

04/2003-03/2004 Medical Residency, Pulmonary Medicine at Gunma University School of Medicine, (Japan)

RESEARCH EXPERIENCE: Organ generative medicine, mouse genetics, cell biology, gene manipulation (piggyback-mediated gene manipulation, adenovirus, lentivirus, CRISPR-Cas9), developmental biology, & stem cell technology, including primary culture of adult stem cells, pluripotent stem cells of various species (mouse, rat, pig, human, and baboon), directed differentiation of mouse or human pluripotent stem cells, conditional blastocyst complementation.

MEDICAL EXPERIENCE: Clinical pulmonology, including bronchoscopy, diagnosis, and internal medicine in Japan.

GAPS IN WORK/TRAINING/EDUCATION

Not Applicable

LICENSES AND CERTIFICATION:

2006 Board Certified by the Japanese Society of Internal Medicine
2003 M.D., Medical License in Japan

HONORS

2021 RX1 bioprinter technology award (PI: Mori)
2021 SHARP company award (PI: Mori)
2019 Peer Reviewed Medical Research Program Investigator-Initiated Research Award (DoD) (PI: Mori)
2019 Peer Reviewed Medical Research Program Expansion Award (DoD) (PI: Mori)
2019 1R0HL148223-01 award (NHLBI) (PI: Mori)
2017 W81XWH-17-1-0139 Department of Defense, Discovery award (PI: Mori)
2015 Poster Award, Development & Genetics Retreat, Columbia University Medical Center
2011 Grant-in-Aid for Young Scientists, Japanese Society for the Promotion of Science (JSPS)
2008 Goto Award for Excellent Research Activity, Gunma Univ. Graduate School of Medicine
2007 The best scientist presentation award in the Department of Medicine and Molecular Science, Gunma University School of Medicine, Gunma, Japan
2006 Board Certified by the Japanese Society of Internal Medicine
2003 Young Scientists' Global Center of Excellence Program Award from the Ministry of Education, Culture, Sports, Science and Technology of Japan

ACADEMIC SERVICE

National

2023-present NIH NIAID Investigator-Initiated Program Project Applications (P01) – Study section reviewer.

Local

2022-current S10 High-End Instrumentation grant, NIH Office of Research Infrastructure Programs (ORIP) - (Leica Stellaris Confocal Microscope), Columbia Center for Human Development – Committee Member

PROFESSIONAL ORGANIZATION AND SOCIETIES

- **Memberships and Positions**

2023-present Member of the American Society of Transplantation (AST)
2013-present Member of the International Society for Stem Cell Research (ISSCR)
2012-present Member of American Thoracic Society
2005-present Member of The Japanese Society of Internal Medicine
2005-2015 Member of The Japanese Respiratory Society

- **Journal Reviewer**

Communications Biology: ISSN: 2399-3642
The EMBO Journal: ISSN: 1460-2075
Cell Reports: ISSN: 2211-1247
Stem Cell Reports: ISSN: 2213-6711

- **Editorial Board**

Associate Editor: Frontiers in Cell and Developmental Biology

FELLOWSHIP AND GRANT SUPPORT

ONGOING RESEARCH SUPPORT:

SHARP CORPORATION AWARD, (PI: Mori) **06/01/21 – 12/31/23** **$137,350 DC** (Yr. 3)
Investigating the SHARP Plasma Cluster Ion (PCI)'s impact on human cells and disinfection efficacy against COVID-19 transmission. The primary goals of the proposal are to elucidate the effectiveness of SARS-CoV2 disinfection by PCI technology as a collaborative work with the SHARP company.

RX1 Bioprinter technology award: Instrumentation grant **12/01/2021 – 08/31/2023**
This project aims to develop a novel respiratory organ generation and maintenance approach by harnessing a microfluidics-assisted bioprinter as a collaborative work with the Aspect biosystems company.

PR191133 (PI: Mori) **09/01/2020-08/31/2023** **$399,990 DC** (Yr. 3)
Department of Defense, Peer Reviewed Medical Research Program Investigator-Initiated Research Award
A Novel Bioengineering Approach for Generation of Functional Lungs in Swine
We will investigate swine lung development and establish the experimental basis of lung generation in swine based on our accomplishment of CBC-mediated lung generation.

PR190557 (PI: Mori) **08/01/2020-07/31/2023** **$166,535 DC** (Yr. 3)
Department of Defense, Peer Reviewed Medical Research Program Expansion Award
Generating Humanized Lungs in Mice for Disease Modeling and Development of Personalized Medicine Therapies
This project focuses on advancing our CBC technology toward modeling humanized lung mice.

1R01HL148223-01 (PI: Mori) **07/15/2019 - 06/30/2023** **$330,797 DC** (Yr. 4)
NIH-NHLBI
Regulatory Mechanisms of Cell Competition in Lung Regeneration
The primary goals of the proposal are to provide new knowledge in the area of stem cell research for the regulation of lung organ niches and stem cell competence through cell competition during lung development and to control donor PSCs for efficient lung generation using mouse analyses.

PAST RESEARCH SUPPORT:

RX1 Bioprinter technology award: Instrumentation grant **12/01/2021 – 08/31/2023**
This project aims to develop a novel respiratory organ generation and maintenance approach by harnessing a microfluidics assisted bioprinter as a collaborative work with the Aspect biosystems company.

W81XWH-17-1-0139 DoD Discovery award (PI: Mori) **05/01/17 – 02/31/19**
Development of a Novel Approach to Regenerate Functional Lungs:
This project focuses on the development of a methodology for the regeneration of functional lungs utilizing blastocyst complementation and lung bud complementation

NIH-NHLBI R35 (PI: Cardoso; Co-investigator: Mori) **01/01/17–12/31/21**
Regulation of Airway Progenitor Cell Fate in Development and Regeneration: This project focuses on identifying and characterizing endogenous airway epithelial progenitors and their role in pulmonary disease.

PENDING RESEARCH SUPPORT:

PR231818 (PI: Mori) **01/01/2024-12/31/2027** **$2,626,293.00 DC** (Yr. 1)
Department of Defense, Peer Reviewed Medical Research Program Investigator-Initiated Research Award
Generating humanized lungs in swine by complementing bona fide lung precursor lineage
We are going to investigate the mechanism of entire human lung generation in swine based on our accomplishment of Foxa2^{+} lung lineage-based CBC lung generation.

1R01EB000000-00, R01 new, (PI: Mori) **04/01/2024 - 03/31/2028** **$499,765 DC** (Yr. 1)
NIH-NHLBI
Regulatory mechanism of interspecific cell competition
The goal of this study is to understand the molecular and cellular mechanism of human-to-swine cell competition in vitro and during embryogenesis

SHARP CORPORATION AWARD, (PI: Mori) **01/01/24 – 12/31/25** **$137,350 DC** (Yr. 1)
Investigating the SHARP Plasma Cluster Ion (PCI)'s impact on human cells and disinfection efficacy against COVID-19 transmission. The primary goals of the proposal are to elucidate the effectiveness of SARS-CoV2 disinfection by PCI technology as a collaborative work with the SHARP company.

1R21DE033532-01 new, (PI: Mori) **09/01/2023 - 08/31/2025** **$120,000 DC** (Yr. 1)
NIH-NIDCR
Explore the Mechanisms of Interspecific Organ Size Regulation During Salivary Gland Development
The goal of this study is to understand the molecular and cellular mechanism of organ size regulators during interspecific salivary gland generation.

United Therapeutics, New, (PI: Mori) **09/01/2023 – estimated $499,765 DC** (Yr. 1)
Explore the Method of Human Lung Organ generation in Swine.
The goal of this study is to develop human organ generation in swine

Cystic Fibrosis Foundation, New, (PI: Mori) **09/01/2023 – estimated $250,000 DC** (Yr. 1)
Generation of human lungs using human iPSC to model cystic fibrosis disease in swine
The goal of this study is to develop human organ generation from the iPSC of cystic fibrosis patients.

EDUCATIONAL CONTRIBUTIONS

- **Direct Teaching/Precepting/Supervising**

- **Advising and Mentorship**

My mentorship of postdoctoral researchers has resulted in significant achievements for our lab. I am pleased to announce that, due to their exceptional work and dedication, two of our lab members, Drs. Akihiro Miura and Youngmin Hwang were selected as oral presenters for the Medicine Grand Rounds Fellows Research Presentations II on June 7, 2023. This special event provided a fantastic opportunity for our researchers to share our innovative work and gain valuable feedback from the broader scientific community. The details below also highlight the valuable contributions they are making to the field. As we move forward, I will continue to foster an environment of diversity, learning, and discovery, supporting our researchers in reaching new heights in their careers.

2021-Present: **Dr. Zurab Ninish**, Senior Technician (Veterinary), Columbia Center for Human Development.

In this role, I provide ongoing guidance to Dr. Ninish, to help him navigate the technical requirements of his position effectively. This mentorship encompasses a broad range of areas, including laboratory work, experimental design, troubleshooting technical issues, and managing finances. At our biweekly meetings, I assist Dr. Ninish in coordinating his tasks, setting goals, and monitoring progress. We also discuss potential areas for improvement and innovative strategies to enhance his performance. Additionally, I oversee his involvement in the financial aspects of our work, guiding him in

managing laboratory expenses efficiently. Through this mentorship, I aim to enhance Dr. Ninish's skills and understanding of our research processes, thereby fostering his career growth and contributing to the overall productivity of our lab.

2020-present: **Dr. Akihiro Miura**, Postdoctoral Fellow, Columbia Center for Human Development.

Dr. Miura, a thoracic surgeon from Japan, joined my lab last year and has since become one of our most productive postdocs. His self-motivated dedication to science has greatly contributed to our lab discussions and advanced our work on the challenging project of whole lung generation in mice. In this project, we sought to push the boundaries of our lung generation technology by utilizing conditional blastocyst complementation and novel mouse models. In simple terms, we aimed to generate vacant niches in both lung epithelial and mesenchymal areas that could be filled by donor pluripotent stem cells. Dr. Miura's exceptional performance led to the successful generation of whole lungs in mice. Nearly the entire lung epithelium and mesenchyme were fully complemented by donor cells, marking a significant milestone in the field of regenerative medicine. This ground-breaking research is currently under the final review for publication (***Miura et al., 2023***). Additionally, Dr. Miura presented this work as a poster at a 2022 FASEB meeting and as an oral presentation for the Medicine Grand Rounds Fellows Research Presentations II on June 7,2023. His achievements bear testament to his dedication and productivity, as well as the fertile ground for scientific advancement that my lab provides.

2020-present: **Dr. Youngmin Hwang**, Postdoctoral Research Scientist, Columbia Center for Human Development.

I have been serving as a mentor for Dr. Youngmin Hwang, a postdoctoral research scientist, Columbia Center for Human Development since 2020. Despite Dr. Hwang's initial background being primarily in material science, with no prior experience in culturing induced pluripotent stem cells (iPSC) or adult airway stem cells, he has excelled under my comprehensive technical and intellectual mentorship. Through his dedicated efforts, Dr. Hwang has been successful in generating rat iPSCs and establishing a novel method of a co-culture model with mouse blastocysts, which he is currently manipulating with adeno-associated viruses (AAV). This work is now under manuscript preparation. In addition, Dr. Hwang has been involved in an exciting project evaluating the effect of Plasmacluster ions (PCI) on differentiation into airway cells. His significant contributions in this area have resulted in two patent applications pending approval. This project was conducted in collaboration with SHARP Corporation, and the work's findings have been recognized through his selection to present at the Medicine Grand Rounds Fellows Research Presentations II on June 7, 2023. Furthermore, he has been conducting collaborative research with Aspect-bio Company utilizing a state-of-the-art microfluidics-based bioprinter. He has established a pioneering isolation and culture method for pig mesothelial cells for bioprinting into scaffolds for cultivating lung organoids (manuscript in preparation). Dr. Hwang's dedication and innovative thinking have made him one of the most productive postdocs in my laboratory. His achievements clearly demonstrate the power of effective mentorship combined with a willingness to learn and venture into unfamiliar scientific territories.

2020-present: **Dr. Anri Sawada**, Postdoctoral Fellow, Columbia Center for Human Development.

Dr. Sawada, a pathologist specializing in renal medicine, was the first postdoc to join my lab. Although he had no prior experience in culturing pluripotent stem cells, his dedication and willingness to learn, combined with my direct mentoring and technical teaching, have made him one of the most skilled individuals in the lab. This skill set enabled him to create a novel medium, referred to as "Medium C," which has proven to be effective in efficient reprogramming from somatic cells to iPSCs and the culture of robust pluripotent stem cells derived from a variety of species, including mice, humans, baboons, and pigs. The advantage provided by "Medium C" has led to significant findings. Notably, Dr. Sawada discovered the interspecific super competition factor (iSCF) during early embryogenesis, a finding that holds significant potential for our understanding of embryonic development across species. The manuscript detailing these findings is currently in preparation. Dr. Sawada's transformation from a postdoc with no experience in stem cell culture to a researcher making significant discoveries is a testament to our approach's productive and nurturing environment.

2020-2023: **Dr. Junichi Tanaka**, Postdoctoral Fellow, Columbia Center for Human Development.

Dr. Tanaka is a dentist and developmental biologist from Japan. He has a strong background in developmental biology and stem cells, particularly in the area of salivary gland biology. Leveraging his solid foundation and my mentorship, he has been able to successfully generate a functional salivary gland in mice using our Conditional Blastocyst Complementation (CBC) model. This impressive accomplishment is currently documented in a manuscript under preparation (**Tanaka et al., 2023, in preparation**). Furthermore, Dr. Tanaka has made a groundbreaking discovery that has the potential to revolutionize the field of organ generation. Using sophisticated interspecific cell-cell contact dependent molecular manipulation, combined with cross-species single-cell RNA sequencing analyses, he has unearthed crucial signaling pathways that regulate the initiation of interspecific cell competition during early embryogenesis. This monumental discovery can potentially resolve the longstanding challenge of interspecific barriers that hinder human lung generation in

host animals. This work is currently being documented in a manuscript under preparation. Dr. Tanaka's scientific acumen, dedication, and the potential for pioneering work in the field of organ generation are a testament to the effectiveness of our collaborative efforts.

2020-present: **Dr. Yuko Shimamura**, Postdoctoral Fellow, Columbia Center for Human Development

As a mentor to Dr. Shimamura, I have provided comprehensive guidance and instruction for her study on the regulatory mechanism for lung organ size, which appears to be conserved between humans and large animals, but not in mice. This complex and challenging project required an understanding of various disciplines, including molecular biology, pathology, and gene manipulation - areas in which Dr. Shimamura initially had no background. We have biweekly meetings, approximately two hours each, to discuss progress and plan future steps. Despite these challenges, under my mentorship, Dr. Shimamura has demonstrated exceptional growth and commitment to her work. She successfully established a human induced pluripotent stem cell (iPSC)-derived lung organoid, swine, and mouse lung explant models using Adeno-Associated Virus (AAV) and a CRISPR-Cas9 inducible system. These achievements were even more impressive considering the intricate cross-disciplinary nature of the methodologies she employed. Moreover, we have collaborated with Dr. Cai from Texas, an expert in AI-based bioinformatics, to perform genome-wide analyses across species. With this collaboration and her hands-on work, Dr. Shimamura has made significant contributions to our understanding of lung organ size regulation. She has identified critical developmental timing and signaling pathways during swine lung development (**Shimamura et al., 2023, under review**). My mentorship has empowered Dr. Shimamura to navigate the complexities of this multidisciplinary project successfully, fostering her skills and knowledge and preparing her for future success in her scientific career.

2022-Present: **Ms. Sherlly Dolmuz**, Undergraduate Columbia University Student, Columbia Center for Human Development.

In my role as a mentor for Ms. Dolmuz, I have undertaken a comprehensive approach to her education and training. This includes addressing technical issues she encounters, assigning experienced lab members to aid in her projects, expanding her scientific knowledge, and providing critical analysis and feedback on her experimental results. We have biweekly meetings, approximately two hours each, to discuss progress and plan future steps. Her current project is to establish a novel genome-editing tool, a program that we initiated in 2023. Through my mentorship, she is not only gaining hands-on experience in groundbreaking research but also developing essential skills for a successful career in scientific research. My overall goal is to inspire, nurture, and cultivate her interest and passion in the field.

2020-2022: **Dr. Hemanta Sarmah**, Postdoctoral Research Scientist, Columbia Center for Human Development.

Dr. Sarmah is a developmental biologist from India. His self-motivated dedication to science advanced our intricate project on swine genome manipulation for the generation of lung agenesis swine. His thorough and diligent approach to the task, coupled with an unwavering commitment to excellence, resulted in a publication in the well-respected journal**,** ***Frontiers in Cell and Developmental Biology*** **(Sarmah et al., 2023)**. This accomplishment speaks volumes about Dr. Sarmah's competency as a scientist and his potential to make significant contributions to the field of developmental biology.

2020-2021: **Dr. Tatsuya Nagano,** Visiting Associate Research Scientist, Columbia Center for Human Development.

As a mentor to Dr. Nagano, I provided guidance and instruction in the development of a knock-in cassette via the CRISPR-Cas9 genome-editing tool. This work was specifically aimed at enabling us to exclude the chimerism of human induced pluripotent stem cells (iPSCs) in the neuronal lineage. Despite the limited duration of his study abroad program, spanning only half a year, Dr. Nagano successfully constructed the knock-in cassette. He further established a directed differentiation protocol for human iPSCs into neuronal lineages. This was an essential step to evaluate the effect of the knock-in before proceeding with the injection into host animal blastocysts. His accomplishments during this short period underscore the effectiveness of my mentorship in nurturing his technical abilities, critical thinking, and experimental planning skills. As he continues in his career, I am confident that he will leverage these valuable experiences in his future scientific endeavors.

Additional Teaching:
2018 – 2020: Yizhuo Zhou, Associate Research Scientist, Columbia Center for Human Development.
2019 – 2021: Ms. Rosemary Gordon-Schneider, Laboratory Technician, Columbia Center for Human Development.
2017 – 2019: Ms. Mayu Ohta, Senior Research Technician, Columbia Center for Human Development.

2015 - 2020: Benjamin van Soldt, Graduate Student, Department of Genetics & Development, Columbia University.
2015 – 2019: Carlos Serra, MD/PhD Candidate – Columbia University Graduate Schoole & Universidade do Minho, Escola de Medicina, Braga, Portugal.
2014 – 2019: Ying Yang, Graduate Student, Department of Genetics & Development, Columbia University.
2013 – 2019: Maria Stupnikov, Graduate Student, Department of Genetics & Development, Columbia University.
2017: Summer Supervisor, Nicholas J. Heller, Columbia University
2016: Summer Supervisor, Tianhao Xu, Columbia University Fu Foundation School of Engineering and Applied Science
2011-2013 John Mahoney, Graduate Student, Boston University.
2010-2011 Kemala Mantilidewi, Graduate Student, Boston University.

- **Educational Administration and Leadership**

2022 – Present Committee member for S10 High-End Instrumentation grant, Columbia Center for Human Development– funded in 2022
2022 Uehara foundation fellowship writing support and review for Dr. Yuri Kondo in my lab. – funded in 2023.
2022 TOYOBO foundation fellowship writing support and review for Dr. Dai Shimizu in my lab. – funded in 2023.
2022 DoD grant writing support and review for Dr. Xin in Wang lab, CCHD. – Pending.
2021 DoD discovery award grant writing support and review for Dr. Huachao in Que lab, CCHD – funded in 2022.
2021 Uehara foundation fellowship writing support and review for Dr. Akihiro Miura in my lab. – funded in 2022.
2020 Uehara foundation fellowship writing support and review for Dr. Junichi Tanaka in my lab. – funded in 2021.
2019 writing support and review for Dr. Akihiro Miura Research Fellowship for Young Scientists from Japan Society for the Promotion of Science (JSPS): Overseas Challenge Program for Young Researchers– funded in 2020.

COMMUNITY EDUCATION:
News TV: (PI: Mori) World's first*1 report: The potential effect of Plasmacluster Technology on reducing viscous airway mucus that may relieve asthma symptoms using airway stem cell culture.
Youtube, in Japan., 610,000 viewers as of July 2023 https://www.youtube.com/watch?v=WBZNdpuaL7k

Clinical or Public Health Innovations

PATENTS & INVENTIONS

- Patents: CU23296/ Mori/ (pending IIA 61888) (SRA 55861)
  1. Suppressive effect of asthma symptoms by ions: (Inventors: Mori, Huang, Yagi (SHARP))
  2. Corona infection control effect by ions: (Inventors: Mori, Huang, Yagi (SHARP))

PEER-REVIEWED SELECTED ARTICLES:

ORIGINAL, PEER-REVIEWED RESEARCH PUBLICATIONS IN PRINT OR OTHER MEDIA

Miura A, Sarmah H, Tanaka J, Hwang Y, Sawada A, Shimamura Y, Fang Y, Shimizu D, Ninish Z, Suer JL, Dubois N, Davis J, Toyooka S, Wu J, Que J, Hawkins FJ, Lin SH, **Mori M†** Conditional blastocyst complementation of a defective Foxa2 lineage efficiently promotes generation of the whole lung, eLife, 2023, ***bioRxiv*** 2022.10.31.514628, doi: org/10.1101/2022.10.31.514628 †: **corresponding author**

Shimamura Y*, Tanaka J*, Miura A, Kakiuchi M, Sarmah H, Miura A, Hwang Y, Sawada A, Ninish Z, Yamada K, Cai J*, **Mori M†*** A developmental program that regulates mammalian organ size offsets evolutionary distance, ***bioRxiv*** 2022.10.19.512107; doi: org/10.1101/2022.10.19.512107†: **corresponding author**

Mori M†, Furuhashi K, Danielsson AJ, Hirata Y, Yamamoto M, Lin SC, Ohta M, Riccio P, Takahashi Y, Xu X, Emala WC, Lu C, Nakauchi H†, Cardoso VW†. Generation of functional lungs via conditional blastocyst complementation using pluripotent stem cells, ***Nat Med.*** 2019, Nov;25(11):1691-1698. doi: 10.1038/s41591-019-0635-8. PMID: 31700187. †: **corresponding author**

Mori M, Hazan R, Danielian PS, Mahoney JE, Li H, Lu J, Miller ES, Zhu X, Lees JA, Cardoso WV. Cytoplasmic E2f4 forms organizing centres for initiation of centriole amplification during multiciliogenesis. ***Nature Commun.*** 2017 Jul 4;8:15857. PMID:28675157

Mori M, Mahoney JE, Stupnikov MR, Paez-Cortez JR, Szymaniak AD, Varelas X, Herrick DB, Schwob J, Zhang H, Cardoso WV.Notch3-Jagged signaling controls the pool of undifferentiated airway progenitors. ***Development.*** 2015 Jan 15;142(2):258-67. PMID:25564622

Kurmann AA, Serra M, Hawkins F, Rankin SA, **Mori M**, Astapova I, Ullas S, Lin S, Bilodeau M, Rossant J, Jean JC, Ikonomou L, Deterding RR, Shannon JM, Zorn AM, Hollenberg AN, Kotton DN. Regeneration of Thyroid Function by Transplantation of Differentiated Pluripotent Stem Cells. ***Cell Stem Cell.*** 2015 Nov 5;17(5):527-42. Epub 2015 Oct 22. PMID:26593959

Murata Y, Kotani T, Supriatna Y, Kitamura Y, Imada S, Kawahara K, Nishio M, Daniwijaya EW, Sadakata H, Kusakari S, **Mori M**, Kanazawa Y, Saito Y, Okawa K, Takeda-Morishita M, Okazawa H, Ohnishi H, Azuma T, Suzuki A, Matozaki T. Protein tyrosine phosphatase SAP-1 protects against colitis through regulation of CEACAM20 in the intestinal epithelium. ***Proc Natl Acad Sci U S A***. 2015 Aug 4;112(31):E4264-71. PMID:26195794

Mahoney JE, **Mori M**, Szymaniak AD, Varelas X, Cardoso WV. The hippo pathway effector Yap controls patterning and differentiation of airway epithelial progenitors. ***Dev Cell.*** 2014 Jul 28;30(2):137-50. Epub 2014 Jul 17. PMID:25043473

Mantilidewi KI, Murata Y, **Mori M**, Otsubo C, Kotani T, Kusakari S, Ohnishi H, Matozaki T.
Shear stress-induced redistribution of vascular endothelial-protein-tyrosine phosphatase (VE-PTP) in endothelial cells and its role in cell elongation. ***J Biol Chem.*** 2014 Mar 7;289(10):6451-61. Epub 2014 Jan 22. PMID:24451369

Mori M, Murata Y, Kotani T, Kusakari S, Ohnishi H, Saito Y, Okazawa H, Ishizuka T, Mori M, Matozaki T. Promotion of cell spreading and migration by vascular endothelial-protein tyrosine phosphatase (VE-PTP) in cooperation with integrins. ***J Cell Physiol.*** 2010 Jul;224(1):195-204. PMID:20301196

Murata Y, **Mori M**, Kotani T, Supriana Y, Okazawa H, Kusakari S, Saito Y, Ohnishi H and Matozaki T. Tyrosine phosphorylation of R3 subtype receptor-type protein tyrosine phosphatase and their complex formations with Grb2 or Fyn. ***Genes. Cells***. 15: 513-524, 2010 PMID: 20398064

Matozaki T, Murata Y, **Mori M**, Kotani T, Okazawa H, Ohnishi H. Expression, localization, and biological function of the R3 subtype of receptor-type protein tyrosine phosphatases in mammals.
Cell Signal. 2010 Dec;22(12):1811-7. Epub 2010 Jul 12. Review. PMID:20633639

OTHER PEER-REVIEWED PUBLICATIONS IN PRINT OR OTHER MEDIA

Tsuji M, Nair S M, Masuda K, Castagna C, Chong Z Darling L T Seehra K, Hwang Y, Ribeiro L A, Ferreira M G, Corredor L, Coelho-Dos-Reis GA J, Tsuji Y, **Mori M**, Boon CM A, Diamond S M, Huang Y, Ho D D. ***Nat Commun.*** 2023 Jul 5;14(1):3959. doi: 10.1038/s41467-023-39738-1.

Tanaka J*, Senpuku H, Ogawa M, Yasuhara R, Ohnuma S, Takamatsu K, Watanabe T, Mabuchi Y, Nakamura Y, Ishida S, Sadaoka T, Takaki T, Shirota T, Shimane T, Inoue T, Sakai T, **Mori M**, Tsuji T, Saito I, and Mishima K. Human induced pluripotent stem cell-derived salivary gland organoids model SARS-CoV-2 infection and replication, ***Nat Cell Biol.,*** Oct (17) 2022, doi.org/10.1038/s41556-022-01007-6

Serra CFH, Liu H, Qian J, **Mori M**, Lu J, Cardoso WV. Prominin 1 and Notch regulate ciliary length and dynamics in multiciliated cells of the airway epithelium. ***iScience***. 2022 Jul 14;25(8):104751. PMID: 35942101

Gwon K, Park JD, Lee S, Choi WI, Hwang Y, **Mori M**, Yu JS, Lee DN. Injectable hyaluronic acid hydrogel encapsulated with Si-based NiO nanoflower by visible light cross-linking: Its antibacterial applications, ***Int J Biol Macromol.*** 2022 May 31;208:149-158. PMID: 35304194.

Hazan R, **Mori M**, Danielian PS, Guen VJ, Rubin SM, Cardoso WV, Lees JAE2F4's cytoplasmic role in multiciliogenesis is mediated via an N-terminal domain that binds two components of the centriole replication machinery, Deup1 and SAS6. **Mol Biol Cell.** 2021 Oct 1;32(20):ar1. doi: 10.1091/mbc.E21-01-0039. Epub 2021 Jul 14.PMID: 34260288.

Yang Y, Riccio P, Schotsaert M, **Mori M**, Lu J, Lee DK, García-Sastre A, Xu J, Cardoso WV. Spatial-Temporal Lineage Restrictions of Embryonic p63+ Progenitors Establish Distinct Stem Cell Pools in Adult Airways. ***Dev Cell.*** 2018 Mar 26;44(6):752-761.e4. PMID: 29587145

Hou Z, Wu Q, Sun X, Chen H, Li Y, Zhang Y, **Mori M**, Yang Y, Que J, Jiang M. Wnt/Fgf crosstalk is required for the specification of basal cells in the mouse trachea. ***Development***. 2019 Feb 11;146(3). PMID: 30696710

Zhang Y, Yang Y, Jiang M, Huang SX, Zhang W, Al Alam D, Danopoulos S, **Mori M**, Chen YW, Balasubramanian R, Chuva de Sousa Lopes SM, Serra C, Bialecka M, Kim E, Lin S, Toste de Carvalho ALR, Riccio PN, Cardoso WV, Zhang X, Snoeck HW, Que J. 3D Modeling of Esophageal Development using Human PSC-Derived Basal Progenitors Reveals a Critical Role for Notch Signaling. ***Cell Stem Cell.*** 2018 Sep 13. PMID: 30244870

Tsao PN, Matsuoka C, Wei SC, Sato A, Sato S, Hasegawa K, Chen HK, Ling TY, **Mori M**, Cardoso WV, Morimoto M. Epithelial Notch signaling regulates lung alveolar morphogenesis and airway epithelial integrity. ***Proc Natl Acad Sci U S A.*** 2016 Jul 19;113(29):8242-7. Epub 2016 Jun 30. PMID:27364009

REVIEWS, CHAPTERS, MONOGRAPHS, EDITORIALS

Sarmah H, Sawada A, Hwang Y, Miura A, Shimamura Y, Tanaka J, Yamada K, **Mori M†**
Towards human organ generation using interspecies blastocyst complementation: Challenges and perspectives for therapy, ***Frontiers, Cell and Developmental Biology,*** 2023 Jan 19;11:1070560. doi: 10.3389/fcell.2023.1070560. eCollection 2023., †: **corresponding author**

Mori M, and Cardoso WV. Lung Progenitor Cell Specification and Morphogenesis. Ed.: R. Harding, K. E. Pinkerton, ***The Lung: Development, Aging and the Environment,*** Elsevier Science, Oct 2014. Academic Press ISBN: 978-0-12-799941-8.

MEETINGS/INVITED POSTER PRESENTATIONS (see oral presentation below)

2017 Poster session, "Cytoplasmic E2f4 forms organizing centers for initiation of centriole amplification during multiciliogenesis." Gordon Research Conference, New Hampshire.
2015 Poster session, "Notch regulation of the balance of airway progenitors in the lung." American Thoracic Society Meeting, Denver, Colorado.
2015 Poster session, "Notch3-Jagged signaling controls the pool of undifferentiated airway progenitors." Keystone, Colorado.
2014 Poster session, "E2f4 regulation of ciliogenesis in the airway epithelium," FASEB, Vermont.
2013 Poster highlight discussion, "The role of E2f4 in airway differentiation," American Thoracic Society Meeting, Philadelphia, PA.
2012 Poster session, "The role of E2f4 in airway differentiation." FASEB Summer Research Conference, Vermont.
2011 Poster session, "VE-PTP regulates cell spreading and migration." FASEB Summer Research Conference, Colorado.

OTHER MEDIA

News TV: (PI: Mori) World's first*1 report: The potential effect of Plasmacluster Technology on reducing viscous airway mucus that may relieve asthma symptoms using airway stem cell culture.
Youtube, in Japan., 610,000 viewers as of July 2023 https://www.youtube.com/watch?v=WBZNdpuaL7k

THESIS

N/A

OTHER NON-PEER REVIEWED PUBLICATIONS IN PRINT OR OTHER MEDIA

SHARP company Press Release: (PI: Mori) World's first*1 report: The potential effect of Plasmacluster Technology on reducing viscous airway mucus that may relieve asthma symptoms using airway stem cell culture. Validated at Columbia University Irving Medical Center, USA. October 13, 2022. https://global.sharp/corporate/news/221013-b.html

Press release and news of World's first*1 report of functional lung generation in USA and Japan, November, 2019: : (PI: Mori)
https://www.technologynetworks.com/cell-science/news/stem-cell-transplants-used-to-grow-fully-functional-lungs-in-mice-327048

https://www.qlifepro.com/news/20191118/generation-of-functional-lungs.html

https://www.qlifepro.com/news/20191118/generation-of-functional-lungs.html

INVITED PEER-SELECTED PRESENTATIONS AT REGIONAL, NATIONAL OR INTERNATIONAL LEVELS:

2023 Invited Oral Speaker, "Conditional blastocyst complementation of a defective Foxa2 lineage efficiently promotes generation of the whole lung," The Japanese Respiratory Society - Annual Meeting 2023, Tokyo, Japan.

2023 Invited Oral Speaker, "Conditional blastocyst complementation of a defective Foxa2 lineage efficiently promotes generation of the whole lung," NIH-NHLBI PCTC conference 2023, Maryland, DC, USA.

2022 Invited Oral Speaker, "Generation of whole lungs by targeting a bona fide lung precursor lineage," CSTE conference 2022, LA, CA, USA.

2022 Invited Oral Speaker, "Exploring the regulatory mechanism of entire lung generation in mice and swine", FASEB conference, The Lung Epithelium Conference: In Health and Disease, Saxtons River, VT

2022 Invited Oral Speaker, "Generation of functional lungs via conditional blastocyst complementation using pluripotent stem cells," International Experimental Biology and Medicine, Memphis, USA

2021 Invited Oral Speaker, "Generation of functional lungs via conditional blastocyst complementation using pluripotent stem cells," The 25th Congress of the Asian Pacific Society of Respirology (APSR) 2021, Japan

2020 Invited Oral Speaker, "Generation of functional lungs via conditional blastocyst complementation using pluripotent stem cells," Stem Cell Club Meeting in U Penn IRM, PA

2019 Invited Oral Speaker, "Cell Specification or Proliferation? Which Will Win for an Organ Generation?", Keystone Symposia: Cell Competition in Development and Disease (B6), CA

2017 Invited Speaker, "Development of Novel Approaches for Functional Lung Regeneration in Vivo", Briscoe-King Lung Club 2017-18, NY

2015 Invited Speaker, "Notch3-Jagged signaling controls the pool of undifferentiated airway progenitors." 2ND ANNUAL Notch Mini-Symposium, Columbia University, NY

2015 Invited Lecture, "Analysis of the mechanism of regenerative regulation of terminally differentiated cells in the lung airways." Satellite Meeting, Japanese Respiratory Society, Tokyo (Japan).

2015 Invited Speaker, "Regulation of progenitor pools and their transition to differentiation in airways." Frontier Topics Seminar at Kobe University, Kobe (Japan).

2015 Invited Speaker: "Transition zone: The dramatic change of lung progenitors to terminally differentiated cells." CDB seminar at Riken Institute, Kobe (Japan).

Teaching statement and teaching Philosophy
Munemasa Mori, M.D., Ph.D.

The motivation to become a researcher evolved from my invaluable clinical experience as a pulmonologist treating patients with refractory pulmonary diseases. The limited treatment options for patients with end-stage pulmonary disease instilled a personal mission to understand better, the underlying mechanisms behind refractory pulmonary diseases. I am passionate about seeking new knowledge. My research interests in lung progenitor expansion, differentiation, and humanized organ generation will lead to innovative discoveries within the emerging field of evolutionary developmental biology and stem cell biology. I welcome the opportunity to share this passion and exciting research direction by serving as a mentor to medical students, technicians, graduate students, postdoctoral fellows, and research scientists. Past and current mentorships have offered the opportunity to work with individuals from diverse backgrounds such as African American, Caucasian and Hispanic American, Pan-Asian (Chinese, Indian, Japanese, Korean, Indonesian), and European. I look forward to educating the next generation of basic and translational scientists and more than welcome the occasion to mentor underrepresented racial minority communities through programs promoting diversity.

My educational background:

Professor Takashi Matozaki at the Institute for Molecular and Cellular Regulation at Gunma University, one of the largest institutes in the North Kanto area of Japan served as my Ph.D. mentor. Dr. Matozaki was a profound influence, who instilled a desire for knowledge and utilized cutting-edge technology in molecular biology. Training included the generation of monoclonal and polyclonal antibodies, the establishment of cell lines by drug selections, gene and genome manipulations, knockdown or knockout technology, production of adenoviruses, and the generation of conditional knockout mice. As a member of Dr. Matozaki's lab, I had the opportunity to teach science in English to undergraduate students studying abroad from Indonesia. My teaching methodology included not only scientific techniques, but also the fundamentals of observation and hypothesis formation.

My postdoctoral training in the United States began at Boston University under the mentorship of Professor Wellington V. Cardoso. Dr. Cardoso's mentorship has been invaluable. In addition to providing opportunities to learn new scientific skills, his enthusiasm for science and care for his students and colleagues inspired my research goals. His management style and his love for human beings encouraged his co-workers to go far beyond standard requirements. Based on this experience, I have refined my teaching to consider the individual student's purpose and goals. I believe that a more personalized approach involving patience, listening and discussion will allow the student to refine a step-wise scientific hypothesis and personal growth experience that will cultivate a passion for science and better research outcomes.

I have had the opportunity to supervise undergraduate students, summer students, and graduate students under the Columbia Center for Human Development (CCHD), director, Wellington V. Cardoso. Now, as a Principal Investigator and mentor, I am establishing a research program that will offer educational opportunities for the post-doctoral researchers, technicians and students that work with me. (See the following list).

TEACHING/MENTORING ACTIVITIES (CURRENT AND PAST LABORATORY TRAINEES):

2023-present Mentor for Yuri Kondo, a postdoc fellow at Columbia Center for Human Development.

2023-present Mentor for Dai Shimizu, a postdoc fellow at Columbia Center for Human Development.

2022-present Mentor and supervisor for Ms. Sherlly V. Dolmuz, an undergraduate student at Columbia Center for Human Development.

2022-present Mentor and supervisor for Ms. Shereya Kumar, an undergraduate student at Columbia Center for Human Development
2021-present Mentor and supervisor for Dr. Zurab Ninish, a leading technician at Columbia Center for Human Development.
2021-present Mentor and supervisor for Ms. Stacey Nozeil, senior research technician, Columbia Center for Human Development.
2021-present Supervisor for Xiangyi Ke – Columbia University Graduate Student, MD/PhD Candidate
2020-2021 Mentor for Dr. Tatsuya Nagano, Visiting Associate Research Scientist, Columbia Center for Human Development.
2021-2023 Mentor for Dr. Hemanta Sarhmah, postdoctoral fellow, Columbia Center for Human Development.
2021-present Mentor for Dr. Yuko Shimamura, postdoctoral fellow, Columbia Center for Human Development.
2020-present Mentor for Dr. Youngmin Hwang, postdoctoral fellow, Columbia Center for Human Development.
2020-present Mentor for Dr. Akihiro Miura, postdoctoral fellow, Columbia Center for Human Development.
2020-present Mentor for Dr. Anri Sawada, postdoctoral fellow, Columbia Center for Human Development.
2020 - Present Supervisor for Yizhuo Zhuo, postdoctoral fellow, Columbia Center for Human Development.
2019-2021, Mentor and supervisor for Ms. Rosemary Gordon-Schneider, lab tech, Columbia Center for Human Development.
2019 -2019 summer: Mentor for Brent Mayfield, graduate student, Dept. of Genetics & Development, Columbia University.
2017 – 2019: Mentor and supervisor for Ms. Mayu Ohta, senior research technician, Columbia Center for Human Development.
2017 - Present Supervisor for Carlos Serra, MD/PhD program – Columbia University Graduate Student, MD/PhD Candidate, Universidade do Minho, Escola de Medicina, Braga, Portugal. **2017: Summer** Supervisor for Nicholas J. Heller, Columbia University
2016: Summer Supervisor for Tianhao Xu, Columbia University Fu Foundation School of Engineering and Applied Science
2013 - Present Teaching Assistant for graduate students: Maria Stupnikov, Ying Yang and Benjamin van Soldt, Department of Genetics & Development, Columbia University.
2011-2013 Teaching assistant for John Mahoney, graduate student, Boston University.
2010-2011 Supervisor for Kemala Mantilidewi, graduate student, Boston University.

Besides the listed opportunities above, I have extensive experience as a trainer for confocal microscopy in the CCHD specialized microscopy core. I have trained more than 60 users from extensive, diverse backgrounds. Based on this, I have now being a committee member for supervising the usage of multiplex Stellaris Leica confocal microscopy.

In addition, as a member of the CCHD, I have had the opportunity to collaborate with faculty from various disciplines within Columbia University, as well as on national and international levels. As a mentor, I will continue my educational journey and share my experiences with my trainees. I firmly believe that science is not just an isolated subject limited to a textbook – educating science under the exciting program allows us to share our scientific passion and provide equal learning opportunities to bridge the community outgrowth regardless of the racial diversities, ultimately harmonizing the miscellaneous uniqueness.

Statement of Contributions to Diversity

Munemasa Mori, MD, Ph.D.

As a biomedical research scientist with experience in intramural and extramural university activities, I am aware that efforts are required to promote diversity programs to recruit outstanding female and underrepresented minority scholars. It has been apparent during my training that some minority groups are clearly underrepresented in numerous fields of biomedical research. At the same time, I also have witnessed how training opportunities have helped underrepresented minorities pursue careers in biomedical research and health care. While at Boston University/Columbia University, I worked with underrepresented minorities at various educational levels in our lab and center. We supported the efforts of our summer students from Hispanic and African American backgrounds. It has been a pleasure to see these research students working and studying together and to help them with their experiments.

As a faculty member, I will follow established principles to help improve diversity and inclusiveness in the biomedical workforce. I am more than happy to engage my lab in training programs designed to enhance diversity to help underrepresented students and scholars move to the next stage of their biomedical research education or career. Diversity is essential in research for organic scientific stimulation in a safe, educational environment that can lead to an interactive, interdisciplinary, and respectful community. As an RO1 (NHLBI) funded principal investigator, I will respond to new academic and support programs from the NIH - supplemental funding opportunities for minority trainees. I will stay informed on national, state, and university policies for programs supporting underrepresented minorities in the biosciences. I will welcome opportunities to participate in diversity programs and be a part of this exciting movement in your University's community.

Contact information of three references:

Wellington V. Cardoso, M.D., PhD

Professor of Medicine and Genetics & Development
Director, Columbia Center for Human Development

650 West 168th Street
BB 8-812
New York, NY 10032
P: (212) 342-3971

wvc2104@cumc.columbia.edu

http://cardosolab.com/members.html

Darrell N. Kotton, MD

David C. Seldin Professor of Medicine
Director, Center for Regenerative Medicine (CReM)
Boston University and Boston Medical Center
670 Albany St, 2nd floor CReM
Boston, MA 02118
P: 617-358-0736
dkotton@bu.edu
www.kottonlab.com
www.bumc.bu.edu/stemcells

Hiromitsu Nakauchi, M.D., PhD

Professor of genetics at Stanford University, Director of newly established Center for Stem Cell Biology and Regenerative Medicine at the Institute of Medical Science at The University of Tokyo (IMSUT)

265 Campus Drive, Lorry I. Lokey Stem Cell Research Building
Rm G3078 (3rd Floor)
Stanford CA 94305

P: (650)497-4365

nakauchi@stanford.edu

noriko.kawahara@stanford.edu(admin)

http://med.stanford.edu/nakauchilab.html

nature medicine

LETTERS

https://doi.org/10.1038/s41591-019-0635-8

Generation of functional lungs via conditional blastocyst complementation using pluripotent stem cells

Munemasa Mori[1,8*], Kazuhiro Furuhashi[2], Jennifer A. Danielsson[3], Yuichi Hirata[2], Miwako Kakiuchi[2], Chyuan-Sheng Lin[4], Mayu Ohta[1], Paul Riccio[1], Yusuke Takahashi[5,6], Xinjing Xu[7], Charles W. Emala[3], Chao Lu[7], Hiromitsu Nakauchi[5,6,8*] and Wellington V. Cardoso[1,7,8*]

Millions of people worldwide with incurable end-stage lung disease die because of inadequate treatment options and limited availability of donor organs for lung transplantation[1]. Current bioengineering strategies to regenerate the lung have not been able to replicate its extraordinary cellular diversity and complex three-dimensional arrangement, which are indispensable for life-sustaining gas exchange[2,3]. Here we report the successful generation of functional lungs in mice through a conditional blastocyst complementation (CBC) approach that vacates a specific niche in chimeric hosts and allows for initiation of organogenesis by donor mouse pluripotent stem cells (PSCs). We show that wild-type donor PSCs rescued lung formation in genetically defective recipient mouse embryos unable to specify (due to *Ctnnb1*^{cnull} mutation) or expand (due to *Fgfr2*^{cnull} mutation) early respiratory endodermal progenitors. Rescued neonates survived into adulthood and had lungs functionally indistinguishable from those of wild-type littermates. Efficient chimera formation and lung complementation required newly developed culture conditions that maintained the developmental potential of the donor PSCs and were associated with global DNA hypomethylation and increased H4 histone acetylation. These results pave the way for the development of new strategies for generating lungs in large animals to enable modeling of human lung disease as well as cell-based therapeutic interventions[4–6].

Nearly 12 million adults in the United States, or 5% of the population, have been diagnosed with chronic obstructive pulmonary disease, and about 180,000 patients die annually with end-stage refractory lung diseases[1]. The only option currently available is lung transplantation, and patients die nearly every day without ever receiving this treatment because of the scarcity of donor organs[7]. Bioengineering approaches for lung regeneration using endogenous progenitors or human PSCs in decellularized scaffolds emerged as promising options[2,8–11]. However, modeling the structural and functional complexities of the lung in vitro has been insurmountably challenging given its extraordinary cellular diversity, with more than 40 cell types from all embryonic layers, and its complex three-dimensional (3D) architecture that demands precise alignment of the epithelial and vascular components to form nearly 480 million alveoli for efficient gas exchange[12,13]. Lastly, maintaining tissue integrity and homeostasis in the presence of the continuous periodic changes in mechanical forces by breathing movement and by the high blood-flow output in the vascular compartment represents a major bioengineering problem to overcome[8,9]. We posited that the generation of a functional lung as a platform for regenerative purposes could be achieved if these challenges were bypassed by modeling lung organogenesis in vivo. Thus, we explored the possibility of generating lungs in chimeric animals from donor PSCs using a blastocyst complementation (BC)-based approach[14–16].

Exogenous PSCs injected into an embryo at the blastocyst stage can join in the recipient's developmental program and compete with the host's cells for a niche. Donor cells can take over a particular progenitor defective niche made vacant by inactivation of a gene that is crucial for the initiation of the developmental program of that organ in the host. BC has been used successfully to generate a PSC-derived pancreas and to rescue the neonatal lethality of Pancreatic and Duodenal homeobox 1 (PDX1)-deficient embryos. Although innovative, BC remained challenging, as it often did not result in postnatal survival[17,18]. Gene deletion, when systemic, could lead to defects in multiple organs not rescued by the donor cells[17]. Moreover, successful BC requires the maintenance of donor PSC's pluripotency and the ability to form chimeras[5]. The PSC must reach the targeted organ niche and faithfully respond to the specific cues of that organogenesis program. Thus, we sought to identify strategies to overcome these issues in the host and donor to allow lung formation. Lung organogenesis initiates when trachea and lung progenitors are collectively specified in the foregut endoderm by Wnt-β-catenin (Ctnnb1) activation[19,20]. Subsequent endodermal activation of fibroblast growth factor receptor 2 (Fgfr2) by local fibroblast growth factor 10 (Fgf10) from the foregut mesoderm is required to selectively expand these lung progenitors to form the primordial lung[21]. Indeed, genetic disruption of *Fgfr2* in mice does

[1]Columbia Center for Human Development and Division of Pulmonary, Allergy, Critical Care, Department of Medicine, Columbia University Irving Medical Center, New York, NY, USA. [2]Columbia Center for Translational Immunology, Department of Medicine, Columbia University Irving Medical Center, New York, NY, USA. [3]Department of Anethesiology, Columbia University Irving Medical Center, New York, NY, USA. [4]Bernard and Shirlee Brown Glaucoma Laboratory, Department of Pathology and Cell Biology, College of Physicians and Surgeons, Columbia University Irving Medical Center, New York, NY, USA. [5]Institute for Stem Cell Biology and Regenerative Medicine, Department of Genetics, Stanford University School of Medicine, Stanford, CA, USA. [6]Division of Stem Cell Therapy, Distinguished Professor Unit, The Institute of Medical Science, The University of Tokyo, Minato-ku, Tokyo, Japan. [7]Department of Genetics and Development and Herbert Irving Comprehensive Cancer Center, Columbia University Irving Medical Center, New York, NY, USA. [8]These authors contributed equally: Munemasa Mori, Hiromitsu Nakauchi, Wellington V. Cardoso. *e-mail: mm4452@cumc.columbia.edu; nakauchi@stanford.edu; wvc2104@cumc.columbia.edu

not prevent tracheal formation but results in lung agenesis[21,22]. Although it is an attractive option for lung BC modeling, systemic *Fgfr2* deletion was problematic because of lethality by impaired trophoblast formation or later due to multiple defects, including limb agenesis[21–23].

To prevent undesired non-lung phenotypes in the host, we devised a conditional gene-ablation strategy using a lineage-specific promoter to vacate a specific niche in the host endoderm for complementation, named conditional blastocyst complementation (CBC). The CBC then should target an endoderm-derived lineage for which the gene of choice has a crucial non-redundant function, independent of its expression in other organs. We tested this concept by generating mice in which *Fgfr2* was conditionally deleted in the foregut endoderm immediately before the onset of lung organogenesis (*Shh*$^{cre/+}$*Fgfr2*$^{flox/flox}$; hereafter, *Fgfr2*^{cnull})[24,25]. Analysis of E13.5 *Fgfr2*^{cnull} embryos revealed the absence of lungs but preserved the trachea and esophagus, as in the wild type (WT) (Fig. 1a), confirming the essential function of Fgfr2 selectively in lung formation[21,23]. The lack of placenta and limb defects in *Fgfr2*^{cnull} further suggested that the targeted gene-deletion strategy was well suited for the generation of hosts for lung CBC (Fig. 1b). In an initial attempt to complement the defective lung organ niche in *Fgfr2*^{cnull} mutants, we used donor PSCs derived from a *Nkx2-1-GFP* knock-in mouse[26]. These cells not only carry both Fgfr2 alleles but also express green fluorescent protein (GFP) from the NK2 homeobox 1 (*Nkx2-1*) locus, marking all lung epithelial progenitors and descendants from their earliest stages. Complemented PSCs$^{Nkx2\text{-}1\text{-}GFP}$ were expected to respond to Fgf10 from the host to form the lungs. PSCs$^{Nkx2\text{-}1\text{-}GFP}$ were cultured in medium containing selective GSK3β and Mek 1/2 inhibitors and Leukemia Inhibitory Factor (2i/LIF)[27], reported to maintain the ground-state pluripotency and the naive state of PSCs, and then were injected into Fgfr2-mutant host blastocysts and transferred to pseudopregnant mothers. The PSC$^{Nkx2\text{-}1\text{-}GFP}$ indeed outcompeted the host *Fgfr2*^{cnull} cells and carried on lung morphogenesis. GFP labeling was detected in nearly 100% of the epithelium overlapping with Nkx2-1, and differentiation markers of airways (Scgb1a1, acetylated α-tubulin) and alveolar (Sftpc, Pdpn) cell types (Extended Data Fig. 1). Although they did not have obvious abnormalities in lobation or branching morphogenesis, these lungs did not form the distal saccules for gas exchange and so remained immature, and pups died at birth (Extended Data Fig. 1b). Thus, 2i/LIF-treated PSC$^{Nkx2\text{-}1\text{-}GFP}$ in *Fgfr2*^{cnull} hosts were likely to be unable to establish the epithelial–mesenchymal cross-talks that are required for the proper maturation of the lung at late gestation.

Then, we systematically tested different culture conditions for optimal maintenance of PSC pluripotency. This included medium with valproic acid (VPA)—a histone deacetylase inhibitor that improves PSC derivation and chimera formation efficiency[28,29]—and alternative 2i (a2i) medium, in which Mek kinase inhibitor is replaced by a Src kinase inhibitor to enhance PSC germline competency and developmental potential[30,31]. The efficiency of these conditions was initially assessed on the basis of the expression of stage-specific embryonic antigen 1 (Ssea1) and platelet endothelial cell adhesion molecule (Pecam), known as pluripotency markers associated with high ability to form chimeras[32] (Table 1). Because it was unclear why donor PSCs$^{Nkx2\text{-}1\text{-}GFP}$ led to inappropriate lung development, we tested additional cell lines. This included commercially available PSCs$^{CAG-GFP}$, which expresses GFP under the cytomegalovirus (CMV) enhancer, chicken β-actin promoter. The 2i/LIF treatment of PSCs$^{CAG-GFP}$ resulted in the lowest Ssea1 mean fluorescent intensity (MFI) and the lowest proportion of Pecam^{+}Ssea1^{+} PSCs among all culture conditions, regardless of the PSC type (Extended Data Fig. 2 and Supplementary Fig. 1). However, treatment with LIF and VPA (VPA/LIF) yielded the highest Ssea1 MFI in both PSCs$^{CAG-GFP}$ and PSCs$^{Nkx2\text{-}1\text{-}GFP}$ (Extended Data Fig. 2b,c). Thus we injected VPA/LIF-treated PSC$^{CAG-GFP}$ into host *Fgfr2*-mutant blastocysts and analyzed the pups at birth (P0, postnatal day 0). Among the 24 pups obtained, only 1 died (non-complemented *Fgfr2*^{cnull}); all others remained alive and active until they were euthanized ~6 h after birth, consistent with rescued functional neonatal lungs. Indeed, the morphological analysis showed well-formed saccules with extensive GFP labeling of alveolar type 1 and 2, and secretory club, multiciliated and neuroendocrine cells in airways (Fig. 1c–e and Extended Figs. 3 and 4). By contrast, mesenchymal GFP labeling, including that in endothelial, vascular and airway smooth muscle cells, was variable and overall was similar in chimeric WT or complemented *Fgfr2*^{cnull} animals (Extended Data Fig. 5a–c and Supplementary Fig. 2). Notably, in PSCs$^{CAG-GFP}$*Fgfr2*^{cnull} animals, the frequency of GFP^{+} epithelial cells in the lung was significantly higher (~80%) than in the trachea (Extended Data Fig. 4c). Thus, the lung agenesis and preserved trachea in *Fgfr2*^{cnull} hosts provided different opportunities for complementation, even within the same organ. Quantitative analysis of GFP^{+} cells in other organs showed no consistent evidence of the high chimerism seen in the lung (Extended Data Fig. 5d–f). This underscores the significance of the vacant organ niche for CBC-mediated lung complementation. However, VPA/LIF-treated PSCs$^{CAG-GFP}$*Fgfr2*^{cnull} embryos displaying low GFP signals in the skin or other organs frequently had lung abnormalities, such as incomplete unilateral rescue (Extended Data Fig. 6 and Table 1). This suggested that donor PSCs were not reaching the host's lung niche efficiently.

VPA is known to improve chimera formation[28,29], so we tested its effect in each culture condition to identify the combination with the greatest capacity to induce pluripotency markers and sustain chimerism throughout development. We found that VPA and LIF (VPA/LIF) and a2i, VPA and LIF (a2i/VPA/LIF) treatments were equally efficient in generating the highest proportion of Ssea^{high}Pecam^{+} PSCs$^{CAG-GFP}$. However, the expression of the key pluripotent factor octamer-binding transcription factor 4 (Oct-4) was significantly higher in a2i/VPA/LIF cultures (Extended Data Fig. 7a,b). When injected into WT blastocysts, donor a2i/VPA/LIF-treated PSC$^{CAG-GFP}$ nearly maximized the chimera-forming ability in all tested conditions (Extended Data Fig. 7c,d and Table 1). This was further confirmed using a population of a2i/VPA/LIF-treated Ssea1^{high} PSCs$^{CAG-GFP}$ isolated by fluorescence-activated cell sorting (FACS) (Ssea1^{high}, 71.4%; Ssea1^{dim}, 15.4%; Fig. 2a).

Injection of a2i/VPA/LIF-cultured Ssea1^{high} PSCs$^{CAG-GFP}$ into blastocysts from *Fgfr2*^{cnull} hosts consistently rescued the lung agenesis phenotype, regardless of host genetic background (Table 1). Of note, the CBC-rescued *Fgfr2*^{cnull} neonates were viable and active at birth, and were indistinguishable from their WT littermates. Flow cytometry analyses of the neonatal lungs from these animals showed that the proportion of GFP^{+} cells was consistently higher in the lung epithelial cells (Epcam^{+}CD45^{-}Pecam^{-}: 94.8 ± 2.1%) than the variable GFP^{+} contribution to the endothelium (Pecam^{+}CD45^{-}Epcam^{-}: 62.0 ± 21.5%) and to other lung mesenchymal cells (the CD45^{-}Epcam^{-}Pecam^{-}: 64.3 ± 24.7%). Moreover, the proportion of GFP^{+} cells in Epcam^{+} epithelial cells from conditional heterozygous mutant *Fgfr2*^{hetero} (43.8 ± 12.4 %) and WT (45.5 ± 13.5%) complemented lungs was always variable and rarely reached the high values found in *Fgfr2*^{cnull} lungs (Extended Data Fig. 8a,b, Table 1 and Supplementary Table 1). It was indeed remarkable that the consistent (epithelial) versus variable (mesenchymal) complementation that resulted from emptying the host's epithelial niche was already evident, even in the relatively small number of *Fgfr2*^{cnull} pups compared with the other genotypes. FACS-based assessment of chimerism in the liver showed only a low proportion of donor GFP^{+} cells, regardless of the host genotype (Extended Data Fig. 8c and Supplementary Table 1). Thus, a2i/VPA/LIF appeared to maintain PSC's pluripotency with high efficiency, which endowed high chimerism in the lungs and efficient complementation to rescue lung agenesis in *Fgfr2*^{cnull} neonates.

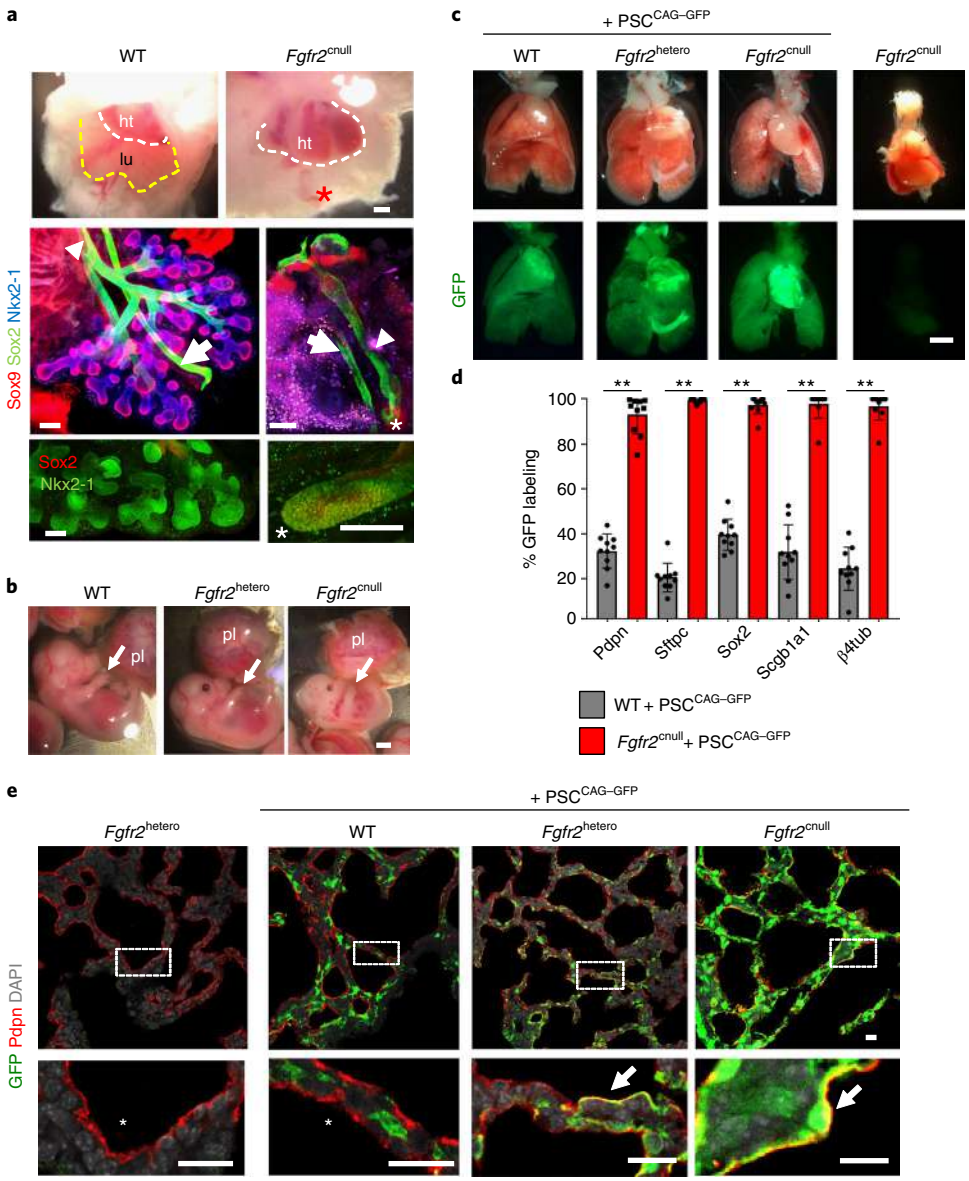

Fig. 1 | CBC rescues lung agenesis in *Fgfr2*-deficient mice. a, Imaging of WT and homozygous *Fgfr2*^{cnull} (*Shh*$^{cre/+}$*Fgfr2*$^{flox/flox}$) E13.5 mouse embryos. Top, whole-mount images of freshly isolated embryos. Dotted lines outline the lung (lu) and heart (Ht). An asterisk indicates the absence of lungs in *Fgfr2*^{cnull} mice. Middle, whole-mount immunofluorescence-confocal imaging of Sox2, Sox9 and Nkx2-1, depicting the esophagus (arrows) and trachea (arrowheads) in both WT (left) and *Fgfr2*^{cnull} (right) mice. Lungs are present in WT but not mutant mice (the asterisk indicates a blunt-ended trachea). Bottom, immunofluorescence imaging of Sox2 and Nkx2-1 depicts distal lung buds in WT mice, contrasting with a blunt-ended trachea in *Fgfr2*^{cnull} mice. **b**, Whole-mount images of freshly isolated E13.5 WT, *Fgfr2*^{hetero} (control heterozygous mutant *Fgfr2*: *Shh*$^{cre/+}$*Fgfr2*$^{flox/+}$) and *Fgfr2*^{cnull} embryos. Limb (arrow) and placenta (pl) are present in mice of all genotypes ($n = 5$ per group). **c**, GFP imaging of freshly isolated lungs from newborn (P0) chimeric WT, *Fgfr2*^{hetero} and *Fgfr2*^{cnull} mice, in which PSC$^{CAG-GFP}$ were used for CBC. The lung from a littermate *Fgfr2*^{cnull} mouse without PSC$^{CAG-GFP}$ injection is shown as a negative control. **d**, Quantitative analysis of GFP distribution in the indicated lung cell types by immunofluorescence co-labeling with markers of differentiation in sections of P0 lungs from WT + PSC$^{CAG-GFP}$ and *Fgfr2*^{cnull} + PSC$^{CAG-GFP}$ mice. The percentage of GFP labeling is shown in alveolar type 1 (Pdpn), type 2 (Sftpc), club (Scgb1a1) and multiciliated (β-tubulin-4) cells, or in the airway compartment regardless of cell type (Sox2). Values are shown as mean ± s.e.m. in ten random fields per sample from a representative WT and mutant lung. Student's *t*-test, $^{**}P < 0.01$. **e**, Representative confocal immunofluorescence images of GFP, Pdpn and DAPI in newborn lungs of WT, *Fgfr2*^{hetero} and *Fgfr2*^{cnull} mice complemented with VPA/LIF-treated PSC$^{CAG-GFP}$. Complementation rescued the formation of distal saccules and alveolar type 1 differentiation. *Fgfr2*^{hetero} mice without complementation were used as a negative control. Boxed areas are shown enlarged in bottom panels and depict thin-walled distal saccules (arrows indicate GFP$^+$Pdpn$^+$ cells; asterisk indicates GFP$^-$Pdpn$^+$ cells). Scale bars, 150 μm (**a**), 2 mm (**b**), 1 mm (**c**) and 5 μm (**e**).

We had, however, no clear indication about why the PSCs cultured with a2i/VPA/LIF were more effective than the others. Given the key role of chromatin modifications and DNA methylation in PSC pluripotency and developmental potential[33], we investigated the epigenetic status of these PSCs to gain insights into the prospective mechanisms underlying these differences. Analysis of global DNA methylation showed significantly lower levels of 5-mC long interspersed nucleotide element 1 (Line-1) repeats in a2i/VPA/LIF-treated PSCs compared with those treated with LIF alone. This overall lower methylation status favoring pluripotency was

Table 1 | Summary of PSC donor lines, culture conditions, host mouse strains and data for chimera formation, lung complementation and survival in mice subjected to CBC

Cell line	Passage number	Donor PSC background	PSC treatment	Number of host blastocysts	Host blastocyst background	Number of injected PSCs per blastocyst	% survival (number of pups or embryos/number of transferred blastocysts)	% chimera formation[a]	% complementation (number of complementation/number of chimeric animals)[b]
$^{c}PSC^{Nkx2\text{-}1\text{-}GFP}$	15	W4/129S6	2i/LIF	25	129×B6×CD1	10	40% (10 neonates at P0)	50% (5 chimeras)	40% (2/5) at P0 (Extended Data Fig. 1) defective complementation ($Fgfr2^{cnull}$)
$ES1^{CAG\text{-}tdTomato}$	12	C57BL/6N	LIF	40	129×B6×CD1	10	40% (10 neonates at P0)	10% (1 chimera)	0% (0/1) at P0 no complementation ($Fgfr2^{cnull}$)
$ES1^{CAG\text{-}tdTomato}$	14	C57BL/6N	LIF	25	129×B6×CD1	10	24% (6 neonates at P0)	33% (2 chimeras)	0% (0/2) at P0 no complementation ($Fgfr2^{cnull}$)
$ES1^{CAG\text{-}tdTomato}$	14	C57BL/6N	a2i/LIF	30	129×B6×CD1	10	23% (7 neonates at P0)	71.4% (5 chimeras)	0% (0/5) at P0 no complementation (Fgfr2 cnull)
$^{c}PSC^{CAG\text{-}GFP}$	10	F_1 hybrid mouse (C57Bl/6×129)	LIF/VPA	43	129×B6×CD1	20	53.5% (23 neonates at P0)	66.6% (15 chimeras)	13.3% (2/15) at P0 (Fig. 1) functional complementation ($Fgfr2^{cnull}$)
$^{c}PSC^{CAG\text{-}GFP}$	10	F_1 hybrid mouse (C57Bl/6×129)	LIF/VPA	12	129×B6×CD1	20	53.5% (6 embryos at E15.5)	88% (5 chimeras)	20% (1/5) at E15.5 (Extended Data Fig. 6) defective complementation ($Fgfr2^{cnull}$)
$PSC^{CAG\text{-}GFP}$	10	F_1 hybrid mouse (C57Bl/6×129)	LIF/VPA	40	129×B6×CD1	20	38% (15 neonates at P0)	33.3% (5 chimeras)	0% (0/5) at P0 no complementation ($Fgfr2^{cnull}$)
$^{c}PSC^{CAG\text{-}GFP}$	11	F_1 hybrid mouse (C57Bl/6×129)	a2i/VPA/LIF	43	B6	20	47% (20 neonates at P0)	85% (17 chimeras)	11.8% (2/17) at P40 functional complementation ($Ctnnb1^{cnull}$)
$^{c}PSC^{CAG\text{-}GFP}$	11	F_1 hybrid mouse (C57Bl/6×129)	a2i/VPA/LIF	40	129×B6×CD1	20	50% (20 neonates at P0)	64.2% (13 chimeras)	30.8% (4/13) at P80 (Fig. 2) functional complementation ($Fgfr2^{cnull}$)
$^{c}PSC^{CAG\text{-}GFP}$	11	F_1 hybrid mouse (C57Bl/6×129)	a2i/VPA/LIF	87	B6	20	35.6% (31 neonates at P0)	65.2% (20 chimeras)	15% (3/20) at P50 (Fig. 3) functional complementation ($Ctnnb1^{cnull}$)
$^{c}PSC^{CAG\text{-}GFP}$	11	F_1 hybrid mouse (C57Bl/6×129)	a2i/VPA/LIF	18	129×B6×CD1	20	50% (9 embryos at E12.5)	100% (9 chimeras at E12.5)	22.22% (2/9) at E12.5 Functional complementation ($Fgfr2^{cnull}$)
$^{c}PSC^{CAG\text{-}GFP}$	13	F_1 hybrid mouse (C57Bl/6×129)	a2i/VPA/LIF	80	129×B6×CD1	20	25% (20 neonates at P0)	70% (14 chimeras)	14.3% (2/14) at P1 (Extended Data Fig. 8) functional complementation ($Fgfr2^{cnull}$)
$PSC^{CAG\text{-}GFP}$	11	F_1 hybrid mouse (C57Bl/6×129)	a2i/VPA/LIF	36	129×B6×CD1	20	44% (16 embryos at E15.5)	100% (16 chimeras at E15.5)	N.A. (Extended Data Fig. 7d)
$PSC^{CAG\text{-}GFP}$	11	F_1 hybrid mouse (C57Bl/6×129)	a2i/VPA/LIF	51	129×B6×CD1	20	50% (26 neonates at P0)	88.9% (23 chimeras)	N.A.
$PSC^{CAG\text{-}GFP}$	11	F_1 hybrid mouse (C57Bl/6×129)	a2i/VPA/LIF	35	129×B6×CD1	20	43% (15 neonates at P0)	100% (15 chimeras)	N.A.
CSL2J2	11	C57BL/6J C2J	2i/VPA/LIF	20	C57BL/6J	10	20% (4 neonates at P0)	25% (1 chimera)	N.A.
FL19 ARR3-1	11	C57BL/6N	a2i/VPA/LIF	20	C57BL/6J	10	60% (12 neonates at P0)	100% (12 chimeras)	N.A.
FL19 ARR3-2	11	C57BL/6N	a2i/VPA/LIF	20	C57BL/6J	10	40% (8 neonates at P0)	100% (8 chimeras)	N.A.
B7	15	C57BL/6N	2i/LIF	40	CD1	10	33% (13 neonates at P0)	62% (8 chimeras)	N.A.
SUN107.4	16	CD1	2i/LIF	20	CD1	8	30% (6 neonates at P0)	50% (3 chimeras)	N.A.

N.A., not applicable for complementation analyses, since host embryos were WT. [a]Percentage chimera formation was based on the presence of different skin color derived from donor cells (GFP, tdTomato fluorescence or pigmentation) of P0 host neonates or embryos, as indicated. [b]Percentage complementation was determined as the number of chimeric animals with CBC-rescued lungs in homozygous $Fgfr2^{cnull}$ or $Ctnnb1^{cnull}$ mutants divided by the total number of chimeric animals in the litter. The genotype of the recipient mice and figure panels containing corresponding representative images are indicated. The degree of complementation is indicated as: (1) functional complementation: CBC rescue of lungs allowed survival postnatally when examined at P0, P1 or as adults (when examined prenatally, lungs had morphological and marker expression compatible with developmental stage); (2) defective complementation: rescued lungs with developmental abnormalities (no postnatal survival); and (3) no complementation: no rescue of lung agenesis. [c]PSCs and conditions that resulted in lung complementation.

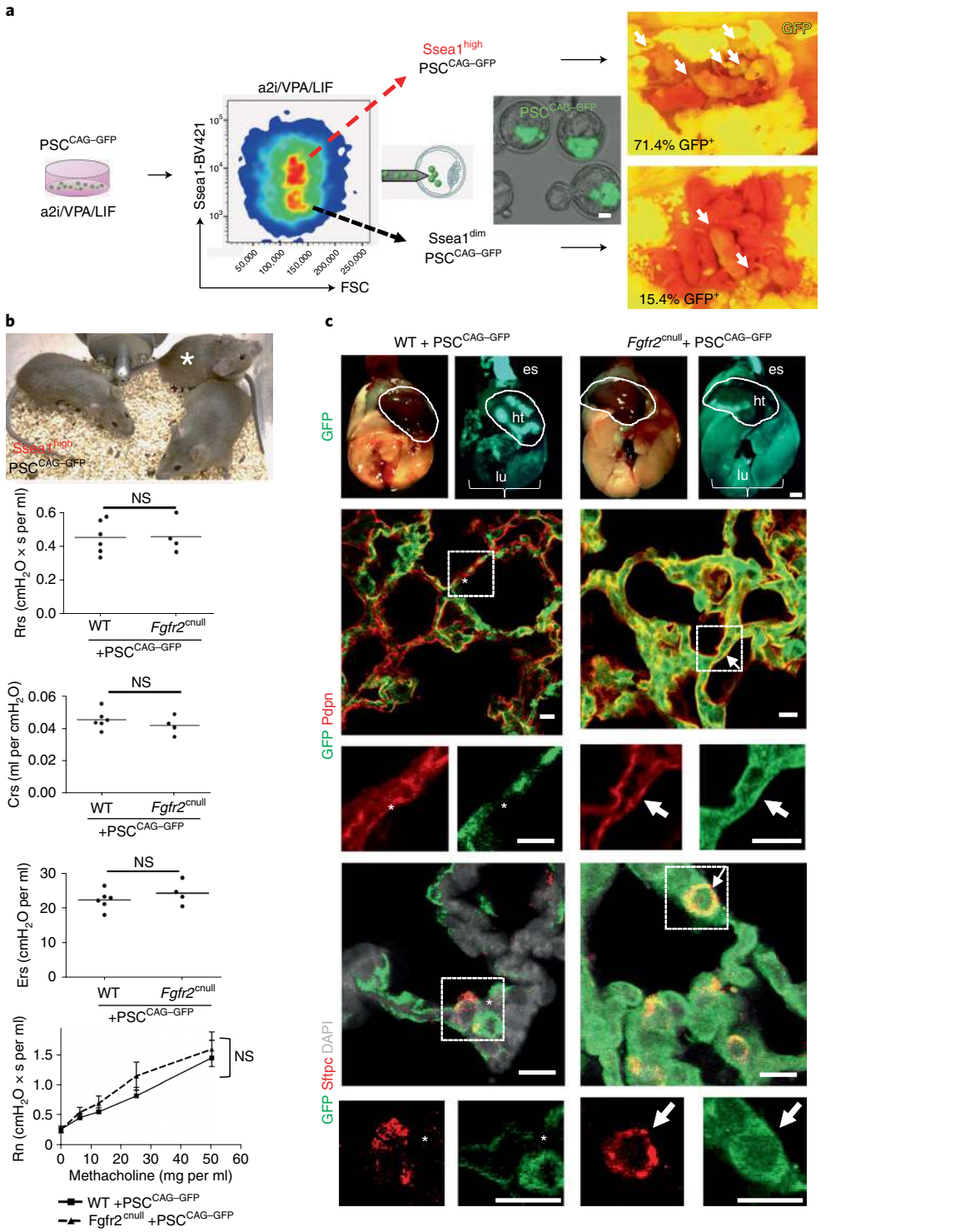

Fig. 2 | Generation of fully functional adult lungs in *Fgfr2*-deficient mice via CBC. a, Schematic of the experimental design: a2i/VPA/LIF-treated PSCs$^{CAG–GFP}$ were sorted into Ssea1^{high} and Ssea1^{dim} subpopulations and injected into WT blastocyst hosts, which were analyzed for chimera formation, as identified by GFP labeling in chimeric blastocysts (middle) or in the skin of chimeric P0 pups (right; arrows indicates GFP$^+$ chimeric neonates). **b**, Top, adult *Fgfr2*^{cnull} (asterisk) and control WT littermates complemented with Ssea1^{high} PSC$^{CAG–GFP}$. Middle, resistance (Rrs), compliance (Crs) and elastance (Ers) of the respiratory system, as assessed by Flexivent analysis, in chimeric WT and *Fgfr2*^{cnull} mice. Bottom, response of lungs to increasing doses of methacholine (Rn, resistance of conducting airways). Graphs represent mean ± s.e.m. of $n = 6$ (WT) and $n = 4$ (mutant) mice per group. Student's *t*-test was used for statistical analysis. NS, statistically non-significant. **c**, Top, whole-mount GFP imaging of freshly isolated postnatal P80 adult lungs (lu), heart (ht) and esophagus (es) from *Fgfr2*^{cnull} + PSC$^{CAG–GFP}$ and littermate control WT + PSC$^{CAG–GFP}$ mice. Brackets indicate areas where GFP staining differed between complemented control and mutant lungs. Middle, immunofluorescence images of GFP and Pdpn (a marker of alveolar type 1 cells). Bottom, immunofluorescence images of GFP and Sftpc (a marker of alveolar type 2 cells) in lung sections. Boxed areas in double-labeled images are shown as single-labeled enlarged images below (arrows, GFP$^+$marker$^+$ cells; asterisk, GFP$^-$marker$^+$ cells). DAPI was used for nuclear staining. Scale bars, 10 μm (**a**), 1 mm (top, **c**) and 10 μm (middle and bottom, **c**).

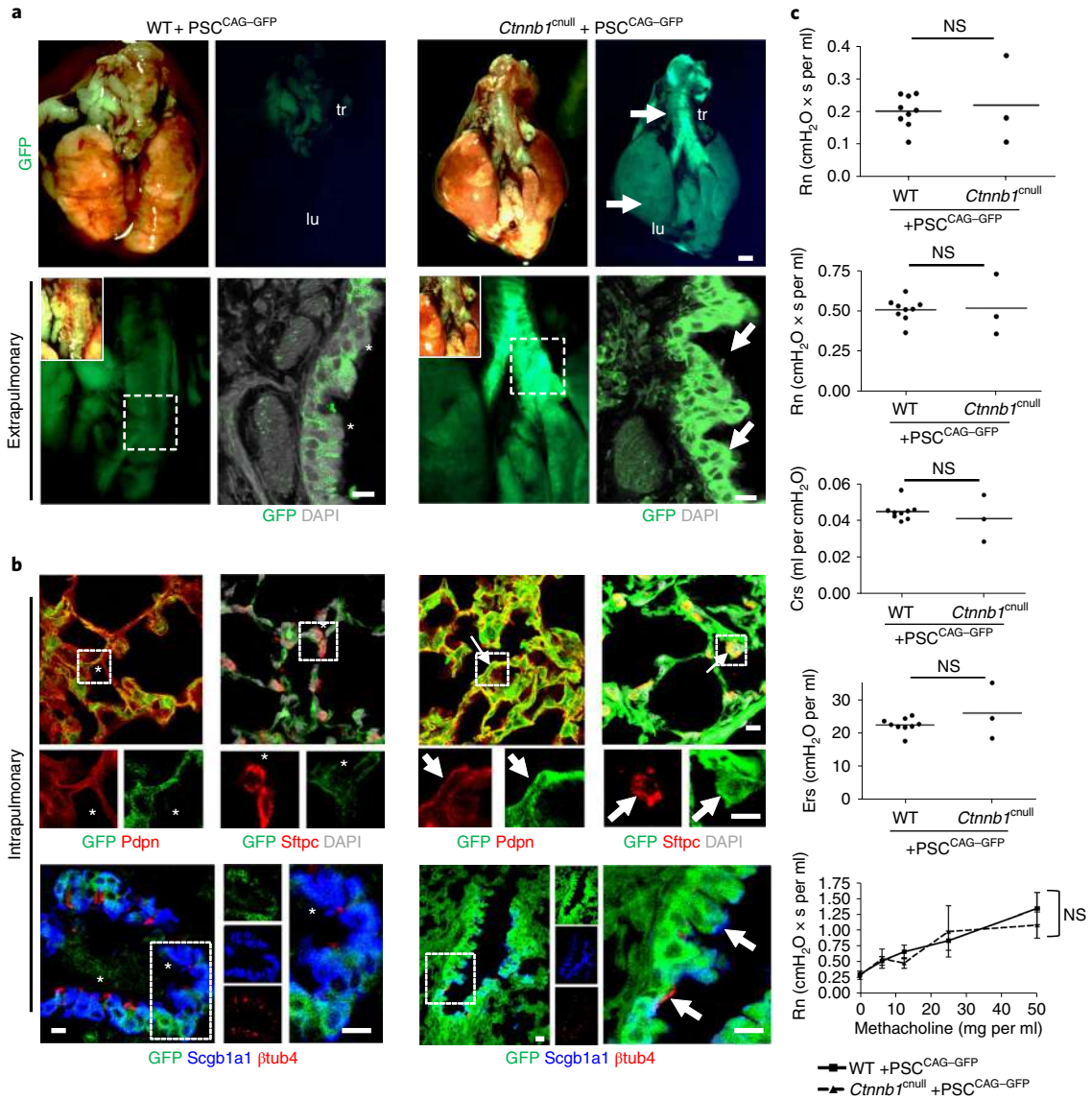

Fig. 3 | CBC overcomes the defect in the specification of early respiratory progenitors in *Ctnnb1*-deficient mice and generates functional trachea and lungs. a, Top, whole-mount GFP imaging of freshly isolated adult postnatal day50 complemented adult lungs (lu) and tracheas (tr) from control (WT, left) and homozygous *Ctnnb1*^{cnull} (*Shh*$^{cre/+}$*Ctnnb1*$^{flox/flox}$, right) blastocysts injected with a2i/VPA/LIF-treated PSC$^{CAG–GFP}$. Bottom, GFP imaging of whole mounts and histological sections of extrapulmonary airways (main bronchi) in WT and mutants. Boxed areas in double-labeled images are shown as single-labeled enlarged images below (arrows, GFP$^+$ cells; asterisk, GFP$^-$ cells. **b**, Representative immunofluorescent staining for Pdpn, Sftpc, β-tubulin4 (βtub4) and Scgb1a1 (CC10) in the lungs of WT and mutant mice. Boxed areas in double-labeled images are shown as single-labeled enlarged images below (arrows, GFP$^+$marker$^+$ cells; asterisk, GFP$^-$marker$^+$ cells. DAPI was used in all panels. **c**, Resistance of conducting airways (Rn), resistance (Rrs), compliance (Crs) and elastance (Ers) of the respiratory system, as assessed by Flexivent analysis, in adult WT and *Ctnnb1*^{cnull} mice complemented with PSC$^{CAG–GFP}$. Bottom, response of lungs to increasing doses of methacholine. A Student's *t*-test was used for statistical analysis. Graphs represent mean and standard error of n = 9 (WT), 3 (mutant) mice per group. Scale bars in (a) 1 mm (top panel), 10 μm (bottom panel); (b): 10 μm.

similarly found in 2i/LIF-treated conditions, consistent with the global DNA hypomethylation reported in the naive state of mouse PSC pluripotency[33] (Extended Data Fig. 9a). Moreover, gene-expression analysis showed that a2i/LIF and 2i/LIF treatment of PSCs led to a trend toward a decrease in levels or significantly lower levels of the de novo DNA methyltransferase Dnmt3b, compared to LIF or VPA/LIF treatments, respectively. Interestingly, the differences in Dnmt3b expression in cells treated with a2i/LIF/VPA compared with other groups and the somewhat decreased but variable changes in expression of Dnmt3a (Extended Data Fig. 9b) and cofactor Dnmt3l (not shown) suggested the presence of additional players, such as the Dnmt-interacting proteins[34].

We next investigated potential differences in patterns of histone modifications. Western blot analyses showed that among all groups, a2i/VPA/LIF PSCs expressed the lowest levels of the repressive chromatin mark H3K27me3 (Extended Data Fig. 9c). Also, a2i/LIF-treated PSCs, regardless of VPA addition, were markedly enriched in H4 pan acetylation compared with 2i-treated PSCs. Immunofluorescence staining of H4 acetylation (Ace-H4) and quantitative analysis of relative MFI showed the strongest signals most consistently in a2i/LIF (with or without VPA) compared to other conditions. Although some LIF-treated PSCs exhibited strong signals, overall, there was a broad range of intensities from very high to low, reflecting high variability and inconsistent effect (Extended

Data Fig. 9d). Notably, activation marks other than Ace-H4, such as H3K4me or H3K27ac (Extended Data Fig. 9c and data not shown) were not enriched by a2i/LIF treatment. Therefore, the a2i/VPA/LIF cocktail generates a unique epigenetic state that includes DNA hypomethylation, low levels of H3K27 methylation and increased abundance of H4 acetylation. We propose that the combination of these epigenetic changes, resulting in a more accessible (open) chromatin, underlie the a2i/VPA/LIF-mediated enhanced expression of pluripotency-associated proteins, such as Oct4, Pecam and Ssea1. A more detailed analysis of these mechanisms is currently under investigation.

We then used our CBC approach to test whether a2i/VPA/LIF enhanced the developmental potential of Ssea1^{high} PSCs$^{CAG-GFP}$ to generate lungs fully functional throughout life. Two distinct mouse models of agenesis were used as hosts: the former *Fgfr2*^{cnull}, in which tracheal and lung progenitors are specified but the lung progenitors are selectively unable to expand, and the *Ctnnb1*^{cnull} (*Shh*$^{cre/+}$*Ctnnb1*$^{flox/flox}$), in which none of these progenitors are specified and thus neither lung nor trachea forms[19,20]. These enabled us to assess whether targeting different genes that are crucial for respiratory organogenesis under the same CBC strategy allowed these phenotypes to be rescued as expected. Remarkably, in both models, the chimeric animals with lung complementation developed normally to adulthood and reached full maturity (Figs. 2 and 3 and Extended Data Fig. 10). Pulmonary function tests (Flexivent) performed in adult mice showed values of airway resistance, lung elastance and compliance comparable with those of WT littermates. When challenged with a spasmogenic agent (methacholine), CBC-complemented lungs showed concentration-dependent bronchoconstriction indistinguishable from the response of controls (Figs. 2b,3c, Extended Data Fig. 10b and Table 1). Macroscopic analysis of *Ctnnb1*^{cnull}, PSC$^{CAG-GFP}$ mice showed strong GFP signals in both trachea and lungs, suggesting efficient donor complementation in all respiratory progenitors (Fig. 3a, Extended Data Fig. 10e). In *Fgfr2*^{cnull}, PSC$^{CAG-GFP}$ complementation occurred preferentially in the lung, compared to the trachea (Fig. 2c, Extended Data Fig. 4c and data not shown). Immunofluorescence of lungs from *Fgfr2*^{cnull}, PSC$^{CAG-GFP}$ and *Ctnnb1*^{cnull}, PSC$^{CAG-GFP}$ animals confirmed extensive GFP overlap with markers of the airway and alveolar epithelial cell types (Figs. 2c and 3a,b and Extended Data Fig. 10a,e).

In summary, we established a conditional gene-ablation strategy to vacate a specific niche for complementation (CBC) coupled with a new methodology for enhancing PSC chimerism and developmental potential, which uniquely maintains an open chromatin status and pluripotency in donor cells. The approach takes advantage of bona fide tissue interactions in vivo to overcome the substantial hurdles in generating lung and trachea in host embryos with a severe genetic defect that prevents these structures from forming. Complementation of defective respiratory progenitor niches resulted in the formation of fully functional lungs in vivo. The observations presented here open exciting perspectives for the use of CBC to generate epithelial and non-epithelial components of the lung employing tissue-specific Cre lines in hosts. Ongoing testing of various strategies of Cre-mediated recombination and our PSCs culture conditions suggest that CBC, coupled with efficient PSC maintenance, is versatile and may be used to complement multiple layers to generate a functional lung wholly from donor cells. Our work also lays the conceptual and technical platforms for investigating mechanisms of cell competition during mammalian organogenesis or as part of the surveillance mechanisms that maintain tissue integrity in adult homeostasis and regeneration–repair. Challenges for future use of this technology in translational and clinical practice include the need for a better understanding of the mechanisms of immune tolerance and interspecific histocompatibility barriers to overcome tissue rejection, and strategies to ablate residual host cells selectively in the targeted organs preserving tissue integrity. Further progress in these areas will facilitate engineering complex organs, such as the lung in large animals, to be ultimately used in cell-based interventions for regenerative purposes in human diseases.

Online content

Any methods, additional references, Nature Research reporting summaries, source data, extended data, supplementary information, acknowledgements, peer review information, details of author contributions and competing interests, and statements of data and code availability are available at https://doi.org/10.1038/s41591-019-0635-8.

Received: 30 January 2019; Accepted: 1 October 2019;
Published online: 07 November 2019

References

1. Murphy, S. L., Xu, J., Kochanek, K. D. & Arias, E. *Mortality in the United States, 2017*. NCHS Data Brief no. 328 (National Center for Health Statistics, 2018).
2. Petersen, T. H. et al. Tissue-engineered lungs for in vivo implantation. *Science* **329**, 538–541 (2010).
3. Kotton, D. N. & Morrisey, E. E. Lung regeneration: mechanisms, applications and emerging stem cell populations. *Nat. Med.* **20**, 822–832 (2014).
4. Matsunari, H. et al. Blastocyst complementation generates exogenic pancreas in vivo in apancreatic cloned pigs. *Proc. Natl Acad. Sci. USA* **110**, 4557–4562 (2013).
5. Wu, J. et al. Interspecies chimerism with mammalian pluripotent stem cells. *Cell* **168**, 473–486.e15 (2017).
6. Suchy, F., Yamaguchi, T. & Nakauchi, H. iPSC-derived organs in vivo: challenges and promise. *Cell Stem Cell* **22**, 21–24 (2018).
7. Valapour, M. et al. OPTN/SRTR 2017 annual data report: lung. *Am. J. Transplant.* **19**, 404–484 (2019).
8. Chen, Y.-W. et al. A three-dimensional model of human lung development and disease from pluripotent stem cells. *Nat. Cell Biol.* **19**, 542–549 (2017).
9. Dye, B. R. et al. A bioengineered niche promotes in vivo engraftment and maturation of pluripotent stem cell derived human lung organoids. *eLife* **5**, 1–18 (2016).
10. Ott, H. C. et al. Regeneration and orthotopic transplantation of a bioartificial lung. *Nat. Med.* **16**, 927–933 (2010).
11. Rosen, C. et al. Preconditioning allows engraftment of mouse and human embryonic lung cells, enabling lung repair in mice. *Nat Med* **21**, 869–879 (2015).
12. Stone, K. C., Mercer, R. R., Gehr, P., Stockstill, B. & Crapo, J. D. Allometric relationships of cell numbers and size in the mammalian lung. *Am. J. Respir. Cell Mol. BioI.* **6**, 235–243 (1992).
13. Crapo, J. D., Barry, B. E., Gehr, P., Bachofen, M. & Weibel, E. R. Cell number and cell characteristics of the normal human lung. *Am. Rev. Respir. Dis.* **126**, 332–337 (1982).
14. Chen, J., Lansford, R., Stewart, V., Young, F. & Alt, F. W. RAG-2-deficient blastocyst complementation: an assay of gene function in lymphocyte development. *Proc. Natl Acad. Sci. USA* **90**, 4528–4532 (1993).
15. Kobayashi, T. et al. Generation of rat pancreas in mouse by interspecific blastocyst injection of pluripotent stem cells. *Cell* **142**, 787–799 (2010).
16. Yamaguchi, T. et al. Interspecies organogenesis generates autologous functional islets. *Nature* **542**, 191–196 (2017).
17. Usui, J. et al. Generation of kidney from pluripotent stem cells via blastocyst complementation. *Am. J. Pathol.* **180**, 2417–2426 (2012).
18. Freedman, B. S. Hopes and difficulties for blastocyst complementation. *Nephron* **139**, 42–47 (2018).
19. Harris-Johnson, K. S., Domyan, E. T., Vezina, C. M. & Sun, X. Beta-catenin promotes respiratory progenitor identity in mouse foregut. *Proc. Natl Acad. Sci. USA* **106**, 16287–16292 (2009).
20. Goss, A. M. et al. Wnt2/2b and β-catenin signaling are necessary and sufficient to specify lung progenitors in the foregut. *Dev. Cell* **17**, 290–298 (2009).
21. Sekine, K. et al. Fgf10 is essential for limb and lung formation. *Nat. Genet.* **21**, 138–141 (1999).
22. De Moerlooze, L. et al. An important role for the IIIb isoform of fibroblast growth factor receptor 2 (FGFR2) in mesenchymal-epithelial signalling during mouse organogenesis. *Development* **127**, 483–492 (2000).
23. Xu, X. et al. Fibroblast growth factor receptor 2 (FGFR2)-mediated reciprocal regulation loop between FGF8 and FGF10 is essential for limb induction. *Development* **125**, 753–765 (1998).
24. Harris, K. S., Zhang, Z., McManus, M. T., Harfe, B. D. & Sun, X. Dicer function is essential for lung epithelium morphogenesis. *Proc. Natl Acad. Sci. USA* **103**, 2208–2213 (2006).
25. Yu, K. Conditional inactivation of FGF receptor 2 reveals an essential role for FGF signaling in the regulation of osteoblast function and bone growth. *Development* **130**, 3063–3074 (2003).

26. Longmire, T. A. et al. Efficient derivation of purified lung and thyroid progenitors from embryonic stem cells. *Cell Stem Cell* **10**, 398–411 (2012).
27. Ying, Q. L. et al. The ground state of embryonic stem cell self-renewal. *Nature* **453**, 519–523 (2008).
28. Kretsovali, A., Hadjimichael, C. & Charmpilas, N. Histone deacetylase inhibitors in cell pluripotency, differentiation, and reprogramming. *Stem Cells Int.* **2012**, 184154 (2012).
29. Stadtfeld, M. et al. Aberrant silencing of imprinted genes on chromosome 12qF1 in mouse induced pluripotent stem cells. *Nature* **465**, 175–181 (2010).
30. Choi, J. et al. Prolonged Mek1/2 suppression impairs the developmental potential of embryonic stem cells. *Nature* **548**, 219–223 (2017).
31. Yagi, M. et al. Derivation of ground-state female ES cells maintaining gamete-derived DNA methylation. *Nature* **548**, 224–227 (2017).
32. Furusawa, T., Ohkoshi, K., Honda, C., Takahashi, S. & Tokunaga, T. Embryonic stem cells expressing both platelet endothelial cell adhesion molecule-1 and stage-specific embryonic antigen-1 differentiate predominantly into epiblast cells in a chimeric embryo1. *Biol. Reprod.* **70**, 1452–1457 (2004).
33. Leitch, H. G. et al. Naive pluripotency is associated with global DNA hypomethylation. *Nat. Struct. Mol. Biol.* **20**, 311–316 (2013).
34. Lyko, F. The DNA methyltransferase family: a versatile toolkit for epigenetic regulation. *Nat. Rev. Genet.* **19**, 81–92 (2017).

Methods

Mouse lines and genotyping. *Shh*$^{Cre/+}$ mice (cat. no. 05622) and *Ctnnb1*$^{flox/flox}$ (Ctnnb1^{tm2Kem}: cat. no. 004152) were obtained from the Jackson Lab. For conditional deletion of Fgfr2 (*Fgfr2*^{cnull}) or Ctnnb1 (*Ctnnb1*^{cnull}), we crossed *Fgfr2*$^{flox/flox}$ or *Ctnnb1*$^{flox/flox}$ females with *Shh*$^{Cre/+}$*Fgfr2*$^{flox/+}$ or *Shh*$^{Cre/+}$*Ctnnb1*$^{flox/+}$ males, respectively. Genotyping of the *Shh*^{Cre} allele was performed by PCR according to the protocol provided by the vendor (Jackson Lab, cat no. 05622). *Fgfr2*$^{flox/flox}$ mice were kindly gifted by X. Zhang. We further backcrossed these mice for more than three generations with CD-1 mice (Charles River, strain code: 022). For the lung complementation analyses, we injected the following PSCs into blastocysts of *Fgfr2*^{cnull} or *Ctnnb1*^{cnull} and littermate controls (WT, *Fgfr2*^{hetero} or *Ctnnb1*^{hetero}): PSC$^{Nkx2\text{-}1\text{-}GFP}$ passage 15 (W4/129S6: a gift from L. Oikonomou and D. Kotton, CReM, Boston University), PSC$^{CAG-GFP}$ passage 10–11 (C57BL/6N × 129S6 background, MTI-GlobalStem: cat. no. GSC-5003). To assess the impact of PSC culture conditions we also injected the following PSC lines into WT blastocysts (Table 1): ES1$^{CAG-tdTomato}$ (C57BL/6N background), B7 (C57BL/6N background), SUN107.4 (CD1 background) derived at Stanford University; CSL2J2 (C57BL/6J C2J background), FL19 ARR3-1 (albino agouti C57BL/6N background), FL19 ARR3-2 (C57BL/6N background) derived at the Columbia University Transgenic Core Facility. Genotyping of Fgfr2 + PSC$^{CAG-GFP}$ or Ctnnb1 + PSC$^{CAG-GFP}$ chimeric animals was confirmed by GFP-negative sorted liver cells or a single-cell colony formation assay of hematopoietic progenitor cells prepared with an EZ Fast Blood/Cell PCR Genotyping Kit (EZ BioResearch cat. no. G1002). Briefly, we performed PCR using the following Tm-adjusted primers, which allowed us to obtain equal band size in heterozygous *Fgfr2* allele: FR2-F1, 5′-ATAGGAGCAACAGGCGG-3′, and FR2-F2, 5′-CAAGAGGCGACCAGTCA-3′ resulting in a 142 base pair (bp) product for the WT allele and a 207 bp product for the conditional, *Fgfr2* floxed, allele 5′-AAG GTA GAG TGA TGA AAG TTG TT-3′, and 5′-CAC CAT GTC CTC TGT CTA TTC-3′ primers were used to detect the *Ctnnb1*-mutant allele (~300 bp) and wild-type allele (223 bp)[35]. A separate set of primers, FR2-F1 and FR2-F3, 5′-CATAGCACAGGCCAGGT-3′ were used to detect the *Fgfr2* locus following recombination by Cre recombinase (244-bp product)[25]. For PSC$^{Nkx2\text{-}1\text{-}GFP}$ mice, we performed PCR for the detection of a *Shh*^{Cre} allele in the tail tissue samples and further confirmed the Fgfr2 expression in the GFP-negative tracheal epithelial layers using Fgfr2-specific antibody (Santa Cruz, sc-6930). The antibody signal was amplified by the Tyramide Signal Amplification kit (Perkin Elmer, NEL704A001KT, TSA-Cy3 1:100 dilution). The GFP fluorophore in P0 pup skin was activated by Dark Reader Handlamp (Clare Chemical Research, HL34T) and monitored by digital camera video mode through the Reader viewing filters (Clare Chemical Research, AG16).

Immunofluorescence. Tissue sections or cultured PSCs were incubated with primary antibodies overnight at 4 °C, washed in PBS and incubated with secondary antibody conjugated with Alexa488, 567 or 647 (1:300) with NucBlue Fixed Cell ReadyProbes Reagent (DAPI) (Life tech., Ra37606) for 1.5 h. Samples were washed with PBS and mounted with ProLong Gold antifade reagent (Invitrogen, P36962). IF analysis was performed in 10-µm sections from WT, *Fgfr2*^{hetero} or chimeric mice at P0 or P80 using the M.O.M. (mouse on mouse) kit (Vector Laboratories) according to the manufacturer's protocol. Antigen retrieval was performed using Unmasking Solution (Vector Laboratories H-3300) and microwaving of samples for 3 min at around 100 °C. The following antibodies were used: anti-acetylated β-tubulin IV (Abcam, ab11315, 1:500), anti-GFP chicken polyclonal antibody (pAb) (Thermo Scientific, 1:500), anti-Scgb1a1 goat (Santa Cruz, sc-9772, 1:500), anti-Pdpn (R&D, AF3244, 1:200), anti-Hop (Santa Cruz sc- 398703, 1:100), anti-Sftpc (Seven Hills WRAB-9337, 1:1,000), anti-Cgrp (Sigma, C8198, 1:1,000), anti-Sox2 rat (eBiosience, 14-9811-82), anti-SMA rabbit (Cell Signaling, 19245), anti-Oct4 (Gentetex, GT486, 1:100), anti-SSEA1 (SantaCruz, sc-101462, 1:50), anti-Oct4 (R&D, AF1759) and Histone H4ac (pan-acetyl) (Active Motif, 39925). Isolectin B4 (Life Tech., I32450) was used at a dilution of 1:500 in PBS overnight at 4 °C prior to the staining above to visualize vascular endothelial cells. For the whole-mount staining, we used SeeDB2 methods[36]. Images were acquired using a Nikon Labophot 2 microscope equipped with a Nikon Digital Sight DS-Ri1 charge-coupled device camera or on a Zeiss LSM710 confocal laser scanning microscope or using 3D-SIM microscopy[37].

Preparation of pluripotent stem cells. We cultured PSC$^{Nkx2\text{-}1\text{-}GFP}$ cells (passage 15) for 5 days before blastocyst injection with 2i/LIF medium[31] containing 1 µM PD0325901 (Tocris, no. 4192), 3 µM CHIR99021 (Tocris, no. 4423) and LIF (1000 U ml^{-1}, Millipore, no. ESG1106) in DMEM based-serum medium (Gibco no. 11995, cat. no. 10569-044) supplemented with 14% ESC qualified FBS (Hyclone SH30070.03E), Glutamax (Giboco, no. 35050061), NEAA (Invitrogen, no. 11140050), 0.1 mM BME (Sigma, no. M6250) and pen/strep (Gibco, no. 30-001-CI). To assess the impact of each defined PSC medium on the maintenance of PSCs (PSC$^{Nkx2\text{-}1\text{-}GFP}$, PSC$^{CAG-GFP}$), these were cultured for 5 days on irradiated MEFs (CF1 mouse embryonic fibroblasts, Life tech, no. A34181) in DMEM-based serum medium containing LIF (2000 U ml^{-1}) for LIF, further supplemented with 0.5 mM VPA (Sigma, no. P4543) for VPA/LIF; 1.5 µM CGP77675 (Sigma no. SML0314) and 3 µM CHIR99021 for a2i/LIF; 1 µM PD0325901 and 3 µM CHIR99021 for 2i/LIF; 1 µM PD0325901 and 3 µM CHIR99021, 0.5 mM VPA (Sigma, no. P4543) for 2i/VPA/LIF; and 3 µM CHIR99021, 1.5 uM CGP77675 (Sigma no. SML0314), 0.5 mM VPA (Sigma, no. P4543) for a2i/VPA/LIF, respectively[29,31]. MEFs were prepared at a density of 2×10^6 per a six-well plate in DMEM-based MEF medium the day before plating PSCs[38]. These PSC cells were passaged at a split ratio of 1:6 every 2–3 d. For the analyses of flow cytometry, we used PSC$^{CAG-GFP}$ cultured for 5 days in each experimental condition. Briefly, cultured cells were trypsinized for 30 s–1 min with 0.05% trypsin, and were resuspended in 10 ml cold DMEM + 10% FBS, immediately. Samples were centrifuged for 3 min at room temperature at 1,000 r.p.m., and the supernatant was removed. After filtering the cells with a 35-µm nylon mesh (FisherScientific, 08-771-23), we performed live-cell staining on ice for 20 min with the following antibodies and dyes in cold flow buffer (PBS + 0.2% BSA) according to the manufacturer's protocol: SSEA1-BV421 (BioLegend, 125613: 1:200 dilution), PECAM-APC (BioLegend, 102509: 1:200 dilution), Zombie Aqua Fixable Viability Kit (BioLegend, 423101). We performed flow cytometry by BD LSR II Flow Cytometer and performed analysis using FlowJo software (Fig. 2a and Extended Data Fig. 2b,c). Statistical analyses were performed using a one-way analysis of variance (ANOVA) for the evaluation of the proportion of Ssea1$^+$Pecam$^+$ PSCs$^{Nkx2\text{-}1\text{-}GFP}$ among the parental population (live cells) in three independent biological samples per each condition. For immunofluorescence analyses of Oct4 and Ssea1 expression, we fixed the cells with 4% PFA for 15 min at room temperature and stained with each antibody, as described above.

Quantification of the pluripotency markers in the colonies of pluripotent stem cells. Images of Oct4, Ssea1 or pan-acetyl Histone H4 staining were captured using the same parameters for each cell culture condition using a DMi8 (Leica Microsystems) inverted microscope. We performed quantitative analyses using ImageJ software. Briefly, we acquired Oct4- or pan-acetyl Histone H4 MFI of each colony cultured in the six different conditions (LIF, 2i/LIF, a2i/LIF, VPA/LIF, 2i/VPA/LIF, a2i/VPA/LIF) on the basis of the histogram of ImageJ program (Analyze > Histogram). The edge of each colony was manually selected using a freehand selection tool of ImageJ. Twenty colonies from five different fields of each cell-culture condition were randomly selected for Oct4 and Ssea1 co-staining or pan-acetyl Histone H4 staining per experiment. To acquire relative MFI, we subtracted the background MFI of randomly selected non-colony area from 5 different fields, and then each subtracted MFI was normalized by dividing the average of MFI of the 20 colonies in LIF condition. The graphs are representative of three independent experiments. Then, we performed a Student's *t*-test for the statistical analyses of Oct4 and Ssea1 co-staining or pan-acetyl Histone H4 staining for the tested conditions. For the quantification of single Ssea1 staining by immunofluorescence, 5 random fields containing 11.5 colonies per field were captured using a DMi8 Leica microscope. Then, we classified those colonies into three categories based on the signal intensity of SSEA1 (Ssea1^{high}, Ssea1^{dim}, or Ssea1$^-$ (representative images in the upper panels of Extended Data Fig. 7a). We generated the graphs to represent means and standard errors ($n = 5$ fields) depicting the proportion of those categories in each condition. Each graph of Ssea1 analyses was representative of three independent experiments. Results from Ssea1^{high} PSC in each condition were subjected to statistical analyses (one-way ANOVA), expressed as mean + s.e.m., and differences were considered statistically significant at $P < 0.05$).

Analysis of GFP$^+$ chimerism by flow cytometry. To obtain the percentage of GFP$^+$ cells in lung endothelial, mesenchymal and epithelial cells simultaneously in the littermate chimeric mice of *Fgfr2*^{cnull}; *Rosa*$^{tdTomato/+}$, *Fgfr2*^{hetero}; *Rosa*$^{tdTomato/+}$ or WT, we used the protocol previously reported[39,40] with minor modification for the P1 respiratory tissue analyses. Briefly, we harvested the lungs and tracheas from those chimeric mice at P1 and placed the tissues into 50-ml tubes containing 10 ml of cold Ham's F12 medium. After transferring the tissues into 1.5-ml Eppendorf tubes, we finely minced the tissues by scissors. We then added 100 µl of pre-warmed dissociation buffer (1 mg ml^{-1} DNase (Sigma), 5 mg ml^{-1} collagen (Worthington Biochemical Corporation) and 15 U ml^{-1} Dispase (Corning) in HBSS). We then minced the tissues again to make them smaller than 3 mm in size. We then added 900 µl of pre-warmed dissociation buffer (total 1 ml dissociation buffer), and incubated them at 37 °C on the rocker with 135 r.p.m. speed. After 30–45 min of the incubation, we put the tubes back on the ice and filtered the digested tissues by the 40-µm filter (FALCON cat. no. 352235). The filtered tissues were centrifuged at 1,400 r.p.m., 4 °C, for 5 min, and we removed its supernatant. We resuspended the cell pellets with 1.5 ml of cold ACK lysis buffer to lyse remaining erythrocytes for 3 min at RT. We added 3 ml cold HBSS and centrifuged them down at 1,400 r.p.m., 4 °C, for 3 min to remove the lysed blood cells. Then, we resuspended the cell pellets with 1 ml cold HBSS + 0.2% BSA and counted the cell number (about 3 million per P1 lung) with a hematocytometer. We transferred 1–1.5 million cells in 500 µl (final volume) of flow buffer (cold HBSS, 0.2% BSA and 5 uM Y27632), and then added 10 µl Fc Block (BD Pharmingen; cat. no. 553141) per sample and incubate for 10 min at 4 °C. Then, we added the following antibodies: PECAM-BV421 (BD Pharmingen, cat. no. 562939, 1/250 dilution), EPCAM-BV711 (BioLegend, 118233, 1/200), Aqua Zombie (BioLegend, 423101, 1/500), CD45-BV605 (BioLegend, 103155, 1/200) for 30 min on ice. After the staining, we washed the samples with flow buffer and resuspended them in 500 µl flow buffer for the subsequent analyses by Flow cytometer (FACS Aria; gating

strategy in Extended Data Fig. 8). For setting up compensation and the voltage of each channel to avoid the background of autofluorescence and spill over each fluorophore signal to the other channels, we acquired 5×10^5 events from unstained control sample (WT CD1 mouse P1 lungs and trachea), each single staining sample (WT CD1 mice P1 lungs and trachea), PSC$^{CAG-GFP}$ (for GFP$^+$ events) and ES1^{tdtomato} (for tdTomato$^+$ events). For Zombie Aqua staining, we used WT CD1 mice P1 lungs and trachea incubated on ice to increase the population of dead cells (shown in Extended Data Fig. 8).

Blastocyst preparation and embryo transfer. Blastocysts were prepared by mating *Shh*^{Cre}; *Fgfr2*$^{flox/+}$ males with superovulated *Fgfr2*$^{flox/flox}$ females. For testing the effect of different culture conditions, we used WT (C57BL/6N × 129S6x CD1) males and females. Briefly, PMSG (pregnant mare serum gonadotropin, 5 IU in 0.1 ml PBS per mouse) was administered 48 h prior to mating, and hCG (5IU in 0.1 ml PBS per mouse) was administered 12 h before its mating as an intraperitoneal injection[15]. Blastocysts were harvested at E2.25, and 8–20 PSCs were injected into each blastocyst (Table 1). After the PSC injection, blastocysts were cultured in M2 medium (Cosmobio) for a few hours in a 37 °C, 5% CO_2 incubator for its recovery. Then, blastocysts were transferred to the uterus of the pseudopregnant foster mother, according to a protocol approved by the Columbia University Institutional Animal Care and Use Committee.

Sorting liver cells for genotyping. Genotyping of the chimeric mice was performed in liver cells prior to fixation for histological analyses. Briefly, the dissected liver tissue from each pup (P0, P1) or embryos (E12.5, E15.5) was sliced (0.5 cm × 0.2 cm) and minced for 5 min using scissors. Tissues were trypsinized with 500 µl 0.25% trypsin (Invitrogen) for 15 min at 37 °C, and the enzyme was inactivated with an equal amount of cold 100% fetal bovine serum (FBS). These cells were centrifuged at 1,000 r.p.m., 4 °C, 5 min, and the supernatant was removed. Cells were resuspended in 1 ml flow buffer (PBS + 0. 2% bovine serum albumin (BSA), passed through a 40-µm-pore nylon-mesh filter and transferred into a flow tube. Cells were stained with DAPI (1/1,000) for 5 min to remove dead cells. More than 10,000 cells per liver were sorted by FACS Area with the GFP-negative gate used for genotyping. The sorting purity was usually more than 90%. After removing the flow buffer by centrifuging at 1,000 r.p.m., 4 °C, 5 min, cells were then stored at −20 °C. We performed PCR with Tm-adjusted primers and the GFP-negative population as a template. The chimerism (measured as % GFP$^+$/live cells) in the liver cells was analyzed from the fcs files of sorted data by FlowJo.

Hematopoietic progenitor cells in colony-forming unit assays for genotyping of adult chimeric mice. To determine the genotyping before the pulmonary function test in the live chimeric adult mice, we performed a colony-formation assay in the MethoCult medium (Stemcells, no. M3434). Briefly, we harvested 0.2 ml into the 1-ml Eppendorf tube containing 20 µl 0.5 mM EDTA blood from the submandibular vein of chimeric mice by using a 5 mm lancet[41]. After the treatment with RBC lysis buffer (BioLegend, no. 420301) to each blood sample according to the manufacture's protocol, we removed lysed blood cells contained in the supernatant and, kept cell pellets it in 100 µl cold PBS. After counting these cell numbers, we plated each 0.4×10^5 cells per well resuspended in 300 µl MethoCult medium containing 100 µg ml^{-1} Primocine (IvivoGen, no. ant-pm-1) in a 24-well plate. Since the MethoCult medium is highly viscous, we used blunt-end needles, 16 gauge (Stemcells, no. 28110) to plate the cells equally in 24-well plates. We could obtain about 10 isolated colonies per 3 wells, and then we manually picked up at least 5 colonies from each mouse blood sample by using a 10-µl pipette for the subsequent genotyping analyses by using EZ Fast Blood/Cell PCR Genotyping Kit (EZ BioResearch cat. no. G1002).

Morphometric analyses. To determine the relative number of specific cell populations in P0 chimeric lungs, 10 non-overlapping random fields per mice were analyzed (×20 magnification) after capturing the images by confocal microscopy (Zeiss LSM710)[42]. For each field, we counted the number of GFP$^+$ cells co-immunostained with specific antibodies. DAPI co-staining was used to determine the cell number for each lineage as identified by differentiation markers, such as Sftpc, β4-tubulin and CC10, for alveolar type 2 cells, multiciliated cells and club secretory cells, respectively. Sox2 was used as a general marker for airway epithelial cell progenitors. Statistical analysis was performed (Student's *t*-test) and differences were considered significant if $P<0.01$. Pdpn$^+$GFP$^+$ area, Pdpn$^+$Hopx$^+$GFP$^+$ triple-positive area for the type 1 cells and PECAM$^+$GFP$^+$ area for vascular endothelial cells were calculated by Image J (NIH). Briefly, 10 non-overlapping random fields per mouse were captured using the same confocal microscopy settings. Each signal threshold of GFP, Pdpn, Hopx and Pecam was determined on the basis of each negative control: non-chimeric mouse tissue section of *Shh*^{Cre}; *Fgfr2*$^{flox/+}$ against GFP signal; secondary antibody only against each signal of Pdpn, Hopx and PECAM. The Hopx$^+$Pdpn$^+$ double-positive area was determined by pasting Hopx stained image on the corresponding field of the Pdpn-stained image, and the non-overlapped area was subtracted by ImageJ. The percentage of GFP labeling is determined by the following formula: Pdpn$^+$GFP$^+$/Pdpn$^+$ × 1.453 (normalization value) × 100, Pdpn$^+$Hopx$^+$GFP$^+$/Pdpn$^+$Hopx$^+$ × 1.406 (normalization value) × 100, Pecam$^+$GFP$^+$/PECAM$^+$ × 1.306 (normalization value) × 100. Each normalization value was determined based on the average ratio of five overlapping fields of *Fgfr2*^{cnull} + GFP samples. For example, in the case of Pdpn, the normalization value was (Pdpn$^+$ area)/(Pdpn$^+$GFP$^+$ area) in the five Pdpn$^+$GFP$^+$ overlapping fields of *Fgfr2*^{cnull} + GFP samples.

Quantitative real-time PCR. We treated the cells for 5 days in 6 different cell-culture conditions (LIF, LIF/2i, LIF/a2i, VAP/LIF, 2i/VPA/LIF and a2i/VPA/LIF). Total RNA from each cell sample was extracted using the RNeasy Mini Kit (Qiagen, no. 74104) and reverse-transcribed using Superscript III (Invitrogen, no. 18080-051). Reactions (25 µl) were performed using ABI 7000 (Applied Biosystems) and SYBR Green Master Mix (Thermo Fisher, no. A25741). The relative abundance of the RNA for each gene to β-actin mRNA was determined using the $2^{-\Delta\Delta Ct}$ method. The following primers were used: Dnmt3a forward 5′-CCTGCAATGACCTCTCCATT-3′; Dnmt3a reverse 5′-CAGGAGGCGGTAGAACTCAA-3′; Dnmt3b forward 5′-TGGTGATTGGTGGAAGCC-3′; Dnmt3b reverse 5′-AATGGACGGTTGTCGCC-3′. Data were represented as mean ± s.e.m. of measurements in each culture condition and analyzed by Student's *t*-test. Differences were considered statistically significant if $P<0.05$; the number of animals per group are provided in the legends

Western blot analysis. PSCs were cultured for 5 days (LIF, LIF/2i, LIF/a2i, VAP/LIF, 2i/VPA/LIF and a2i/VPA/LIF) and Western blot analysis was performed as reported previously[43]. Cells were lysed in laemmli buffer (Sigma, no. S3401) and boiled for 15 min at 95 °C. Lysates were then separated by SDS–polyacrylamide gel electrophoresis (SDS–PAGE), transferred to a nitrocellulose membrane, blocked in 5% nonfat milk in PBS plus 0.5% Tween-20, probed with primary antibodies, and detected with horseradish-peroxidase-conjugated anti-rabbit or anti-mouse secondary antibodies (GE Healthcare). The following primary antibodies were used: anti-Histone H4ac (pan-acetyl) (Active Motif, no. 39925, dilution 1:1,000), Histone H3K27me3 antibody (monoclonal antibody) (Cell Signaling Tech, no. 2901, dilution 1:1,000) and Histone H3K4me3 antibody (pAb) (Active Motif, no. 39915, dilution 1:1,000). Anti-Histone H3 (Abcam, no. ab1791, dilution 1:1,000) antibodies were used as internal controls. Enhanced chemiluminescence was detected using LAS 4000 (GE Health Care). Quantitative analysis for the western blots was performed by calculating the relative density of the immunoreactive bands after the acquisition of the blot image with a LAS 4000 CCD video camera module and analyzing with the Image 152 g program (Wayne Rasband, NIH, Research Service Branch, NIMH, Bethesda, MD). Briefly, we subtracted the background density value (the average of five randomly selected equal size of the area) to the acquired density value of each blot. Then, we divided each subtracted density value by the subtracted value of the LIF sample for obtaining normalized relative values.

LINE-1 ELISA analyses. To measure 5-mC levels of Long Interspersed Nucleotide Element 1 (LINE-1) repeats, we treated the cells for 5 days in 6 different cell culture conditions (LIF, LIF/2i, LIF/a2i, VAP/LIF, 2i/VPA/LIF and a2i/VPA/LIF). We performed ELISA-based LINE-1 analyses according to the manufactured protocol (Active Motif, no. 55017). Briefly, genomic DNA was enzymatically digested with MseI enzyme to generate the appropriate fragments to hybridize to a biotinylated consensus sequence. Hybridized samples were immobilized to a 96-well plate, and methylated cytosines are identified using a 5-methylcytosine antibody, HRP-conjugated secondary antibody and colorimetric detection reagents. Generating a standard curve using the included DNA standards with known LINE-1 methylation levels provided the relative level of 5-methylcytosine in each DNA sample. Statistical analyses were performed using one-way ANOVA. Results were expressed as mean + s.e.m., and differences are considered statistically significant if $P<0.05$.

3D structured illumination microscopy. To further demonstrate chimerism and complementation of alveolar type 1 cells (GFP and IF with Pdpn) at high resolution we used structured illumination microscopy (SIM), performed with a Nikon N-SIM based on an Eclipse Ti inverted microscope using an SR Apo-TIRF ×100/1.49 oil-immersion objective and an Andor iXon 3 EMCCD camera, as described previously[37]. Briefly, the images for each lung cell were acquired in 3D-SIM mode using excitation at 405 nm, 488 nm and 561 nm and standard filter sets for blue, green and red emission. Image *z*-stacks were collected with a *z* interval of 200 nm. SIM image reconstruction, channel alignment and 3D reconstruction were performed using NIS-Elements AR software. The images were visualized using an alpha-rendering mode that can show the signal of the structural surface.

Pulmonary function assessment. Chimeric mutant mice (*Fgfr2*^{cnull} + PSC$^{CAG-GFP}$ or *Ctnnb1*^{cnull} + PSC$^{CAG-GFP}$) and its littermate control WT mice were anesthetized with pentobarbital (intraperitoneally, 50 mg per kg (body weight)). Once surgical anesthesia was achieved, mice were tracheotomized with an 18G cannula and connected to a flexiVent (SciReq, Montreal, Quebec, Canada) with an FX1.

Module and an in-line nebulizer were described previously[44]. Mice were mechanically ventilated at 150 breaths per min, with a tidal volume of 10 ml per kg and a positive end-expiratory pressure of 3 cm H_2O. Muscle paralysis was achieved

with succinylcholine (i.p., 10 mg per kg (body weight)) to prevent respiratory effort. By using the forced oscillation technique, baseline measurements of the resistance (Rrs), compliance (Crs) and elastance (Ers) of the respiratory system were measured. A baseline measure of central airway resistance (Rn) was performed, followed by subsequent Rn measurements during nebulized methacholine (0, 6.25, 12.5, 25 and 50 mg ml^{-1}) challenge (10-s nebulization, 50% duty cycle). Values for all measurements represent an average of three replicates. EKG and temperature were continuously monitored. Statistical analysis was performed by Student's *t*-test, paired. Results were expressed as mean + s.e.m. and differences considered statistically significant if $P < 0.05$. The number of animals per group are provided in the legends.

Study approval. All experiments involving animals were performed according to the protocol approved by the Columbia University Institutional Animal Care and Use Committee and USAMRMC Animal Care and Use Review Office (ACURO).

Reporting Summary. Further information on research design is available in the Nature Research Reporting Summary linked to this article.

Data availability

All files and processed data are also available from the corresponding author upon request. No database was generated. Source Data for Figs. 1–3 and Extended Data Figs. 2, 4, 5 and 7–10 are available online.

References

35. Brault, V. et al. Inactivation of the beta-catenin gene by Wnt1-Cre-mediated deletion results in dramatic brain malformation and failure of craniofacial development. *Development* **128**, 1253–1264 (2001).
36. Ke, M. T. et al. Super-resolution mapping of neuronal circuitry with an index-optimized clearing agent. *Cell Rep.* **14**, 2718–2732 (2016).
37. Mori, M. et al. Cytoplasmic E2f4 forms organizing centres for initiation of centriole amplification during multiciliogenesis. *Nat. Commun.* **8**, 15857 (2017).
38. Huang, S. X. L. et al. The in vitro generation of lung and airway progenitor cells from human pluripotent stem cells. *Nat. Protoc.* **10**, 413–425 (2015).
39. Singer, X. B. D. et al. Flow-cytometric method for simultaneous analysis of mouse lung epithelial, endothelial, and hematopoietic lineage cells. *Am. J. Physiol. Lung Cell Mol. Physiol.* **310**, L796–L801 (2016).
40. Chapman, H. A. et al. Lineage-negative progenitors mobilize to regenerate lung epithelium after major injury. *Nature* **517**, 621–625 (2015).
41. Golde, W. T., Gollobin, P. & Rodriguez, L. L. A rapid, simple, and humane method for submandibular bleeding of mice using a lancet. *Lab Anim. (NY)* **34**, 39–43 (2005).
42. Mori, M. et al. Notch3-Jagged signaling controls the pool of undifferentiated airway progenitors. *Development* **142**, 258–267 (2015).
43. Lu, C. et al. Histone H3K36 mutations promote sarcomagenesis through altered histone methylation landscape. *Science* **352**, 844–849 (2016).
44. Mikami, M. et al. Impaired relaxation of airway smooth muscle in mice lacking the actin-binding protein gelsolin. *Am. J. Respir. Cell Mol. Biol.* **56**, 628–636 (2017).

Acknowledgements

We thank J. Qian, J. Huang, A. Kuforiji and M. Jiang for technical assistance, and D. Kotton and L. Oikonomou (CReM, Boston University) for invaluable reagents. We also thank the helpful scientific input from members of the Cardoso's lab and the Columbia Center for Human Development (J. Lu, H. Snoeck, S. Huang, J. Que, F. Constantini, J. Bhattacharya and M. Bacchetta) as well as from M. Morimoto (RIKEN, Japan), T. Matozaki (Kobe University), H. Masaki, S. Hamanaka (University of Tokyo) and T. Nishimura (Stanford University). We also thank K. Kennedy for help in editing the manuscript. We would like to acknowledge the support from the CCTI flow cytometry core (LSRII: NIH S10RR027050) and Columbia Stem Cell Initiative (CSCI) Flow Cytometry core (FACS Area). This work was funded by the Department of Defense, PR161857 and NIH-NHLBI 1 R01 HL148223-01 to M.M., CIRM Research Leadership Award, LA1_C12-06917 to H.N., NIH-NHLBI R35-HL135834-01 to W.V.C., Giannandrea Family Dale F. Frey Breakthrough Scientist of the Damon Runyon Foundation (DFS-28-18) and a Pew-Stewart Scholar for Cancer Research to C.L.

Author contributions

M.M. designed and conducted all experiments; J.A.D. and C.W.E. performed pulmonary function assessment; C.-S.L. and Y.T. supported and performed microinjection and embryo transfer; M.M., P.R. and M.O. maintained mutant mice for the injection; K.F. supported imaging of whole-mount staining; K.F., Y.H., M.O. and M.K. supported and performed hematopoietic cell-colony-formation assay; X.X. and C.L. performed epigenetic experiments; M.M., C.L. and W.V.C wrote the paper; H.N. gave crucial insights on the experiments and the manuscript.

Competing interests

The authors declare no competing interests.

Additional information

Extended data is available for this paper at https://doi.org/10.1038/s41591-019-0635-8.

Supplementary information is available for this paper at https://doi.org/10.1038/s41591-019-0635-8.

Correspondence and requests for materials should be addressed to M.M., H.N. or W.V.C.

Peer review information Michael Basson was the primary editor on this article and managed its editorial process and peer review in collaboration with the rest of the editorial team.

Reprints and permissions information is available at www.nature.com/reprints.

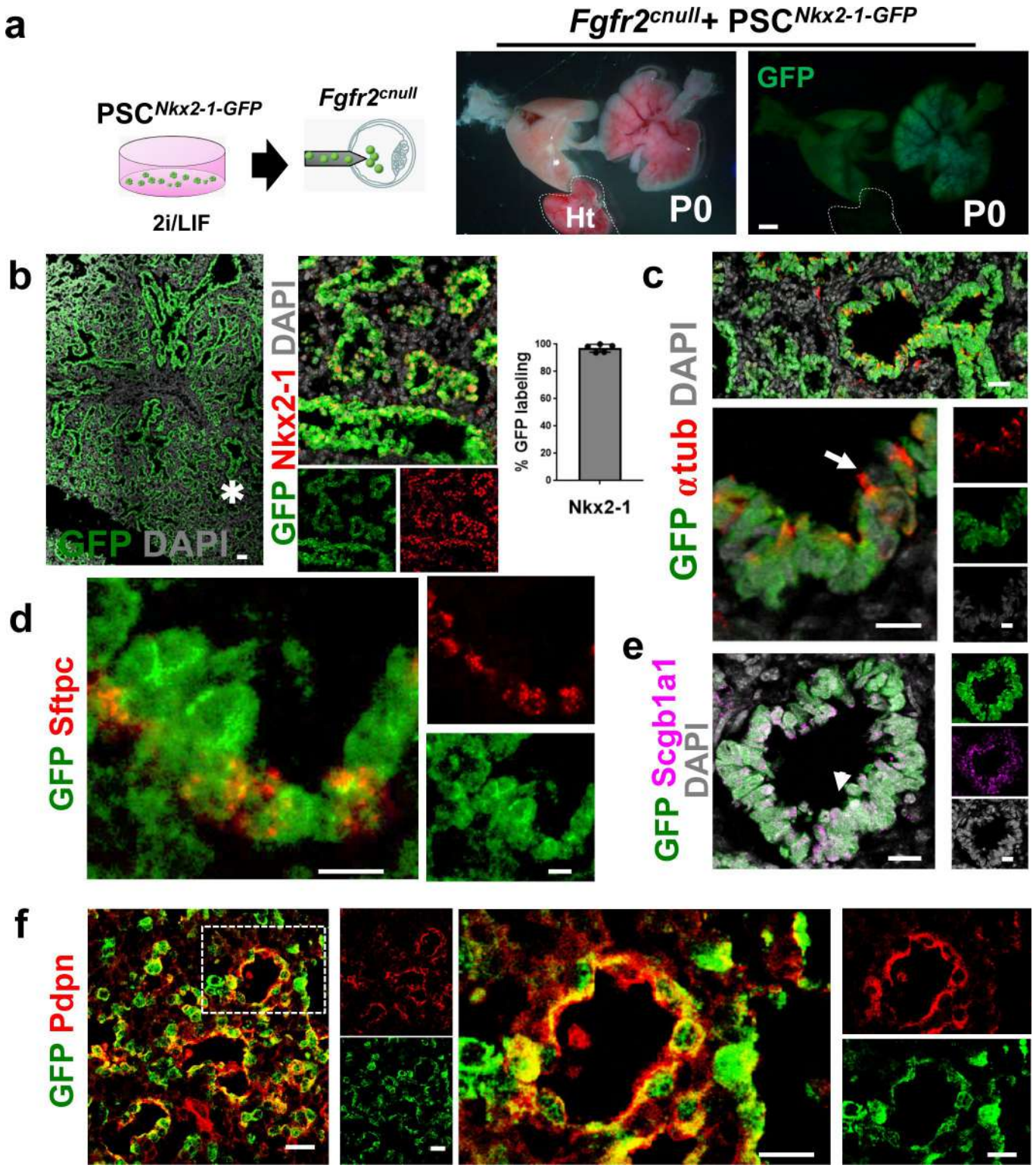

Extended Data Fig. 1 | PSC$^{Nkx2\text{-}1\text{-}GFP}$ rescues lung agenesis in *Fgfr2*-deficient mutants, but lungs are immature. a, Schematic of experimental procedure (left) and representative macroscopic view of the lungs and heart (ht) from newborn (P0) mice *Fgfr2*^{cnull} complemented by donor 2i/LIF-cultured *PSC*$^{Nkx2\text{-}1\text{-}GFP}$. Right panel depicts GFP signals in the lungs not present in the heart (outlined). **b**, Representative GFP expression in lung section of P0 *Fgfr2*^{cnull} + PSC$^{Nkx2\text{-}1\text{-}GFP}$: strong signals throughout all epithelial tubes, less prominent in the mesenchyme and its derivatives (Ex. large vessels, center). Asterisk (*) marks distal epithelial tubules unable to form distal saccules resulting in immature non-functional lungs. Immunofluorescence of Nkx2-1 and quantitative analysis confirming extensive double-labeling with GFP (single channels shown in small panels). Graph represents mean ± s.e.m. of % GFP$^+$ lung epithelial cells in five random fields per sample ($n = 2$ animals). **c**–**f**, Representative immunofluorescence and confocal images of lungs double-labeled with GFP and markers of alveolar type 1 (Pdpn) and type 2 (Sftpc) or airway multiciliated (acetylated α-tub) or secretory (Scgb1a1) cells ($n = 3$–4 per group). Boxed area (**f**) enlarged in the right panels. **b**–**f**, images also displayed as single channels; DAPI in grey. Scale bars: **a**, **b**, **c**–**e**, **f**: 1 mm, 20 μm, 10 μm, and 20 μm, respectively.

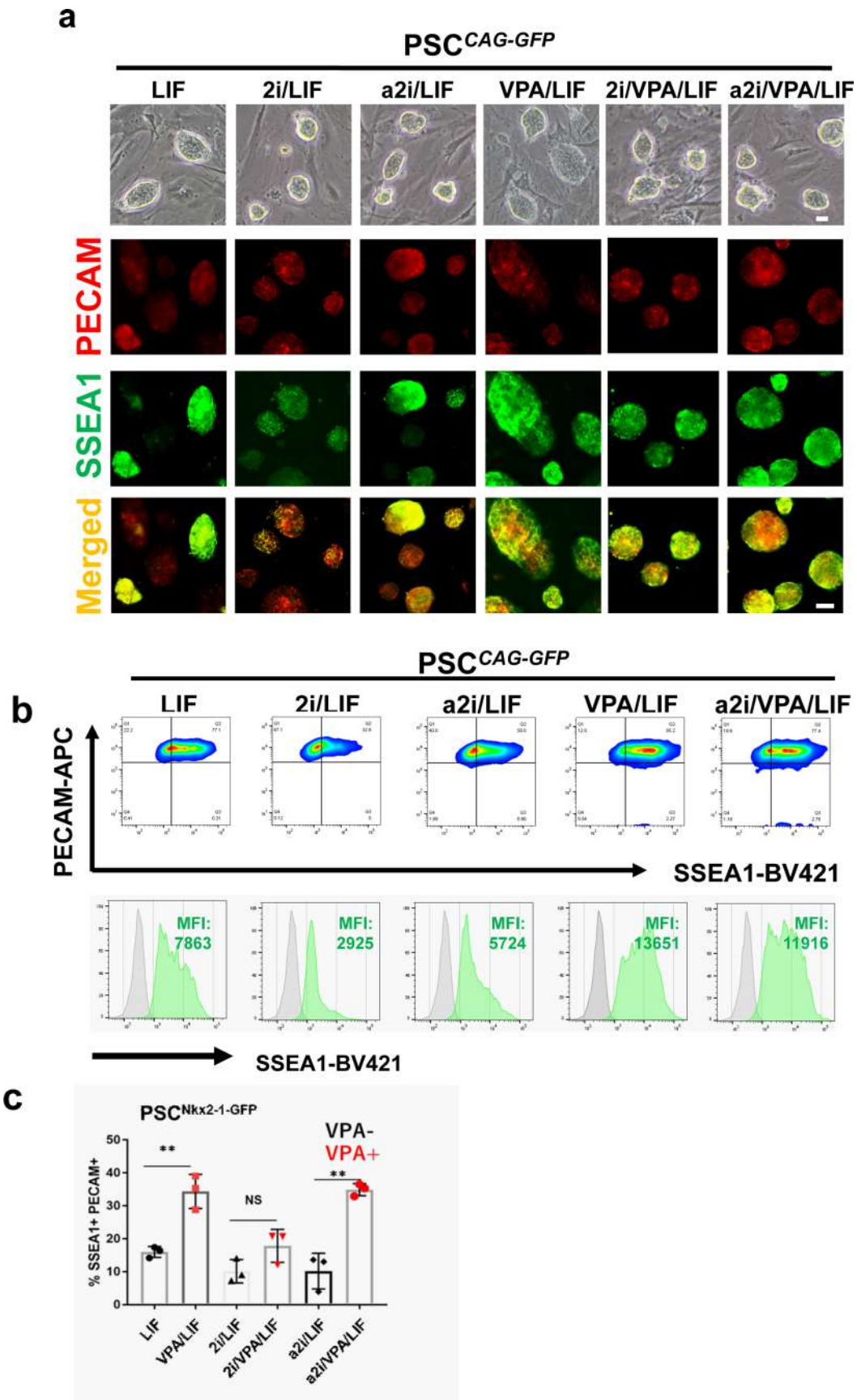

Extended Data Fig. 2 | See next page for caption.

Extended Data Fig. 2 | Effect of PSC cell culture conditions in pluripotency markers. a, Representative morphology of $PSC^{CAG-GFP}$ colonies and immunofluorescence image of Ssea1 and Pecam expression under the culture conditions listed. **b**, Representative flow cytometry pseudocolor images (top) and respective histograms (bottom) showing the increased yield of the $Ssea1^{high}Pecam^{+}$ $PSC^{CAG-GFP}$ population and high Ssea1 MFI in cultures treated with VPA/LIF and a2i/VPA/LIF. **c**, FACS analysis of $PSC^{Nkx2\text{-}1\text{-}GFP}$ cultured on the conditions indicated. Graph shows differences in the yield of $Ssea1^{+}Pecam^{+}$ (%). Note the effect of the addition of VPA to LIF or a2i/LIF treatment. Bars are mean ± standard error of $n = 3$ independent experiments in each culture condition. Data were analyzed by one-way ANOVA; differences were significant at $^{**}P < 0.01$. Scale bars: **a** = 10 μm.

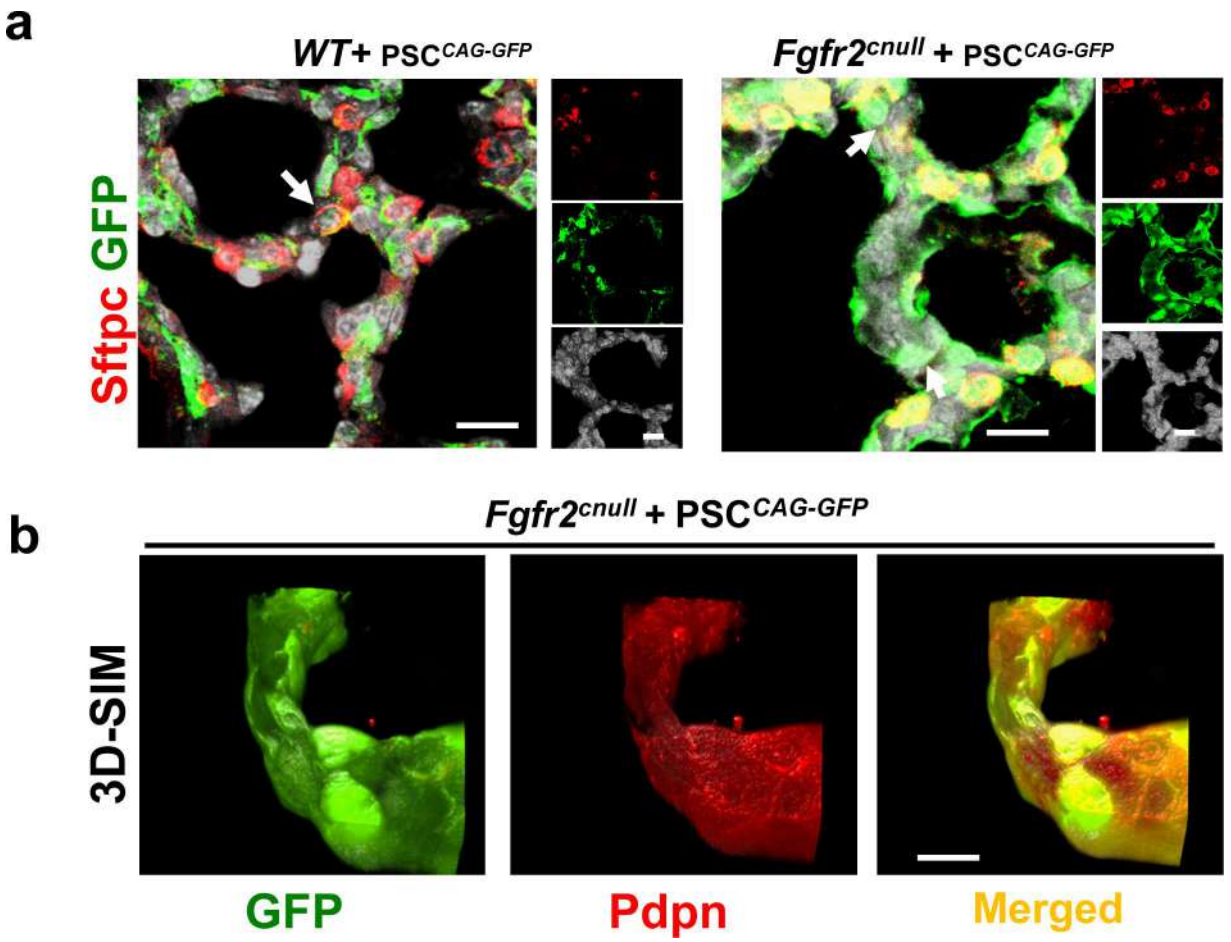

Extended Data Fig. 3 | Complemented distal lung of VPA/LIF-treated PSC$^{CAG-GFP}$ *Fgfr2* mutants undergo sacculation. a Representative immunofluorescence confocal imaging depicting the expression of GFP and markers for alveolar type 2 (Sftpc) in the walls of distal saccules in lung sections of P0 VPA/LIF-treated PSC$^{CAG-GFP}$ *Fgfr2*^{cnull} mice (left panel, WT P0 littermate). **b**, the 3D-SIM image of PSC$^{CAG-GFP}$ *Fgfr2*^{cnull} mice showing at high resolution the staining of alveolar type I surface double-labeled with GFP. Scale bars: **a** and **b**,10 μm.

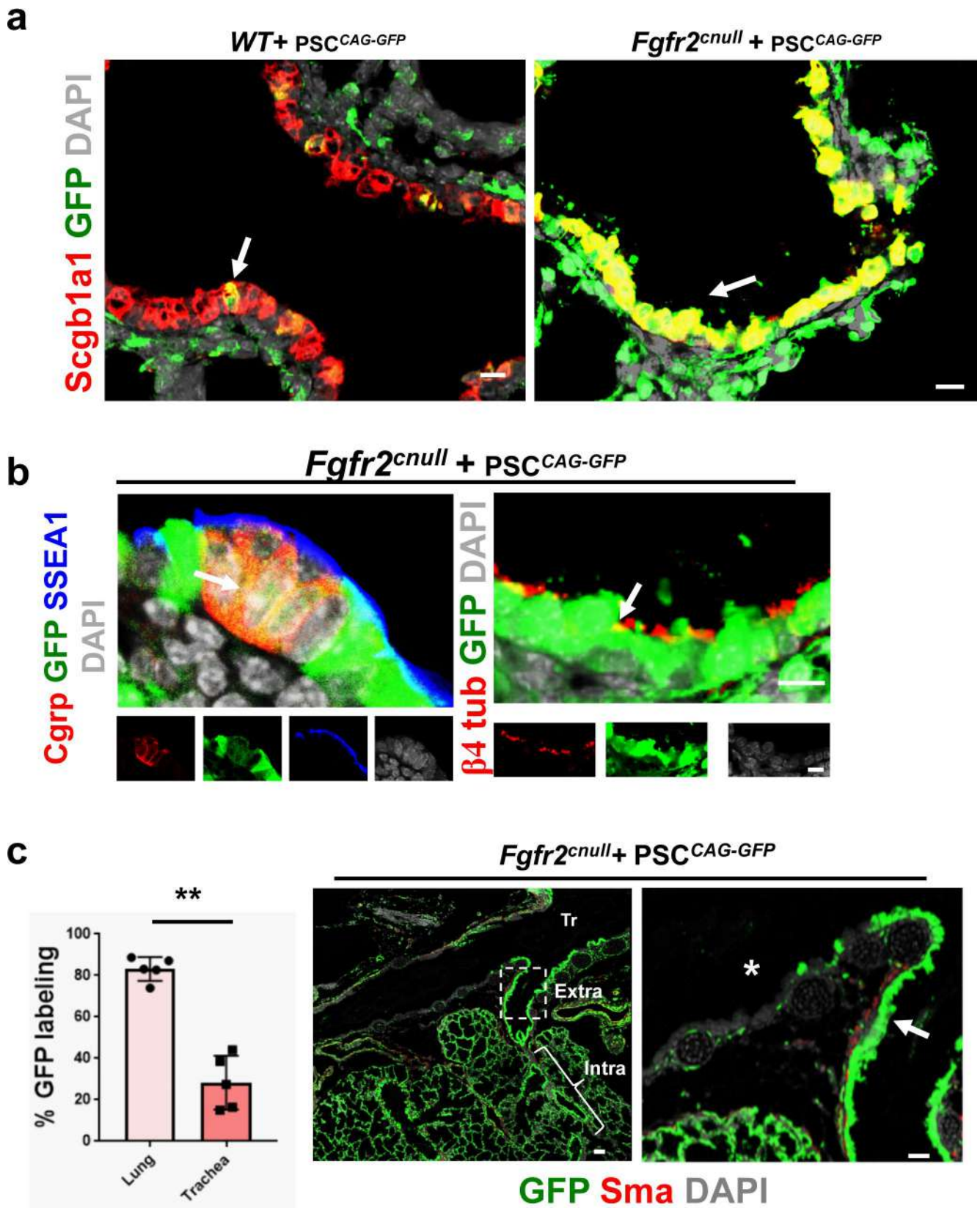

Extended Data Fig. 4 | See next page for caption.

Extended Data Fig. 4 | Airway epithelial complementation in *Fgfr2*^{cnull} PSC$^{CAG-GFP}$newborn chimeric pups. a,**b**, Immunofluorescence and confocal imaging depicting GFP double-labeling (arrows) with cell differentiation markers Scgb1a1 (secretory), β-tubulin4 (multiciliated) and Cgrp (neuroendocrine) in lung sections of P0 mice from VPA/LIF-treated PSC$^{CAG-GFP}$ + *Fgfr2*^{cnull} and WT chimeric littermates; small panels in **b** depict single channels). **c**, Percentage of GFP^{+} cells in the lung and tracheal epithelium as determined by quantitative analysis of GFP signals in sections of newborn P0 PSC$^{CAG-GFP}$ *Fgfr2*^{cnull} animals. Graph, Mean ± s.e.m. of measurements in 5 random fields per section per sample. Student's *t*-test; $^{**}P < 0.01$. Right panel, Representative GFP and Sma immunostaining in a histological section of P0 complemented mutant depicting epithelial signals (arrows) consistently strong in intrapulmonary airways (bracket), but variable or low (asterisks) in the extrapulmonary airway (dashed box) and trachea (Tr). Boxed area enlarged on the right. Sma (alpha-smooth muscle actin) labeling airway smooth muscle. Scale bars: **a**, **b**, **c**: 10 μm, 10 μm, and 20 μm, respectively.

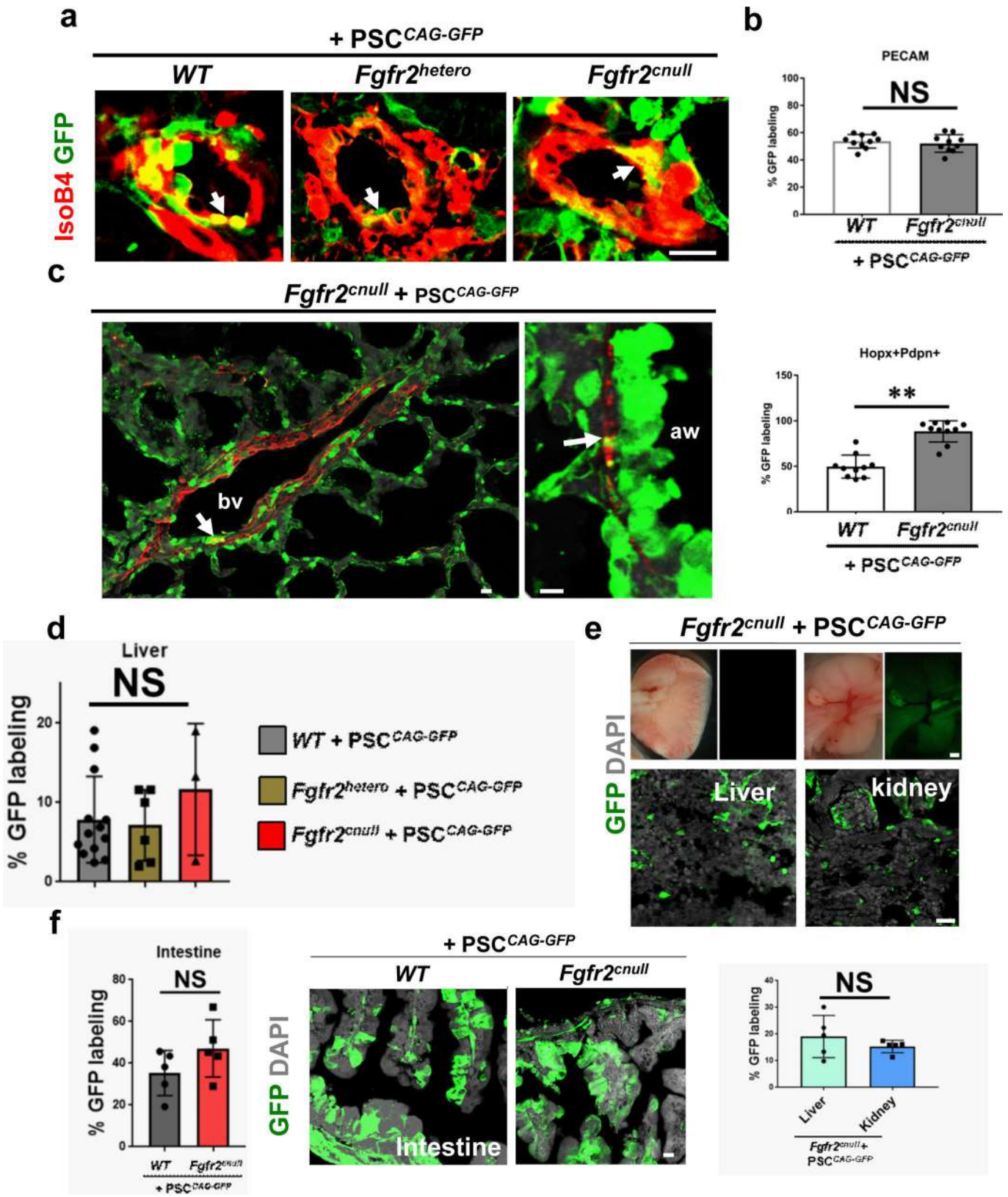

Extended Data Fig. 5 | See next page for caption.

Extended Data Fig. 5 | Chimerism in the lung alveolar vascular compartment (a–c) and extrapulmonary organs of animals complemented with VPA/LIF-treated PSC$^{CAG-GFP}$ (d–f). a, Immunofluorescence and confocal imaging of newborn (P0) WT + PSC$^{CAG-GFP}$, *Fgfr2*^{hetero} + PSC$^{CAG-GFP}$ and *Fgfr2*^{cnull} + PSC$^{CAG-GFP}$ chimeric lungs. Representative image of blood vessels showing GFP-Isolectin B4 double-labeled endothelial cells (arrows). **b**, Percentage of GFP labeling in endothelial (top) and alveolar type I (bottom) cells in P0 WT + PSC$^{CAG-GFP}$ and *Fgfr2*^{cnull} + PSC$^{CAG-GFP}$ chimeric lungs as determined by morphometric analysis of sections immunostained with Pecam (top) or Hopx and Pdpn (bottom). Graphs: mean ± s.e.m. of measurements in ten non-overlapping random fields per group (see also Supplementary Fig. 2 and Methods). **c**, GFP-Sma double-labeling of smooth muscle cells (arrow) in blood vessels (bv) and airways (aw) by immunofluorescence of P0 lungs from PSC$^{CAG-GFP}$ complemented *Fgfr2*^{cnull} mice. **d**, Proportion of GFP$^+$ cells in the liver from E15.5 and P0 chimeric mice isolated by FACS. Graph represents mean ± s.e.m. of PSC$^{CAG-GFP}$-complemented WT, *Fgfr2*^{hetero} *or Fgfr2*^{cnull} animals ($n = 13, 6, 3$ animals, respectively). **e**, Representative images of GFP expression in liver (left) and kidney (right) from P0 *Fgfr2*^{cnull} + PSC$^{CAG-GFP}$ (whole-mount and histological sections) and quantitative analysis (bottom) of GFP labeling; graph: mean ± s.e.m. of % GFP$^+$ cells per field in 5 random fields per group. **f**, Representative images of GFP expression in the intestine from WT or *Fgfr2*^{cnull} injected with PSC$^{CAG-GFP}$ (histological sections) and graph showing % GFP + (mean ± s.e.m., 5 random fields per 5 per group). Statistical analysis (**b**,**d**–**f**): Student's *t*-test; $^{**}P < 0.01$, NS: statistically non-significant. Scale bars: **a**, **b** = 10 μm, 5 μm, respectively; **e**: top panel: 20 μm, bottom panel: 1 mm; **f**: 10 μm.

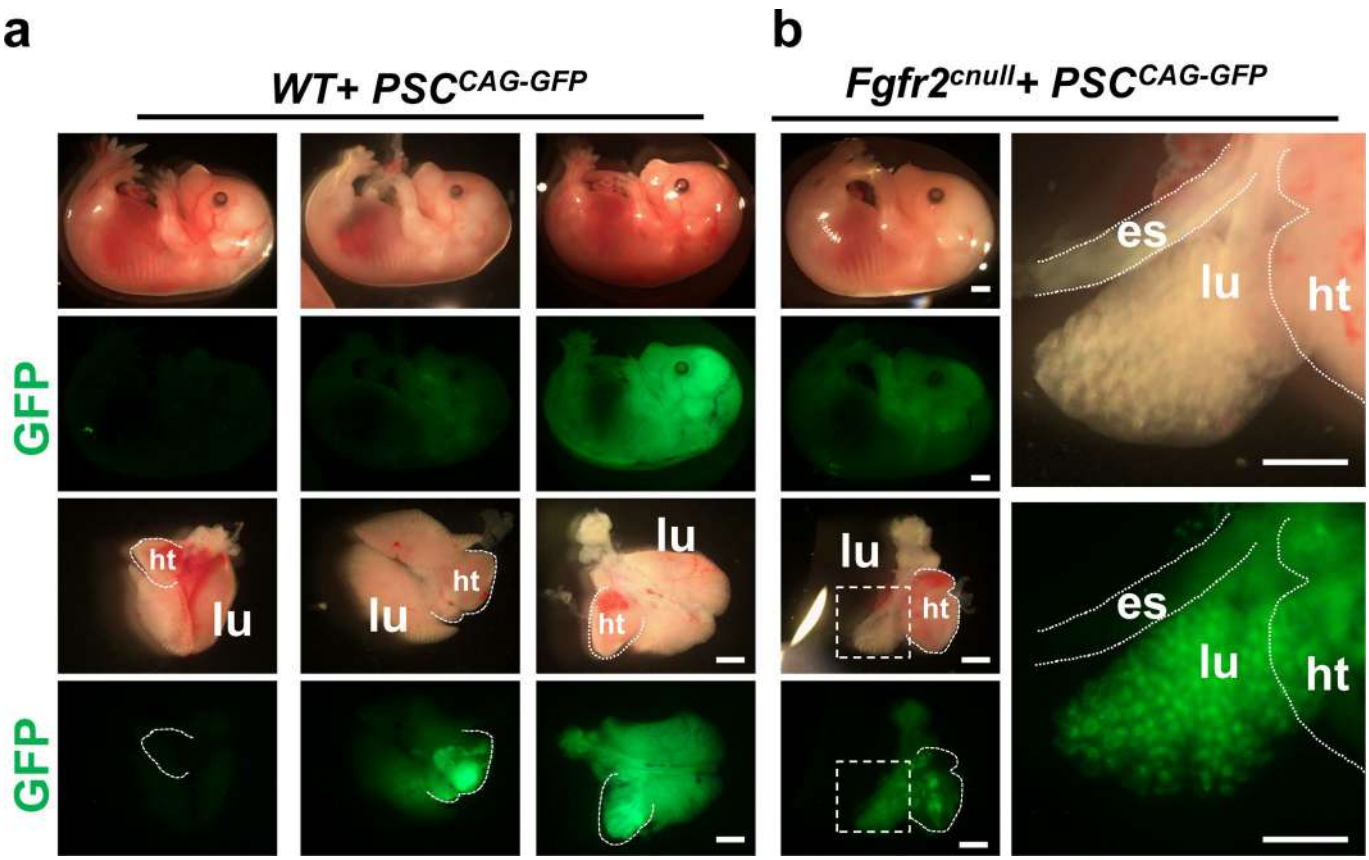

Extended Data Fig. 6 | Low chimerism in VPA/LIF-treated PSCs$^{CAG-GFP}$ *Fgfr2*^{cnull} embryos and defective lung organogenesis. GFP expression in whole-mount E15.5 embryos and tissues. **a**, Variable chimerism in E15.5 WT + PSCs$^{CAG-GFP}$ embryos with different levels of GFP signals in the skin, lung (lu) and heart (ht: outlined). **b**, Unilateral rescue of the lung (boxed) in E15.5 *Fgfr2*^{cnull} embryos complemented with VPA/LIF PSCs$^{CAG-GFP}$; note low chimerism in the esophagus (es) and heart. Scale bars: 1 mm.

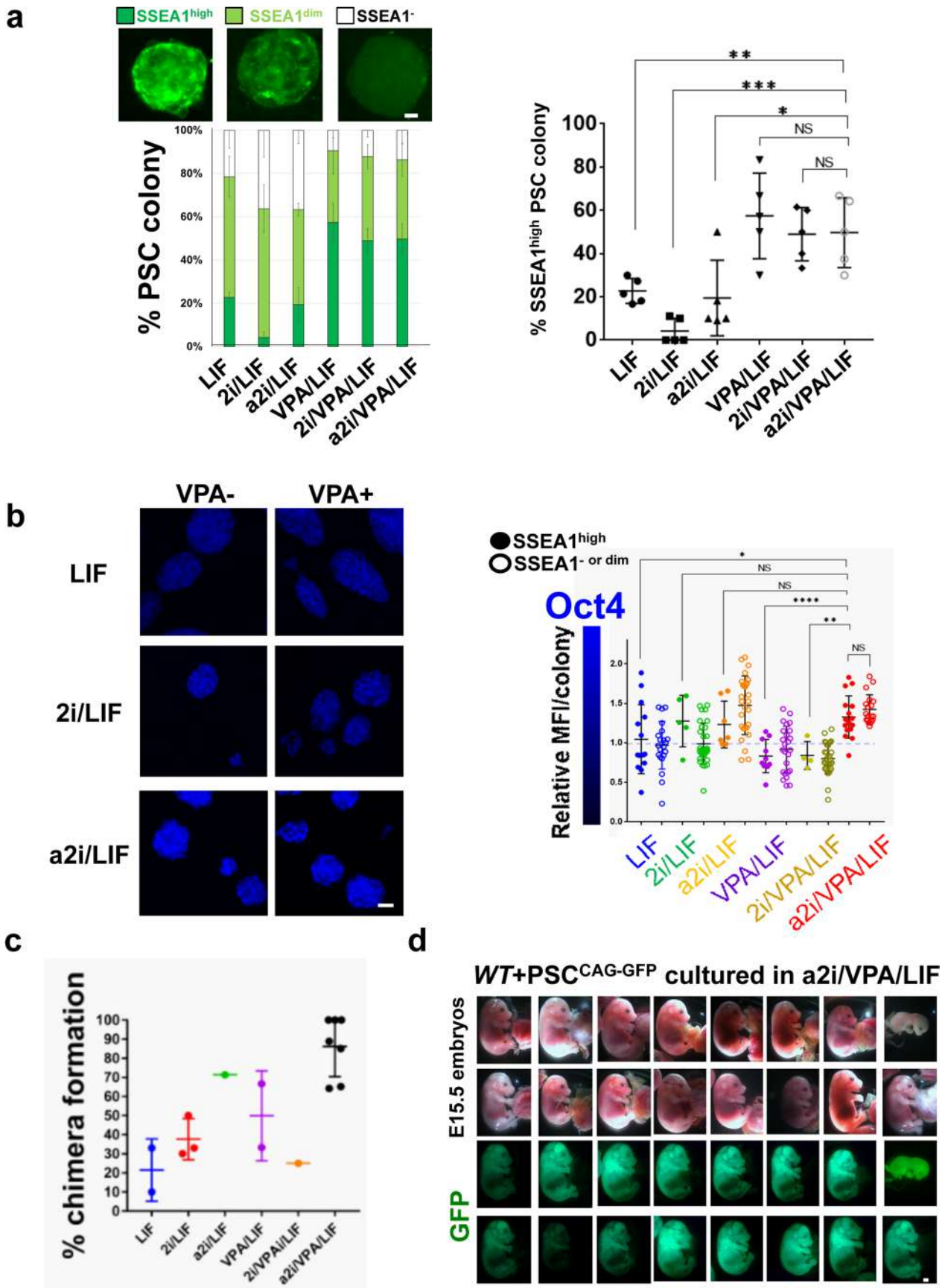

Extended Data Fig. 7 | See next page for caption.

Extended Data Fig. 7 | Comparative effects of a2i/VPA/LIF with other culture conditions in PSC pluripotency and chimerism. a, Immunofluorescence and quantitative analysis of Ssea1 expression in $PSC^{CAG-GFP}$ colonies in the various media tested. Top panel, representative images of $Ssea1^{high}$, $Ssea1^{dim}$ and $Ssea1^{negative}$ colonies. Bottom panel, graphs showing the percent of Ssea1-expressing colonies high, dim or negative as above (left) and percent of $Ssea1^{high}$ colonies (right) in each culture condition. Data are mean ± s.e.m of the number of colonies per field in five non-overlapping random fields per condition. **b**, IF of Oct4 and SSEA1in $PSC^{CAG-GFP}$ cultured in the conditions indicated. Left: representative image of Oct4 staining. Right: Graph showing Oct4 expression levels in $SSEA1^{high}$ (dots) or Ssea1 dim/negative pooled (empty dots) PSC colonies cultured as indicated. Mean fluorescent intensity (MFI) of Oct4 as assessed by imaging of 35 random colonies per culture condition (ImageJ). Relative MFI per colony shown as the Oct4 MFI of each colony normalized by the average fluorescent intensity of the PSCs cultured in LIF condition. Graphs in **a** and **b** depicting the VPA's ability to enrich for $Ssea1^{high}$ PSCs and the a2i/VPA/LIF effect in enhancing Oct4 expression but no significant difference in Oct4 levels between $Ssea1^{high}$ and $Ssea1^{dim}$ a2i/VPA/LIF-treated PSCs. **c**, Percentage of chimera formation as determined by analysis of skin/coat color in pups at P0 from blastocysts injected with PSCs cultured in each condition and transferred to foster mothers. Graph represents mean ± s.e.m. of the percentage of chimeric pups generated from the PSCs indicated (number of experiments represented by each point in the graph, see Methods). **d**) Whole-mount brightfield and GFP images of E15.5 embryos showing the high frequency of GFP-expressing chimera formation from WT hosts injected with a2i/VPA/LIF-treated $PSC^{CAG-GFP}$ (see also Table 1). Statistical analysis: one-way ANOVA (**a**,**b**) and Student's *t*-test (**c**); differences considered statistically significant if $^{*}P < 0.05$, $^{**}P < 0.01$, $^{***}P < 0.001$, $^{****}P < 0.0001$, NS: non-significant. Scale bars: **a**, **b**, **d** = 10 μm, 20 μm, 1mm respectively.

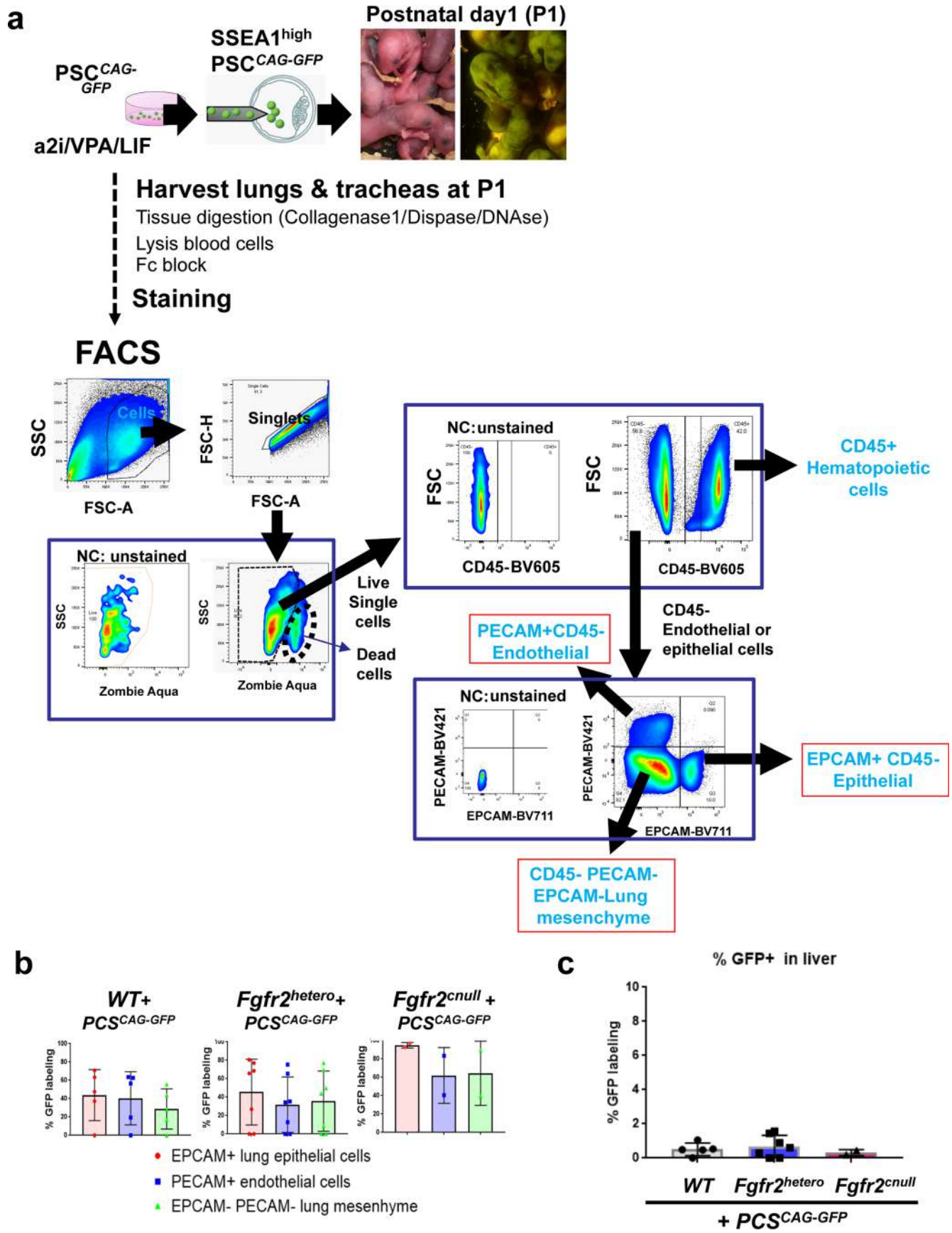

Extended Data Fig. 8 | See next page for caption.

Extended Data Fig. 8 | FACS-based assessment of cell type-specific chimerism in lung and liver from a2i/VPA/LIF -treated Ssea1^{high} PSC$^{CAG-GFP}$ WT, *Fgfr2*^{hetero}, or *Fgfr2*^{cnull} hosts. a, Schematics of the CBC approach (Ssea1^{high} a2i/VPA/LIF-treated PSC donor cells injected into blastocysts hosts, chimeric pups identified at birth), tissue isolation/dissociation and gating strategy for flow cytometry (FACS) analysis of different cell types in the lung. Lung cells (FSC/SCC panels) and singlets (FSC-H/FSC-A) were selected. Within the lung singlets, live cells were gated as an unstained negative control (NC) and hematopoietic (CD45$^+$ versus CD45$^-$). In the CD45$^-$ gate, we separated epithelial (Epcam$^+$), endothelial (Pecam$^+$) and other non-endothelial lung mesenchymal cells (Pecam/Epcam double negative). The percentage of GFP$^+$ cells was calculated based on the unstained WT negative control gate. **b**, FACS analysis of complemented lungs (left panels) and liver (right panel) from Ssea1^{high} a2i/VPA/LIF -treated PSC$^{CAG-GFP}$ + WT ($n=5$) *Fgfr2*^{hetero} ($n=7$) or *Fgfr2*^{cnull} ($n=2$) animals showing the percentage of GFP labeling in lung (epithelial, endothelial or non-endothelial lung mesenchymal) cells and liver. Graphs (mean ± s.e.m) depicting GFP labeling in nearly all lung epithelial cells from *Fgfr2*^{cnull} compared to heterozygous and WT, inconsistent variable labeling in lung endothelial/mesenchymal cells and low proportion of GFP$^+$ cells in liver regardless of the genotype.

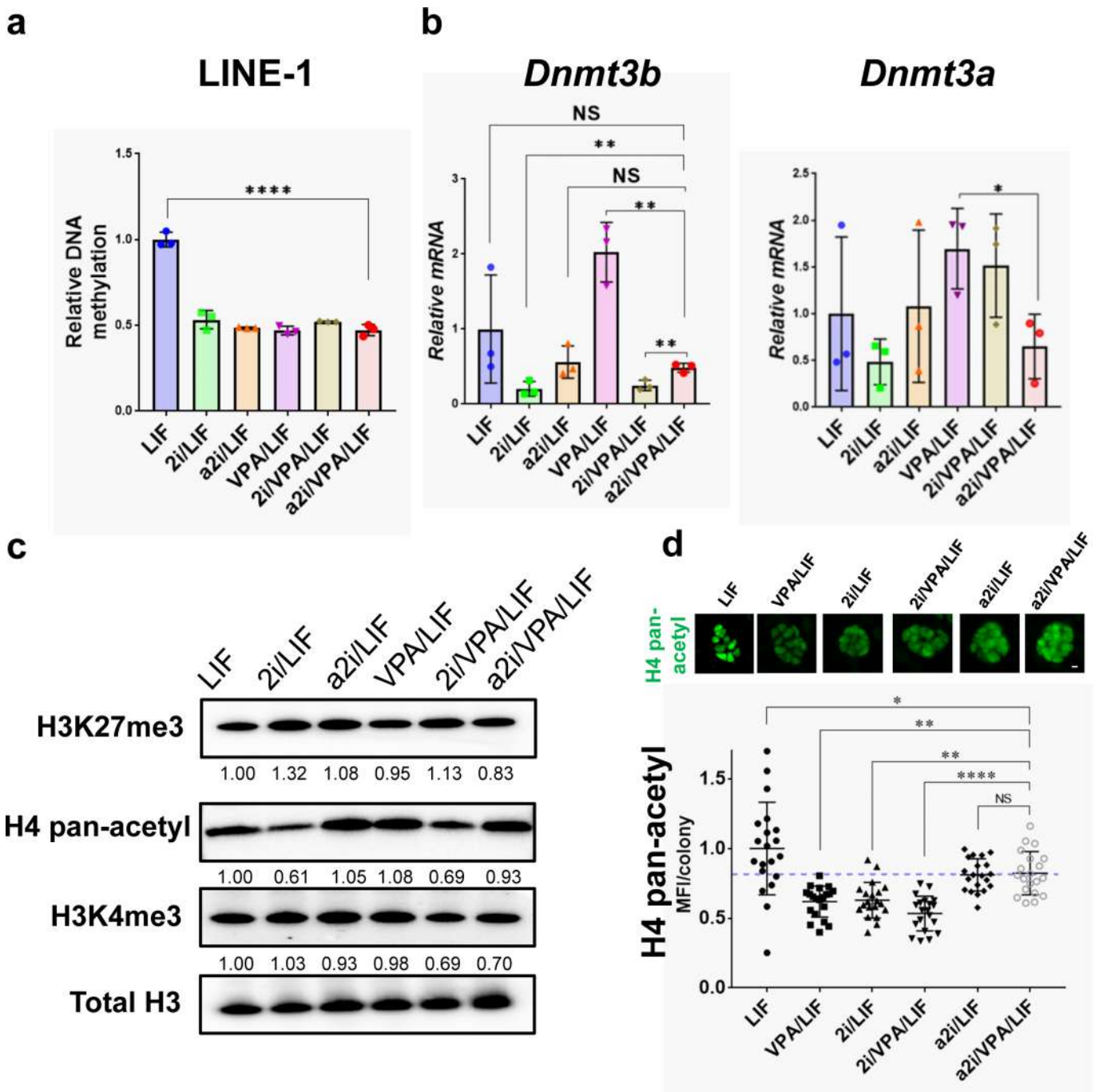

Extended Data Fig. 9 | Effect of culture conditions in global DNA methylation, DNA methyltransferase gene expression and the patterns of histone modifications by PSC$^{CAG-GFP}$. **a**, Analysis of 5-mC levels of Line-1 repeats in cell homogenates from PSC$^{CAG-GFP}$ cultures in the conditions indicated ($n=3$ independent experiments); graph represents mean ± s.e.m. showing significantly lower levels of relative DNA methylation in all conditions compared to LIF. **b**, Relative levels expression of *Dnmt3b* and *Dnmt3a* in PSC$^{CAG-GFP}$ cultures by qPCR analysis; data were normalized by the LIF averaged values and represented as mean ± s.e.m ($n=3$ independent experiments). **c**, Western blot of histone methyltransferases and acetylase from PSCs homogenates ($n=3$ per condition); expression levels quantitated by densitometry analyses and normalized by LIF values. **d**, Immunofluorescence of histone H4ac in the PSC-treated cultures indicated (top: representative images). Mean fluorescent intensity (MFI) per colony as assessed by imaging of 20 random colonies per condition, 5 random fields (ImageJ). Graph (bottom) depicting mean ± s.e.m of MFI confirm the consistently high levels of H4-pan-acetyl expression in a2i/VPA/LIF also seen in Western blots. Statistical analyses: one-way ANOVA (**a**,**b**) and unpaired Student's *t*-test (**d**), significance at $^{*}P<0.05$, $^{**}P<0.01$, $^{****}P<0.0001$, NS: non-significant.

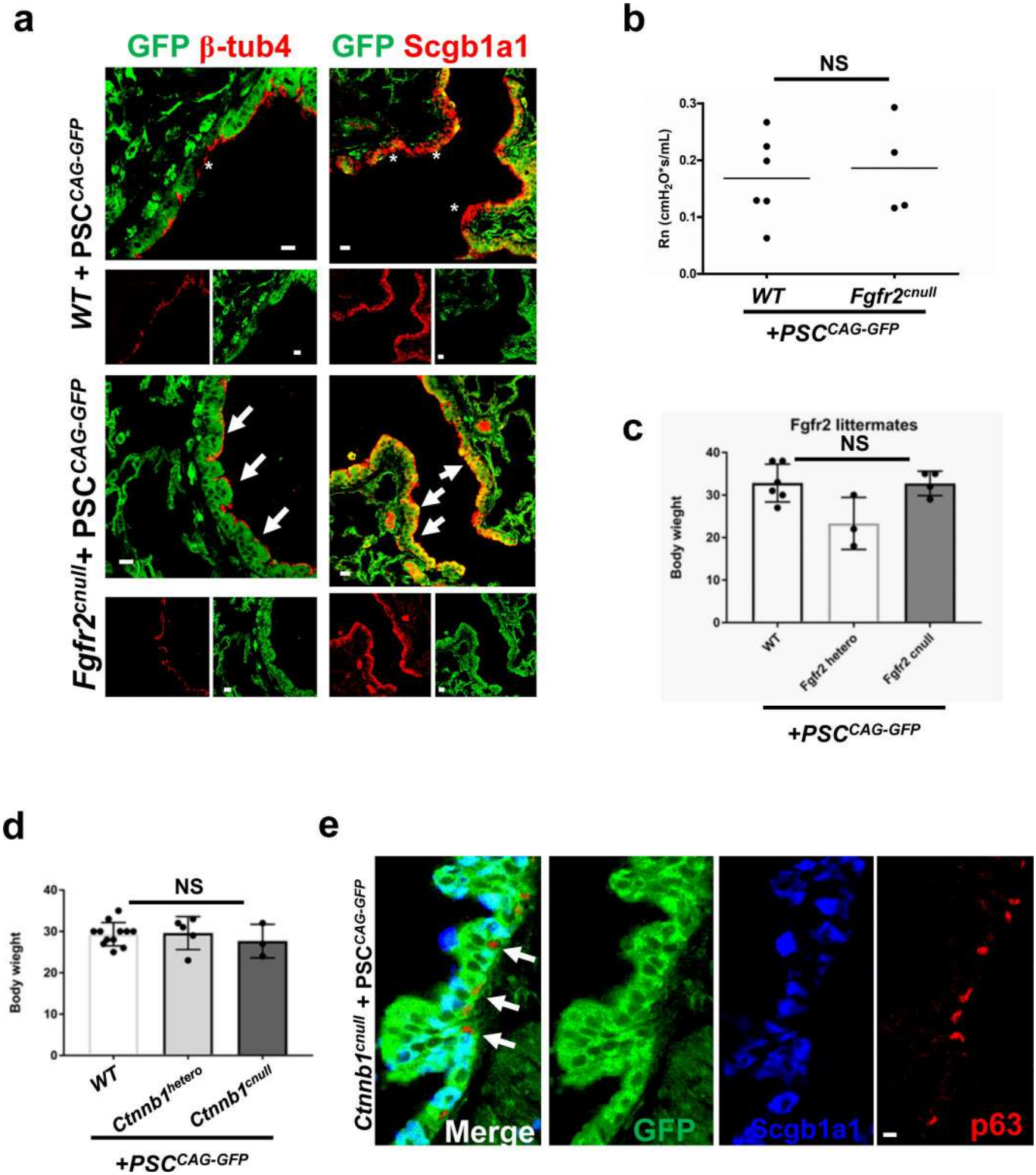

Extended Data Fig. 10 | Normal growth, differentiation and function of adult lungs from complemented a2i/VPA/LIF-treated PSC$^{CAG-GFP}$ mature animals (see also Figs. 2 and 3). a, Representative immunofluorescence confocal imaging of P80 a2i/VPA/LIF-treated PSC$^{CAG-GFP}$ *Fgfr2*^{cnull} and control WT + PSC$^{CAG-GFP}$ lungs double-labeled with GFP and airway differentiation markers multiciliated (β-tubulin4) and secretory (Scgb1a1) cells. Arrows: strong GFP overlapping signals in *Fgfr2*^{cnull} mutants, contrasting with the less prominent signals (* asterisks) in WT; lower panels: single-channel images. **b**, Flexivent analysis of pulmonary function in CBC-complemented day 80 WT ($n=6$) and *Fgfr2*^{cnull} ($n=4$); graph (mean ± s.e.m) showing non-significant (NS) difference in the resistance of conducting airways (Rn). **c**,**d**, Analysis of body weight in a2i/VPA/LIF PSC$^{CAG-GFP}$ complemented day 80 WT ($n=6$), *Fgfr2*^{hetero} ($n=3$), *Fgfr2*^{cnull} ($n=4$) animals (**c**), and day 50 WT ($n=12$), *Ctnnb1*^{hetero} ($n=5$), *Ctnnb1*^{cnull} ($n=3$) animals (**d**). Graph (mean ± s.e.m) indicating no significant difference in body weight between genotypes in both *Fgfr2* and *Ctnnb1* models. **e**, IF of day50 a2i/VPA/LIF-treated PSC$^{CAG-GFP}$ + *Ctnnb1*^{cnull} lungs ($n=3$). Representative image of GFP double labeling with markers of secretory (Scgb1a1) or basal (p63) cells in adult airways (arrows: depicts strong GFP staining contrasting). Statistical analyses: Student's *t*-test (**b**), one-way ANOVA (**c**,**d**); NS: statistically non-significant: $P > 0.05$. Scale bars: **a**,**e** = 10 μm, 5 μm, respectively.

nature research

Corresponding author(s): Munemasa Mori, Hiromitsu Nakauchi, Wellington Cardoso
NMED-L95737A

Last updated by author(s): Aug 21, 2019

Reporting Summary

Nature Research wishes to improve the reproducibility of the work that we publish. This form provides structure for consistency and transparency in reporting. For further information on Nature Research policies, see Authors & Referees and the Editorial Policy Checklist.

Statistics

For all statistical analyses, confirm that the following items are present in the figure legend, table legend, main text, or Methods section.

n/a	Confirmed	
☐	☒	The exact sample size (*n*) for each experimental group/condition, given as a discrete number and unit of measurement
☐	☒	A statement on whether measurements were taken from distinct samples or whether the same sample was measured repeatedly
☐	☒	The statistical test(s) used AND whether they are one- or two-sided *Only common tests should be described solely by name; describe more complex techniques in the Methods section.*
☐	☒	A description of all covariates tested
☐	☒	A description of any assumptions or corrections, such as tests of normality and adjustment for multiple comparisons
☐	☒	A full description of the statistical parameters including central tendency (e.g. means) or other basic estimates (e.g. regression coefficient) AND variation (e.g. standard deviation) or associated estimates of uncertainty (e.g. confidence intervals)
☐	☒	For null hypothesis testing, the test statistic (e.g. *F*, *t*, *r*) with confidence intervals, effect sizes, degrees of freedom and *P* value noted *Give P values as exact values whenever suitable.*
☒	☐	For Bayesian analysis, information on the choice of priors and Markov chain Monte Carlo settings
☒	☐	For hierarchical and complex designs, identification of the appropriate level for tests and full reporting of outcomes
☒	☐	Estimates of effect sizes (e.g. Cohen's *d*, Pearson's *r*), indicating how they were calculated

Our web collection on statistics for biologists contains articles on many of the points above.

Software and code

Policy information about availability of computer code

Data collection	Prism8 SOFTWARE for statistical analyses, Zen 2.3 SP1 (Black edition from Zeiss company) equipped with Zeiss LSM710 confocal microscopy for the acquisition of the confocal imaging, Leica imaging software (LAS X 3.4.2.18368) equipped with DMi8 station for the acquisition of the PSC culture imaging, and Image J (1.52n from NIH) software for the analyses of tissue or PSC imaging.
Data analysis	Prism8 (https://www.graphpad.com/scientific-software/prism/) Zen, LASX software will be available in Zeiss or Leica microscopy company, respectively. Image J is available from NIH (https://imagej.nih.gov/ij/).

For manuscripts utilizing custom algorithms or software that are central to the research but not yet described in published literature, software must be made available to editors/reviewers. We strongly encourage code deposition in a community repository (e.g. GitHub). See the Nature Research guidelines for submitting code & software for further information.

Data

Policy information about availability of data

All manuscripts must include a data availability statement. This statement should provide the following information, where applicable:

- Accession codes, unique identifiers, or web links for publicly available datasets
- A list of figures that have associated raw data
- A description of any restrictions on data availability

The data that support the findings of this study are available from the corresponding author (M.M., W.C.) upon request.

Field-specific reporting

Please select the one below that is the best fit for your research. If you are not sure, read the appropriate sections before making your selection.

☒ Life sciences ☐ Behavioural & social sciences ☐ Ecological, evolutionary & environmental sciences

For a reference copy of the document with all sections, see nature.com/documents/nr-reporting-summary-flat.pdf

Life sciences study design

All studies must disclose on these points even when the disclosure is negative.

Sample size	Sample size for each of the experiments involving molecular or phenotypic characterization of the chimeric/BC animals or manipulation of PSCs culture conditions were estimated based on our previous reports (analysis of mouse genetic models) and studies from others (Stadfeld et al. Nature 2010 ; Kobayashi et al. Cell 2010). In all experiments a minimum of 3 replicates was tested per condition . The number of replicates (n) was provided for all parameters measured and sample sizes are listed in the figure legends. In the relatively few cases we found high variability in the results, sample size was increased to infer about statistical significance
Data exclusions	none.
Replication	All data analyzed resulted from observations performed in 3 or more independent experiments per culture conditions and tested in at least 3 animals per group in the experiments involving generation of chimeric mice and BC . All attempts at replication of these experiments were successful.
Randomization	Methods of randomization were not required in this study. Samples and corresponding controls were always processed at the same time.
Blinding	The investigators were not blinded to group allocation during experiments and outcome assessment of the cultures and animal experiments. Blinding was not used because the genotyping was determined in advance and the presence of GFP was obvious in the analyses of the specimens.

Reporting for specific materials, systems and methods

We require information from authors about some types of materials, experimental systems and methods used in many studies. Here, indicate whether each material, system or method listed is relevant to your study. If you are not sure if a list item applies to your research, read the appropriate section before selecting a response.

Materials & experimental systems

n/a	Involved in the study
☐	☒ Antibodies
☐	☒ Eukaryotic cell lines
☒	☐ Palaeontology
☐	☒ Animals and other organisms
☒	☐ Human research participants
☒	☐ Clinical data

Methods

n/a	Involved in the study
☒	☐ ChIP-seq
☐	☒ Flow cytometry
☒	☐ MRI-based neuroimaging

Antibodies

Antibodies used	The following antibodies were used for Immunofluorescence analyses (Page#20-21): anti-acetylated β-tubulin IV (Abcam, ab11315, 1:500), anti-GFP chicken pAb (Thermo Scientific, 1:500), anti-Scgb1a1 goat (Santa Cruz, #sc-9772, 1:500), anti-Pdpn (R&D, #AF3244, 1:200), anti-Hop (Santa Cruz #sc- 398703, 1:100), anti-Sftpc (Seven Hills #WRAB-9337, 1:1000), anti-Cgrp (Sigma, #C8198, 1:1000), anti-Sox2 rat (eBiosience, #14-9811-82), anti-SMA rabbit (Cell signaling, #19245), anti-Oct4 (Gentetex, #GT486, 1:100), anti-SSEA1 (SantaCruz, sc-101462, 1:50), anti-Oct4 (R & D, #AF1759), and Histone H4ac (pan-acetyl) (Active Motif, #39925). Isolectin B4 (Life tech., I32450) was used at a dilution of 1:500 in PBS overnight at 4 degrees prior to the staining above to visualize vascular endothelial cells. The following antibodies were used for flowcytometry analyses (Page#21, #22): For the PSC marker analyses (Page#21), we used SSEA1-BV421 (BioLegend, 125613: 1:200 dilution), PECAM-APC (BioLegend, 102509: 1:200 dilution), Zombie Aqua™ Fixable Viability Kit (BioLegend, 423101). For the chimerism analyses to postnatal chimeric animals (Page#22), we used Fc Block (BD Pharmingen; Cat# 553141), CD31-BV421 (BD Pharmingen, # 562939, 1/250 dilution), EPCAM-BV711 (BioLegend, 118233, 1/200), Aqua Zombie (BioLegend, 423101, 1/500), and CD45-BV605 (BioLegend, 103155, 1/200).
Validation	All antibodies used in the current study have been previously validated by the manufacturers (see below) and the previous studies in our lab (Mori et al., Development 2015; Mori et al., Nature Communications 2017; Yang et al. Dev Cell 2018;) and used according to the manufacturers' instructions. Antibodies were also validated by titration studies and comparison with positive controls and negative controls. anti-acetylated β-tubulin IV (Abcam, ab11315, 1:500)

https://www.abcam.com/beta-iv-tubulin-antibody-ons1a6-ab11315.html
anti-GFP chicken pAb (Thermo Scientific, 1:500)
https://www.thermofisher.com/antibody/product/GFP-Antibody-Polyclonal/A10262
anti-Scgb1a1 goat
https://www.scbt.com/browse/cc10-Antibodies/_/N-1lzf3a9
anti-Pdpn (R&D, #AF3244, 1:200)
https://www.rndsystems.com/products/mouse-podoplanin-antibody_af3244
anti-Hop (Santa Cruz #sc- 398703, 1:100)
https://www.scbt.com/p/hop-antibody-e-1
anti-Sftpc (Seven Hills #WRAB-9337, 1:1000)
https://www.sevenhillsbioreagents.com/products/anti-pro-sp-c-rabbit-n-terminal
anti-Cgrp (Sigma, #C8198, 1:1000)
https://www.sigmaaldrich.com/catalog/product/sigma/c8198?lang=en&region=US
anti-Sox2 rat (eBiosience, #14-9811-82)
https://www.fishersci.se/shop/products/sox2-rat-anti-human-mouse-clone-btjce-ebioscience/15218187
anti-SMA rabbit (Cell signaling, #19245)
https://www.cellsignal.com/products/primary-antibodies/a-smooth-muscle-actin-d4k9n-xp-rabbit-mab/19245
anti-Oct4 (Gentetex, #GT486, 1:100)
https://www.genetex.com/Product/Detail/Oct4-antibody-GT486/GTX627419?
utm_source=Biocompare&utm_medium=referral&utm_campaign=Biocompare_GeneTex
anti-SSEA1 (SantaCruz, sc-101462, 1:50)
https://www.scbt.com/p/ssea-1-antibody-mc-480
Histone H4ac (pan-acetyl) (Active Motif, #39925)
https://www.activemotif.com/catalog/details/39925/histone-h4-pan-acetyl-antibody-pab-1
Isolectin B4 (Life tech., I32450)
https://www.thermofisher.com/order/catalog/product/I32450
SSEA1-BV421 (BioLegend, 125613: 1:200 dilution)
https://www.biolegend.com/en-gb/products/brilliant-violet-421-anti-mouse-human-cd15-ssea-1-antibody-8995
PECAM-APC (BioLegend, 102509: 1:200 dilution)
https://www.biolegend.com/en-gb/products/apc-anti-mouse-cd31-antibody-375
Zombie Aqua™ Fixable Viability Kit (BioLegend, 423101)
https://www.biolegend.com/en-gb/products/zombie-aqua-fixable-viability-kit-8444
Fc Block (BD Pharmingen; Cat# 553141)
https://www.bdbiosciences.com/us/applications/research/b-cell-research/surface-markers/mouse/purified-rat-anti-mouse-cd16cd32-mouse-bd-fc-block-24g2/p/553141
CD31-BV421 (BD Pharmingen, # 562939, 1/250 dilution)
https://www.bdbiosciences.com/us/applications/research/stem-cell-research/cancer-research/mouse/bv421-rat-anti-mouse-cd31-mec-133/p/562939
EPCAM-BV711 (BioLegend, 118233, 1/200)
https://www.biolegend.com/en-us/search-results/brilliant-violet-711-anti-mouse-cd326-ep-cam-antibody-13763
CD45-BV605 (BioLegend, 103155, 1/200)
https://www.biolegend.com/en-us/products/brilliant-violet-605-anti-mouse-cd45-antibody-8721

Eukaryotic cell lines

Policy information about cell lines

Cell line source(s)	All of the cell lines used in this manuscript are described in Page#20-21 in Materials and Methods (See also below).
Authentication	The PSC CAG-GFP cell line was authenticated by MTI-GlobalStem at purchase. PSC CAG-GFP and MEFs are commercially available from Life tech (CF1 mouse embryonic fibroblasts, #A34181) or MTI-GlobalStem (C57BL/6N x 129S6 background: Cat# GSC-5003), respectively and maintained according to the manufacture's protocol. ES1 CAG-tdTomato(C57BL/6N background), B7 (C57BL/6N background), SUN107.4 (CD1 background) were derived and authenticated by Dr. Hiromitsu Nakauchi's lab at Stanford University; CSL2J2 (C57BL/6J C2J background), FL19 ARR3-1 (albino agouti C57BL/6N background), FL19 ARR3-2 (C57BL/6N background)derived and authenticated by Dr. Lin Chyuan-Sheng at the Columbia University Transgenic Core Facility. These PSC lines are available upon request. The authenticated PSCNkx2-1-GFP passage 15 (W4/129S6) were kindly gifted by Dr. Laertis Oikonomou and Dr. Darrell Kotton, CReM, Boston University.
Mycoplasma contamination	All of the cells were tested negative for Mycoplasma contamination.
Commonly misidentified lines (See ICLAC register)	No misidentified cell line was used.

Animals and other organisms

Policy information about studies involving animals; ARRIVE guidelines recommended for reporting animal research

Laboratory animals	All lines used for generation of chimeric and CBC mice in this manuscript are described in Page#20 in the Materials and Methods section and Table1.
Wild animals	This study did not involve wild-animals.
Field-collected samples	This study did not involve field-collected samples at all.

Ethics oversight	All experiments involving animals were performed according to the protocol approved by the Columbia University Institutional Animal Care and Use Committee and USAMRMC Animal Care and Use Review Office (ACURO).

Note that full information on the approval of the study protocol must also be provided in the manuscript.

Flow Cytometry

Plots

Confirm that:

☒ The axis labels state the marker and fluorochrome used (e.g. CD4-FITC).

☒ The axis scales are clearly visible. Include numbers along axes only for bottom left plot of group (a 'group' is an analysis of identical markers).

☒ All plots are contour plots with outliers or pseudocolor plots.

☒ A numerical value for number of cells or percentage (with statistics) is provided.

Methodology

Sample preparation	The methodology for sample preparation is detailed in Page#22 in Materials and methods.
Instrument	FACS Aria flow cytometer (Becton Dickinson).
Software	Data were analyzed on FlowJo software.
Cell population abundance	More than 10,000 cells/liver or PSC -CAG-GFP were sorted using FACS Aria flow cytometer. GFP negative gate was used for genotyping. SSEA1 high or dim PSC -CAG-GFP populations were compared for checking efficacy of chimera formation (Fig. 2c). The sorting purity was checked by re-sorting the cells and purity was found to be more than 90% (Page #23).
Gating strategy	The gating strategy is detailed in Supp. Fig. 9 and its legend.

☒ Tick this box to confirm that a figure exemplifying the gating strategy is provided in the Supplementary Information.

nature COMMUNICATIONS

ARTICLE

Received 13 Feb 2017 | Accepted 8 May 2017 | Published 4 Jul 2017

DOI: 10.1038/ncomms15857 OPEN

Cytoplasmic E2f4 forms organizing centres for initiation of centriole amplification during multiciliogenesis

Munemasa Mori[1], Renin Hazan[2], Paul S. Danielian[2], John E. Mahoney[1,†], Huijun Li[1], Jining Lu[1], Emily S. Miller[2], Xueliang Zhu[3], Jacqueline A. Lees[2] & Wellington V. Cardoso[1]

Abnormal development of multiciliated cells is a hallmark of a variety of human conditions associated with chronic airway diseases, hydrocephalus and infertility. Multiciliogenesis requires both activation of a specialized transcriptional program and assembly of cytoplasmic structures for large-scale centriole amplification that generates basal bodies. It remains unclear, however, what mechanism initiates formation of these multiprotein complexes in epithelial progenitors. Here we show that this is triggered by nucleocytoplasmic translocation of the transcription factor E2f4. After inducing a transcriptional program of centriole biogenesis, E2f4 forms apical cytoplasmic organizing centres for assembly and nucleation of deuterosomes. Using genetically altered mice and E2F4 mutant proteins we demonstrate that centriole amplification is crucially dependent on these organizing centres and that, without cytoplasmic E2f4, deuterosomes are not assembled, halting multiciliogenesis. Thus, E2f4 integrates nuclear and previously unsuspected cytoplasmic events of centriole amplification, providing new perspectives for the understanding of normal ciliogenesis, ciliopathies and cancer.

[1] Columbia Center for Human Development, Department of Medicine, Pulmonary Allergy Critical Care, Columbia University Medical Center, New York City, New York 10032, USA. [2] David H. Koch Institute for Integrative Cancer Research, MIT, Cambridge, Massachusetts 02139, USA. [3] State Key Laboratory of Cell Biology, Institute of Biochemistry and Cell Biology, Shanghai Institutes for Biological Sciences, Chinese Academy of Sciences, 320 Yueyang Road, Shanghai 200031, China. † Present address: Cystic Fibrosis Foundation, Lexington, Massachusetts 02421, USA. Correspondence and requests for materials should be addressed to W.V.C. (email: wvc2104@cumc.columbia.edu).

Cilia are microtubule-enriched structures that protrude from the surface of eukaryotic cells, appearing in different forms and with distinct biological roles[1–3]. Primary cilia act as sensory antenna and signalling hubs that transmit signals into the cell. In contrast, multicilia are motile structures that decorate the apical surface of epithelial cells in the respiratory and the reproductive tracts, ependyma and choroid plexus. Multiciliated cells play key roles in fluid movement and absorption[4], as well as in organ defence by acting on mucociliary clearance[5]. Dysfunction of primary cilia or multicilia results in human ciliopathies, conditions associated with high morbidity and mortality[6]. Primary cilium appears in G0/G1 phase cells when the centrosome migrates to the cell surface, whereupon the mother centriole forms a basal body that gives rise to the cilium[7,8]. The process begins with formation of a complex between the centrosomal proteins Cep152 and Cep63 on the proximal side of the mother centriole followed by recruitment of Plk4 (polo-kinase 4), Sas6 (centriolar assembly protein), Centrin and other centriolar proteins, which create a cartwheel-like structure that nucleates the microtubule protuberances to form the cilium[9–13]. Primary cilia formation is entirely mother centriole-dependent, which replicates only a single daughter centriole during cell cycle. While the mother centriole pathway also contributes to multiciliogenesis, it is wholly insufficient for this role due to its inability to generate the large number of centrioles required for multicilia formation[6,14]. Classical electron microscopy studies of multiciliogenesis identified 40–80 micron electron–dense granular organelles, called fibrous granules (FGs), and numerous ring-like structures, the deuterosomes, present within and adjacent to FGs[15–18]. Subsequent studies showed that FG are enriched for Pcm1 (ref. 19), which was originally thought to be dispensable for multiciliogenesis based on RNAi knockdown[20]. Deuterosomes share many molecular similarities, but also key differences, with the mother centriole[2]. Many constituent proteins are conserved between the two structures, including Plk4, Cep152, Sas6 and Centrin[10,12,21,22]. In contrast, Cep63—of the mother centriole complex—is replaced by a related protein Deup1 (or Ccdc67) for deuterosome formation[21]. Deuterosome is crucial for procentriole multiplication. A single deuterosome can hold multiple procentrioles, and efficiently produce the few hundreds centrioles required for multiciliogenesis. The existence of this deuterosome-dependent (DD) process allows centriole amplification and the development of multiciliated cell uncoupled from cell cycle control.

There is evidence that multiciliogenesis is triggered by induction of an E2f4-dependent transcriptional program of centriole biogenesis in multiciliated cell precursors[23,24]. E2f4 along with other E2f family members are transcription factors best known for regulating cell proliferation[25–28]. Notably, E2f4 has been recently shown to mediate the transcriptional responses of Multicilin (*Mcidas*), a human ciliopathy-associated gene encoding a well-conserved regulator of multiciliogenesis in *Xenopus*[24] and mice[23,29]. Although these studies show activation of a panel of multiciliogenesis genes, including Deup1, it is still unknown what mechanism leads to initiation of deuterosome assembly in multiciliated precursor cells following the activation of the centriole biogenesis transcriptional program. Some studies propose that FGs seed this process[15,16,18], but others argue that deuterosomes assembly is spontaneous[2,21] or caused by other, yet to be determined, proteins[22].

Here, we show that this mechanism is crucially dependent on the nucleocytoplasmic translocation of E2f4. We provide evidence that cytoplasmic E2f4 forms organizing centres for assembly and nucleation of deuterosomes to initiate large-scale centriole amplification in epithelial progenitors.

Results

E2f4 undergoes nucleocytoplasmic shift during multiciliogenesis. To gain initial insights into the ontogeny of E2f4 in differentiating epithelial cells, we mapped its expression pattern during step-wise initiation of multiciliogenesis in airway epithelial progenitors using a well-established model of air–liquid interface (ALI) culture[30–33]. In this assay, adult airway epithelial progenitors isolated from adult trachea are expanded to confluence and exposed to an ALI, which triggers differentiation, identified through a series of well-defined stages. Indirect immunofluorescence (IF) for E2f4 and confocal imaging of confluent multipotent progenitors prior to ALI induction (Stage 1, ALI day 0) showed nuclear-specific localization of E2f4 (Fig. 1a, Supplementary Fig. 1a). However, once the cells were exposed to an ALI, E2f4 underwent a striking nuclear-to-cytoplasmic translocation to later become essentially cytoplasmic in multiciliated cells (Fig. 1a). Small apical cytoplasmic E2f4 granules ($<1\,\mu m$) were initially seen in monociliated cells (Stage 2; ALI day 0–2). Larger apical E2f4 aggregates ($>1\,\mu m$ diameter) then became evident in $\sim$80% of the cells as multicilia started to form (Stage 3; ALI day 2–4) (Fig. 1a, Supplementary Fig. 1a,b). At a later stage, smaller E2f4 granules ($<1\,\mu m$) were again observed in mature multiciliated cells bearing longer cilia (Stage 4; after ALI day 4). Importantly, we found that E2f4 cytoplasmic localization occurred essentially in cells undergoing multiciliogenesis, but not in secretory progenitors, which predominantly retained nuclear E2f4 (Supplementary Fig. 1c). The subcellular localization of E2f4 was further demonstrated by cell fractionation and western blotting (Fig. 1b, Supplementary Fig. 10). We extended our analyses to examine the E2f4 subcellular localization during airway differentiation *in vivo*. Immunostaining of developing (E12.5–E18.5) and adult murine lungs showed apical accumulation of E2f4 clearly apparent at E16.5, coincident with the emergence of multicilia (Supplementary Fig. 1d). Furthermore, IF analysis of adult human lung sections detected strong cytoplasmic E2F4 in multiciliated cells marked by acetylated α-tubulin in stark comparison to the lower level nuclear E2F4 staining in the airway progenitor basal cells (Supplementary Fig. 1e). Thus, our data suggest that the E2f4 nucleocytoplasmic shift during multiciliogenesis is evolutionary conserved between mouse and human airways.

E2f4 localizes to areas of procentrioles initiation. To gain insights into the cellular events mediated by cytoplasmic E2f4, we coupled IF with confocal and super-resolution three-dimensional-structured illumination microscopy (3D-SIM) and examined how the distribution of E2f4 protein correlated with the appearance of early markers of ciliogenesis. Already early in stage 2 cells, E2f4 cytoplasmic signals were clearly detected at two distinct apical sites: beneath primary cilia, partially overlapping with the ciliary markers acetylated α-tubulin, γ-tubulin and glutamylated tubulin (Gt335), and in its immediate neighbourhood as multiple small foci or granules (Fig. 1c,d). At the primary cilium 3D-SIM revealed E2f4 forming ring-like structures with Cep63 in a region enriched in Cep152, Plk4 and C-Nap1 (centrosomal protein Cep250), which marks sites of procentriole nucleation in parental centrioles[34]. The multiple other apical E2f4 foci outside the centrosomal region, also showed ring-like structures enriched in Cep152, centrin and the deuterosome protein Deup1, but not Cep63 (Fig. 1d, Supplementary Fig. 2a,b). Thus, at the onset of multiciliogenesis both sites of E2f4 expression correlated with markers of procentrioles initiation. We reasoned that cytoplasmic E2f4 foci could be active sites of centriole biogenesis in these epithelial progenitors. This was

reinforced by our analysis of stage 2–3 cells showing that cells expressing Plk4, a crucial kinase recruited by Cep152 to initiate centriogenesis[12,21], were mostly double-labelled with E2f4 (80%) or with those cells expressing both E2f4 and Cep152 (~65–70%) (Supplementary Fig. 2a).

E2f4-Pcm1 form organizing centres for centriole biogenesis. Interestingly, the timing of appearance and spatial distribution of cytoplasmic E2f4 was reminiscent of that described for FG that form during initiation of large-scale centriole amplification[15,19,35]. Indeed, as multipotent progenitors

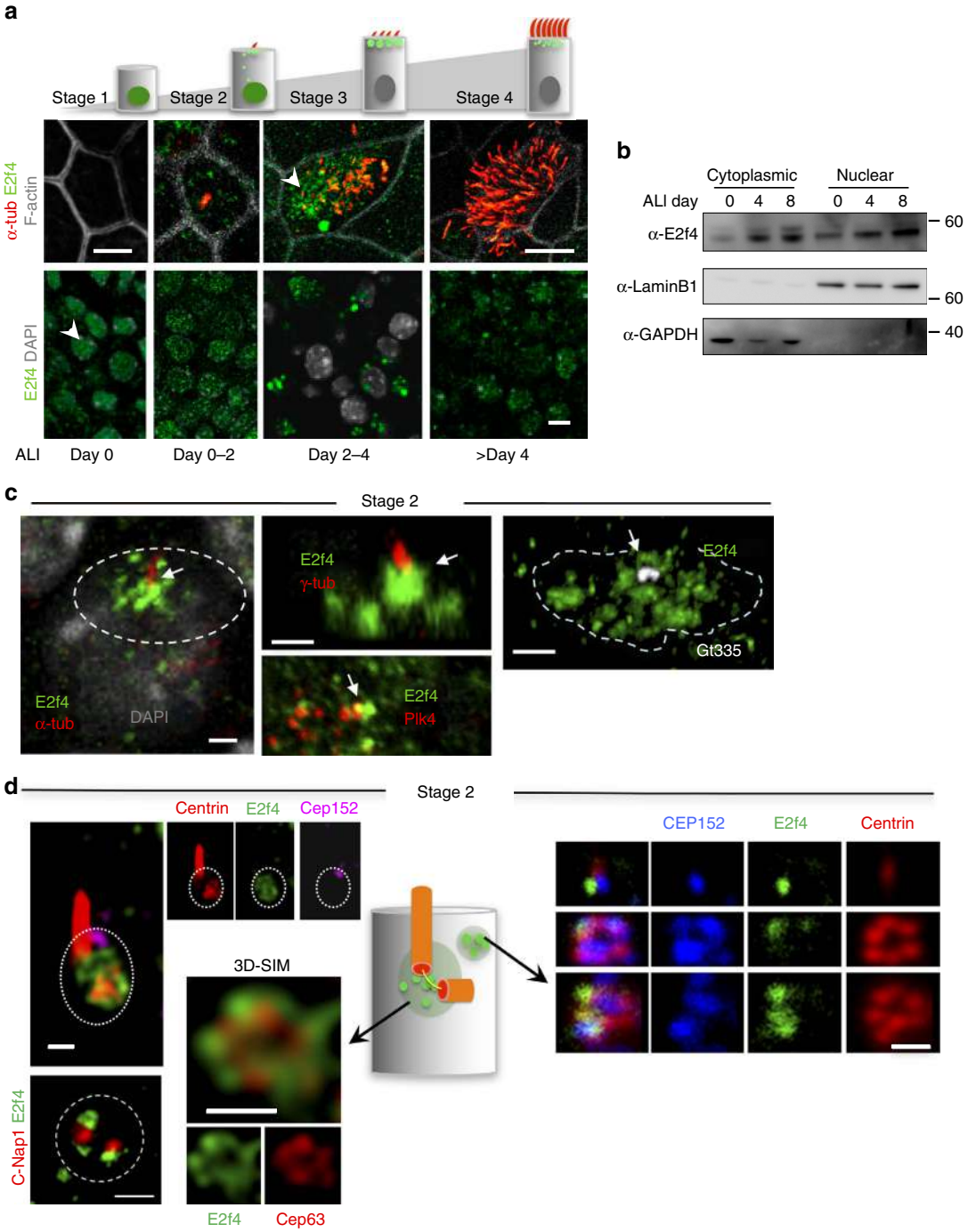

Figure 1 | E2f4 undergoes nucleocytoplasmic translocation to form apical aggregates with centriole biogenesis components during multiciliogenesis. (**a**) Immunofluorescence (IF)-confocal imaging depicting apical and basal aspects of adult airway progenitors at distinct stages of multiciliogenesis in air-liquid interface (ALI) cultures (acetylated α-tub, E2f4; top panels, cells outlined by F-actin; bottom panels: DAPI: nuclear staining). Arrowheads depict E2f4 subcellular localization along with the markers indicated. (**b**) Western blotting of E2f4 nuclear and cytoplasmic fractions of ALI culture extracts at days 0, 4, 8: E2f4 accumulation in cytoplasm during differentiation (controls for cellular fractionation: nuclear LaminB1, cytoplasmic GAPDH). (**c**) Confocal analyses, maximum projection view, stage 2 cells: E2f4 apical aggregates (circled areas, arrows) underneath primary cilium marked by acetylated α-tub, γ-tub, Gt335 or in adjacent regions; partial overlap of E2f4 with Plk4 (arrow). (**d**) IF imaging and diagram depicting cytoplasmic E2f4 at the centrosomal region (circled area in left panel, associated with c-Nap1, centrin, Cep152) forming ring-like structure with Cep63 (3D-SIM) and at non-centrosomal regions (right panel) forming similar structures with Cep152 and centrin in stage 2 cells. Bars: **a**,**c**,**d** = 10, 2.5, 0.5 μm, respectively.

transitioned to stage 2 and E2f4 protein started undergoing nucleocytoplasmic shift, Pcm1 could be detected as discrete punctate cytoplasmic signals closely associated with E2f4. Both signals subsequently overlapped to form small apical aggregates around and underneath monocilia (marked by acetylated α–tubulin and Gt335; Fig. 2a,b). By stage 2–3 confocal analysis demonstrated E2f4-Pcm1 overlap in aggregates of variable sizes. Colocalization was demonstrated by quantification of signal intensities in double-labelled sections, which showed the highest E2f4 signal between Pcm1 peaks (Supplementary Fig. 2c). 3D-SIM further confirmed that E2f4 signals are surrounded by Pcm1, clearly establishing the E2f4's location at the core of Pcm1-containing FG (Fig. 2b; Supplementary Fig. 2c; Supplementary Movie 1). The enrichment in centriole biogenesis components in E2f4-Pcm1 granules suggested a role as organizing centres for nucleation of centrioles.

Deuterosomes assemble in cytoplasmic E2f4-Pcm1 granules. To further understand the involvement of cytoplasmic E2f4 in centriole amplification, we examined assembly of deuterosomes in our system. Deup1 specifically label deuterosomes, the structures that support large-scale (*de novo*) centriole amplification for multiciliogenesis[2,21]. Deup1 is a crucial regulator of deuterosome assembly and known to interact with Cep152 and recruit Plk4 to activate centriole biogenesis[21,22]. Confocal and 3D-SIM imaging of epithelial progenitors transitioning to Stage 2 cells showed Deup1 signals associated with emerging cytoplasmic E2f4 and assembling into characteristic ring-like structures with Cep152. Notably, small cytoplasmic E2f4 granules ($<1\,\mu m$) were clearly localized around the Deup1 rings (Fig. 2c). Deup1-E2f4-Cep152 co-immunostaining and profile analysis of confocal sections demonstrated extensive signal overlap as more apical granules accumulated later in Stage 2 cells. This was prominent in the larger apical granules of stage 2–3 cells, suggesting these to be sites of active deuterosome assembly (Supplementary Fig. 2d). We then further examined the association between E2f4 and Deup1 in our cells by performing immunoprecipitation and western blot assays in extracts from adult ALI airway epithelial cultures, and in 293FT cell lines transfected with E2f4 and Deup1. These analyses revealed a clear interaction between E2f4 and Deup1 for both the endogenous and ectopically expressed proteins (Fig. 2e, Supplementary Fig. 10). We also gathered biochemical evidence of E2f4 interaction with Sas6, another centriole biogenesis core component expressed in these cells (Supplementary Figs 2e,f and 10). Next, we probed the intimate association of E2f4 and Deup1 during multiciliogenesis by performing Proximity Ligation Assay (PLA) in ALI cultures from $E2f4^{f/f}$; $R26^{CreERT2/+}$ adult airway progenitors (Tm-treated cultures as negative controls). This revealed strong E2f4-Deup1 PLA signals specifically in E2f4-sufficient, but not E2f4-deficient cells (Fig. 2d, Supplementary Fig. 4a). Importantly, we found that E2f4-Deup1 PLA signals overlapped with a subset of Pcm1 foci demonstrating that all three proteins co-exist in close proximity. Collectively, our data show that cytoplasmic E2f4 is present in complexes with two known deuterosome components, Deup1 and Sas6. These complexes appear to occur in the same location as the Pcm1-containing FG.

To more precisely define the spatial–temporal relationship between FGs and deuterosomes during centriole amplification, we performed triple IF staining for Pcm1, Deup1 and the centriolar marker Centrin. Quantitative analysis showed an increasing number of deuterosomes per cell and increasing Centrin-decorated deuterosomes as cells differentiate during stages 1–3 (Supplementary Fig. 3). Interestingly, while in immature cells at stage 2 the vast majority of Deup1 signals were found in Pcm1-enriched areas, the Deup1-Pcm1 co-localization decreased later as cells matured and underwent centriole amplification (Supplementary Fig. 3, Supplementary Movie 3–5). Indeed, at later stages centrin-decorated deuterosomes were increasingly more frequent outside Pcm1 areas (Supplementary Fig. 3a,b,g). Moreover, 3D-SIM imaging of Deup1-E2f4 double-labelled cells and assessment of deuterosome size showed that mature deuterosomes, harbouring compact rings with larger diameters[21], were most frequently found at the periphery or outside the E2f4-rich regions (Fig. 2f, *i,ii,iii* in right panel and in Supplementary Fig. 4b,c; Supplementary Movie 2). The abundant centrin labelling outside the E2f4-Pcm1 regions and dissociated from deuterosomes in stage 4 cells suggested a lesser role for E2f4 after centriole amplification. Our observations are consistent with the idea that deuterosomes arise and start nucleating in Pcm1-E2f4 enriched areas, as formerly proposed for FG[16,19,35].

Conserved E2f4's role in centriole biogenesis gene transcription. We examined whether key Multicilin-E2f4 targets identified during *Xenopus* multiciliogenesis[24] were similarly regulated by endogenous E2f4 in our system. Mice with systemic E2f4 deficiency were previously shown to be unable to form multicilia in the respiratory epithelium[23]. However further insights into the cellular events and targets regulated by E2f4 were limited by neonatal lethality due to multiple defects[23]. To overcome this limitation, we generated $E2f4^{f/f}$; $R26^{CreERT2/+}$ mice to delete *E2f4* selectively in epithelial progenitors either *in vivo* using a $Shh^{Cre/+}$ line that induces recombination early in the lung epithelium ($E2f4^{f/f}$;$Shh^{Cre/+}$, herein $E2f4^{cnull}$) or in vitro in adult ALI cultures upon 4-hydroxytamoxifen treatment (Tm)[36]. Results from both approaches showed that E2f4 deletion does not prevent primary cilia formation but abolishes multiciliated cells (Supplementary Fig. 5a and 6a–d). We then performed whole-genome expression profiling of adult control and Tm-treated $E2f4^{f/f}$; $R26^{CreERT2/+}$ airway epithelial progenitors prior to and during initiation of multiciliogenesis (ALI days 0, 2 and 4). Remarkably, this confirmed the enrichment in centriole biogenesis genes and extensive overlap with the E2f4 targets formerly reported in *Xenopus*[24]. Clustering analysis and qPCR analyses revealed *Deup1*, *Ccno*, *Myb* and others in this group (*Deup1* cluster) significantly reduced at ALI day 0, while *Plk4*, *Sas6*, *Stil* mRNAs (*Plk4* cluster) decreased at ALI day2 (Supplementary Fig. 5). A comprehensive characterization of the E2f4 transcriptional targets from these studies will be reported elsewhere. Analysis of E18.5 lungs and adult ALI cultures demonstrated the loss of Foxj1, β-tubulin expression and disruption of multiciliogenesis in E2f4-deficient epithelium. Importantly, IF showed none of the large apical aggregates of Deup1, Cep152, Pcm1 present in E2f4-sufficient cells (Supplementary Fig. 6).

Multiciliogenesis depends on E2f4 nucleocytoplasmic localization. The observations above supported a broader role for E2f4 in multiciliogenesis, beyond that originally associated with its transcriptional activity[24] and not yet tested in functional studies. These results, however, could not provide us with direct insights into a role for cytoplasmic E2f4 as they could be ascribed to disruption of the transcriptional program of centriole biogenesis. To resolve this issue, we generated E2F4 mutants that discriminate nuclear from cytoplasmic functions, and compared their ability to rescue multiciliogenesis in E2f4-deficient airway progenitors. Lentivirus constructs were generated carrying point mutations that specifically disrupt the E2f4's DNA binding domain resulting in a transcriptionally inactive form ($E2F4^{\Delta DBD}$), or that disrupt its nuclear export signal, preventing cytoplasmic localization ($E2F4^{\Delta NES}$)[37]. Flag-HA-tagged versions of $E2F4^{\Delta DBD}$,

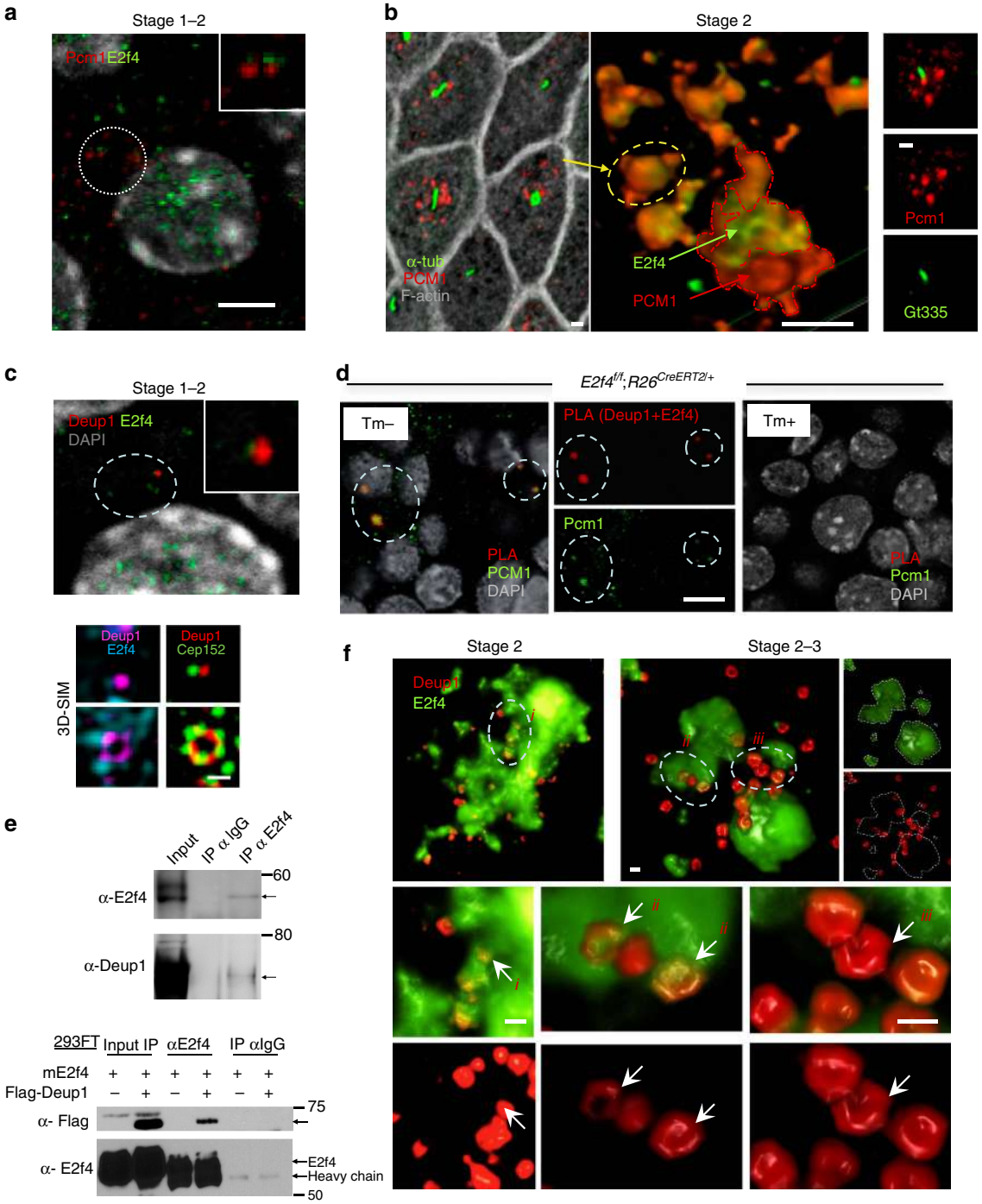

Figure 2 | Deuterosomes assemble in cytoplasmic E2f4-Pcm1 granules. (**a**) E2f4-Pcm1 IF confocal image, stage1-2 transition during E2f4 nucleocytoplasmic shift: Pcm1-E2f4 signals adjacent but still not overlapping (inset, enlarged from circled area). (**b**) Left panel: confocal image stage 2 cells showing apical Pcm1-labelled granules nearby primary cilia (acetylated α-tub); middle panel: 3D-SIM: Pcm1-E2f4 colocalization (circled area representative of apical granule on left): E2f4 at the core of Pcm1 granules); right panel: confocal image depicts Pcm1 underneath and nearby Gt335-labelled primary cilium. See also Supplementary Movie 1. (**c**) IF confocal (upper panel) and 3D-SIM (lower panel) of stage 1–2 cells: E2f4 nucleocytoplasmic translocation and initial association with Deup1 (inset, enlarged from circled area). Assembly of Deup1, Cep152 and cytoplasmic E2f4 into deuterosomes. (**d**) Proximity ligation assay (PLA): Deup1 + E2f4 proximity signal overlapping with Pcm1 (left and split panels: circled areas in ALI day3 from *E2f4*$^{f/f}$; *R26*$^{CreERT2/+}$ no Tm administration); specificity of signals confirmed in E2f4-deficient cells (right panel; Tm-treated *E2f4*$^{f/f}$; *R26*$^{CreERT2/+}$ cultures; see also Supplementary Fig. 4a). (**e**) Co-immunoprecipitation (coIP) assays: binding of endogenous (top) or exogenous (bottom) E2f4 to Deup1 in ALI day 3 (stage 2) or Deup1-Flag in 293FT homogenates, respectively (see methods). (**f**) Deup1-E2f4 IF, 3D-SIM reconstruction of stage 2 cells (top left) and cells transitioning to stage 3 (top right). Small Deup1 dots assemble into rings inside E2f4 granules but, later, more mature deuterosomes with larger rings locate at the periphery or outside the E2f4 granules. Arrows *i,ii,iii*: representative Deup1 rings from circled areas enlarged in lower panels shown by split channel (E2f4) or double Deup1-E2f4 labelling (less to more mature deuterosomes from left to right). Bars: **a**–**d**,**f** = 5, 1, 0.5, 5, 0.5 μm, respectively.

$E2F4^{\Delta NES}$ or controls mCherry and wild type ($E2F4^{WT}$) were transduced in Tm-treated $E2f4^{f/f}$; $R26^{CreERT2/+}$ adult airway progenitors and multiciliogenesis was assessed in ALI cultures. qPCR analyses confirmed that both $E2F4^{\Delta NES}$ and $E2F4^{WT}$ were indeed transcriptionally active, unlike *mCherry* and $E2F4^{\Delta DBD}$ mutants, which were unable to induce expression of the E2f4 target genes *Deup1* and *Foxj1* (Fig. 3, left panels). HA immunofluorescence analyses confirmed the nucleocytoplasmic localization of all mutants (Fig. 3). Expected cytoplasmic HA signal was particularly evident in the cells transduced with the $E2F4^{WT}$construct, which showed large and small apical granules double-labelled with HA and E2f4 antibodies (Fig. 4b). Importantly, $E2F4^{\Delta NES}$-transduced cells displayed HA signals highly restricted to the nucleus, supporting reliability of our targeting approach (Figs 3c and 4d).

Analysis of $E2F4^{WT}$ ALI day 6 cultures showed robust rescue of multiciliogenesis with HA-labelled cells expressing Foxj1, centrin and acetylated α–tubulin-labelled structures compatible with multicilia (Fig. 3a; Supplementary Fig. 7). This contrasted with the inability to form multicilia in the cultures transduced with mCherry (control) and the transcriptionally inactive $E2F4^{\Delta DBD}$. Notably, although $E2F4^{\Delta NES}$ was present in the nucleus and able to induce *Foxj1 mRNA*, no Foxj1 immunostaining was detected by day 6 in cultures, in agreement with the $E2F4^{\Delta NES}$ failure to initiate multiciliogenesis in E2f4-deficient cells (Fig. 3b,c, Supplementary Fig. 7).

Cytoplasmic E2f4 is required for deuterosome assembly. Consistent with the presence of cytoplasmic HA-E2F4 and the rescue of multiciliogenesis, we found accumulation of apical Deup1 granules in $E2F4^{WT}$–transduced cells (Fig. 4a). Thus, $E2F4^{WT}$ expression in the nucleus induced *Deup1* and its ability to localize to the cytoplasm allowed assembly of deuterosomes. In addition, $E2F4^{WT}$ supported induction and accumulation of Pcm1 in the cytoplasm of these cells. The HA-regions were often associated with Pcm1 staining in a pattern reminiscent of the FG that we identified *in vivo* (Fig. 4a,b). This pattern, however, was not always clear due to the high expression levels of the HA-tagged constructs, making HA to often appear more evenly distributed in the cytoplasm. As expected, no Deup1 or Pcm1 signals were detected in $E2F4^{\Delta DBD}$ cells (Fig. 4c). Remarkably, although $E2F4^{\Delta NES}$ was competent to induce *Deup1*, its inability to undergo nucleocytoplasmic shift resulted in inappropriate localization of Deup1 protein. In the absence of cytoplasmic E2F4, Deup1 was unable to form the characteristic apical cytoplasmic aggregates. Instead, Deup1 accumulated in the nucleus as early as ALI day 2 or could be found less frequently non-aggregated in the cytoplasm (Fig. 4d; Supplementary Fig. 8). Morphometric assessment of the subcellular distribution of Deup1 revealed nuclear signals in nearly 50% of ALI day6 $E2F4^{\Delta NES}$–transduced cells. This was in sharp contrast with $E2F4^{WT}$, in which nuclear Deup1 was found in ~5% of the population (Supplementary Fig. 8c). Moreover, in the absence of cytoplasmic E2F4 there was no evidence of the Pcm1-containing apical granules or nucleating centrioles in the $E2F4^{\Delta NES}$ cells (Fig. 4d; Supplementary Fig. 7c).

At last, we investigated the co-requirement of nuclear and cytoplasmic E2F4 to assemble deuterosomes and initiate multiciliogenesis. Thus, we transduced simultaneously the two mutant constructs that failed individually to rescue the E2f4-deficient phenotype. Lentiviral-mediated cotransduction of $E2F4^{\Delta NES}$ and $E2F4^{\Delta DBD}$ in *E2f4* null cells resulted in transcription and apical targeting of Deup1, formation of Pcm1-containing granules and multicilia formation (Fig. 5). Taken together, we conclude that the multiciliogenesis program is crucially dependent on both nuclear and cytoplasmic functions of E2f4.

Discussion

Here we provide evidence of an unsuspected role for cytoplasmic E2f4 as a core component of apical multiprotein complexes crucial for multiciliogenesis. The close association of E2f4 with Pcm1, as well as the timing and spatial distribution in airway progenitors strongly suggest that cytoplasmic E2f4-Pcm1 aggregates represent the FG classically described during multiciliogenesis. E2f4 is then likely the FG's most relevant component, since others, such as Pcm1 and Bbs4 (Bardet–Biedl syndrome 4) have been shown not to be essential for multicilia formation[20].

Our data support a model in which cytoplasmic E2f4 acts as the organizing centre for the recruitment and accumulation of early regulators of centriole biogenesis, to enable assembly and nucleation of deuterosomes (Supplementary Fig. 9). Thus, E2f4 acts in a sequential manner to link two distinct but interrelated processes in multiciliogenesis, first by inducing a transcriptional program of centriole biogenesis and then by promoting assembly of the resulting protein products in the cytoplasm to initiate centriole amplification.

These observations offer a new paradigm to understand the mechanisms that regulate multiciliogenesis in the lung and potentially other organs, such as the brain and reproductive tract, where multiciliated cells are abundant. They can also illuminate mechanisms of pathogenesis of ciliopathies and cancers in these organs.

Methods

Mouse strains and genotyping. The BAC clone 104J05 containing the *E2f4* genomic locus (129S6/SvEvTac genomic library; RPCI-22, BACPAC Resource Center, Children's Hospital Oakland Research Institute) was used for generation of the targeting construct via recombineering using standard procedures (http://redrecombineering.ncifcrf.gov/)[38]. A DNA fragment harbouring a *FRT* flanked *PGKEM7neobpA* positive selection cassette containing one *loxP* sequence and 50 bp of homology to sequences in the first intron of *E2f4* at each end was generated by PCR (Expand High Fidelity PCR System, Roche) from PL451 and integrated into the *E2f4* genomic locus clone via recombineering (reagents provided by Drs Neal Copeland and Nancy Jenkins, NCI). Subsequently the plasmid pBR.DT-A (Addgene #35955) containing a diphtheria toxin A negative selection cassette was amplified using primers containing 50 bp of homology to sequences located 4.2 kb upstream and 5.8 kb downstream of the first exon of *E2f4* and the targeted locus was transferred into this vector via gap repair. The second *loxP* sequence was inserted into a *Kpn1* site located in intron four using standard cloning procedures. All modifications and the exons within the targeting vector were verified by DNA sequencing. Primer sequences are available on request. Following linearization the targeting vector was electroporated into v6.5 hybrid (C57BL/6 x 129S4/Jae) ES cells and DNA isolated from G418 resistant colonies was screened for homologous recombination by Southern blotting using probes 5′ and 3′ to the targeted locus and standard procedures. ES cells containing correctly targeted loci were additionally screened using a probe to the *neo* cassette to screen out clones carrying additional integrations of the targeting vector. Out of 223 clones picked, 8 were correctly targeted. C57BL/6 blastocysts were injected with correctly targeted ES cells and transplanted into pseudopregnant CD1 mice to generate chimeras. Chimeras were crossed with C57BL/6 females and following determination of germline transmission by Southern blotting. Mice heterozygous for the targeted allele were crossed with mice expressing FLPe recombinase from the *ROSA* locus (Jackson Laboratories, stock number 003946) to delete the *neo* cassette and generate a conditional floxed allele of *E2f4*, designated as *f*. In this allele Cre mediated recombination would delete exons 2 through 4, which is predicted to generate a null allele of *E2f4*. Genotyping was performed by PCR using the following primers for the *E2f4* conditional allele: F4cC, gccattaagcctcagctctgtctgg and F4cU, gtgcaccctgagatgtttagtctgg resulting in a 200 bp product for the wild-type allele and a 293 bp product for the conditional, floxed, allele. F4cC and a separate primer, ctggaacttgcaatgtagacaagg were used to detect the locus following recombination by Cre recombinase (244 bp product). The *ZsGreen1* Cre recombinase reporter allele[39] and the *Shh-Cre* allele were purchased from Jackson Laboratories (stock numbers 007906 and 005622); the *Rosa26-CreERT2* allele[40] was provided by Tyler Jacks' laboratory at MIT (NCI Mouse Repository stock number 01XAB). Mice were maintained on a mixed C57BL/6 × 129Sv background. All animal procedures and experiments were approved by the Institutional Animal Care and Use Committees at Columbia University and MIT.

Air–liquid interface culture of airway epithelial progenitors. Airway epithelial progenitors were isolated from adult tracheas of wild type mice or E2f4 mouse mutants and cultured using well-established protocol (see Methods)[41,42]. For the

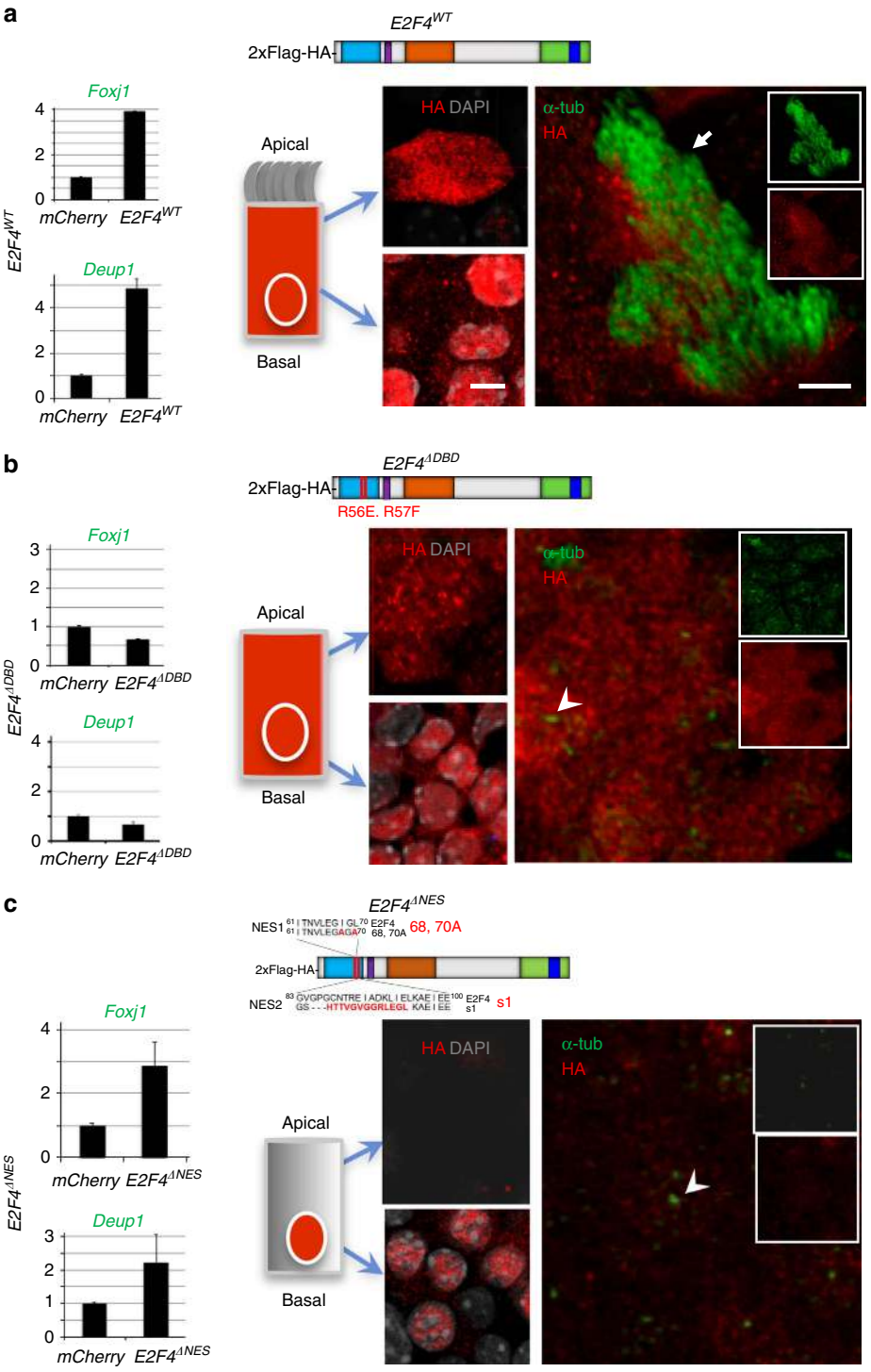

Figure 3 | E2f4 nucleocytoplasmic shift is crucial for multicilia formation. Lentiviral-mediated transduction of HA-tagged E2F4 (diagrams: *E2F4*^{WT}, *E2F4*$^{\Delta DBD}$, *E2F4*$^{\Delta NES}$) or mCherry control constructs in *E2f4*$^{f/f}$;*R26*$^{CreERT2/+}$ airway progenitors treated with Tm (Tamoxifen). Left panels: qPCR of ALI day6: increased *Foxj1* and *Deup1* mRNAs by *E2F4*^{WT} or *E2F4*$^{\Delta NES}$ or but not *E2F4*$^{\Delta DBD}$, compared to *mCherry*. Bars are mean (+s.e.m.). (**a**–**c**) Right panels: Immunofluorescence/confocal imaging: HA, acetylated α-tubulin, DAPI (diagram, apical and basal aspects). HA signals in both nucleus and cytoplasm in *E2F4*^{WT} and *E2F4*$^{\Delta DBD}$ but only in nuclei of *E2F4*$^{\Delta NES}$. Rescue of multiciliogenesis (arrow) in E2f4-deficient cells by transduction of *E2F4*^{WT} but not *E2F4*$^{\Delta DBD}$ or *E2F4*$^{\Delta NES}$ (arrowheads: monocilia). Bar in **a** = 5 μm.

functional analysis of E2f4 in ALI cultures we used adult *E2f4*$^{+/+}$, *E2f4*$^{+/f}$; *R26*$^{CreERT2/LSLZsGreen1}$ or *E2f4*$^{f/f}$; *R26*$^{CreERT2/LSLZsGreen1}$ mice, as well as mice lacking the *R26LSLZsGreen1* allele. Briefly, after treatment with 0.5% pronase overnight, cells were cultured on collagen1-coated Transwell dishes (Corning) under submerged conditions in media that allowed expansion of airway progenitors[42] until confluence (7 days). The ALI was established by removing media from the upper chamber of Transwell (Day 0 ALI) and culturing cells in differentiation media (mTEC/serum free, RA media)[42] up to 8 days (Day 8 ALI). Treatment with 1 μM 4-hydroxytamoxifen (Tm) from day −5 to day 0 was used to induce Cre mediated recombination[36]. The efficiency of recombination was analysed by qPCR, IF for E2f4 and expression of ZsGreen1, where appropriate.

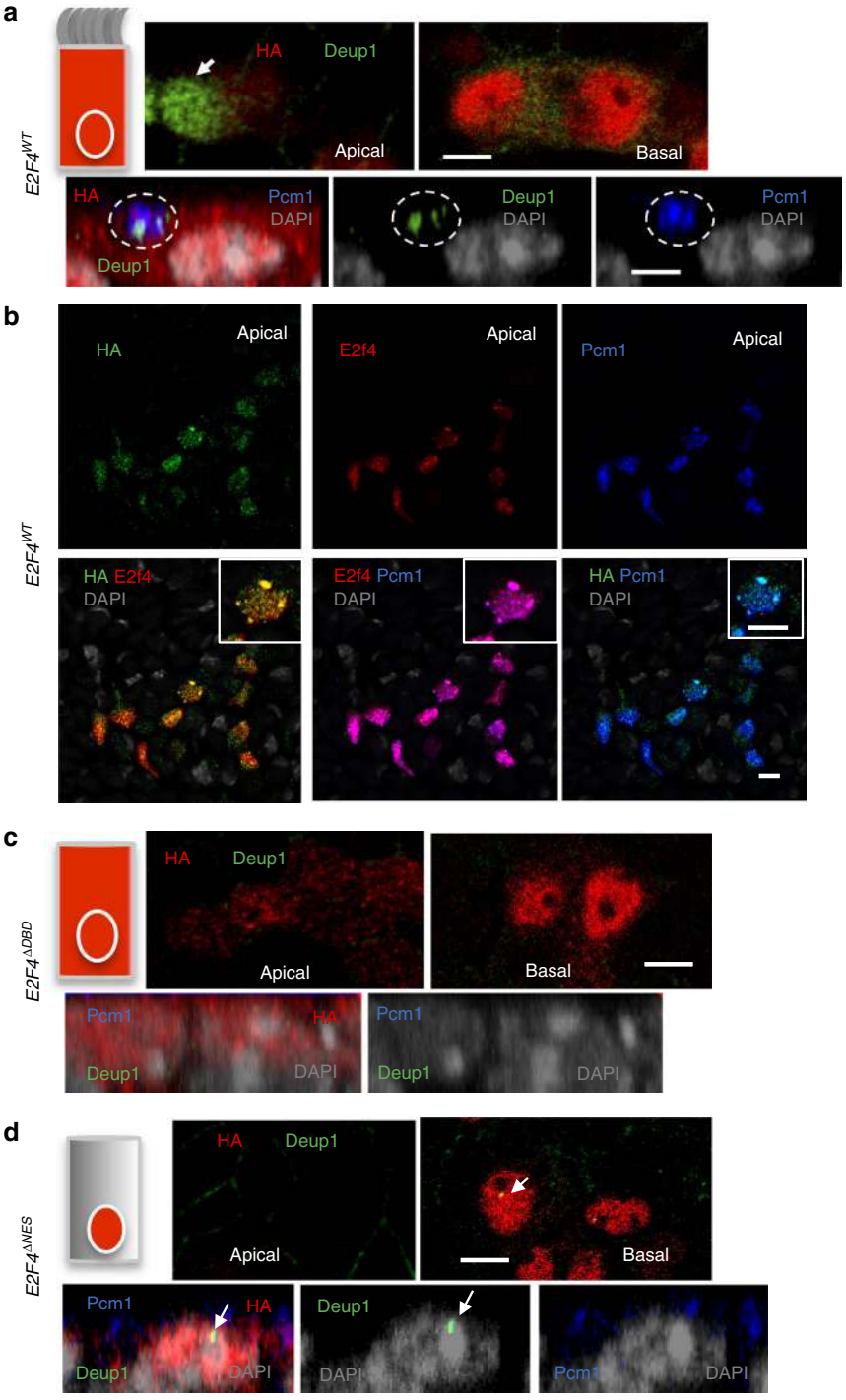

Figure 4 | Cytoplasmic E2f4 is required for apical accumulation of Deup1 and Pcm1. (**a**) Strong apical cytoplasmic induction of Deup1 in Tm-treated *E2f4*$^{f/f}$;*R26*$^{CreERT2/+}$ transduced with *E2F4*^{WT} (arrow in top panel: ALI day6 cells); HA-Deup1-Pcm1 aggregates confirmed in side projection views at ALI day2 (circled area in bottom panel). (**b**) *E2F4*^{WT}-transduced cells express HA, E2f4, and Pcm1 in overlapping patterns in large and smaller cytoplasmic granules (single channels and double-labelled low magnification panels; inset: representative double-labelled cell at high magnification; DAPI). (**c**) *E2F4*$^{\Delta DBD}$-transduced cells: HA expression in nucleus and cytoplasm but no Deup1 or Pcm1 signals. (**d**) *E2F4*$^{\Delta NES}$-transduced cells: HA expression selectively nuclear; Deup1 mislocalized in nuclei (arrow) and unable to form apical aggregates with Pcm1. All bars = 5 μm.

E2F mutant constructs and lentiviral-mediated gene transduction. Lentiviral vectors were constructed to express 2 × Flag-HA-tagged wild-type E2F4, nuclear export signal mutant (ΔNES 68, 70A + E2F4 s1)[37] or a DNA binding domain mutant (ΔDBD, encoding two amino acid replacements in the DNA recognition helix, R56E, R57F) for rescue experiments. Briefly, we amplified Not1-2 × Flag-HA-*E2F4* WT-BamH1 and Not1-2 × Flag-HA-*E2F4* NES (68, 70A + E2F4s1)-BamH1 PCR fragments by polymerase chain reaction (PCR) using pCMV-*E2F4* WT[43] or pcDNA-*E2F4* NES (68, 70A, + E2F4s1) as templates and the primer sets of Not1-2 × Flag-HA-Forward primer: 5′gtcactGCGGCCGCACCGGTTAACccaccatgGACTACAAA-GACCATGACGGTGATTATAAAGATCATGACATCGATTACagtTacccatac-gacgtcccagactacgctATGGCGGAGGCCGGG-3′, and stop codon-BamH1-Reverse primer: 5′-tcactGGATCCACGCGTTTAACtcaGAGGTTGAGAACGGCACATC-3′. This PCR fragment was subcloned into the BamH1/Not1 sites of pHAGE-EF1a-Luciferase-W vector. Subsequently, we amplified Not1-2 × Flag-HA-E2F4 ΔDBD (R56E, R57F)-BamH1 PCR fragment by PCR-ligation mutagenesis[44] with pHAGE-2 × Flag-HA-*E2F4* WT–w vector as the template and the primers which include R56E, R57F mutation: Forward 5′-CGCCAGAAGgagttcATTTACGACATTA-CCAATGTTTTGGAAGGT-3′, Reverse 5′-AGCTGTACGCCAGAAGgagttcA-

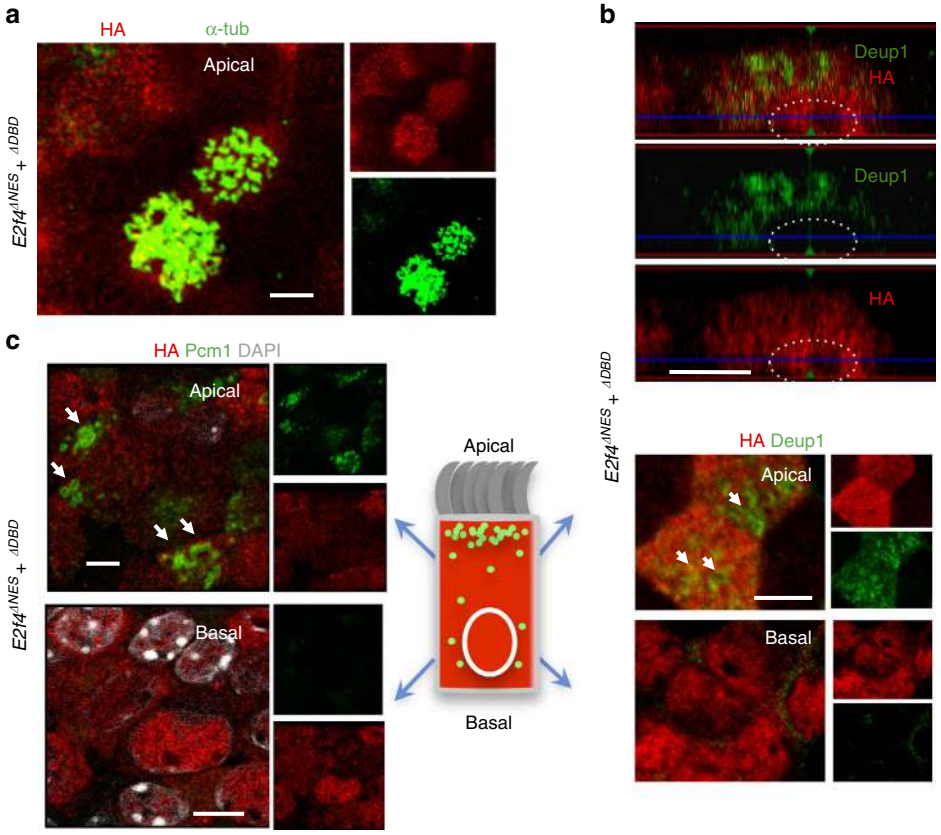

Figure 5 | Restoration of nuclear and cytoplasmic E2f4 function rescues deuterosome formation and multiciliogenesis in E2f4-deficient cells. Co-transduction of *E2F4*$^{\Delta DBD}$ and *E2F4*$^{\Delta NES}$ in E2f-deficient cells; IF/confocal imaging. (**a**) Multicilia formation (acetylated α-tubulin) in HA-labelled cells. (**b**) Induction of multiple Deup1 apical aggregates (top: side projection view; bottom: apical and basal view, arrows). (**c**) Formation of apical HA-Pcm1 granules (arrows). All bars = 5 μm.

TTTACGACA-3′. PCR products were generated using pHAGE-2 × Flag-HA-*E2F4* WT-w vector as the template and the following primer sets: Not1-2 × Flag-HA-Forward primer with R56E, R57F mutation-Reverse primer, and R56E, R57F mutation-Forward primer with stop codon-BamH1-Reverse primer. To obtain the Not1-2 × Flag-HA-*E2F4* ΔDBD (R56E, R57F)-BamH1 PCR fragment, we subsequently performed PCR with the mixture of these PCR products (1:1) as the template, and the primer sets of Not1-2 × Flag-HA-Forward primer and stop codon-BamH1-Reverse primer. The PCR fragment was subcloned into the pHAGE-EF1a-Luciferase-W vector. All of the PCR products were verified by sequencing (Genewiz). The lentiviral vectors pHAGE-EF1a-Cre-w[41] and pHAGE-EF1a-mCherry-w were kindly gifted from Dr Darrell N. Kotton, Boston University. Lentiviral vectors were transfected into the packaging cell line HEK293 (ref. 41). After packaging the virus, supernatant was concentrated by ultracentrifugation to around 0.5–1 × 10^9 PFU ml^{-1} titre. Lentiviral-mediated gene transduction was performed at the time of plating (Day −7 ALI) by infecting cells with lentivirus at ~30 MOI in mTEC proliferation media supplemented with 5 μM of the Rho kinase inhibitor Y-27632 (Sigma)[41,42], and washed with media a few days after virus transduction. Overall transduction efficiency was 30–60%, as judged by mCherry expression or indirect immunofluorescence using anti-HA-tag antibodies.

Immunofluorescence and Immunohistochemistry. Lungs (embryonic, adult) were fixed in 4% paraformaldehyde (PFA) overnight at 4 °C; ALI cultures were fixed with 4% (PFA) for 10 min, room temperature or with 100% methanol for 20 min[41,42]. Human bronchial tissue sections were obtained from healthy non-identified donors. Immunostaining was performed on 5 μm paraffin lung sections (mouse, human) or on mouse ALI cultures, as described in refs 41,42. Briefly, samples were incubated with primary antibodies for 2 h or overnight at 4 °C, washed in PBS and incubated with secondary antibody conjugated with Alexa488, 567 or 647 (Life Technologies, anti-Mouse: A21202, A10037, A31571, 1:300; anti-rabbit: A21206, A10042, A3157, 1:300) for 2 h. When necessary, antigen retrieval was performed using Unmasking Solution Tris-EDTA buffer (1 mM EDTA/Tris–HCL pH 8.3) for 15 min at 110 °C in a pressure cooker. The following antibodies were used: Anti-E2F4 (Millipore, LLF4.2, 1:100)[43], anti-glutamylated tubulin (Adipogene, GT335, 1:250)[22], anti-centrin (Millipore, 04-1624, 1:500)[22], anti-centrin (Proteintech, 12794-AP-1, 1:500)[21], anti-Pcm1 (Cell Signaling, #5213, 1:50; Santa Cruz, D-19, 1:50), anti-Scgb3a2 (ref. 33) (gift from Dr S. Kimura, NIH, 1:1000), anti-Foxj1 (ref. 45) (eBioscience, #2A, 1:100), anti-acetylated α–tubulin (Abcam, ab125356, 1:1000), anti-acetylated α–tubulin (Sigma T7451, 1:2000), anti-β-tubulin IV (Abcam, ab11315, 1:500), Anti-Cre (Millipore MAB3120, 1:100)[41,42], and anti-Cre (Millipore, #69050, 1:200,; Cell signaling, #69050, 1:200)[41,42], anti-HA (Cell signaling, #2367, #3724, 1:100)[41], anti-C-Nap1 (Proteintech, 14498-1-AP, 1:100), anti-CEP63 (Proteintech, 16268-1-AP, 1:100)[21]. Anti-Deup1 (1:500), anti-CEP152 (1:500), anti-PLK4 (1:250) antibodies were produced in Dr Xueliang Zhu's lab and previously published[21]. F-actin and nuclei were visualized by Alexa Fluor 647 phalloidin (Life tech. A22287, 1:100) and NucBlue Fixed Cell ReadyProbes Reagent (DAPI) (Life tech. R37606)[41,42], respectively. To determine the specificity of signal from each antibody we used, as a negative control, normal rabbit, mouse or goat IgG (Santa Cruz) corresponding to the species of each primary antibody. The lack of epithelial signals in sections of *E2f4*$^{+/f}$; *Shh*$^{Cre/+}$ lungs served as an additional negative control for the specificity of the E2f4 antibody (LLF4.2) (Fig. 4b, Supplementary Figs 6a,b and 11). Further demonstration of specificity of the E2f4 antibody is provided in Supplementary Fig. 11. Images were acquired using a Nikon Labophot 2 microscope equipped with a Nikon Digital Sight DS-Ri1 charge-coupled device camera or on a Zeiss LSM 700 or LSM710 confocal laser-scanning microscope equipped with a Motorized Stage, an oil-immersion × 40 or × 63 objective lens and argon laser. For Z-stack analysis, scanning was performed at 0.25 μm per layer.

3D structured illumination (3D-SIM) microscopy. Structured illumination microscopy (SIM) was performed with a Nikon N-SIM based on an Eclipse Ti inverted microscope using an SR Apo-TIRF × 100/1.49 oil-immersion objective and an Andor iXon 3 EMCCD camera. Images were acquired in 3D-SIM mode using excitation at 488 nm and 561 nm and standard filter sets for green and red emission. Image z-stacks were collected with a z interval of 125 nm. SIM image reconstruction, channel alignment and 3D reconstruction were performed using NIS-Elements AR software.

Morphometric analysis. For quantitative assessment of the changes in E2f4 subcellular localization we performed E2f4 immunostaining in airway epithelial cells isolated from WT adult tracheas cultured at ALI days 0, 2, 4 and 8 (as representative of stages 1, 2, 3 and 4, respectively). The subcellular localization of E2f4 was determined as signals present in the nucleus (overlapping with DAPI)

or as cytoplasmic aggregates (>1 μm). The size of E2f4 granules (aggregates) was determined by measuring the longest diameter of the aggregate based on the signal intensity in each confocal image. Approximately 100 cells were counted per time point in five confocal Z-stack sections of three cultures and results were represented as percentage of E2f4-labelled cells with signals in nucleus or in cytoplasm (Supplementary Fig. 1). Moreover we analysed the temporal changes in cytoplasmic E2f4 in ALI cultures by counting the number of large cytoplasmic E2f4 granules (>1 μm) in 100 cells in 3 fields per time point at ALI days 0, 2, 4, 8. For the quantitative analysis of E2f4 association with early markers of centriole, we counted dot-like immunofluorescence signals of E2f4, Deup1, Plk4 or Cep152 in Z-stack images (0.25 μm per layer), typically 15–30 layers, in 3–5 non-overlapping random fields per experimental condition in confocal images captured at ×40 magnification (digital zoom of ×1.5–×2.7). We analysed 10–50 cells for each marker based on nuclear staining marked by DAPI, using Zen software (Zeiss). To estimate how abundance of deuterosomes changes during multiciliogenesis we counted the total number of Deup1 dots per cell across confocal Z-stacks (0.25 μm per layer; 15–30 layers per cell) in ALI cultures from stages 2–4 (stage 1 has no deuterosomes) in 31 cells per group. Results were expressed mean (+s.e.) (Supplementary Fig. 3e). Changes in the proportion of deuterosomes present in Pcm1-enriched areas as a function of the number of deuterosomes per cell were determined by counting Deup1-Pcm1 double labelled dots (fully or partially overlapping signals were considered as positive) and the total number of Deup1 dots per cell across Z-plane stacks (15–30 layers per cell); the percentage of Deup1 double labelling (mean, +s.e.) was plotted against the number of deuterosomes per cell (in groups of 20) in 48 cells from 3 cultures. Similarly, we determined the number of Deup1 dots double labelled with centrin (partial and total overlap considered positive) in cells with different number of deuterosomes, and represented the results as described above (Supplementary Fig. 3f,g). For quantification of the diameter of Deup1-rings (cradles) we used Zeiss software (Zeiss, Blue edition) following reconstruction as 3D-SIM images[21]. Briefly, the Deup1 signal intensity peak was detected by profile analyses of each Deup1 rings (Zeiss software; see Supplementary Fig. 4b,c) and the diameters of Deup1-rings were calculated as follows: diameter = $(a+b)/2$; where a = longest diameter of a Deup1-ring and b = shortest diameter of Deup1-ring[21] using 3D-reconstructed images. The presence of Deup1-rings either inside, at the periphery, or outside E2f4 granules (as represented in Fig. 2f, Supplementary Fig. 4c by *i,ii,iii* respectively, in the lateral panels) was determined at stage 3 (E2f4 granules >1 μm). We determined the relationship between size of deuterosome (diameter of Deup1 ring) and its position in the E2f4 granule (*i,* inside; *ii*, at the periphery, or *iii,* outside). If the highest signal intensity of the Deup1 ring found by profile analyses was detected inside or at the edge of the E2f4 granule, it was categorized as *(i) or (ii),* respectively, otherwise it was categorized as *(iii).* Deup1 structures that still did not form a ring (typically those <200 nm) were ignored because small Deup1-dots were already identified as immature deuterosome components in a previous report[21]. We counted the number of cells in each category randomly in 10 cells at stage 3 and represented the results as the average size of deuterosome (mean ± s.e., nanometre diameter) in each group *(i, ii, iii).* Statistical analysis was performed (Student's *t*-test) and differences were considered significant if $^*P<0.05$.

Quantitative real-time PCR. Total RNA from each sample was extracted using the RNeasy Mini Kit (Qiagen, #74104) and reverse-transcribed using Superscript III (Invitrogen, #18080-051)[41,42]. ABI 7000 (Applied Biosystems, Foster City, CA, USA) and Taqman probes for *E2f4*, *Plk4*, *Cep63*, *Deup1*, *Foxj1* and β-*actin* were used (Assays-on-Demand, Applied Biosystems, Austin, TX, USA). Reactions (25 μl) were performed using the TaqMan Gene Expression Assay (Applied Biosystems, TX, USA). The relative concentration of the RNA for each gene to beta-actin mRNA was determined using the equation 2–DCT, where D CT = (CT mRNA–CT β − *actin* R).

Western blotting analysis. Cell extracts were prepared using a cell fractionation kit (Thermo Scientific, NE-PER Nuclear and Cytoplasmic Extraction Reagents) according to the manufacture's protocol. For Western blotting[41,42], samples were subjected to 4–12% gradient SDS-PAGE electrophoresis and transferred to PVDF membrane after quantification of the protein concentration via Bradford protein assay (Pierce Coomassie Plus (Bradford) Assay Kit from Thermo Scientific, Cat# 23236). Membranes were blocked with 8% (for E2f4 blot) or 5% (for all of other blots) Skim milk (2 h, R.T.) and probed with Anti-E2F4 (LLF4.2)(1:500)[43], anti-Deup1 (1:3,000)[21], Sas6 (91.390.21, Santa Cruz Biotechnology, 1:10). Anti-GAPDH (Cell signaling, #2118s, 1:5,000) and anti- LaminB1 (Abcam, ab65986, 1: 8,000) were used for the internal controls designating the cytoplasmic and nuclear fractions, respectively. Antigen–antibody complexes were identified wi\th HRP-conjugated secondary antibodies (Jackson lab). Enhanced chemiluminescence was detected using LAS 4000 (GE Health Care).

Immunoprecipitation. 293FT cells (Thermo Scientific, Cat# R70007) were transfected with with the following plasmids; pcDNA mouse E2f4, human SAS6 (Addgene #46382) or pcDNA-Flag-Deup1 using TransIT-LT1 reagent (Mirus). We also used mTECs at ALI day3 for endogenous protein interaction analyses. Cells were collected and lysed with NP40-based Lysis Buffer (NP-40 soluble fraction); 20 mM HEPES, 15% Glycerol (Thermo Scientific), 250 mM KCl, 1.2 mM EDTA (Thermo Scientific), 1% NP-40 (Thermo Scientific), Glutamax ×5 (Thermo Scientific), Proteinase & ×1 Phosphatase inhibitor (Thermo Scientific, Cat# 78443) and 0.1 mM Phenylmethanesulfonyl fluoride (PMSF) (Sigma Cat# P7626, add just before use from 200 mM stock) and 1 mM Sodium orthovanadate (200 mM stock) (Sigma Cat# S6508). The cell lysates were cleared by centrifugation at 3000G for 10 min at 4 °C. Immunoprecipitation for each samples (2 mg per sample) using 40 μl anti-E2F4 agarose beads (Santa Cruz, Cat# sc-866 AC) (prewashed with Lysis buffer to make 50% slurry) or anti-rabbit IgG agarose beads (Santa Cruz, Cat# sc-2345) as a control was carried out for 1–2 h on rocker on ice. After washing five times with cold 1 ml lysis buffer and centrifugation (168G, 1 min), 50 μl pH 2.5 Glycine buffer 2× SDS loading buffer was added to elute protein complexes from each antibody. After gently tapping, these samples were centrifuged at 168G for 1 min at 4 °C. Each supernatant was transferred to another tube immediately to neutralize the pH to be 7.4 by adding 12ul pH8.5 Tris-HCL on ice. Then, approximately 12 μl ×6 SDS sample buffer (Reducing, Boston BioProducts, BP-111R) and DTT (final conc. 0.1 M) was added prior to boiling the samples for 10 min at 95 °C. Half of the samples (1 mg input) were loaded in a SDS-PAGE gel and westerns were performed as above. We used Mouse TrueBlot ULTRA: Anti-Mouse Ig HRP (Rockland, Cat# 18-8817-30, 1:1,000) to the E2F4 blots to decrease the signal of heavy chain. 80 μg per lane was loaded for the ALI culture input samples.

Proximity ligation assay. PLA was performed according to the manufacturer's protocol (Sigma, DUO92102)[46]. Briefly, ALI day 4 cultures *from* $E2f4^{f/f}$; $R26^{CreERT2/+}$ with or without Tamoxifen treatment were fixed with 4% PFA room temperature for 10 min. Samples were incubated with primary antibodies (anti E2f4, anti Deup1 or the relevant control IgGs, as indicated) using the immunofluorescence microscopy protocol described above, followed by incubation with the PLA probe set (anti-rabbit plus strand/anti-mouse minus strand) at 37 °C for 2 h. Ligation of probes in close proximity was carried out at 37 °C for 30 min, followed by a 100-min amplification step. Subsequently, we performed immunofluorescence staining for anti-Pcm1 antibody as described above. All processed slides were mounted using ProLong Gold antifade reagent (Life Technologies, catalogue no. P36930), and images were captured using a confocal microscope system (Carl Zeiss, LSM 710).

Microarray analysis. Briefly, airway epithelial progenitors isolated from Tm or vehicle-treated cultures from adult $E2f4^{f/f}$; $R26^{CreERT2/+}$ tracheas were analysed at ALI days 0, 2 and 4 (representative of Stages 1, 2,3). Triplicate samples (each 2 wells per sample) of each group were incubated at 4 °C with RNA-later (Sigma) overnight at each time point (day 0, day 2, day 4). Total RNA was extracted from these samples (total 18) using a RNeasy Mini Kit (Qiagen, #74104). We used Mouse Gene 1.0 ST arrays; data were normalized using the Robust Multiarray Average (RMA) algorithm and a CDF (Chip Definition File) that maps the probes on the array to unique Entrez Gene identifiers. The technical quality of the arrays was assessed by two quality metrics: Relative Log Expression (RLE) and Normalized Unscaled Standard Error (NUSE). Pairwise Student *t* tests were performed between the control and mutant (KO) groups for comparisons within each time point. To identify centriole biogenesis genes differentially altered in *E2f4* mutant (KO) cultures and control, we first examined the expression of 724 genes associated with centriole biogenesis reported in Ma *et al.* (Table 1 of reference[24]). This revealed expression of 266 of these genes significantly altered at D0 in *E2f4* KO cultures. Clustering analysis showed that 10 genes are clustered together with *Deup1/Ccdc67* (downregulated in KO samples at ALI day0) and 16 genes are clustered together with *Plk4* (downregulated in KO samples at day2). This contrasted with the relatively unchanged levels of Cep63 (consistent with results from Ma *et al.*[24]. Changes in gene expression were confirmed by qRT-PCR.

Data availability. All relevant data are included in this article and Supplementary Information files or available from the authors upon request. Microarray datasets have been deposited in the NCBI GEO database (GEO Submission No. GSE73331).

References

1. Sánchez, I. & Dynlacht, B. D. Cilium assembly and disassembly. *Nat. Publ. Gr* **18,** 711–717 (2016).
2. Yan, X., Zhao, H. & Zhu, X. Production of basal bodies in bulk for dense multicilia formation. *F1000Research* **5,** 1533 (2016).
3. Ishikawa, H. & Marshall, W. F. Ciliogenesis: building the cell's antenna. *Nat. Rev. Mol. Cell Biol.* **12,** 222–234 (2011).
4. Shah, A. S. Motile cilia of human airway are chemosensory. *Science* **325,** 1131–1134 (2009).
5. Brooks, E. R. & Wallingford, J. B. Multiciliated cells. *Curr. Biol.* **24,** R973–R982 (2014).
6. Nigg, E. a. & Raff, J. W. Centrioles, centrosomes, and cilia in health and disease. *Cell* **139,** 663–678 (2009).
7. Azimzadeh, J. & Marshall, W. Building the centriole. *Curr. Biol.* **20,** 816–825 (2010).

8. Song, M. H., Miliaras, N. B., Peel, N. & O'Connell, K. F. Centrioles: some self-assembly required. *Curr. Opin. Cell Biol.* **20,** 688–693 (2008).
9. Kobayashi, T. & Dynlacht, B. D. Regulating the transition from centriole to basal body. *J. Cell Biol.* **193,** 435–444 (2011).
10. Carvalho-Santos, Z. *et al.* Stepwise evolution of the centriole-assembly pathway. *J. Cell Sci.* **123,** 1414–1426 (2010).
11. Nakazawa, Y., Hiraki, M., Kamiya, R. & Hirono, M. SAS-6 is a cartwheel protein that establishes the 9-fold symmetry of the centriole. *Curr. Biol.* **17,** 2169–2174 (2007).
12. KlosDehring, D. A. *et al.* Deuterosome-mediated centriole biogenesis. *Dev. Cell* **27,** 103–112 (2013).
13. Brown, N. J., Marjanović, M., Lüders, J., Stracker, T. H. & Costanzo, V. Cep63 and Cep152 cooperate to ensure centriole duplication. *PLoS ONE* **8,** e69986 (2013).
14. Tsou, M.-F. B. & Stearns, T. Controlling centrosome number: licenses and blocks. *Curr. Opin. Cell Biol.* **18,** 74–78 (2006).
15. Sorokin, S. P. Reconstructions of centriole formation and ciliogenesis in mammalian lungs. *J. Cell Sci.* **3,** 207–230 (1968).
16. Anderson, R. G. & Brenner, R. R. M. The formation of basal bodies (centrioles) in the rhesus monkey oviduct. *J. Cell Biol.* **50,** 10–34 (1971).
17. Dirksen, E. R. Centriole and basal body formation during ciliogenesis revisited. *Biol. Cell* **72,** 31–38 (1991).
18. Dirksen, E. R. Centriole morphogenesis in developing ciliated epithelium of the mouse oviduct. *J. Cell Biol.* **51,** 286–302 (1971).
19. Kubo, A. & Tsukita, S. Non-membranous granular organelle consisting of PCM-1: subcellular distribution and cell-cycle-dependent assembly/disassembly. *J. Cell Sci.* **116,** 919–928 (2003).
20. Vladar, E. K. & Stearns, T. Molecular characterization of centriole assembly in ciliated epithelial cells. *J. Cell Biol.* **178,** 31–42 (2007).
21. Zhao, H. *et al.* The Cep63 paralogue Deup1 enables massive *de novo* centriole biogenesis for vertebrate multiciliogenesis. *Nat. Cell Biol.* **15,** 1434–1444 (2013).
22. Jord, A. A. l. *et al.* Centriole amplification by mother and daughter centrioles differs in multiciliated cells. *Nature* **516,** 104–107 (2014).
23. Danielian, P. S. *et al.* E2f4 is required for normal development of the airway epithelium. *Dev. Biol.* **305,** 564–576 (2007).
24. Ma, L., Quigley, I., Omran, H. & Kintner, C. Multicilin drives centriole biogenesis via E2f proteins. *Genes Dev.* **28,** 1461–1471 (2014).
25. Blais, A. & Dynlacht, B. D. Hitting their targets: an emerging picture of E2F and cell cycle control. *Curr. Opin. Genet. Dev.* **14,** 527–532 (2004).
26. Trimarchi, J. M. & Lees, J. a. , Sibling rivalry in the E2F family. *Nat. Rev. Mol. Cell Biol.* **3,** 11–20 (2002).
27. Attwooll, C., Lazzerini Denchi, E. & Helin, K. The E2F family: specific functions and overlapping interests. *EMBO J.* **23,** 4709–4716 (2004).
28. Cam, H. & Dynlacht, B. D. Emerging roles for E2F: beyond the G1/S transition and DNA replication. *Cancer Cell* **3,** 311–316 (2003).
29. Stubbs, J. L., Vladar, E. K., Axelrod, J. D. & Kintner, C. Multicilin promotes centriole assembly and ciliogenesis during multiciliate cell differentiation. *Nat. Cell Biol.* **14,** 140–147 (2012).
30. Kesimer, M. *et al.* Tracheobronchial air-liquid interface cell culture: a model for innate mucosal defense of the upper airways? *Am. J. Physiol. Lung Cell. Mol. Physiol.* **296,** L92–L100 (2009).
31. Dvorak, A., Tilley, A. E., Shaykhiev, R., Wang, R. & Crystal, R. G. Do airway epithelium air-liquid cultures represent the *in vivo* airway epithelium transcriptome? *Am. J. Respir. Cell Mol. Biol.* **44,** 465–473 (2011).
32. Horani, A., Dickinson, J. D. & Brody, S. L. in *Mouse Models of Allergic Disease* (ed. Allen, I. C.) 91–107 (2013).
33. You, Y., Richer, E. J., Huang, T. & Brody, S. L. Growth and differentiation of mouse tracheal epithelial cells: selection of a proliferative population. *Am. J. Physiol. Lung Cell Mol. Physiol.* **6,** L1315–L1321 (2002).
34. Tsou, M.-F. B. & Stearns, T. Mechanism limiting centrosome duplication to once per cell cycle. *Nature* **442,** 947–951 (2006).
35. Hagiwara, H., Ohwada, N. & Takata, K. Cell biology of normal and abnormal ciliogenesis in the ciliated epithelium. *Int. Rev. Cytol.* **234,** 101–141 (2004).
36. Ostrowski, L. E. *et al.* Conditional deletion of dnaic1 in a murine model of primary ciliary dyskinesia causes chronic rhinosinusitis. *Am. J. Respir. Cell Mol. Biol.* **43,** 55–63 (2010).
37. Gaubatz, S., Lees, J. A., Lindeman, G. J. & Livingston, D. M. E2F4 is exported from the nucleus in a CRM1-dependent manner. *Mol. Cell Biol.* **21,** 1384–1392 (2001).
38. Liu, P., Jenkins, N. & Copeland, N. A highly efficient recombineering-based method for generating conditional knockout mutations. *Genome Res.* **13,** 476–484 (2003).
39. Madisen, L. *et al.* A robust and high-throughput Cre reporting and characterization system for the whole mouse brain. *Nat. Neurosci.* **13,** 133–140 (2010).
40. Ventura, A. *et al.* Restoration of p53 function leads to tumour regression *in vivo*. *Nature* **445,** 661–665 (2007).
41. Mori, M. *et al.* Notch3-Jagged signaling controls the pool of undifferentiated airway progenitors. *Development* **142,** 258–267 (2015).
42. Mahoney, J. E., Mori, M., Szymaniak, A. D., Varelas, X. & Cardoso, W. V. The Hippo pathway effector Yap controls patterning and differentiation of airway epithelial progenitors. *Dev. Cell* **30,** 137–150 (2014).
43. Moberg, K. *et al.* E2F-4 switches from p130 to p107 and pRB in response to cell cycle reentry. *Mol. Cell Biol.* **16,** 1436–1449 (1996).
44. Mori, M. *et al.* Promotion of cell spreading and migration by vascular endothelial-protein tyrosine phosphatase (VE-PTP) in cooperation with integrins. *J. Cell. Physiol.* **224,** 195–204 (2010).
45. You, Y. *et al.* Role of f-box factor foxj1 in differentiation of ciliated airway epithelial cells. *Am. J. Physiol. Lung Cell. Mol. Physiol.* **286,** L650–L657 (2004).
46. Szymaniak, A. D., Mahoney, J. E., Cardoso, W. V. & Varelas, X. Crumbs3-mediated polarity directs airway epithelial cell fate through the Hippo pathway effector Yap. *Dev. Cell* **34,** 283–296 (2015).

Acknowledgements

We thank Jun Qian and Jingshu Huang for technical assistance; Adam Gower and Eduard Drizik for microarray analyses; Minoree Kohwi for assistance with confocal imaging; Theresa Swayne for assistance with 3D-SIM analysis; Gopal Singh and Matthew Bacchetta for surgical specimens; Shioko Kimura (NIH) for antibodies, and Tyler Jacks (MIT) for transgenic mouse strain; Stefan Gaubatz for plasmids; Dr Neal Copland (NCI) for recombineering reagents and Darrell Kotton (Boston University) for thoughtful discussion and lentiviral vectors. We also thank the Koch Institute Swanson Biotechnology Center for technical support, specifically the ES Cell and Transgenics facility. This work was funded by NIH-NHLBI R01 HL119836-01 and R01 HL105971-01 to W.V.C., and NIH/NCI PO1-CA42063 and P30-CA14051 to J.A.L.; J.A.L. is a Ludwig Scholar.

Author contributions

M.M., P.S.D., J.A.L. and W.V.C. designed the study; M.M., P.S.D., J.E.M., R.H., H.L. performed experiments; J.L. conducted bioinformatics analyses. E.S.M., X.Z. provided reagents; M.M., P.S.D., J.A.L. and W.V.C. wrote the paper with comments from all authors.

Additional information

Supplementary Information accompanies this paper at http://www.nature.com/naturecommunications

Competing interests: The authors declare no competing financial interests.

Reprints and permission information is available online at http://npg.nature.com/reprintsandpermissions/

How to cite this article: Mori, M. *et al.* Cytoplasmic E2f4 forms organizing centres for initiation of centriole amplification during multiciliogenesis. *Nat. Commun.* **8,** 15857 doi: 10.1038/ncomms15857 (2017).

Publisher's note: Springer Nature remains neutral with regard to jurisdictional claims in published maps and institutional affiliations.

nature COMMUNICATIONS

DOI: 10.1038/ncomms16157 OPEN

Author Correction: Cytoplasmic E2f4 forms organizing centres for initiation of centriole amplification during multiciliogenesis

Munemasa Mori, Renin Hazan, Paul S. Danielian, John E. Mahoney, Huijun Li, Jining Lu, Emily S. Miller, Xueliang Zhu, Jacqueline A. Lees & Wellington V. Cardoso

Nature Communications 8:15857 doi: 10.1038/ncomms15857 (2018); Published 4 Jul 2017; Updated 19 Nov 2018.

This Article contains an error in reference 1. The correct reference is as follows:

Sánchez, I. & Dynlacht, B. D. Cilium assembly and disassembly. *Nat. Cell Biol.* **18**, 711–717 (2016).

Entire lung generation by targeting a bona fide lineage enough for lung generation

Akihiro Miura[1, 2], Hemanta Sarmah[1], Junichi Tanaka[1], Youngmin Hwang[1], Anri Sawada, [1] Yuko Shimamura[1], Yinshan Fang[1], Dai Shimizu[2], Zurab Ninish[1], Jake Le Suer[3, 4], Nicole C. Dubois[5], Jennifer Davis[6], Shinichi Toyooka[2], Jun Wu[7], Jianwen Que[1], Finn J. Hawkins[3, 4], Chyuan-Sheng Lin[8], Munemasa Mori[1] †

1 Columbia Center for Human Development and Division of Pulmonary, Allergy, Critical Care, Department of Medicine, Columbia University Medical Center, New York, NY 10032, USA.
2 Department of Thoracic, Breast and Endocrinological Surgery, Okayama University Graduate School of Medicine, Dentistry and Pharmaceutical Sciences, Okayama, 7008558, Japan.
3 The Pulmonary Center and Department of Medicine, Boston University School of Medicine, Boston, MA 02118, USA
4 Center for Regenerative Medicine, Boston University and Boston Medical Center, Boston, MA 02118, USA
5 Department of Cell, Developmental and Regenerative Biology, Icahn School of Medicine at Mount Sinai, New York, NY 10029, USA.
6 Department of Pathology, University of Washington, Seattle, WA 98109, USA.
7 Department of Molecular Biology, University of Texas Southwestern Medical Center, Dallas, TX, USA
8 Bernard and Shirlee Brown Glaucoma Laboratory, Department of Pathology and Cell Biology, College of Physicians and Surgeons, Columbia University Irving Medical Center, New York, NY 10032, USA.

† To whom correspondence should be addressed:
Munemasa Mori, M.D., Ph.D.
650W 168th St, New York, NY 10032, USA
E-mail: mm4452@cumc.columbia.edu

Millions worldwide suffer from incurable lung diseases, and organ transplantation remains their only hope. Bioengineering and regenerative medicine are promising for lung tissue production. However, no technology is available for the entire lung manufacturing composed of tissue-specific mesenchyme, epithelium, and endothelium. We postulated that targeting a single lineage, permissive for all cell type differentiation in a specific organ, to vacant a bona fide organ-generative lineage (BFL) will lead to the whole organ production via conditional blastocyst complementation. Here, by lineage tracing, we demonstrated that Foxa2-lineage contributed to both parenchymal and mesenchymal tissues of a developing lung. This was due to the partial overlap of the Foxa2-lineage with the Pdgfrα^{+} mesendoderm lineage during gastrulation that gives rise to the entire lung mesoderm. The induction of Fgfr2 gene depletion, specifically in the Foxa2-lineage, resulted in defects in the endodermal and mesodermal lung niches, leading to lung agenesis phenotype. Strikingly, donor iPSCs complemented the lung agenesis phenotype and produced the entire lungs, including epithelium, mesenchyme, and endothelium, following blastocyst injection. Together, targeting BFL represents a novel paradigm for whole organ manufacturing, holding great potential for future human whole lung generation in large animals.

KEYWORDS (3-10)
Entire organ generation
Conditional blastocyst complementation
Lung generation
Lung mesenchyme precursors
Lung mesenchyme origin
Lateral plate mesoderm

Lung manufacturing to cure various refractory lung diseases has been challenging for many decades[1–4]. Lung regeneration strategies such as recellularizing tissue-specific progenitors into the decellularized scaffolds, induced pluripotent stem cells (iPSC)-derived organoids, and 3d-bioprinters have been promising for next-generation tissue transplantation therapies[3,5–7], while the mammalian lung is one of the most demanding organs to replicate, which contains hundreds of airway branching, inflatable well-vascularized micron-sized thin alveolar layer, composed of more than 50 various cell types, and the origin of those cells is largely unknown[5,8–10]. Despite the severe scarcity of donor lungs for lung transplantation worldwide, none of the technologies overcame all of those issues and achieved the entire lung production.

Blastocyst complementation (BC) has been proposed as an auspicious option for tissue-specific niche complementation[11]. This unique BC technology was further developed for intra- and inter-specific tissue generations such as kidneys, pancreas, and vessels[12–15]. However, producing the entire organs, including endothelial cells and tissue-specific epithelium and mesenchyme, has still been challenging. Previously, we established a refined BC technique, named the conditional blastocyst complementation (CBC) approach, that targets the specific lineage to be complemented by donor pluripotent stem cells[16]. Using lineage-specific drivers in the CBC system, we can avoid the gene ablation effect in the off-target organs for generating the vacant organ niche. Briefly, we rescued the lung agenesis phenotype caused by the conditional ablation of Fgfr2 under the sonic hedgehog (*Shh*) promoter ($Shh^{Cre/+}$; $Fgfr2^{flox/flox}$) via injecting GFP-labelled pluripotent stem cells ($PSC^{CAG\text{-}GFP}$) in host blastocysts[16]. Those neonates survived until adulthood with fully functional lungs holding nearly 100% replacement of lung epithelial cells by donor cells. The CBC model achieved a highly efficient complementation rate and functional chimeric lung generation never previously accomplished in any other chimeric lung generation model[17,18]. However, lung mesenchyme and endothelium were still comprised in the host mouse at about 50% chimerism, which was the limitation of the previous Shh-based model of CBC[16]. Identifying a novel cell lineage critical for the organogenesis program responsible for controlling the cell traits and composition in the targeted organs can lead to whole-organ bioengineering.

We postulated that targeting a single lineage when genetically defective, in which the donor cells would complement the defective niche is sufficient for generating the entire lungs, can work as a bona fide organ generative lineage (BFL), enough to repopulate donor cells that lead to the entire lung production following the blastocyst injection. To explore the prospective existence of BFL, we focused on the stage of mesendoderm in the primitive streak that may form both definitive endoderm (DE) and lateral plate mesoderm (LPM) because of the success of chimeric lung generation using the Shh Cre driver[19], which targets DE lineage[16].

Mesendoderm is the transition state between primitive streak and nascent mesoderm marked with Mixl1 and Brachyury (T) during gastrulation that can give rise to both DE and mesoderm via epithelial-mesenchymal transition (EMT)[20,21]. There was no evidence of genetic lineage tracing on whether mesendoderm can give rise to both $Nkx2\text{-}1^{+}$ lung endoderm[22,23] and $wnt2^{+}$ cardiopulmonary progenitors (CPP)[24]. Foxa2 are known to be expressed in the DE[25,26], while Foxa2 and Pdgfrα are also expressed during the conversion from mesendoderm to mesenchyme[20,27–29]. It has been unclear whether Pdgfrα lineage would differentiate into DE or LPM.

Using $Pdgfr\alpha^{CreERT2/+}$; $Rosa^{tdTomato/+}$ lineage-tracing mice, we found that the entire lung mesenchyme and a part of lung epithelium were labeled by tdTomato at E14.5 upon a tamoxifen injection at E5.5 (**Fig. 1a, Extended Data Fig. 1a, b**). This result suggested that the origin of the

entire lung mesenchyme is Pdgfrα$^+$ mesendoderm. Since the Pdgfrα$^+$ lineage labeled only partial lung endoderm (**Extended Data Fig. 1b**), we explored the BFL possibility further using the Foxa2-lineage.

Foxa2 is known as a pioneering transcription factor that epithelializes the cells during gastrulation[30,31]. The previous study of the extensive immunostaining analyses in the Foxa2 reporter mouse line showed that Foxa2-lineage might give rise to both LPM and DE [27]. Foxa2 plays a pivotal role in alveolarization and airway goblet cell expansion[32], while there was a knowledge gap in Foxa2-lineage studies in lung development. Foxa2-lineage tracing mice (*Foxa2$^{Cre/+}$; Rosa$^{tdTomato/+}$*) faithfully target Nkx2-5$^+$ cardiac progenitors, associated with the origin of Wnt2$^+$ Isl1$^+$ CPP[24,33]. Thus, we explored the possibility of BFL in the Foxa2-lineage. First, we checked whether the Foxa2-lineage would label Pdgfrα expressing cells at E6.5 during gastrulation using the Foxa2-lineage tracing mice (*Foxa2$^{Cre/+}$; Rosa$^{tdTomato/+}$*)[34]. Foxa2-lineage partially marked Pdgfrα$^+$ mesendodermal cells on nascent mesoderm invaginating from the primitive streak (**Fig. 1b)**. Based on this, we further explored whether Foxa2-lineage would label lung mesenchyme. We found that Foxa2-lineage cells markedly labeled the entire lung epithelium and robustly variety of the mesenchyme, including endothelial cells (**Fig. 1c, Extended Data Fig. 2**). Quantitative analyses by flow cytometry (**Fig. 2a**) showed that Foxa2-lineage labeled the entire lung endoderm (89.6%± 1.80) and lung mesoderm (24.1%± 5.31), including endothelial cells (18.3 %± 8.05) at E14.5 (**Fig. 2b-d, Extended Data Fig. 3, 4**). Unexpectedly, we observed that the Foxa2-lineage covered nearly the entire lung mesenchyme, endothelial cells, and lung epithelial cells during the post-natal periods (**Extended Data Fig. 3**). Using wild-type control (*Foxa2$^{+/+}$; Rosa$^{+/+}$*) to determine the gate's threshold of the flow cytometry, the lineage labeling at postnatal day0 showed nearly 100% (**Extended Data Fig. 3b**). However, we noticed that the *Foxa2$^{+/+}$; Rosa$^{tdTomato/+}$* lineage tracing mice showed a leaky signal of the weak tdTomato expression in lung mesenchyme and endothelial cells (**Extended Data Fig. 3b**). Therefore, we used Cre negative littermate control mice (*Foxa2$^{+/+}$; Rosa$^{tdTomato/+}$*) for deciding the stringent gating threshold and reanalyzed its percentage. This adjusted gate setting revealed the lineage labeling was about 98.98%± 0.171 in lung epithelium, 45.43%± 7.30 in lung mesenchyme, and 61.48%± 9.49 in lung vascular endothelial cells in adulthood (**Fig. 2c, d**). These results suggested that the Foxa2-lineage labels the entire lung epithelium and about half of the lung mesenchyme.

To explore whether Foxa2 or Pdgfrα lineage is evolutionally conserved and can give rise to both lung endoderm and mesoderm, we established lung endoderm-mesoderm co-developing directed differentiation protocol with a minor modification from the previously reported protocols[26,35–38] (**Fig. 3a**). In this optimized protocol, we confirmed that the various hiPSC lines efficiently induced lung bud-like appearance marked by NKX2-1$^+$ in lung epithelial cells[37,38]. TBX4$^+$ lung mesenchyme appeared and surrounded the NKX2-1$^+$SOX9$^+$ lung epithelium (**Fig. 3b, c**) on day10. qPCR kinetics analyses across the time point further supported the appearance of lung mesenchyme represented by the LPM marker expression peaked on day6~8; *OSR1, FGF10, BMP4, PDGFRα*, and smooth muscle markers peaked on day8~10; *ACTA2* and *PDGFRβ*, and CPP markers peaked on day8~12; *ISL1, WNT2, FOXF1,* and *TBX4*, concomitant with the lung epithelial markers peaked on day10~14; *NKX2-1* and *CPM* (**Fig. 3d**).

In this directed differentiation protocol, both NKX2-1$^+$ lung endoderm and WNT2$^+$TBX4$^+$ lung mesoderm around day15 were derived from anteriorized ventral endoderm and mesoderm after Activin-mediated definitive endoderm and LPM induction[26,36]. During the primitive streak induction from day0 to day3, PDGFRα and EPCAM cell surface markers and intracellular FOXA2 and MIXL1 kinetics were analyzed every 12 hours by flow cytometry (**Fig. 3e)**. Briefly, 12 hours

after the Activin induction, more than 60% of the EPCAM$^+$PDGFRα$^-$ primitive streak first turned on MIXL1, the mesendoderm marker[20,21]. Subsequently, the epithelial-mesenchymal transition occurred 24 hours later, as represented by the PDGFRα induction in the EPCAM$^+$MIXL1$^+$ mesendoderm. 36 hours later, more than 90% of the MIXL1$^+$EPCAM$^+$ mesendodermal cells expressed PDGFRα. At the same time, FOXA2 expression appeared in the part of those mesendodermal cells (**Fig. 3f)**. After that, PDGFRα expression was diminished, and reciprocal FOXA2 induction appeared when the EPCAM$^+$FOXA2$^+$ definitive endoderm and EPCAM$^-$ FOXA2$^-$ LPM presented at 72 hours (**Fig. 3g)**. The MIXL1, PDGFRα, and FOXA2 kinetics were further evident by qPCR analyses (**Extended Data Fig. 5**). These results suggested that the PDGFRα$^+$ expressing cells and FOXA2$^+$ expressing cells are redundant but distinct phases of mesendoderm, which can give rise to both endodermal and mesodermal lung cells in an evolutionarily conserved manner (**Extended Data Fig. 6**).

Since the Foxa2-lineage appeared in the late phase of mesendoderm to form both DE and part of the LPM, giving rise to endodermal and mesodermal lungs, respectively, we speculated that the Foxa2-lineage could serve as BFL that generates the entire lungs after the donor cell injection into the vacant Foxa2-lineage niche. To explore this possibility, we performed CBC using Foxa2-driven Fgfr2 conditional knockout mice (*Foxa2$^{Cre/+}$; Fgfr2$^{flox/flox,}$* hereafter, *Foxa2$^{Cre/+}$; Fgfr2^{cnull}*). Since Fgfr2-mediated mitotic signaling is required for both lung epithelium and mesenchyme and Fgf10 or Fgfr2 systemic knockout mice showed lung agenesis phenotype[39–42], we expected to generate the vacant niche both in lung epithelium and mesenchyme using *Foxa2$^{Cre/+}$; Fgfr2^{cnull}* mice. Indeed, it showed a lung agenesis phenotype (**Extended Data Fig. 7**). However, we did not observe agenesis phenotype in other major internal organs related to the Fgfr2 systemic knockout phenotype (**Extended Data Fig. 8**) [39–42]. To examine whether donor cells would complement the lung agenesis phenotype, we generated nGFP$^+$iPSCs from Rosa$^{nT\text{-}nG}$ mice (hereafter, nGFP$^+$iPSCs) via Sendai virus-mediated reprogramming[26] (**Extended Data Fig. 9**). We injected nGFP$^+$iPSCs into mouse blastocysts (**Fig. 4a**) and analyzed the chimerism at E17.5 by flow cytometry. Notably, donor nGFP$^+$iPSCs generated entire lungs in *Foxa2$^{Cre/+}$; Fgfr2^{cnull}* mice, while its general chimerism on the skin varied (**Fig. 4b, Extended Data Fig. 11**). Significantly, nearly entire lung epithelial, mesenchymal, and endothelial cells were composed only of nGFP$^+$iPSCs at E17.5. In contrast, wild-type, Shh-driven hetero, or knockout mice showed around 50~70% chimerism in lung mesenchyme and endothelium but never constantly reached 100% (**Fig. 4c, d, Extended Data Fig. 10**). These results implicate that the generation of genetically defective niches in the Foxa2-lineage-labeled mesendoderm and its descendants are critical for outcompeting donor iPSCs against the host lung precursor niches (**Fig. 2b**). We reasoned that Shh-lineage was insufficient for generating the lungs because Shh-lineage covers putative DE lineage (**Extended Data Fig. 12**) but not Pdgfrα$^+$ mesendoderm, the origin of the entire lung mesoderm including endothelium (**Fig. 1a**). Single-cell RNA-seq (scRNA-seq)-based embryonic lineage analyses[43] supported this idea (**Extended Data Fig. 13-16**). A part of Pdgfrα$^+$ mesendoderm expresses *Etv2, a specifier of* the endothelium, in the NM, most likely the lung endothelium origin, consistent with our Pdgfrα-lineage tracing analyses (**Fig. 1a**, **Extended Data Fig. 1a, b, 13-16**).

Together, we defined that Foxa2-lineage, but not Shh-lineage, can serve as a BFL for the lungs. To be the lung BFL, generating a low percentage (20%~ at E14.5) of vacancy in the mesenchymal lung niche when complete vacant in the endodermal lung was enough for the entire lung generation. The Foxa2-lineage served as a mighty, potent lung BFL lineage sufficient for generating the entire lungs composed of lung epithelium, mesenchyme, including endothelium.

Our strategy is promising for the future human whole lung generation in mice and large animals via a BFL-based CBC approach.

Methods

Mouse. *Shh*$^{Cre/+}$ mice (cat. 05622), *Rosa26*$^{tdTomato/\,tdTomato}$ mice (cat. 07914), Rosa26$^{nT\text{-}nG/nT\text{-}nG}$ mice (cat. 023035) and *Pdgfrα*$^{CreERT2/+}$ mice (cat. 032770) were obtained from the Jackson Lab. X. Zhang kindly gifted *Fgfr2*$^{flox/flox}$ mice. We further backcrossed these mice for over three generations with CD-1 mice (cat. 022) from the Charles River. Dr. Nicole C Dubois kindly provided *Foxa2*$^{Cre/Cre}$ mice. For conditional deletion of *Fgfr2* (*Fgfr2*^{cnull}), we crossed *Fgfr2*$^{flox/flox}$*; Rosa26*$^{tdTomato/tdTomato}$ females with *Foxa2*$^{Cre/Cre}$*; Fgfr2*$^{flox/+}$, *Foxa2*$^{Cre/+}$*; Fgfr2*$^{flox/+}$ or *Shh*$^{Cre/+}$*; Fgfr2*$^{flox/+}$ males, respectively. PCR performed genotyping of the *Shh-Cre*, *Pdgfr α-CreERT2*, *Rosa26-nTnG,* and *Rosa26-tdTomato* alleles according to the protocol provided by the vendor. For the CBC, genotyping of chimeric animals was confirmed by GFP-negative sorted liver cells and lung cells. For detecting the *Fgfr2* floxed allele, we performed PCR using the primer sets: FR2-F1, 5′-ATAGGAGCAACAGGCGG-3′, and FR2-F2, 5′-CAAGAGGCGACCAGTCA-3′[16]. For lineage tracing with Pdgfrα$^{CreERT2/+}$; Rosa26$^{tdTomato/+}$ mice, 1 dose of 200 μg tamoxifen (MedChem Express, HY-13757A) per g of body weight was given via oral gavage injection. All animal experiments were approved by Columbia University Institutional Animal Care and Use Committee in accordance with US National Institutes of Health guidelines.

Culture of mouse iPSC. We cultured iPSC in a2i/VPA/LIF medium on a feeder, as previously reported[16]. These PSC cells were passaged at a split ratio of 1:10 every 2–3 d.

Culture of human iPSCs (hiPSCs). All iPSC lines were maintained in feeder-free conditions on laminin iMatrix-511 silk E8 (Amsbio, AMS.892021) in StemFit 04 complete Medium (Amsbio, SFB-504), supplemented with Primocin (Invivogen, ant-pm-1), and passaged with TrypLE Select (Gibco, A1285901). All human iPSC lines used were characterized for pluripotency and were found to be karyotypically normal. The BU3NGST cell line was kindly gifted by Dr. Finn Hawkins and Dr. Darrell Kotton at Boston University, Boston, MA. Dr. Jennifer Davis at the University of Washington School of Medicine, Seattle, WA, kindly gifted the Rainbow cell line. PD2 and TD1 hiPSC were generated from deidentified commercially available human peripheral blood mononuclear cell and tracheal epithelial cell lines via the manufacturing protocol of Sendai virus-mediated reprogramming (CytoTune2.0) (ThermoFisher, A16517). Every other month all iPSC lines screened negative for mycoplasma contamination using MycoAlert PLUS detection kit (Lonza, LT07-710).

Differentiation of hiPSCs into lung epithelial and mesenchymal cells. The directed differentiation protocols were modified from previous protocols to maximize lung mesenchymal cell generation concomitantly with NKX2-1^{+} lung epithelium. Briefly, DE and LPM precursors were induced once seeded hiPSC-formed colonies by the Activin induction using the STEMdiff Definitive Endoderm Kit (StemCell Technologies, 05110) for 72 hours. Differentiated cells were dissociated and passaged in Laminin511-coated tissue culture plates in a complete serum-free differentiation medium (cSFDM)[36]. To induce DE and LPM into the anterior foregut endoderm and mesoderm, the cSFDM was supplemented with 10μM SB431542 (MedChem Express, HY-10431) and 2μM Dorsomorphin (Tocris, 3093) for 48 hours and 10μM SB431542 and 2μM IWP2 (Tocris, 3533) for 24 hours. Cells were then cultured for 7-10 additional days in cSFDM containing

3μM CHIR99021, 10ng/ml recombinant human FGF10 (R&D Systems, 345-FG), 10ng/ml recombinant human KGF (R&D Systems, 251-KG), 10 ng/mL recombinant human BMP4 (R&D Systems, 314-BP), and 50nM retinoid acid (Sigma-Aldrich, R2625) to induce NKX2-1 positive lung epithelial cells and $WNT2^{+}TBX4^{+}$ lung mesenchymal cells.

Immunofluorescence (IF). Before the immunostaining, antigen retrieval was performed using Unmasking Solution (Vector Laboratories, H-3300) for 10 min at around 100 °C by microwave. 7-μm tissue sections were incubated with primary antibodies (Supplementary Table 1) in the buffer of M.O.M. kit (Vector Laboratories, MKB-2213-1) overnight at 4 °C, washed in PBS, and incubated with secondary antibodies conjugated with Alexa488, 567, or 647 (ThermoScientific, 1:400) with NucBlue Fixed Cell Ready Probes Reagent (Hoechst) (ThermoScientific, R37605) for 1.5 h, and mounted with ProLong Gold antifade reagent (Invitrogen, P36930). The images were captured by a Zeiss confocal 710 microscopy.

Immunocytochemistry. Cells on culture dishes were fixed with 4% Paraformaldehyde (PFA) for 30 min at room temperature (RT), permeabilized, and blocked with staining buffer containing 0.025% Triton X-100 and 1% BSA for 1 hour at RT. Primary antibodies (Supplementary Table 1) were incubated overnight at 4 °C in the staining buffer. After three washes in PBS, secondary antibodies (Supplementary Table 1) and NucBlue Fixed Cell Ready Probes Reagent (Hoechst) were incubated for 1 h. The samples were imaged using DMi8 Leica widefield microscope.

Flow cytometry (FCM) analyses of mouse lung tissue. Lungs from lineage tracing mice at E14.5, E18.5, P0, and four weeks were harvested and prepared for the FCM, as previously described[16]. Briefly, tissues were minced with microscissors, and 1 ml of pre-warmed dissociation buffer (1 mg/ml Dnase (Sigma, DN25), 5 mg/ml collagen (Roche, 10103578001), and 15 U/ml Dispase II (Stemcell Technologies, 7913) in HBSS), incubated at 37 °C on the rocker with 50 r.p.m. speed, and neutralized with the dissociation buffer by FACS buffer containing 2% FBS, Glutamax, 2mM EDTA and 10mM HEPES in HBSS after the 30 min incubation. Digested cells were filtered by the. After filtrating the cells with 40-μm filter (FALCON, 352235), cell pellets were resuspended with 1 ml of cold RBC lysis buffer (Biolegend, 420301) to lyse the remaining erythrocytes for 5 min on ice, and neutralized by 1 ml cold FACS buffer. After that, it was centrifuged them at 350 rcf, 4 °C, for 3 min to remove the lysed blood cells. For FCM analysis, one million cells were transferred in 100 μl of FACS buffer supplemented with 0.5μM Y27632 and then added 2 μl Fc Block (BD Pharmingen, 553141) per sample followed by 10 min incubation on ice. Cells were incubated with the following antibodies: CD31-APC (Biolegend, 102510, 1/50), Epcam-BV711 (BioLegend, 118233, 1/50) or Epcam-BV421 (Biolegend, 118225, 1/50), Aqua Zombie (BioLegend, 423101, 1/100), CD45-BV605 (BioLegend, 103104, 1/50) for 30 min on ice. After staining, cells were washed twice with FACS buffer before resuspending in 500 μl FACS buffer for the subsequent analyses using SONY MA900 or NovoCyte.

$nGFP^{+}$iPSC establishment and preparation for CBC donor.
E14.5 lung tissues of *Rosa26*$^{nTnG/nTnG}$ mice (JAX, cat. 023035, C57BL/6NJ background) were harvested in a dissociation buffer described above. The dissociated cells were seeded on a 10cm dish, and only lung fibroblast survived after 1 week in MEF medium[16]. The fibroblasts were passaged using Accutase (Innovative Cell Technologies, AT104), and seeded on gelatin (Millipore-Sigma, ES006B)-coated 6 well plates with a density of 0.1 million cells per well. Upon

cell attachment, Yamanaka reprogramming factors were induced to iPSCs via Sendai virus using CytoTune2.0 (ThermoFisher, A16517). To establish $nGFP^+$ iPSCs, the Cre plasmid was transfected using Fugene HD transfection reagent (Promega, E2311), then sorted out $GFP^+tdTomato^-$ live cells by FACS (SONYMA900), and single clones were expanded.

For the CBC donor cell preparation, $nGFP^+$iPSCs cultured in a2i/VPA/LIF[16] were trypsinized and resuspended in 4 ml cold DMEM + 10% FBS immediately and filtering the cells with a 40-μm filter. Cells were centrifuged at 350 rcf, 4 °C, for 3 min, and the supernatant was removed. After being washed by flow buffer containing 0.2% BSA, 1% Glutamax, and 1μM Y27632, the cells were resuspended in 100μl/1 million cells with flow buffer, then the following antibodies were added: Epcam-BV421 (1:50), SSEA1-PE (1:50), CD31-APC (1:50), Zombie Aqua Fixable Viability Kit (1:100). $Epcam^{high}SSEA1^{high}CD31^{high}$ cells were sorted by FACS (SONYMA900) and subsequently prepared for the injection.

Blastocyst preparation and embryo transfer. Blastocysts were prepared by mating *Foxa2*$^{Cre/Cre}$*; Fgfr2*$^{flox/+}$, *Foxa2*$^{Cre/+}$*; Fgfr2*$^{flox/+}$ or *Shh*$^{Cre/+}$*; Fgfr2*$^{flox/+}$ males (all 129 x B6 x CD-1 background) with superovulated $Fgfr2^{flox/flox}$; $Rosa26^{tdTomato/tdTomato}$ females (129 x B6 x CD-1 background). Blastocysts were harvested at E3.5 after superovulation[16]. 20 sorted $nGFP^+$iPSCs were injected into each blastocyst. After the iPSC injection, blastocysts were cultured in an M2 medium (Cosmobio) for a few hours in a 37 °C, 5% CO2 incubator for recovery. Then, blastocysts were transferred to the uterus of the pseudopregnant foster mother.

Real-time-quantitative RT-PCR (qRT-PCR). Total RNA was extracted using a Direct-zol™ RNA MiniPrep Plus kit (Zymo Research, R2072), and cDNA was synthesized using Primescript™ RT Master Mix (Takara, RR036B). The cDNAs were then used as templates for qRT-PCR analysis with gene-specific primers. Reactions (10 μl) were performed Luna® Universal qPCR Master Mix (New England Biolabs, M3003X). mRNA abundance for each gene was determined relative to GAPDH mRNA using the $2^{-\Delta\Delta Ct}$ method. The primers were listed in the Supplemental Table. 2. Data were represented as mean ± SD. Of measurements. The number of animals or cells per group is provided in the legends. The undetected values in each biological experiment in Fig.3d were removed from the graphs.

Statistical analysis. Data analysis was performed using Prism 8. Data acquired by performing biological replicas of two or three independent experiments are presented as the mean ± SD. Statistical significance was determined using a two-tailed t-test and unpaired one-way or two-way ANOVA with the Tukey post hoc test. $*P < 0.05$, $**P < 0.01$, $***P < 0.001$, ns: non-significant.

Data availability. The authors declare that all data supporting the results of this study are available within the paper and the Supplementary Information. Raw data are available from the corresponding author upon reasonable request.

Author contributions

A.M. and M.M. designed all experiments; Z.N. and A.M. maintained mutant mice for the injection; C.S.L. performed blastocyst injection and embryo transfer; J.T., A.S., Y.S., Y.H., H.S., supported lineage-tracing, chimera analyses, and genotyping; H.S., D.S., and S. T. helped to generate mouse and human iPSCs, J.S. and F.H. kept human iPSC-directed differentiation, N.D. provided

Foxa2$^{Cre/+}$ mice, A.M. and M.M. wrote the paper; Y.H., H.S., J.W., J.Q., and F.H. gave crucial insights on the experiments and the manuscripts. There is no competing financial interest.

Acknowledgments
We thank Zurab Ninish for his technical assistance. We sincerely appreciate the generous support from Dr. Hiromitsu Nakauchi at Stanford University and the considerate support and scientific input from Dr. Wellington Cardoso at the Columbia Center for Human Development (CCHD) and the members of Cardoso's lab and CCHD. We acknowledge the support from the CCHD Medicine Microscopy core (MMC), Columbia Stem Cell Initiative (CSCI) Flow Cytometry core (SONY MA900), and Genetically Modified Mouse Model Shared Resource (GMMMSR) for blastocyst injection. This work was funded by NIH-NHLBI 1R01 HL148223-01, DoD PR190557, PR191133 to M. M., JSPS202080340, The Uehara Memorial Foundation to A. M.

Competing interests
The authors declare no competing interests.

References
1. Wang, X. Bioartificial Organ Manufacturing Technologies. *Cell Transplant.* **28**, 5–17 (2019).
2. Ott, H. C. *et al.* Regeneration and orthotopic transplantation of a bioartificial lung. *Nat. Med.* **16**, 927–33 (2010).
3. Petersen, T. H. *et al.* Tissue-engineered lungs for in vivo implantation. *Science (80-.).* **329**, 538–541 (2010).
4. Hackett, T. L., Knight, D. a & Sin, D. D. Potential role of stem cells in management of COPD. *Int. J. Chron. Obstruct. Pulmon. Dis.* **5**, 81–8 (2010).
5. Kotton, D. N. & Morrisey, E. E. Lung regeneration: Mechanisms, applications and emerging stem cell populations. *Nat. Med.* **20**, 822–832 (2014).
6. Tian, L. *et al.* Human pluripotent stem cell-derived lung organoids: Potential applications in development and disease modeling. *Wiley Interdiscip. Rev. Dev. Biol.* **10**, 1–16 (2021).
7. Guyette, J. P. *et al.* Perfusion decellularization of whole organs. *Nat. Protoc.* **9**, 1451–68 (2014).
8. Travaglini, K. J. *et al.* A molecular cell atlas of the human lung from single-cell RNA sequencing. *Nature* **587**, 619–625 (2020).
9. Crapo, J. D., Barry, B. E., Gehr, P., Bachofen, M. & Weibel, E. R. Cell number and cell characteristics of the normal human lung. *Am. Rev. Respir. Dis.* **126**, 332–337 (1982).
10. Stone, K. C., Mercer, R. R., Gehr, P., Stockstill, B. & Crapo, J. D. Allometric Relationships of Cell Numbers and Size in the Mammalian Lung. *Am. J. Respir. Cell Mol. BioI.* **6**, 235–243 (1992).
11. Chen, J., Lansford, R., Stewart, V., Young, F. & Alt, F. W. RAG-2-deficient blastocyst complementation: an assay of gene function in lymphocyte development. *Proc. Natl. Acad. Sci.* **90**, 4528–4532 (1993).
12. Usui, J. *et al.* Generation of kidney from pluripotent stem cells via blastocyst complementation. *Am. J. Pathol.* **180**, 2417–26 (2012).
13. Yamaguchi, T. *et al.* Interspecies organogenesis generates autologous functional islets. *Nature* **542**, 191–196 (2017).

14. Hamanaka, S. *et al.* Generation of Vascular Endothelial Cells and Hematopoietic Cells by Blastocyst Complementation. *Stem Cell Reports* **11**, 988–997 (2018).
15. Kobayashi, T. *et al.* Generation of rat pancreas in mouse by interspecific blastocyst injection of pluripotent stem cells. *Cell* **142**, 787–99 (2010).
16. Mori, M. *et al.* Generation of functional lungs via conditional blastocyst complementation using pluripotent stem cells. *Nat. Med.* **25**, 1691–1698 (2019).
17. Kitahara, A. *et al.* Generation of Lungs by Blastocyst Complementation in Apneumic Fgf10-Deficient Mice. *Cell Rep.* **31**, (2020).
18. Wen, B. *et al.* In vivo generation of lung and thyroid tissues from embryonic stem cells using blastocyst complementation. *Am. J. Respir. Crit. Care Med.* **203**, 471–483 (2021).
19. Harris, K. S., Zhang, Z., McManus, M. T., Harfe, B. D. & Sun, X. Dicer function is essential for lung epithelium morphogenesis. *Proc. Natl. Acad. Sci. U. S. A.* **103**, 2208–13 (2006).
20. Tada, S. *et al.* Characterization of mesendoderm: A diverging point of the definitive endoderm and mesoderm in embryonic stem cell differentiation culture. *Development* **132**, 4363–4374 (2005).
21. Hart, A. H. *et al.* Mixl1 is required for axial mesendoderm morphogenesis and patterning in the murine embryo. *Development* **129**, 3597–608 (2002).
22. Cardoso, W. V & Lü, J. Regulation of early lung morphogenesis: questions, facts and controversies. *Development* **133**, 1611–24 (2006).
23. Mori, M. & Cardoso, W. V. Chapter 1 - Lung Progenitor Cell Specification and Morphogenesis. in *The Lung: Development, Aging and the Environment* (ed. Pinkerton, R. H. E. B. T.-T. L. (Second E.) 3–9 (Academic Press, 2014). doi:http://dx.doi.org/10.1016/B978-0-12-799941-8.00001-8.
24. Peng, T. *et al.* Coordination of heart and lung co-development by a multipotent cardiopulmonary progenitor. *Nature* **500**, 589–592 (2013).
25. Green, M. D. *et al.* Generation of anterior foregut endoderm from human embryonic and induced pluripotent stem cells. *Nat. Biotechnol.* **29**, 267–72 (2011).
26. Huang, S. X. L. *et al.* Efficient generation of lung and airway epithelial cells from human pluripotent stem cells. *Nat. Biotechnol.* **32**, 84–91 (2014).
27. Scheibner, K. *et al.* Epithelial cell plasticity drives endoderm formation during gastrulation. *Nat. Cell Biol.* **23**, 692–703 (2021).
28. Kopper, O. & Benvenisty, N. Stepwise differentiation of human embryonic stem cells into early endoderm derivatives and their molecular characterization. *Stem Cell Res.* **8**, 335–345 (2012).
29. Artus, J., Panthier, J. J. & Hadjantonakis, A. K. A role for PDGF signaling in expansion of the extra-embryonic endoderm lineage of the mouse blastocyst. *Development* **137**, 3361–3372 (2010).
30. Wang, A. *et al.* Epigenetic priming of enhancers predicts developmental competence of hESC-derived endodermal lineage intermediates. *Cell Stem Cell* **16**, 386–399 (2015).
31. Burtscher, I. & Lickert, H. Foxa2 regulates polarity and epithelialization in the endoderm germ layer of the mouse embryo. *Development* **136**, 1029–1038 (2009).
32. Wan, H. *et al.* Foxa2 regulates alveolarization and goblet cell hyperplasia. *Development* **131**, 953–964 (2004).
33. Bardot, E. *et al.* Foxa2 identifies a cardiac progenitor population with ventricular differentiation potential. *Nat. Commun.* **8**, 1–15 (2017).

34. Horn, S. *et al.* Mind bomb 1 is required for pancreatic β-cell formation. *Proc. Natl. Acad. Sci. U. S. A.* **109**, 7356–7361 (2012).
35. Hawkins, F. *et al.* Prospective isolation of NKX2-1 – expressing human lung progenitors derived from pluripotent stem cells. *J. Clin. Invest.* **127**, 1–18 (2017).
36. Chen, Y.-W. *et al.* A three-dimensional model of human lung development and disease from pluripotent stem cells. *Nat. Cell Biol.* **19**, 542–549 (2017).
37. Gotoh, S. *et al.* Generation of alveolar epithelial spheroids via isolated progenitor cells from human pluripotent stem cells. *Stem Cell Reports* **3**, 394–403 (2014).
38. Konishi, S. *et al.* Directed Induction of Functional Multi-ciliated Cells in Proximal Airway Epithelial Spheroids from Human Pluripotent Stem Cells. *Stem Cell Reports* **6**, 18–25 (2016).
39. De Langhe, S. P., Carraro, G., Warburton, D., Hajihosseini, M. K. & Bellusci, S. Levels of mesenchymal FGFR2 signaling modulate smooth muscle progenitor cell commitment in the lung. *Dev. Biol.* **299**, 52–62 (2006).
40. De Moerlooze, L. *et al.* An important role for the IIIb isoform of fibroblast growth factor receptor 2 (FGFR2) in mesenchymal-epithelial signalling during mouse organogenesis. *Development* **127**, 483–92 (2000).
41. Arman, E., Haffner-Krausz, R., Gorivodsky, M. & Lonai, P. Fgfr2 is required for limb outgrowth and lung-branching morphogenesis. *Proc. Natl. Acad. Sci.* **96**, 11895–11899 (1999).
42. Sekine, K. *et al.* Fgf10 is essential for limb and lung formation. *Nat. Genet.* **21**, 138–41 (1999).
43. Pijuan-Sala, B. *et al.* A single-cell molecular map of mouse gastrulation and early organogenesis. *Nature* **566**, 490–495 (2019).

FIGURES

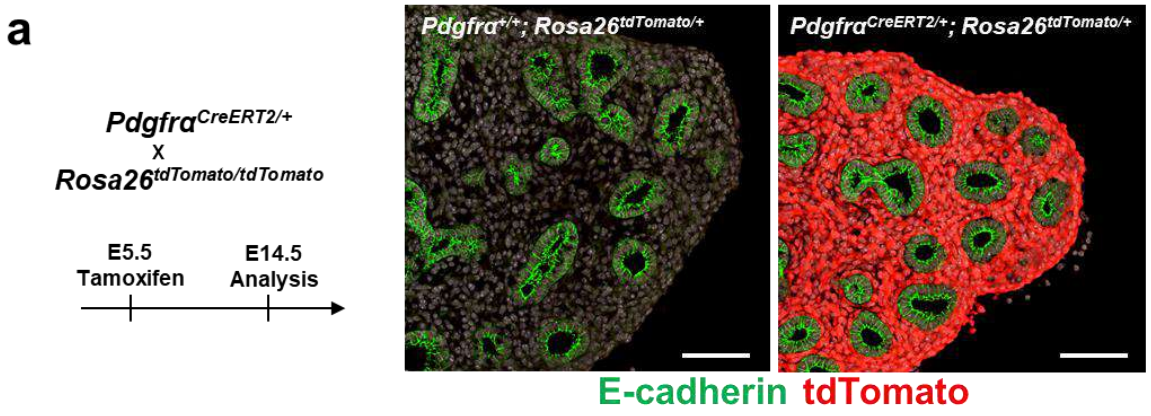
a
Pdgfra^CreERT2/+
x
Rosa26^tdTomato/tdTomato
E5.5
Tamoxifen
E14.5
Analysis
Pdgfra+/+; Rosa26tdTomato/+
PdgfraCreERT2/+; Rosa26tdTomato/+
E-cadherin tdTomato

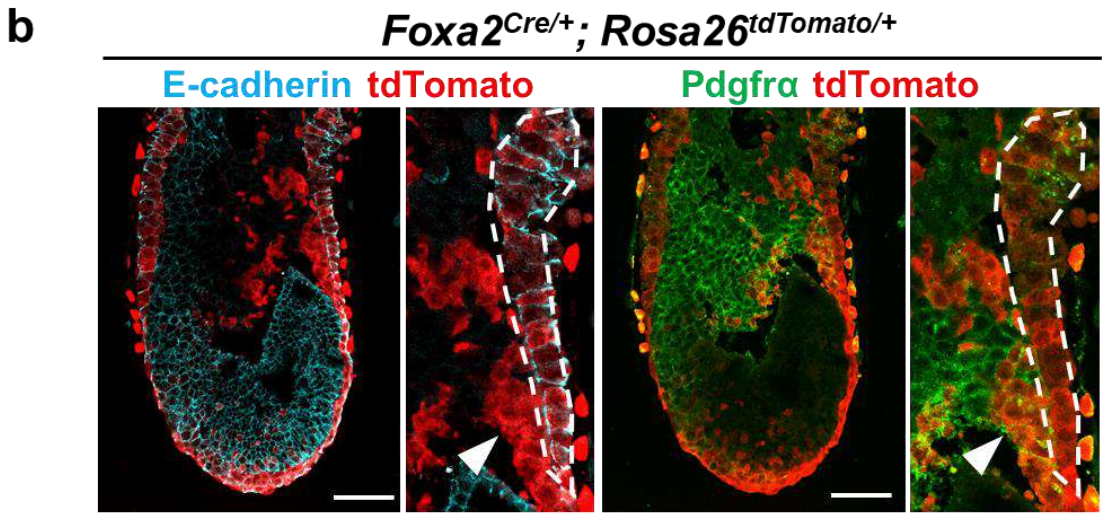
b
Foxa2Cre/+; Rosa26tdTomato/+
E-cadherin tdTomato
Pdgfrα tdTomato

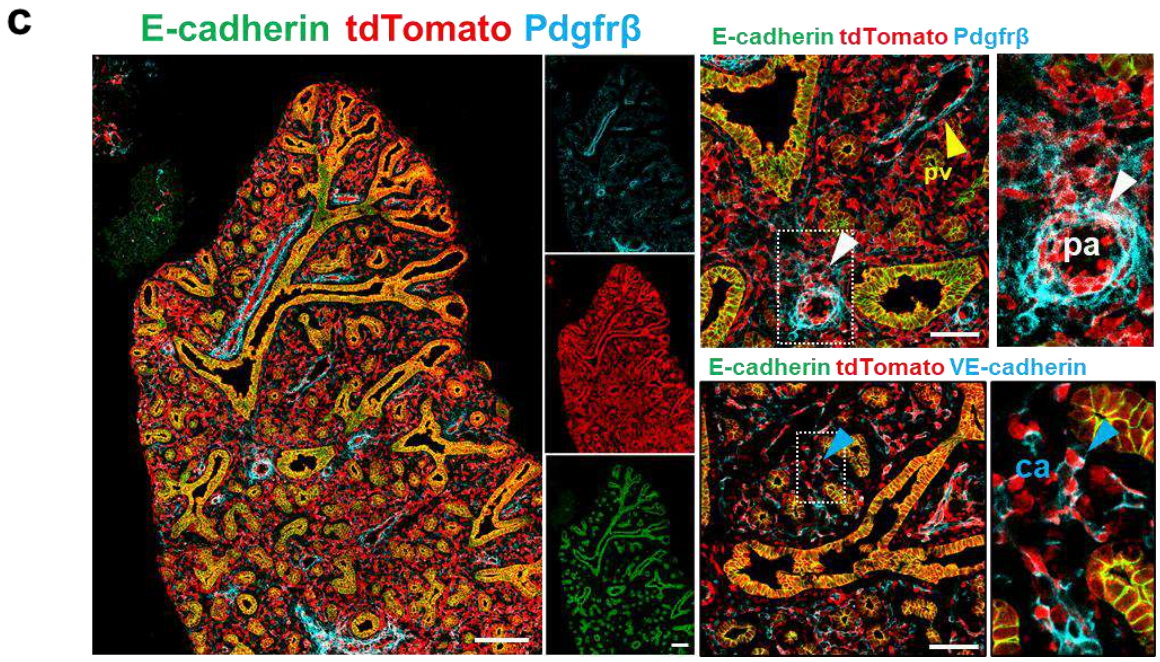
c
E-cadherin tdTomato Pdgfrβ
E-cadherin tdTomato Pdgfrβ
pv
pa
E-cadherin tdTomato VE-cadherin
ca

Figure 1. Mesendoderm-derived lineage labeled entire lung epithelium and most of the lung mesenchyme, including lung endothelium. (a) Left: Schematic diagram of Tamoxifen injection. Right: representative immunofluorescent staining analysis (IF) for *Pdgfrα*$^{CreERT2/+}$*; Rosa26*$^{tdTomato/+}$ mice. tdTomato labeled the whole lung mesenchyme. Cre^{-} littermate control (left panel) and *Pdgfrα*$^{CreERT2/+}$*; Rosa26*$^{tdTomato/+}$ (right panel) (*n = 3* per group). **(b)** Representative IF analyses of E6.5 *Foxa2*$^{Cre/+}$*; Rosa26*$^{tdTomato/+}$ mice: Foxa2-lineage labeled both E-cadherin^{+} primitive streak (dotted areas) and Pdgfrα^{+} nascent mesoderm (arrowheads) arising from primitive streak (*n = 3* per group). **(c)** Representative IF staining of E16.5 Foxa2-lineage tracing mouse lung. Foxa2-lineage occupied the entire lung epithelium and most of the Pdgfrβ^{+} or VE-cadherin^{+} mesenchyme. Foxa2-lineage also partially labeled VE-cadherin^{+} endothelial cells. Foxa2-lineage labeling to VE-cadherin^{+} capillary (ca) (enlarged box, blue arrowhead), the Pdgfrβ^{+} smooth muscle cells of the pulmonary artery (pa) (enlarged box, white arrowhead), and pulmonary vein (pv, yellow arrowhead). Scale bars: **a, b, c** (left and right) = 100μm, 50μm, 200μm, and 100μm, respectively.

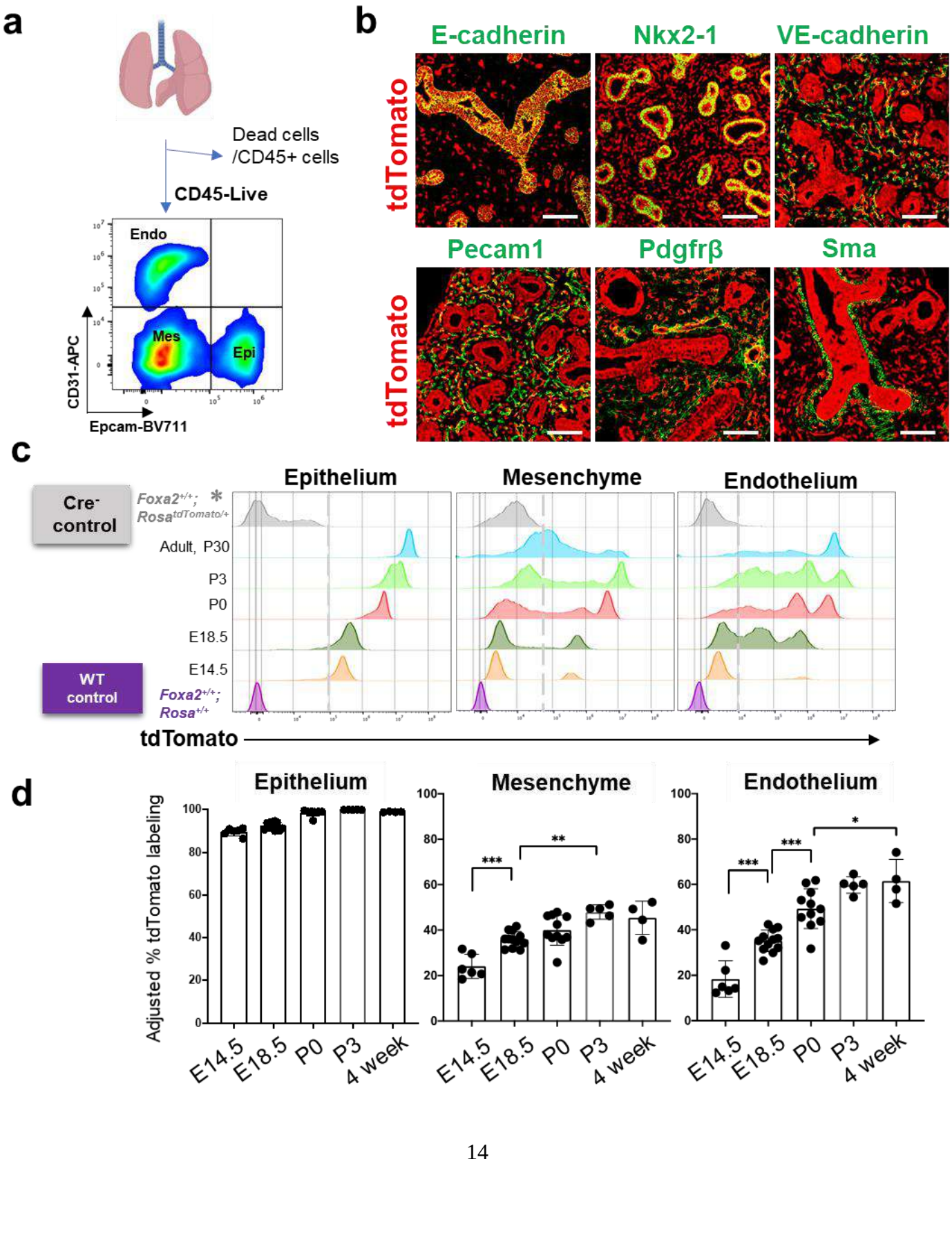
a
Dead cells
/CD45+ cells
CD45-Live
Endo
Mes
Epi
CD31-APC
Epcam-BV711
b
E-cadherin
Nkx2-1
VE-cadherin
tdTomato
Pecam1
Pdgfrβ
Sma
tdTomato
c
Epithelium
Mesenchyme
Endothelium
Cre- control
Foxa2+/+; Rosa tdTomato/+
Adult, P30
P3
P0
E18.5
E14.5
WT control
Foxa2+/+; Rosa+/+
tdTomato
d
Epithelium
Mesenchyme
Endothelium
Adjusted % tdTomato labeling
E14.5
E18.5
P0
P3
4 week

Figure 2. Foxa2-lineage gradually increased in the mesenchyme and endothelium during mouse lung development. (a) Flow cytometry (FCM) sorting strategy: $CD45^-$ live cells were selected, and subsequently, the proportion of Lung mesenchyme (mes), endothelium (endo), and epithelium (epi) were analyzed by the CD31 and Epcam staining signals. **(b)** Representative immunostainings of lung sections from E14.5 *Foxa2*$^{Cre/+}$*; Rosa*$^{tdTomato/+}$ embryos. tdTomato co-labeled entirely with lung epithelial markers (E-cadherin or Nkx2-1); but partially co-labeled with mesenchymal (Pdgfrβ and Sma), and endothelial (VE-cadherin, Pecam1) cell markers. (*n = 3* per group). Representative FCM histograms (**c**) and the graphs of FCM quantitative analyses (**d**) for $CD31^-Epcam^+$ lung epithelium, $CD31^-Epcam^-$ mesenchyme, and $CD31^+Epcam^-$ endothelium at E14.5, E18.5, P0, P3, and four weeks (n = 6, 12, 7, 5 and 4, independent biological replicates, respectively) of *Foxa2*$^{Cre/+}$*; Rosa*$^{tdTomato/+}$ lungs. The gradual increase of % $tdTomato^+$ lineage labeling in both lung mesenchyme and endothelium. The FCM gating threshold by Cre^- littermate control (grey asterisks and dotted grey lines). Statistical analysis: one-way ANOVA with the Tukey post hoc test.; differences considered statistically significant if $*P < 0.05$, $**P < 0.01$ $***P < 0.001$, ns: non-significant. Scale bars: **b** = 50μm.

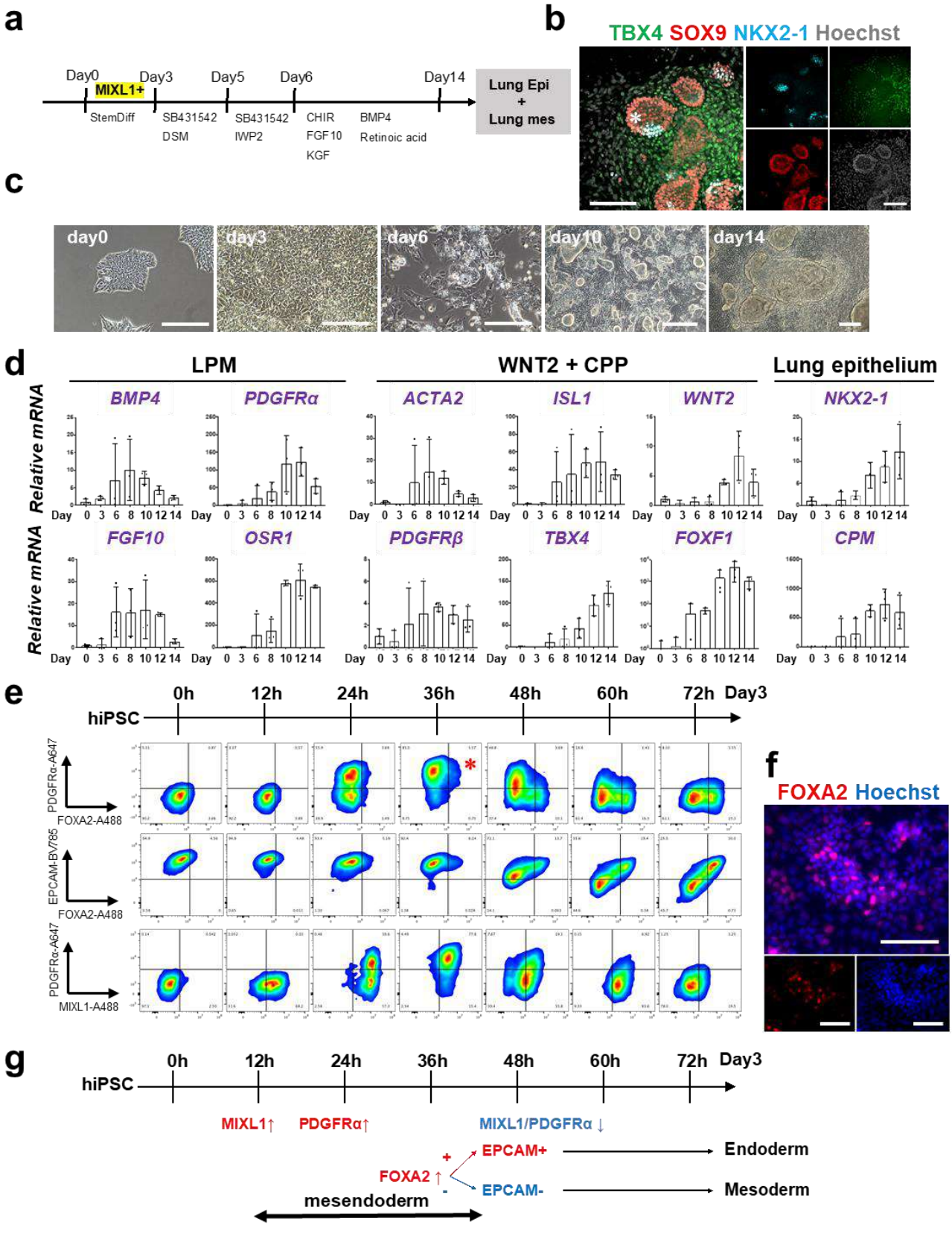
a
Day0
MIXL1+
StemDiff
Day3
SB431542
DSM
Day5
SB431542
IWP2
Day6
CHIR
FGF10
KGF
BMP4
Retinoic acid
Day14
Lung Epi
+
Lung mes
b
TBX4 SOX9 NKX2-1 Hoechst
c
day0
day3
day6
day10
day14
d
LPM
WNT2 + CPP
Lung epithelium
Relative mRNA
BMP4
PDGFRα
ACTA2
ISL1
WNT2
NKX2-1
FGF10
OSR1
PDGFRβ
TBX4
FOXF1
CPM
Day 0 3 6 8 10 12 14
e
hiPSC
0h
12h
24h
36h
48h
60h
72h
Day3
PDGFRα-A647
FOXA2-A488
EPCAM-BV785
MIXL1-A488
f
FOXA2 Hoechst
g
hiPSC
0h
12h
24h
36h
48h
60h
72h
Day3
MIXL1↑
PDGFRα↑
MIXL1/PDGFRα ↓
FOXA2 ↑
+
-
EPCAM+
EPCAM-
Endoderm
Mesoderm
mesendoderm

Figure 3. Co-development of endodermal and mesodermal lung progenitors derived from MXIL1$^+$ PDGFRα^+ FOXA2$^+$ mesendoderm in the directed differentiation protocol using hiPSC. (a) Culture protocol of hiPSC-derived endodermal and mesodermal lung progenitor cell co-differentiation. **(b)** Representative IF staining of differentiating hiPSCs after the 10 days culture. Lung epithelial (NKX2-1), distal lung bud epithelial (SOX9), and mesenchyme (TBX4) cell markers. The budding structures expressed SOX9 and partially NKX2-1 (asterisk), and monolayer cells expressed TBX4. Representative brightfield of directed differentiation time course **(c),** Representative FCM-based protein kinetic analyses during DE and LPM induction, and qRT-PCR analyses of lung mesenchyme and epithelium markers **(d)** in time course according to the protocol shown in **a**. Data normalized by undifferentiated hiPSCs. Graph: Each plot shows different biological experiments. Error bars represent mean ± SD. Representative FCM plot showed preceded MIXL1 expression compared to PDGFRα or FOXA2. FOXA2 appearance in the subset of the PDGFRα$^+$ population (red asterisk). ($n = 3$ independent experiments) **(f)** Representative IF staining of 36 hours-cultured hiPSCs. **(g)** Schematic summary of MIXL1, PDGFRα, EPCAM, and FOXA2 expression. Scale bars: **b, c, f** = 100μm, 200μm, 200μm respectively.

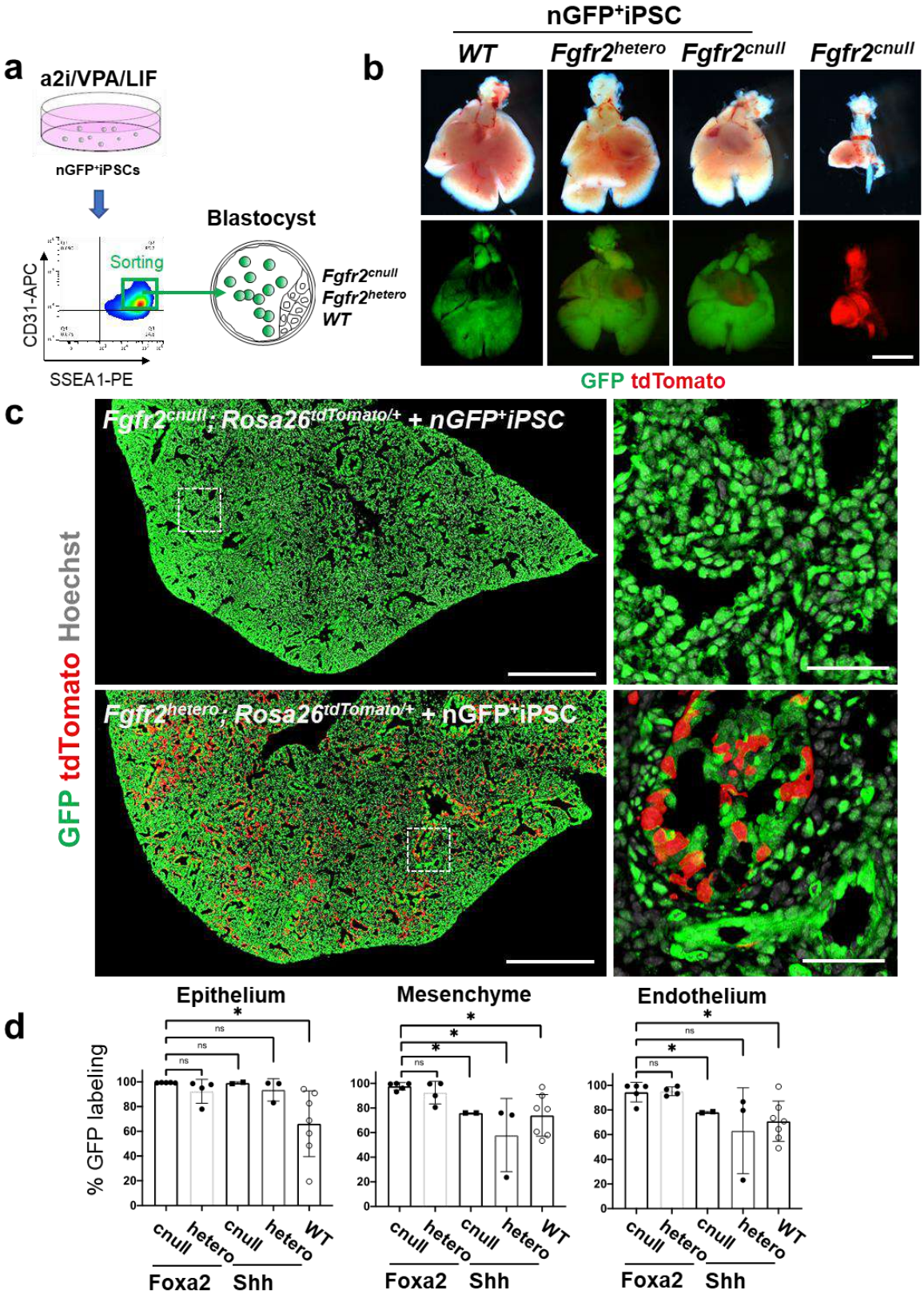
a
a2i/VPA/LIF
nGFP+iPSCs
Blastocyst
Sorting
CD31-APC
SSEA1-PE
Fgfr2cnull
Fgfr2hetero
WT
b
nGFP+iPSC
WT
Fgfr2hetero
Fgfr2cnull
Fgfr2cnull
GFP tdTomato
c
Fgfr2cnull; Rosa26tdTomato/+ + nGFP+iPSC
Fgfr2hetero; Rosa26tdTomato/+ + nGFP+iPSC
GFP tdTomato Hoechst
d
Epithelium
Mesenchyme
Endothelium
% GFP labeling
cnull
hetero
cnull
hetero
WT
Foxa2
Shh
ns
*

Figure 4. Generation of the entire lungs in *Foxa2*-driven *Fgfr2*-deficient mice via CBC. (a) Schema of CBC's experimental design: a2i/VPA/LIF-treated SSEA1^{high} CD31^{high} nGFP^{+}iPSCs were sorted and injected into WT, *Fgfr2^{hetero}* (heterozygous: *Foxa2$^{cre/+}$; Fgfr2$^{flox/+}$; Rosa26$^{tdTomato/+}$*), and *Fgfr2^{cnull}* (homozygous: *Foxa2$^{cre/+}$; Fgfr2$^{flox/flox}$; Rosa26$^{tdTomato/+}$*) blastocysts. **(b)** GFP, tdTomato, and bright field imaging of freshly isolated lungs from E17.5 chimeric *WT*, *Fgfr2^{hetero}*, and *Fgfr2^{cnull}*, in which nGFP^{+}iPSCs were used for CBC. The lung from a littermate *Fgfr2^{cnull}* mouse without iPSC injection is shown as a negative control. Lung agenesis phenotype (right panels) in the *Fgfr2^{cnull}* at E17.5 was completely rescued by injecting nGFP^{+}iPSCs (right middle panels). GFP and tdTomato indicating donor derived cells and host derived Foxa2-lineage cells. **(c)** Representative image of the confocal IF of E17.5 lungs of *Fgfr2^{cnull}* and *Fgfr2^{hetero}*. Compared with littermate control, *Fgfr2^{cnull}* lungs were entirely consisted of donor derived nGFP^{+} cells. **(d)** Graphs of FCM quantitative analyses for CD31^{-}Epcam^{+} lung epithelium, CD31^{-}Epcam^{-} mesenchyme, and CD31^{+}Epcam^{-} endothelium (see the gating strategy in **Fig. 2, Extended Data Fig. 3**). FCM analyses showed nearly 100% of chimerism among the lung epithelium, endothelium, and mesenchyme in *Foxa2$^{Cre/+}$; Fgfr2^{cnull}; Rosa$^{tdTomato/+}$*(*n=5,* independent biological replicates.). Conversely, various chimerism in each cell type in *Foxa2$^{Cre/+}$; Fgfr2^{hetero}; Rosa$^{tdTomato/+}$*(*n=4*). *Shh$^{Cre/+}$; Fgfr2^{cnull}; Rosa$^{tdTomato/+}$* (*n=2*), *Shh$^{Cre/+}$; Fgfr2^{hetero}; Rosa$^{tdTomato/+}$*(*n=3*), and *WT* (*n=7*). Each plot: a different biological animal. Shh-driven Fgfr2-deficient mouse[16] was also used as an experimental control side-by-side on the same round of iPSC injections. Scale bars: **b, c** (left and right) = 1mm, 500μm, 50μm respectively. Statistical analyses: unpaired Student's t-test, significance at $*P < 0.05$, ns: non-significant.

EXTENDED DATA FIGURES.

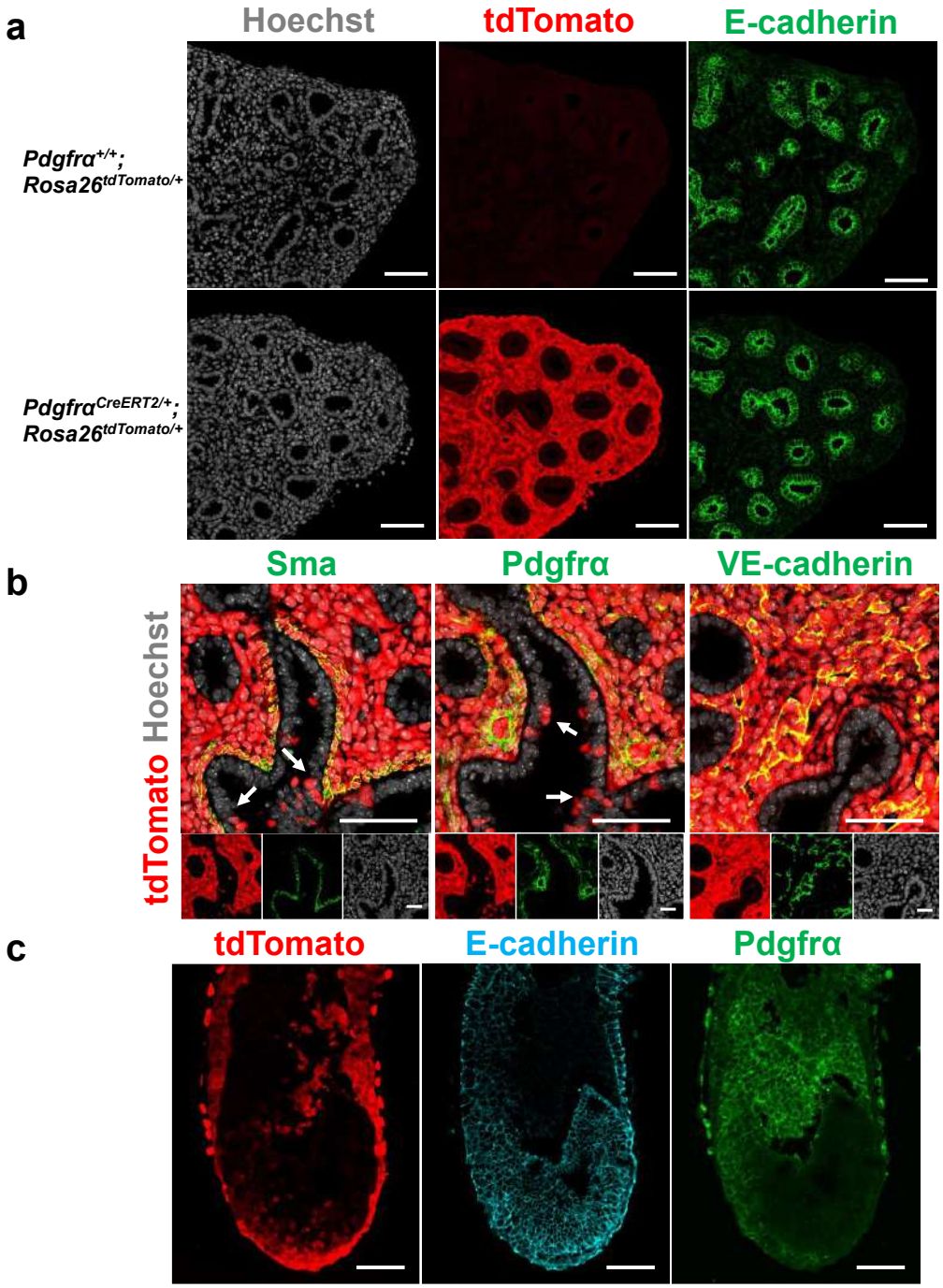

Extended data Fig. 1. Mesendodermal-derived Pdgfrα-lineage traced entire lung mesenchyme and partial lung epithelium (a) single channel images of confocal IF analyses from E14.5 Pdgfrα lineage tracing mouse lungs, shown in **Fig. 1a**. Pdgfrα-lineage labeled the entire pulmonary mesenchyme. **(b)** Representative IF staining of E14.5 *Pdgfrα*$^{CreERT2/+}$*; Rosa26*$^{tdTomato/+}$ lineage tracing mouse lungs. Pdgfrα-lineage at E5.5 during gastrulation labeled entire lung mesenchyme, including Sma^{+} airway mesenchyme, Pdgfrα^{+}mesenchyme, and VE-cadherin^{+} capillaries, and partial epithelial cells (white arrows). Scale bars: **a, b** = 100μm, 50μm, respectively.

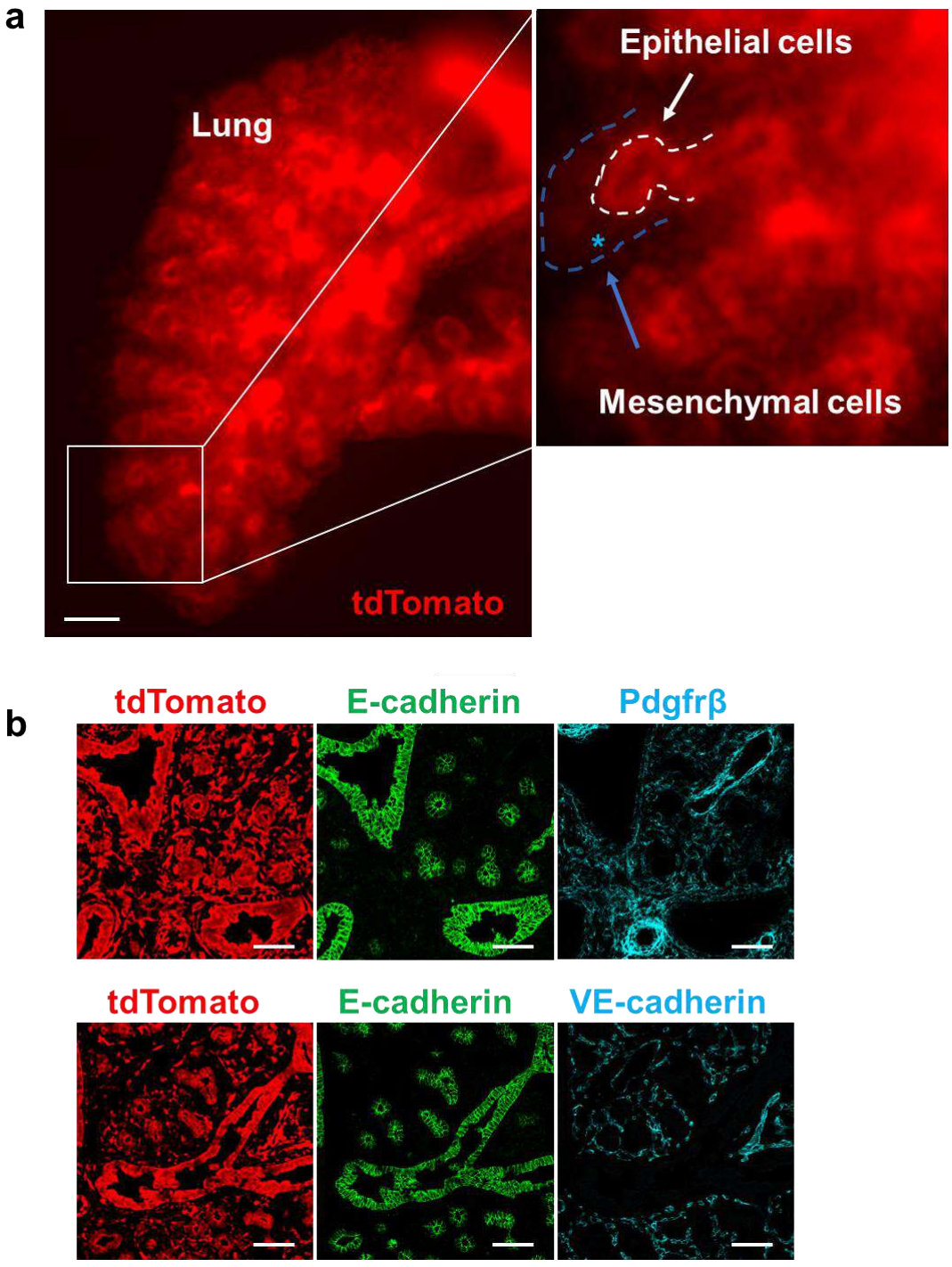

Extended data Fig. 2. Foxa2-lineage labeled entire lung epithelium and partial lung mesenchyme. (a) Whole mount tdTomato image of freshly isolated E14.5 Foxa2-lineage tracing lung taken by fluorescent dissection microscopy. tdTomato labeled the entire epithelium (White dotted line) and partially surround mesenchyme (Blue asterisk and dotted line). **(b)** single channel images of confocal IF analyses from E16.5 Foxa2-lineage tracing mouse lungs, shown in **Fig. 1c**. Scale bars: **a, b** = 200μm, and 100μm, respectively.

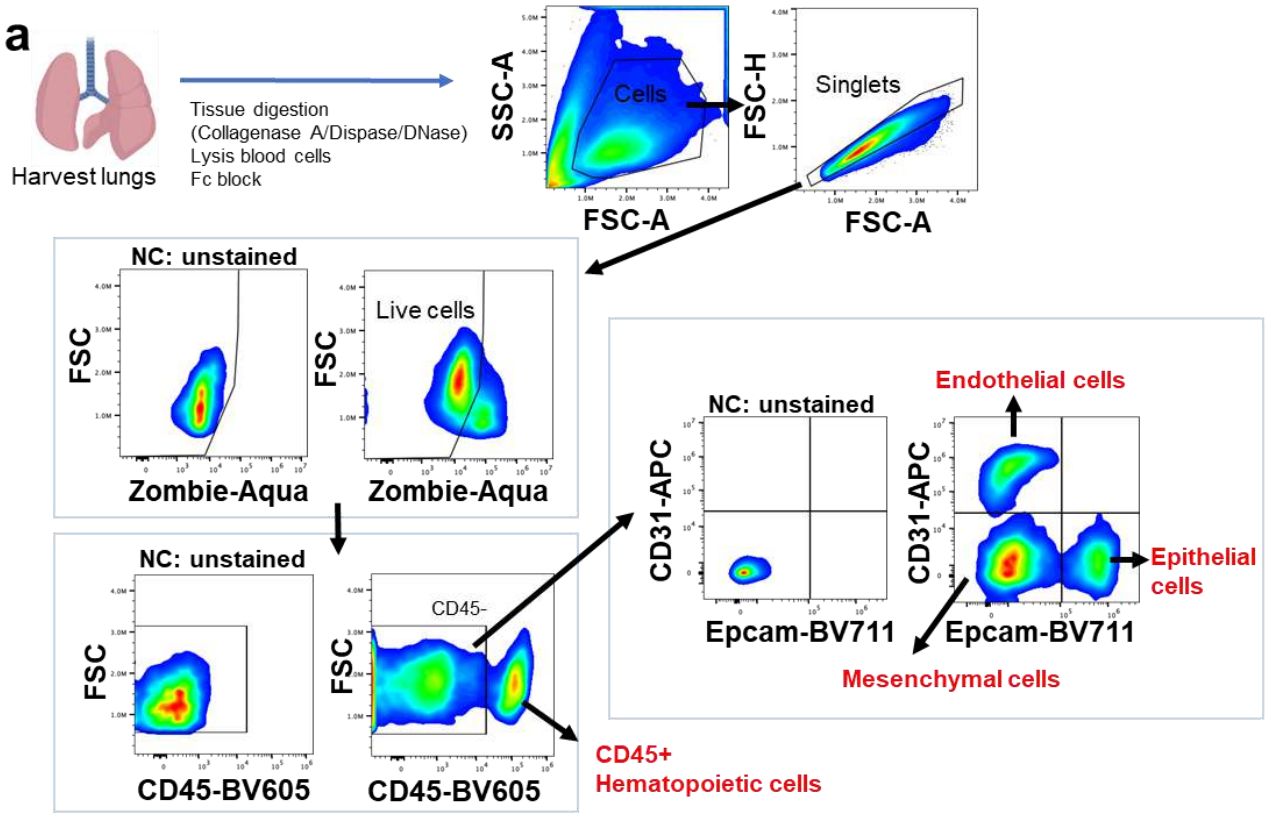
a
Harvest lungs
Tissue digestion
(Collagenase A/Dispase/DNase)
Lysis blood cells
Fc block
SSC-A
FSC-A
Cells
FSC-H
FSC-A
Singlets
NC: unstained
FSC
Zombie-Aqua
Live cells
FSC
Zombie-Aqua
NC: unstained
FSC
CD45-BV605
CD45-
FSC
CD45-BV605
CD45+
Hematopoietic cells
NC: unstained
CD31-APC
Epcam-BV711
Endothelial cells
CD31-APC
Epcam-BV711
Epithelial
cells
Mesenchymal cells

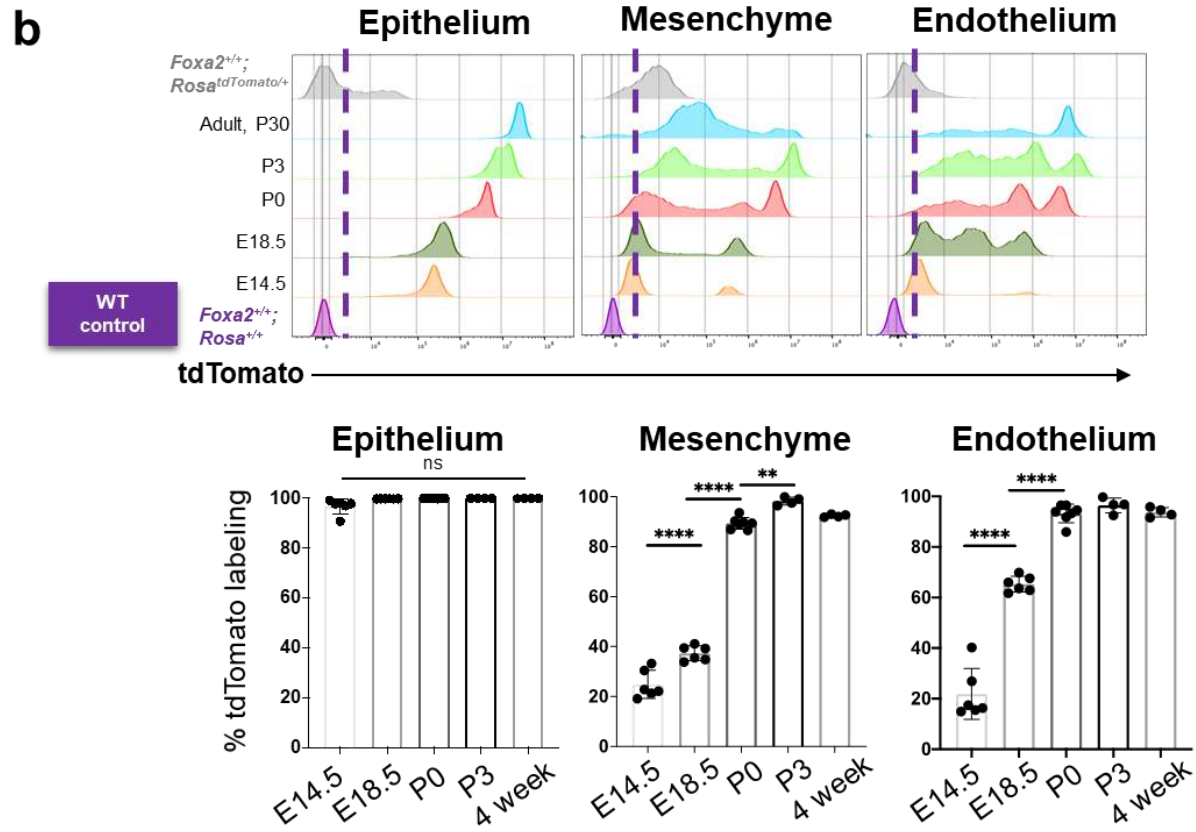
b
Epithelium
Mesenchyme
Endothelium
Foxa2+/+; RosatdTomato/+
Adult, P30
P3
P0
E18.5
E14.5
WT control
Foxa2+/+; Rosa+/+
tdTomato
Epithelium
Mesenchyme
Endothelium
% tdTomato labeling
ns
****
**
E14.5
E18.5
P0
P3
4 week

Extended data Fig. 3. FCM-based lineage tracing analyses. (a) Schematics of tissue isolation/dissociation and gating strategy for FCM analysis of different cell types in the lung. Lung cells (FSC/SCC panels) and singlets (FSC-H/FSC-A) were selected. Within the lung singlets, live cells were gated as an unstained negative control (NC) and hematopoietic ($CD45^+$ versus $CD45^-$). In the $CD45^-$ gate, we separated epithelial ($Epcam^+$), endothelial ($CD31^+$) and other non-endothelial lung mesenchymal cells (CD31/Epcam double negative). The percentage of $tdTomato^+$ cells was calculated based on the *Foxa2*$^{+/+}$*; Rosa*$^{+/+}$ *or Foxa2*$^{+/+}$*; Rosa*$^{tdTomato/+}$ control gate. **(b)** Top: representative histograms with the threshold of wild-type control (*Foxa2*$^{+/+}$*; Rosa*$^{+/+}$) (purple lines). Bottom: % of tdTomato in *Foxa2*$^{Cre/+}$*; Rosa*$^{tdTomato/+}$ at E14.5, E18.5, P0, P3, and four weeks (n = 6, 12, 7, 5 and 4, respectively) based on the *WT* control (*Foxa2*$^{+/+}$*; Rosa*$^{+/+}$). Foxa2-lineage covered nearly the entire lung mesenchyme, endothelium, and lung epithelium during the post-natal periods using *WT* control (*Foxa2*$^{+/+}$*; Rosa*$^{+/+}$). Statistical analysis: one-way ANOVA with the Tukey post hoc test.; differences considered statistically significant if $^{**}P < 0.01$ $^{****}P < 0.0001$, ns: non-significant.

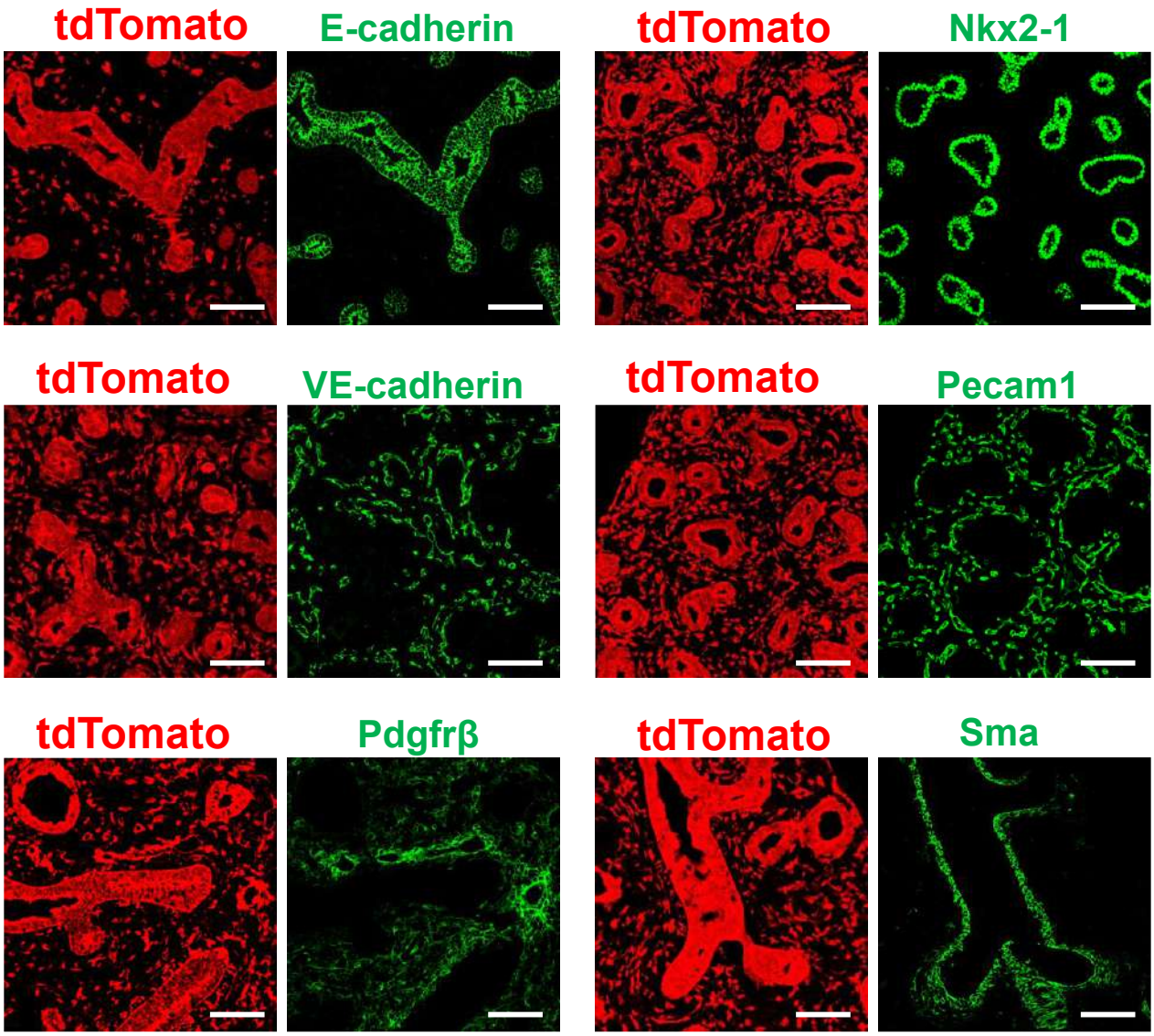

Extended data Fig. 4. Representative IF staining of E14.5 Foxa2-lineage tracing mouse lung. Foxa2-lineage labeled several types of mesenchyme. Scale bar = 50μm.

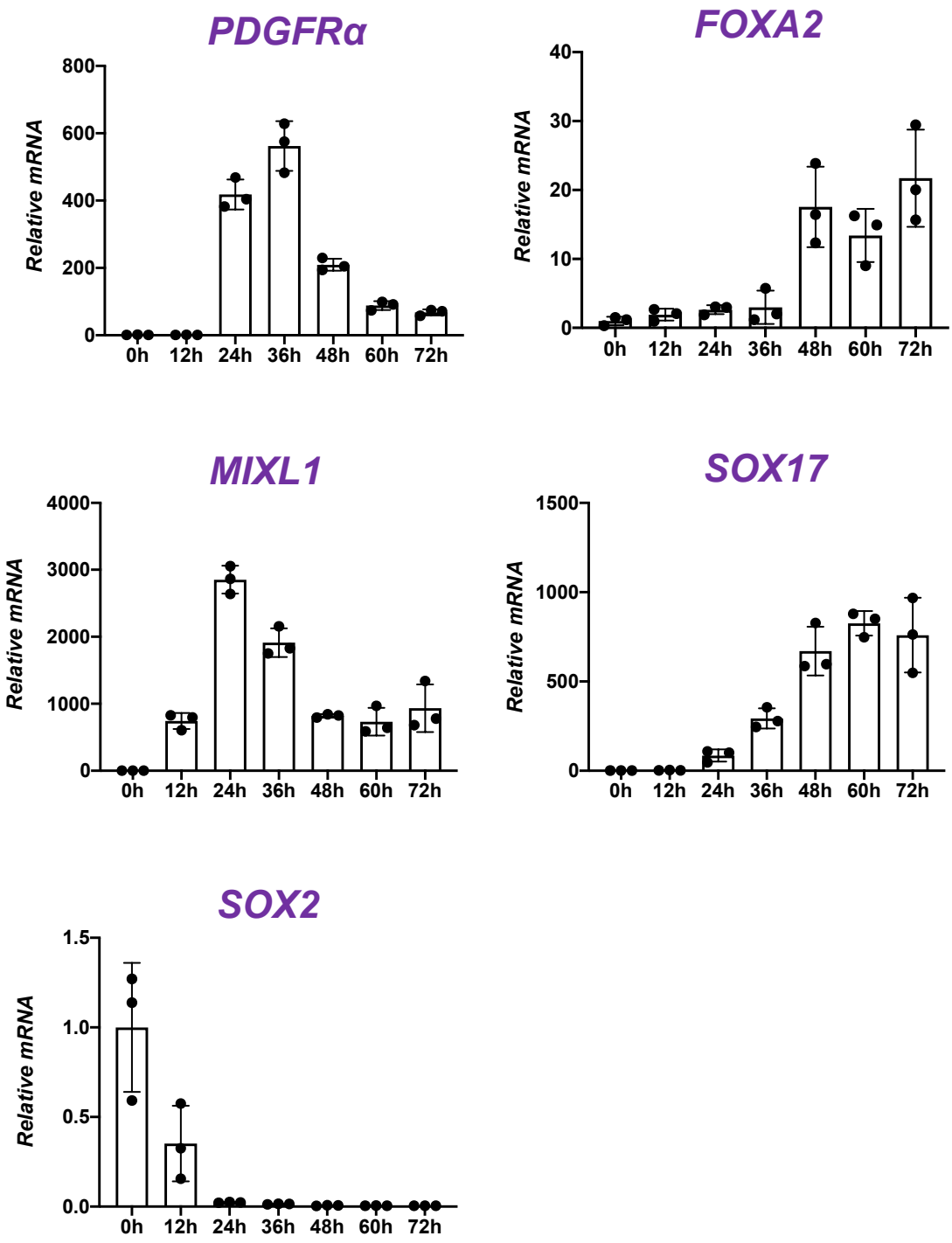

Extended data Fig. 5. mRNA kinetics of pluripotency and differentiation markers by the quantitative RT-PCR analyses during mesendoderm induction. The preceded *MIXL1* induction and subsequent expression of *PDGFRα*, and *FOXA2*. Conversely, drastic decrease of *SOX2*, a pluripotency marker after 12 hours. Data normalized by undifferentiated iPSCs. Each plot showed different biological experiment. Error bars represent mean ±SD.

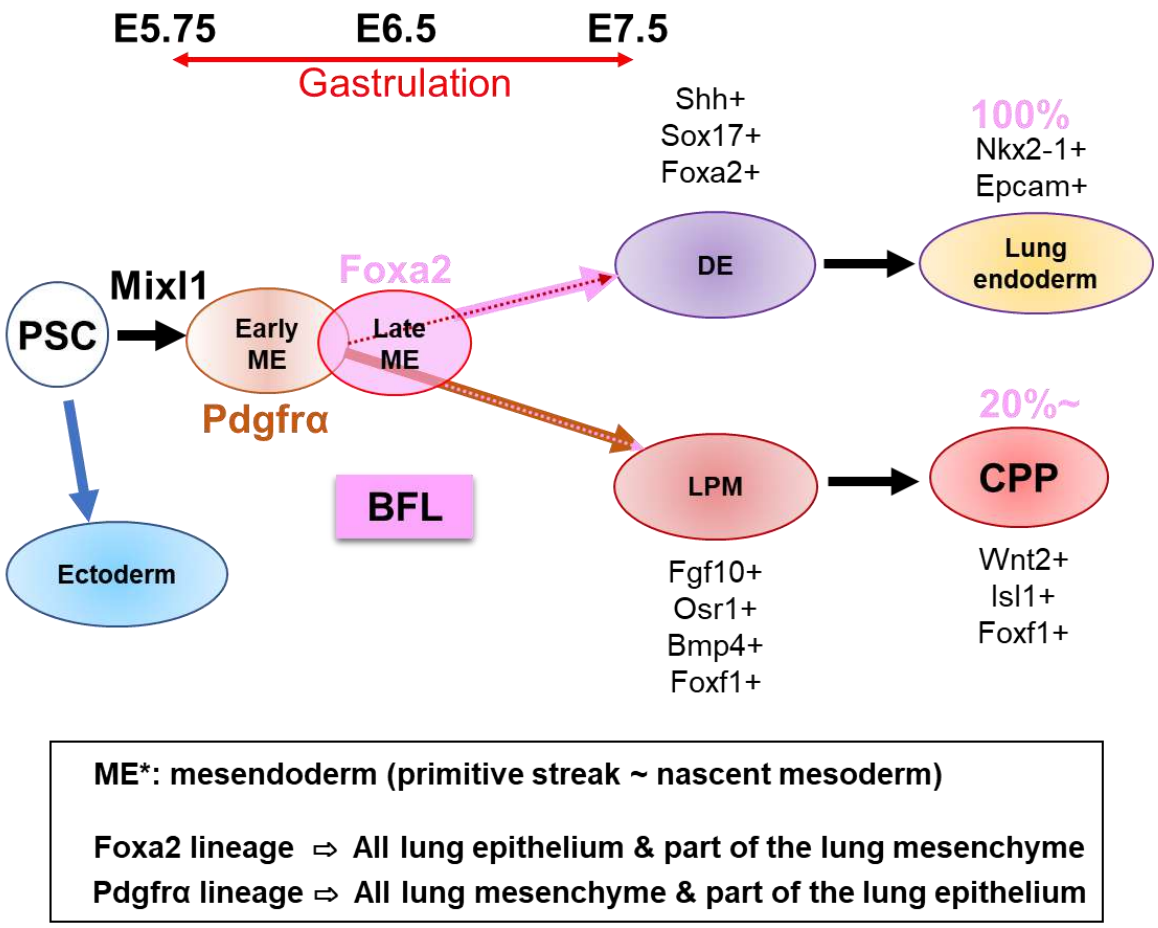

Extended data Fig. 6. Summary of the results and proposed model of lineage specification from pluripotent stem cells to endoderm or mesoderm through mesendoderm cells.
Pluripotent stem cell (PSC) differentiation will be initiated by the Mixl1^{+} induction and the subsequent temporal expression of an early mesendoderm (ME) marker, Pdgfrα. After that, the late mesendoderm marker marked by Foxa2 will turn on. Pdgfrα and Foxa2-lineage partially overlap at the primitive streak stage during gastrulation. Pdgfrα^{+} early ME lineage gives rise to the partial lung epithelial cells, most likely by the overlapping Foxa2^{+} lineage, and entire lung mesenchyme through lateral plate mesoderm (LPM) induction and cardiopulmonary lineage (CPP). On the other hand, the Foxa2-lineage gives rise to the entire lung epithelium and about 20% of CPP in early lung development at E12.5~E14.5. Strikingly, the whole lungs, including lung epithelium, mesenchyme, and endothelial cells, were produced solely by donor iPSCs via complementing the Foxa2-lineage's mitotic defective lung niches. It proves that a Foxa2-lineage works as a bona fide lung generative lineage (BFL), enough to generate entire lungs by donor iPSCs via CBC.

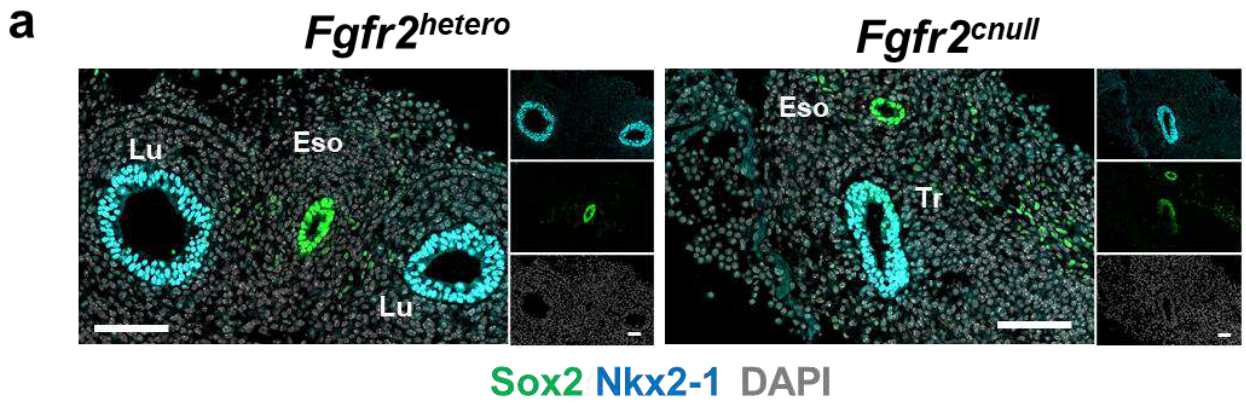
a
Fgfr2hetero
Fgfr2cnull
Lu
Eso
Lu
Eso
Tr
Sox2 Nkx2-1 DAPI

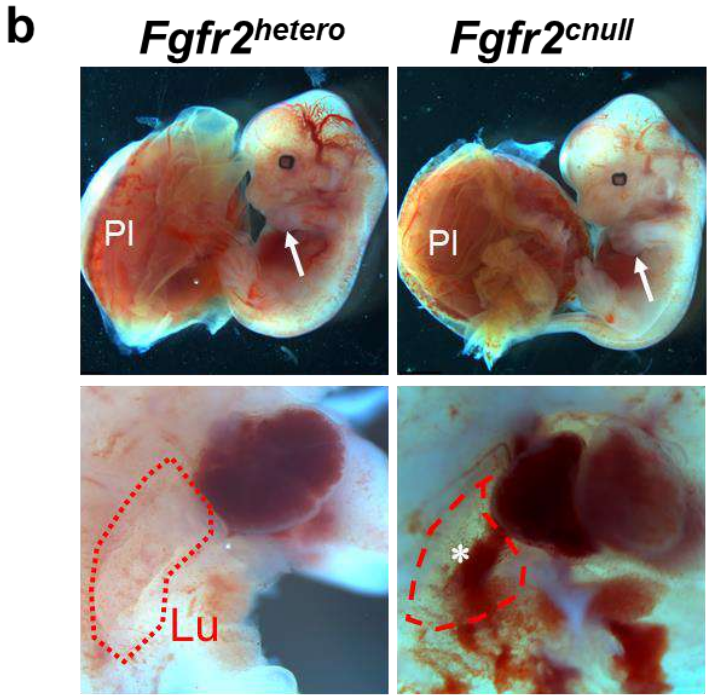
b
Fgfr2hetero
Fgfr2cnull
Pl
Pl
Lu
*

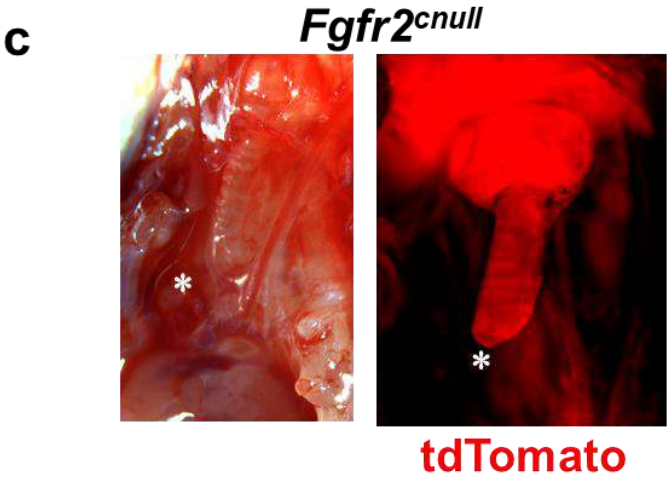
c
Fgfr2cnull
*
*
tdTomato

Extended data Fig. 7. Lung agenesis phenotype in the *Foxa2$^{Cre/+}$Fgfr2^{cnull}* mice. (a) IF analyses of E10.5 *Foxa2$^{Cre/+}$Fgfr2^{hetero}* and *Foxa2$^{Cre/+}$Fgfr2^{cnull}*: *Fgfr2^{cnull}* did not show branching morphogenesis. **(b)** Embryo images of E14.5 *Foxa2$^{Cre/+}$Fgfr2^{hetero}* and *Foxa2$^{Cre/+}$Fgfr2^{cnull}*: There is no difference in embryo morphology between *Fgfr2^{hetero}* and *Fgfr2^{cnull}* (Top). Limb (arrow) and placenta (pl) are present in mice of all genotypes (n = 6 per 6 *Fgfr2^{cnull}* embryos). However, the *Fgfr2^{cnull}* embryo showed lung agenesis phenotype (Bottom, asterisk) (n = 6 per 6 *Fgfr2^{cnull}* embryos). **(c)** Representative image of *Fgfr2^{cnull}* lung. The trachea ends in the middle of the thoracic cavity (asterisk). Scale bar: **a** = 200μm.

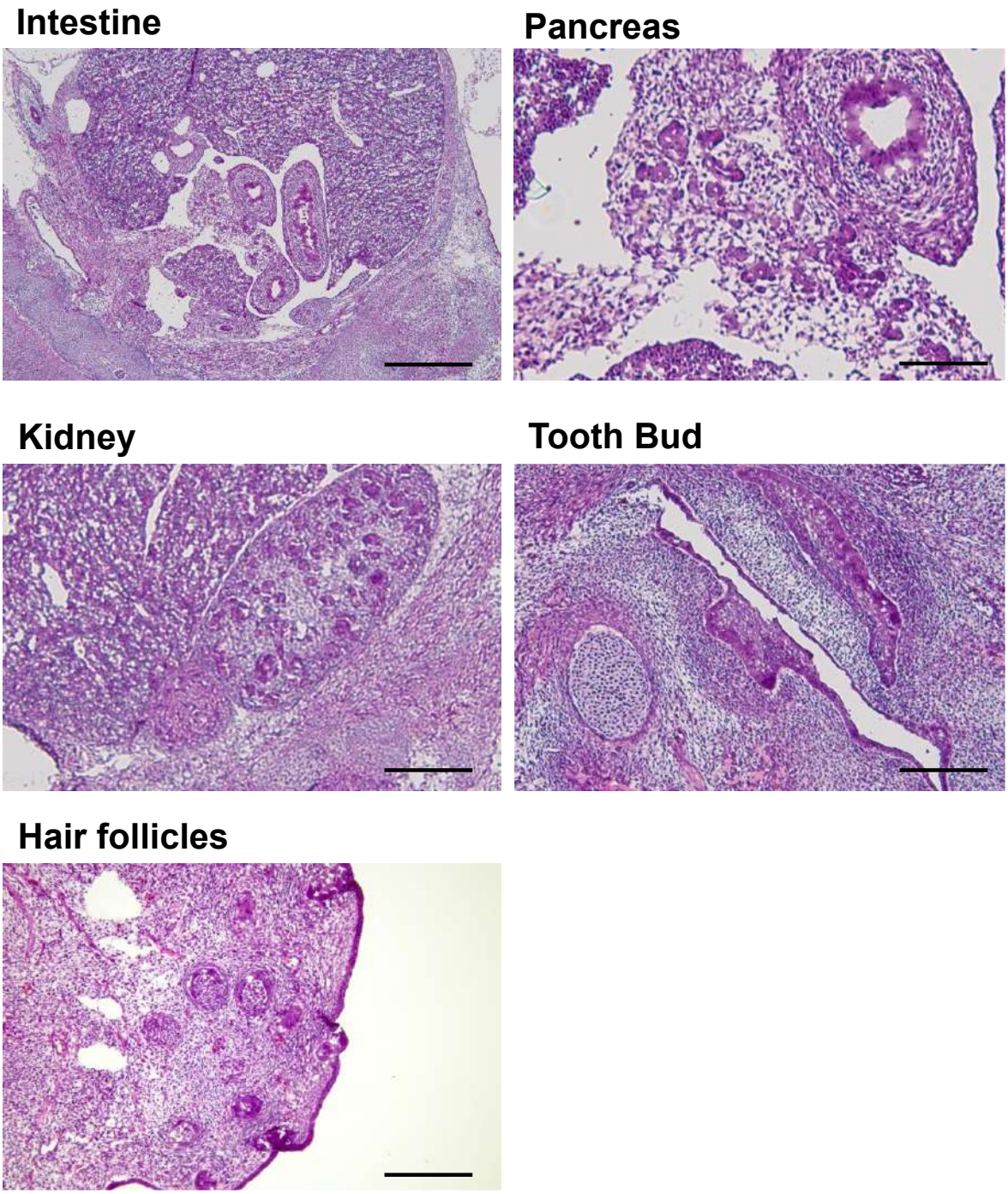

Extended data Fig. 8. Intact organ formations in the *Foxa2*$^{Cre/+}$*Fgfr2*^{cnull}. Representative pictures of Hematoxylin & Eosin staining from E15.5 *Foxa2*$^{Cre/+}$*Fgfr2*^{cnull} embryos: The internal organs such as the intestine, pancreas, kidney, tooth buds, and hair follicles were normally formed. Scale bar = 500μm.

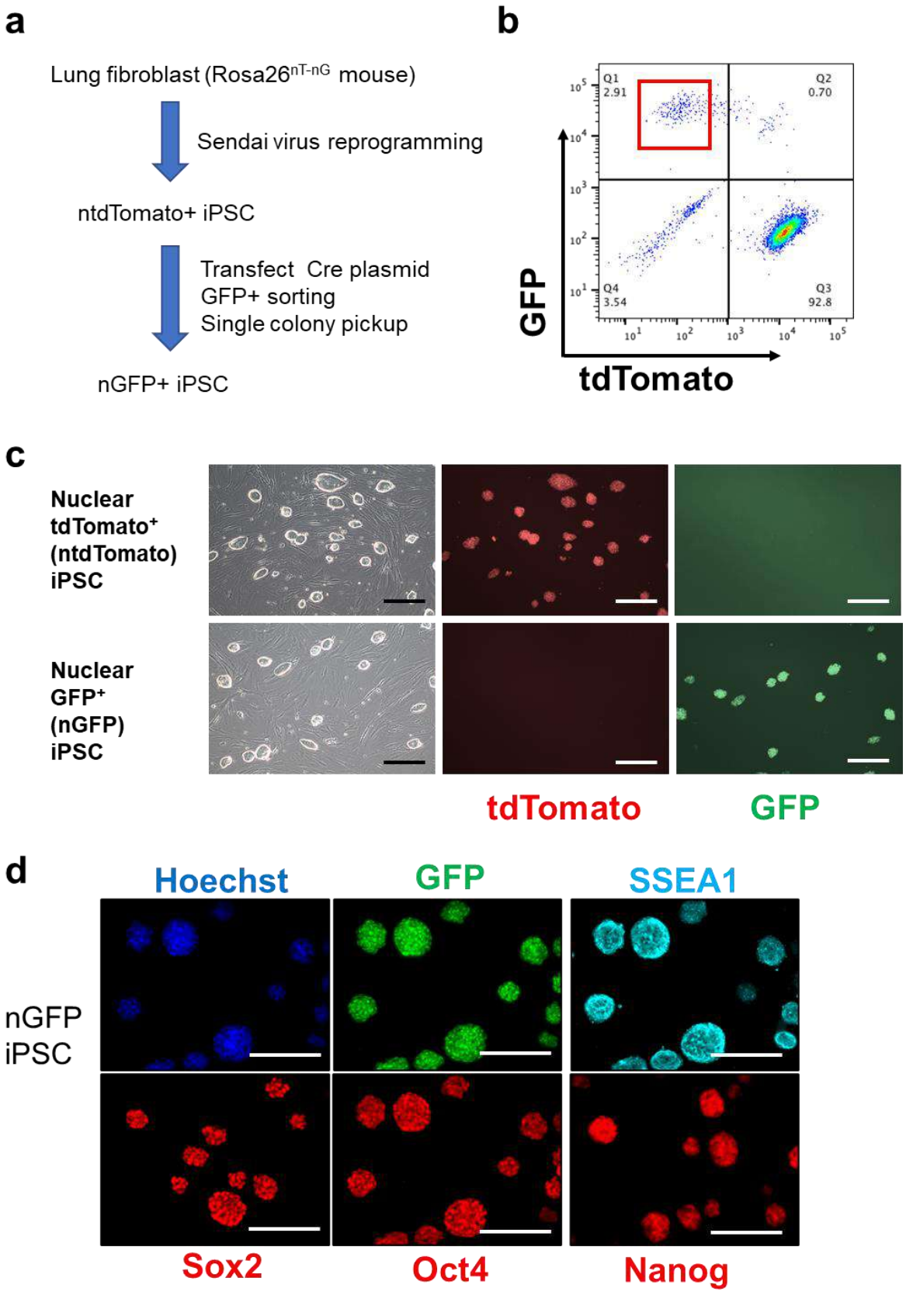
a
Lung fibroblast (Rosa26nT-nG mouse)
Sendai virus reprogramming
ntdTomato+ iPSC
Transfect Cre plasmid
GFP+ sorting
Single colony pickup
nGFP+ iPSC
b
Q1
2.91
Q2
0.70
Q4
3.54
Q3
92.8
GFP
tdTomato
c
Nuclear
tdTomato+
(ntdTomato)
iPSC
Nuclear
GFP+
(nGFP)
iPSC
tdTomato
GFP
d
Hoechst
GFP
SSEA1
nGFP
iPSC
Sox2
Oct4
Nanog

Extended data Fig. 9. Establishment of nGFP$^+$iPSCs from the *Rosa$^{nT\text{-}nG/nT\text{-}nG}$* mice. **(a)** Schematic diagram of nGFP$^+$iPSC generation from *Rosa$^{nT\text{-}nG/nT\text{-}nG}$* mouse. **(b)** FCM panel: GFP$^+$ tdTomato$^-$ cells (*Rosa$^{nG/nG}$*) after Cre induction were sorted using an FCM gate (a red box area). **(c)** Representative images of established mouse iPSCs. The nuclear GFP (nGFP)$^+$ cells (*Rosa$^{nG/nG}$*) after the sorting or Cre-uninduced cells: nuclear tdTomato$^+$ (ntdTomato) cells (*Rosa$^{nT\text{-}nG/nT\text{-}nG}$*) were maintained for in vivo injection. **(d)** Representative IF staining of pluripotency markers on established nGFP$^+$iPSCs. Scale bars: c and d = 200μm.

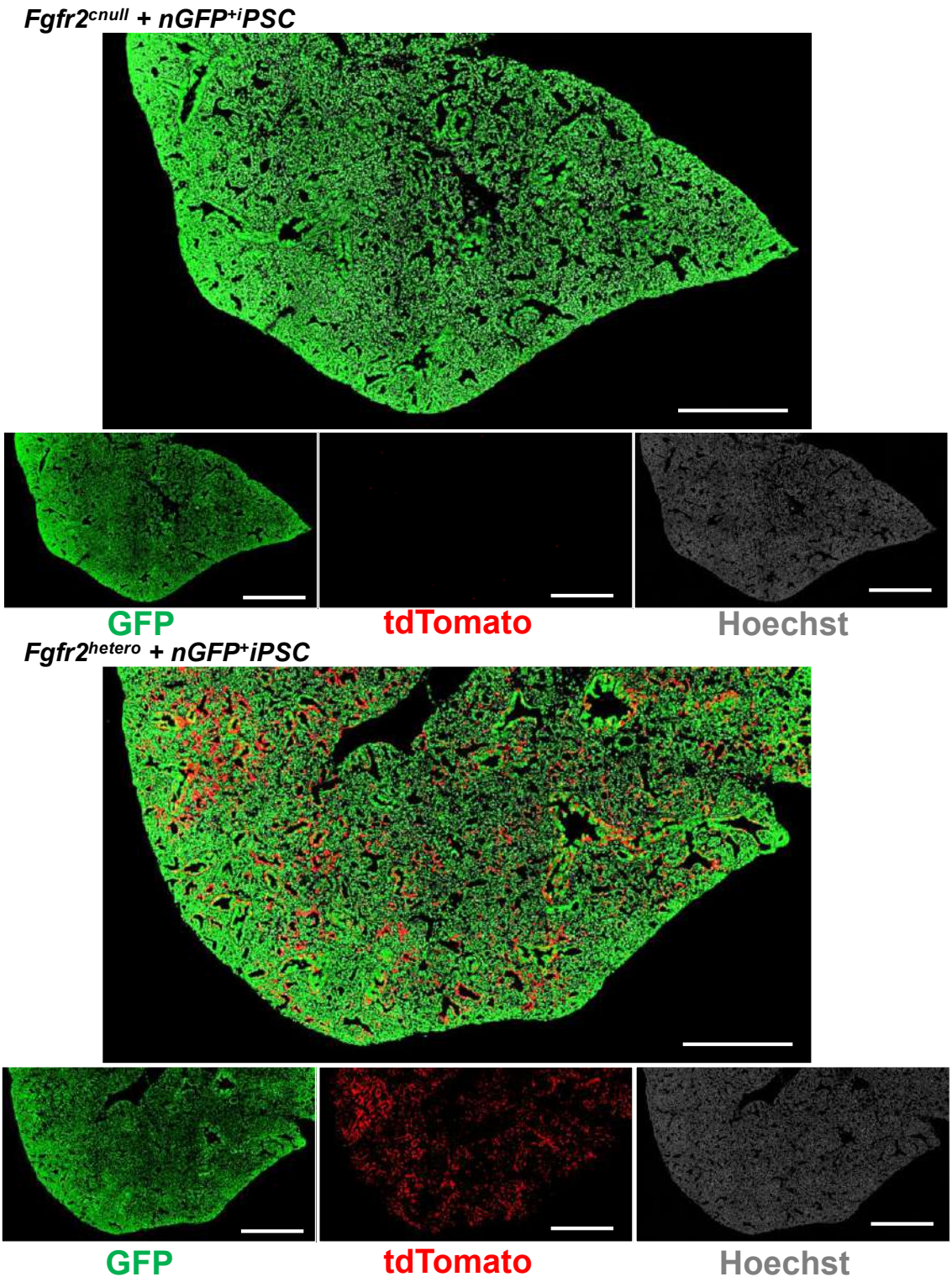

Extended data Fig. 10. Single channel images of confocal IF analyses from E17.5 lungs of *Fgfr2*^{cnull}, compared with littermate control shown in Fig. 4c. A lot of tdTomato^{+} cells were observed in *Fgfr2*^{hetero} mice, on the other hand, A few tdTomato^{+} cells were observed in *Fgfr2*^{cnull} complemented lung**.** Scale bar = 500μm.

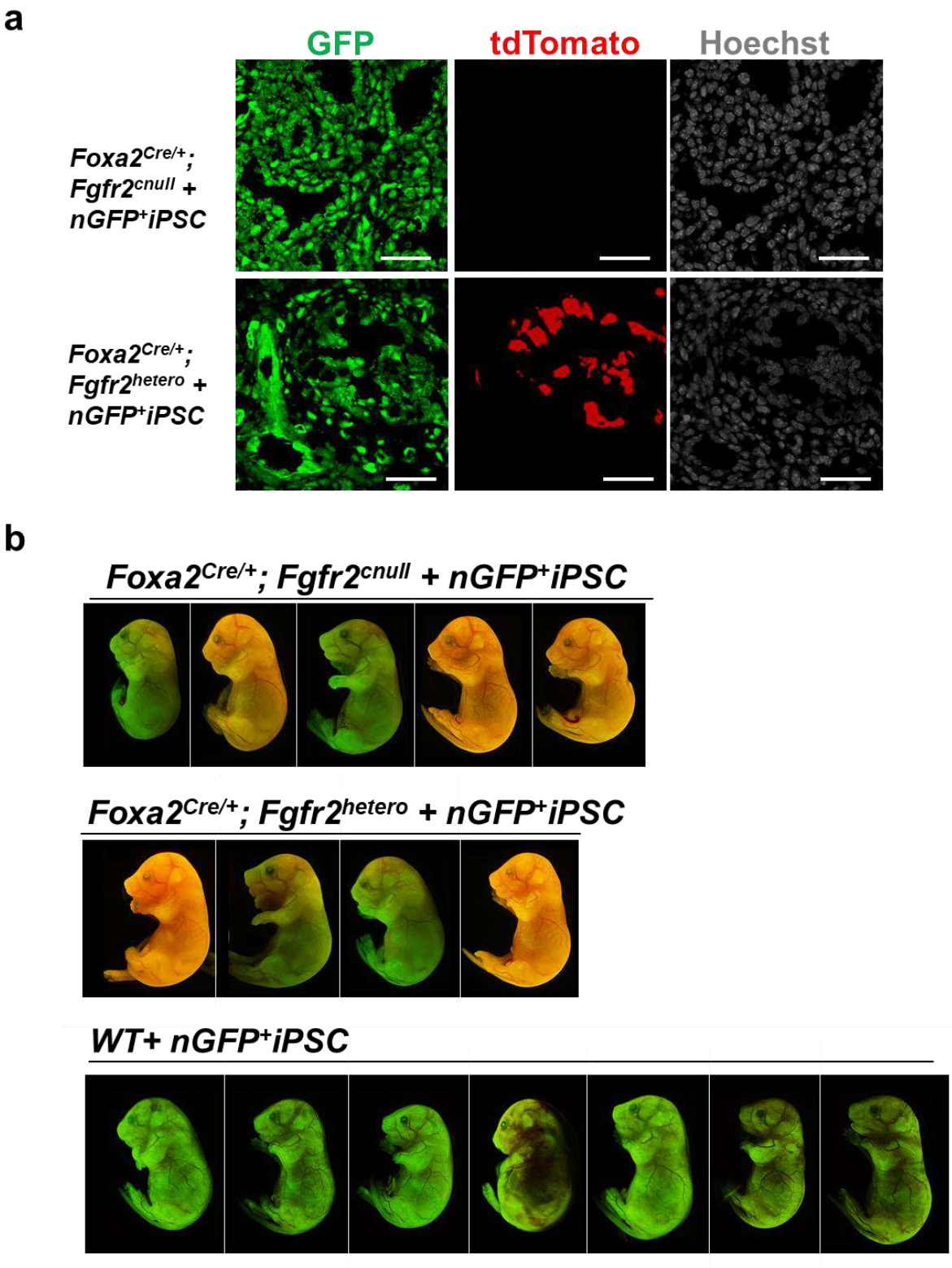
a
GFP
tdTomato
Hoechst
Foxa2Cre/+; Fgfr2cnull + nGFP+iPSC
Foxa2Cre/+; Fgfr2hetero + nGFP+iPSC
b
Foxa2Cre/+; Fgfr2cnull + nGFP+iPSC
Foxa2Cre/+; Fgfr2hetero + nGFP+iPSC
WT+ nGFP+iPSC

Extended data Fig. 11. Chimeric mouse phenotypes after nGFP^{+}iPSC injection. (a) Single channel images of confocal IF analyses from E17.5 lungs of *Foxa2$^{Cre/+}$; Fgfr2^{cnull}*, compared with littermate control shown in **Fig. 4c**. Scale bar = 50μm.
(b) Representative gross morphology of chimeric embryos of *WT* + nGFP^{+}iPSCs, *Foxa2$^{Cre/+}$; Fgfr2^{hetero}* + nGFP^{+}iPSCs, *Foxa2$^{Cre/+}$; Fgfr2^{cnull}* +nGFP^{+}iPSCs. The color indicated GFP and tdTomato signals on the skin of those embryos.

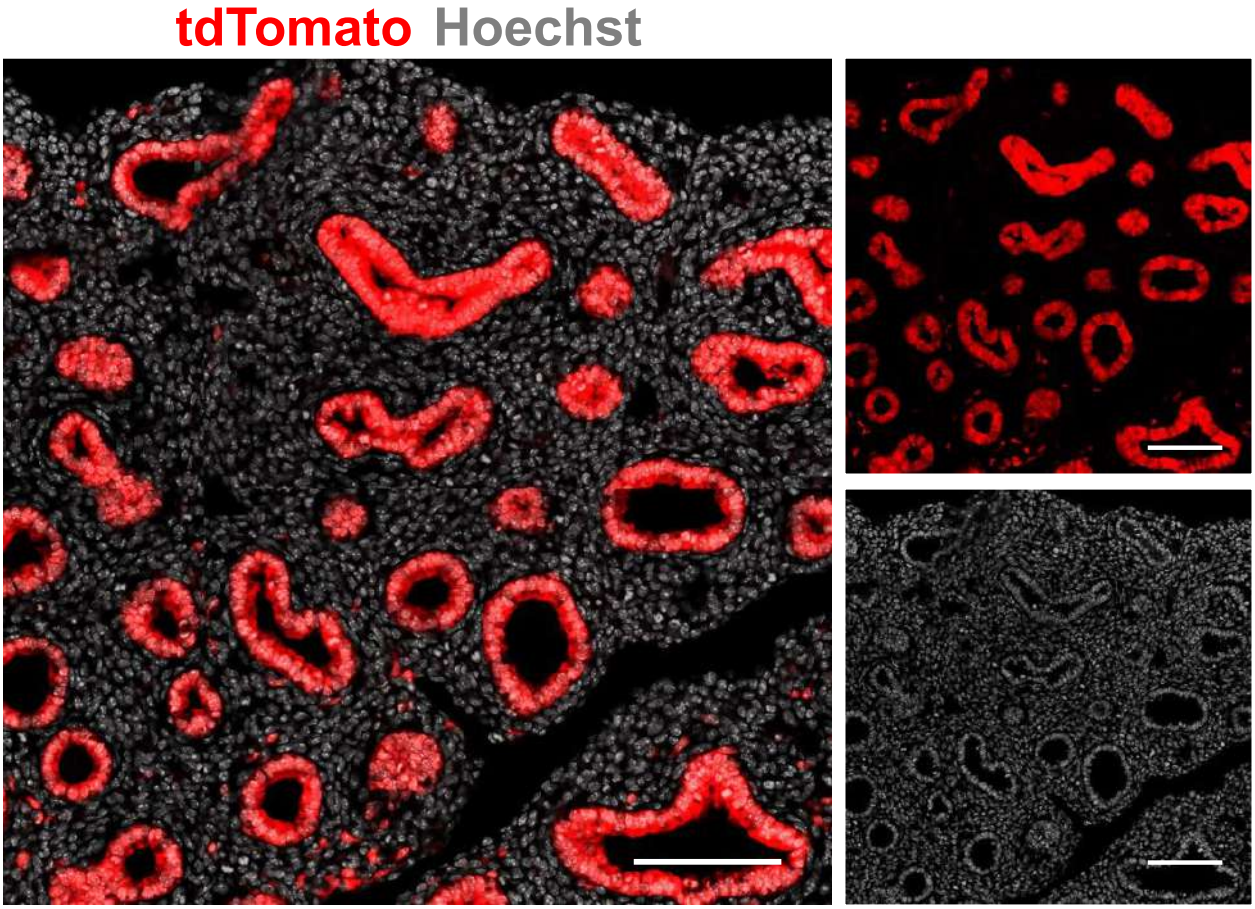

Extended data Fig. 12. Shh-lineage labeled lung epithelial cells but rarely mesenchyme. Representative IF staining of E14.5 Shh-lineage tracing mouse lung. Scale bar = 100μm

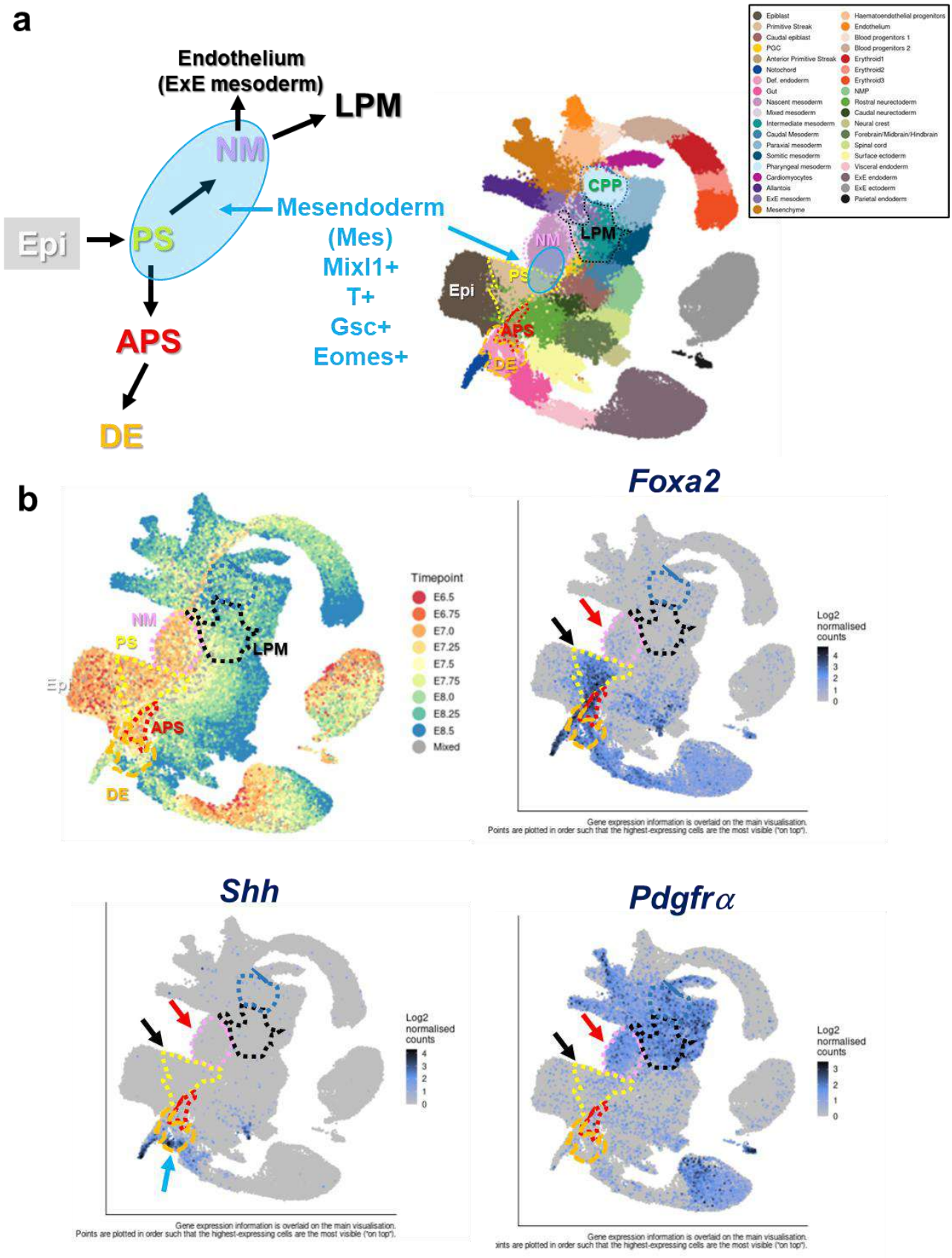
a
Endothelium
(ExE mesoderm)
LPM
NM
Epi
PS
Mesendoderm
(Mes)
Mixl1+
T+
Gsc+
Eomes+
APS
DE
CPP
NM
LPM
PS
Epi
APS
DE
Epiblast
Primitive Streak
Caudal epiblast
PGC
Anterior Primitive Streak
Notochord
Def. endoderm
Gut
Nascent mesoderm
Mixed mesoderm
Intermediate mesoderm
Caudal Mesoderm
Paraxial mesoderm
Somitic mesoderm
Pharyngeal mesoderm
Cardiomyocytes
Allantois
ExE mesoderm
Mesenchyme
Haematoendothelial progenitors
Endothelium
Blood progenitors 1
Blood progenitors 2
Erythroid1
Erythroid2
Erythroid3
NMP
Rostral neurectoderm
Caudal neurectoderm
Neural crest
Forebrain/Midbrain/Hindbrain
Spinal cord
Surface ectoderm
Visceral endoderm
ExE endoderm
ExE ectoderm
Parietal endoderm
b
NM
PS
LPM
Epi
APS
DE
Timepoint
E6.5
E6.75
E7.0
E7.25
E7.5
E7.75
E8.0
E8.25
E8.5
Mixed
Foxa2
Log2
normalised
counts
4
3
2
1
0
Gene expression information is overlaid on the main visualisation.
Points are plotted in order such that the highest-expressing cells are the most visible ("on top").
Shh
Log2
normalised
counts
4
3
2
1
0
Gene expression information is overlaid on the main visualisation.
Points are plotted in order such that the highest-expressing cells are the most visible ("on top").
Pdgfrα
Log2
normalised
counts
3
2
1
0
Gene expression information is overlaid on the main visualisation.
xints are plotted in order such that the highest-expressing cells are the most visible ("on top").

Extended data Fig. 13. Single-cell RNA-seq prominent deposited database[43] supported the lineage trajectory of Foxa2, Pdgfrα mesendoderm (ME) lineage, distinct from Shh DE lineage. (a) Left panel: Schematic diagram of mesendoderm lineage trajectory for lung formation based on the single cell RNA-seq (scRNA-seq) deposited database[43]. During gastrulation, a bipotent mesendoderm (Mes: rounded blue area) appears in the transition from primitive streak (PM) and nascent mesoderm (NM), labeled by *Mixl1, T, Gsc, and Eomes* (**Extended data Fig. 14**). Nascent mesoderm forms lateral plate mesoderm (LPM). Mesendoderm will also develop anteriolar PS (APS) and subsequently definitive endoderm (DE). Right panel: Clustering analyses of scRNA-seq provided in the deposited database[43]. Based on the LPM and CPM marker expression (**Extended data Fig. 15**), mixed mesoderm and intermediate mesoderm region are classified as LPM and pharyngeal mesendoderm as CPP, respectively. **(b)** Left top panel: Timepoint analyses of scRNA-seq provided in the deposited database[43]. scRNA-seq revealed that *Foxa2* is expressed in the PS (black arrow) and the part of NM (red arrow). In contrast, *Shh* appeared in DE but not in PS, NM, or APS. A few cells showed *Pdgfrα* in PS (black arrow) but most expressed *Pdgfrα* in NM (red arrow) and LPM.

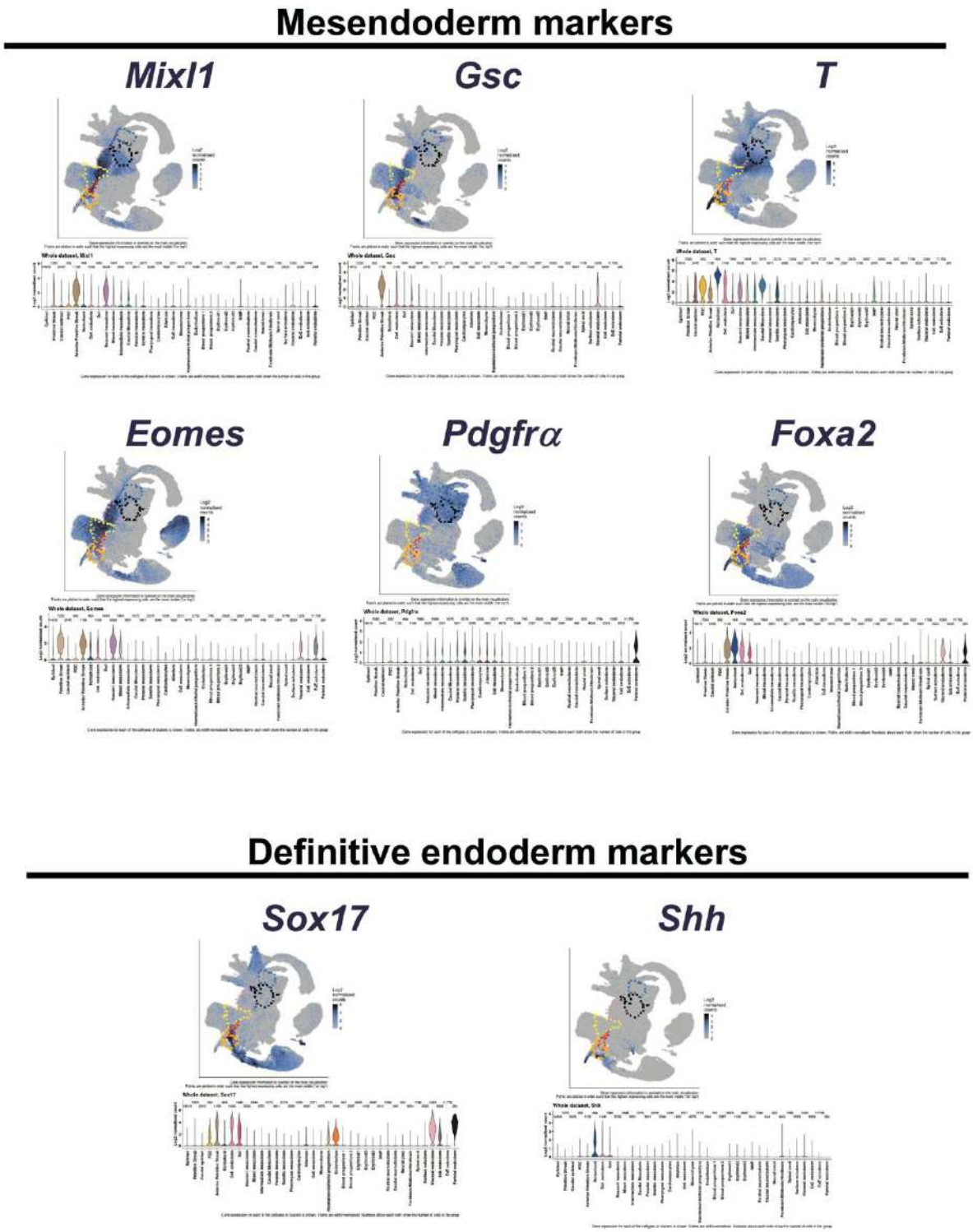

Extended data Fig. 14. Mesendoderm and DE markers in Single-cell RNA-seq large database[43]. Representative mesendoderm markers (*T, Gsc, T, Eomes*) confirmed the appearance of mesendoderm in PS and NM. DE was marked with Sox17 and Shh.

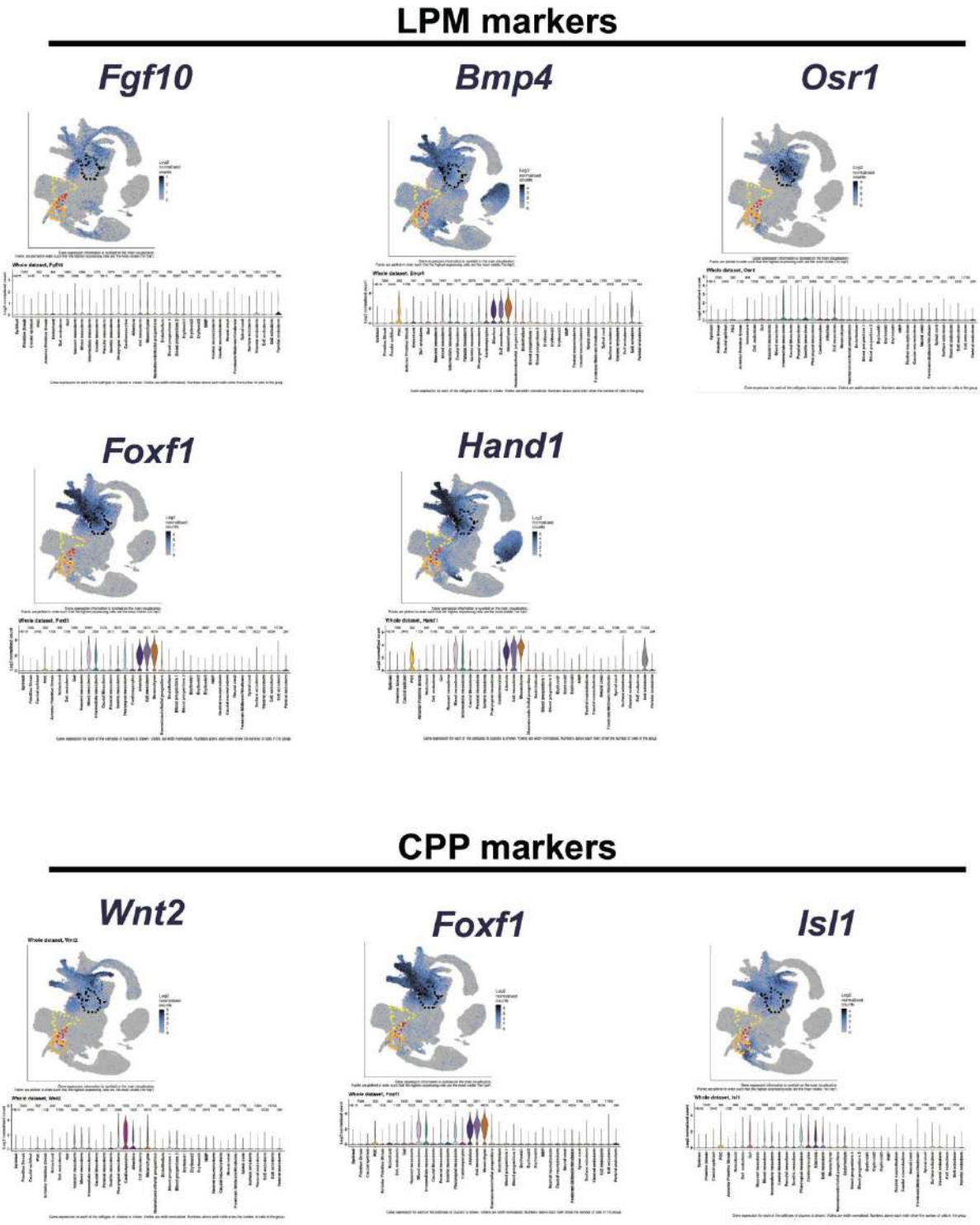

Extended data Fig. 15. LPM and CPP markers in Single-cell RNA-seq large database[43]. Representative LPM markers *(Fgf10, Bmp4, Foxf1, Hand1, and Osr1*) and CPP markers (*Wnt2, Foxf1, and Isl1*).

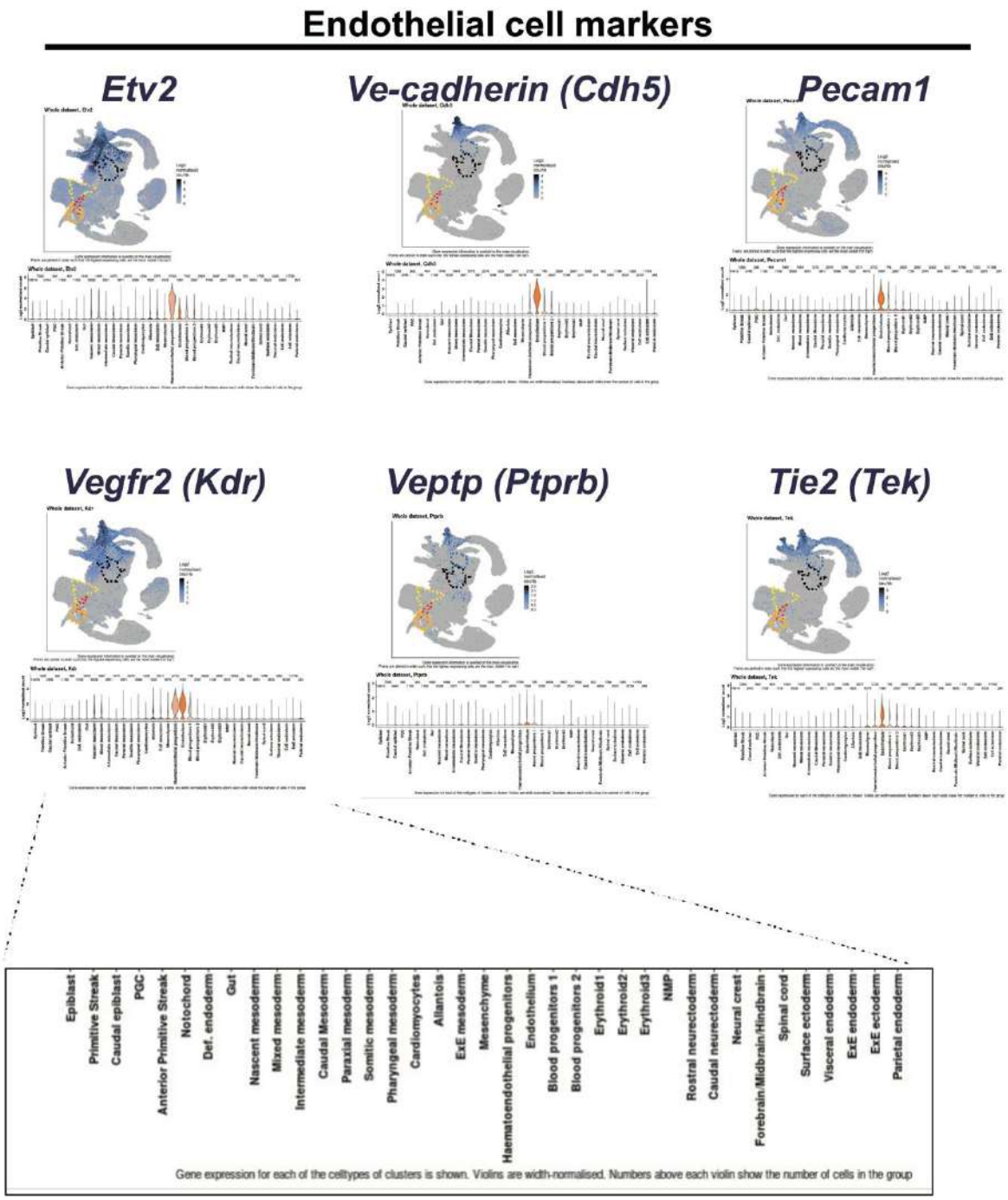

Extended data Fig. 16. Endothelial cell markers in Single-cell RNA-seq large database[43]. Representative endothelial markers *(Etv2, Ve-cadherin, Vegfr2, Pecam1, Tie2, and Ptprb*). Endothelial cell specifier, *Etv2* appeared in the part of NM with Vegfr2 expression. Those markers were not expressed in LPM, suggesting that lung endothelial cells mainly were derived from NM, labeled by *Pdgfrα* (**Fig. 1a, Extended data Fig. 1a, b, Fig. 13**).

Supplemental Table 1 | Antibodies.

Name	Company	Catalog Number	Dilution
E-cadherin	Invitrogen	131900	1 : 100
tdTomato	biorbyt	orb182397	1 : 200
Pdgfrβ	CST	3169S	1 : 100
VE-cadherin	R&D Systems	AF1002SP	1 : 200
αSma	Sigma-Aldrich	A2547	1 : 200
Pdgfra	CST	3174S	1 : 100
Pecam1	CST	77699	1 : 200
Nkx2-1	Seven Hills Bioreagents	WRAB-1231	1 : 500
FOXA2	CST	8186S	1 : 200
SOX9	R&D Systems	AF3075	1 : 200
TBX4	Santa Cruz Biotechnology	sc-515196	1 : 50
Sox2	ebioscience	14-9811-82	1 : 200
Oct4	GeneTex	GTX627419	1 : 200
Nanog	CST	4903S	1 : 200
SSEA1	CST	4744S	1 : 200
MIXL1	Novus Biologicals	NBP2-55175	1 : 200
GFP	MBL International Corporation	598	1 : 200
GFP	Aves Labs	GFP1020	1 : 200
Donkey anti Rat IgG (H+L), Alexa Fluor 488	Invitrogen	A21208	1 : 400
Donkey anti Rabbit IgG (H+L), Alexa Fluor 488	Invitrogen	A21206	1 : 400
Donkey anti Mouse IgG (H+L), Alexa Fluor 488	Invitrogen	A21202	1 : 400
Donkey anti Chicken IgY (H+L), Alexa Fluor 488	Jackson Immunoresearch	703545155	1 : 400
Donkey anti Rabbit IgG (H+L), Alexa Fluor 568	Invitrogen	A10042	1 : 400
Donkey anti Goat IgG (H+L), Alexa Fluor 568	Invitrogen	A11057	1 : 400
Donkey anti Rat IgG (H+L), Alexa Fluor 647	Invitrogen	A78947	1 : 400
Donkey anti Rabbit IgG (H+L), Alexa Fluor 647	Invitrogen	A31573	1 : 400
Donkey anti Goat IgG (H+L), Alexa Fluor 647	Invitrogen	A21447	1 : 400
Zombie Aqua™ Fixable Viability Kit	BioLegend	423101	1 : 100
SSEA1-PE	BioLegend	125606	1 : 50
CD45-BV605	BioLegend	103104	1 : 50
CD326-BV421	BioLegend	118225	1 : 50
CD326-BV711	BioLegend	118233	1 : 50
CD31-APC	BioLegend	102510	1 : 50
EPCAM-BV785	BioLegend	324238	1 : 50
PDGFRα-Alexa647	Bioscience	562798	1 : 50

Supplemental Table 2 | Primers

Gene	Forward primer sequence	Reverse primer sequence
hBMP4	CAAACTTGCTGGAAAGGCTC	CCGCTACTGCAGGGACCTAT
hPDGFRa	TTGAAGGCAGGCACATTTACA	GCGACAAGGTATAATGGCAGAAT
hACTA2	CTATGAGGGCTATGCCTTGCC	GCTCAGCAGTAGTAACGAAGGA
hISL1	AGATTATATCAGGTTGTACGGGATCA	ACACAGCGGAAACACTCGAT
hWNT2	CTGTATCAGGGACCGAGAGG	CCCACAGCACATGACTTCAC
hNKX2-1	AGCACACGACTCCGTTCTC	GCCCACTTTCTTGTAGCTTTCC
hFGF10	CCGTACAGCATCCTGGAGATAAC	TCCTCTCCTTCAGCTTACAGTCA
hOSR1	CAGCTCACCAACTACTCCTTCCTTCA	TGCAACGCGCTGAAACCATACA
hPDGFRb	ATCCCCAGTGCCGAGTTAGAAGAC	AGGACAGTGGGCGGTGGGTAGG
hTBX4	CCATCGCTACAAGTTCTGTGAC	GAATCCGGGTGGACATACAG
hFOXF1	AGCAGCCGTATCTGCACCAGAA	CTCCTTTCGGTCACACATGCTG
hCPM	TCCAAGGTGGAATGCAAGAT	TCAAAAACTTGACCCTTTACACC
hFOXA2	TCGCTCTCCTTCAACGACTGTTTCC	TTCTCGAACATGTTGCCCGAGTCAG
hMIXL1	GGTACCCCGACATCCACTTG	TAATCTCCGGCCTAGCCAAA
hSOX17	CGCTTTCATGGTGTGGGCTAAGGACG	TAGTTGGGGTGGTCCTGCATGTGCTG
hSOX2	AGTCTCCAAGCGACGAAAAA	TTTCACGTTTGCAACTGTCC
hGAPDH	GAAGGTGAAGGTCGGAGTCA	TTGATGGCAACAATATCCACTT

frontiers | Frontiers in Cell and Developmental Biology

TYPE Review
PUBLISHED 19 January 2023
DOI 10.3389/fcell.2023.1070560

OPEN ACCESS

EDITED BY
Jun Wu,
University of Texas Southwestern Medical Center, United States

REVIEWED BY
Fabian Suchy,
Stanford University, United States
Daniel Garry,
University of Minnesota Twin Cities, United States

*CORRESPONDENCE
Munemasa Mori,
mm4452@cumc.columbia.edu

SPECIALTY SECTION
This article was submitted to Stem Cell Research, a section of the journal Frontiers in Cell and Developmental Biology

RECEIVED 15 October 2022
ACCEPTED 05 January 2023
PUBLISHED 19 January 2023

CITATION
Sarmah H, Sawada A, Hwang Y, Miura A, Shimamura Y, Tanaka J, Yamada K and Mori M (2023), Towards human organ generation using interspecies blastocyst complementation: Challenges and perspectives for therapy.
Front. Cell Dev. Biol. 11:1070560.
doi: 10.3389/fcell.2023.1070560

Towards human organ generation using interspecies blastocyst complementation: Challenges and perspectives for therapy

Hemanta Sarmah[1], Anri Sawada[1], Youngmin Hwang[1], Akihiro Miura[1], Yuko Shimamura[1], Junichi Tanaka[1], Kazuhiko Yamada[2] and Munemasa Mori[1]*

[1]Department of Medicine, Columbia Center for Human Development, Columbia University Medical Center, New York, NY, United States, [2]Department of Surgery, Johns Hopkins University, Baltimore, MD, United States

Millions of people suffer from end-stage refractory diseases. The ideal treatment option for terminally ill patients is organ transplantation. However, donor organs are in absolute shortage, and sadly, most patients die while waiting for a donor organ. To date, no technology has achieved long-term sustainable patient-derived organ generation. In this regard, emerging technologies of chimeric human organ production *via* blastocyst complementation (BC) holds great promise. To take human organ generation *via* BC and transplantation to the next step, we reviewed current emerging organ generation technologies and the associated efficiency of chimera formation in human cells from the standpoint of developmental biology.

KEYWORDS

interspecies blastocyst complementation, xenotransplantation, bioengineering, human organ generation, swine model, human pluripotent stem cell, chimera

1 Introduction

Organ transplantation is the ultimate treatment option for patients suffering from refractory diseases. However, there has been an absolute scarcity of donor organs, and the gap between available donors vs. waitlisted recipients continues to expand (Giwa et al., 2017). In 2017, approximately 114,000 patients in the United States waited for an organ transplant (Sykes and Sachs, 2019). Presently, in the United States, another person is added to an organ transplant list every 10 min, 17 people die each day while waiting for donor organs, and approximately 105,800 patients are waitlisted for an organ transplant according to the health resources and services administration (HRSA). To overcome this significant crisis, researchers are investigating various approaches involving direct xenotransplantation, organoids, decellularization, and recellularization, and more recently, organ bioengineering using blastocyst complementation (BC). Depending on the patient's medical condition, a refractory disease patient also requires an on-time selective option, such as less invasive cellular therapy options or curative organ transplantation that can function immediately after transplantation. In this regard, whole organ generation *via* the BC approach holds great promise with a ready resource (livestock) for cellular therapies and as a radical treatment option for most terminal diseases. However, though BC is emerging as a potential organ transplant option, challenges regarding organ size scalability, immune system incompatibilities, long-term maintenance, potential evolutionary distance, or unveiled mechanisms between donor and host cells remain. These challenges can be overcome by a multifaceted approach, especially by filling

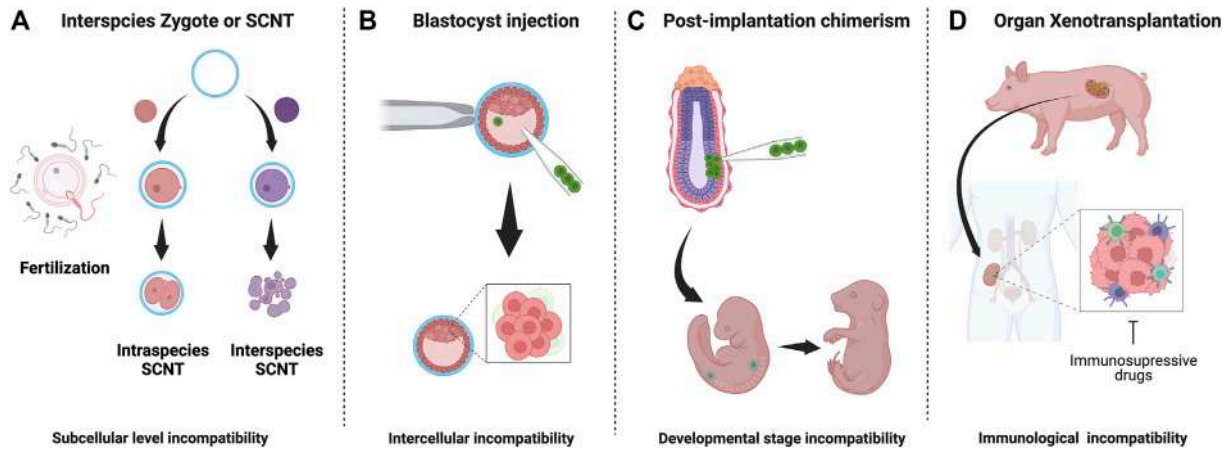

FIGURE 1
Interspecies embryo incompatibilities and barriers in interspecies chimerism: **(A)** Interspecies zygotes cannot reprogram and fail to develop due to subcellular level incompatibilities **(B)** Cell competition eliminates less fit (donor) cells donor cells in host blastocyst **(C)** Stage-matching of donor cells is challenging and unknown factor contribute to apoptosis of donor cells **(D)** Recipient immune system reacts strongly against graft tissue/organ. Despite long-term immunosuppression, organ failure occurs.

in the knowledge gaps on the mechanisms of interspecies chimera formation. In this review, we summarize the history of interspecies chimerism in various animal models to find hints for BC application and describe the challenges and prospects of utilizing BC for human organ generation.

2 Hybrids vs. chimeras

In ancient history, humans used the term "chimera" to describe mythical creatures and hybrids. Animals sexually derived from the fusion of gametes from two different organisms, such as mules, are considered "hybrids." On the other hand, a chimera is defined as an organism in which cells from two or more different organisms have contributed. In nature, hybrids and chimeras are rare due to incompatibilities and developmental divergence during evolution. At the organismal level, evolutionary distance is defined by genome-wide sequence homology between species. Humans, and other species, such as mice, swine, birds, etc., have diverged from one another. A molecular program that causes the interspecific barrier might be independent of genome-wide evolution. Instead, it may depend on the host and donor molecular similarities or distinctions critical for the organogenesis program. For instance, human LIF protein can signal *via* LIF receptors to help maintain a high degree of stemness in mice and rats, but the converse is ineffective (Dahéron et al., 2004). How evolutionary distance affects the formation of hybrids and chimeras is an open question that may vary from situation to situation.

3 Interspecies barriers in clone technologies *via* somatic cell nuclear transfer (SCNT)

In 1997, a breakthrough discovery was made: Dolly the sheep. Dolly was the first mammal cloned from an adult cell using somatic cell nuclear transfer (SCNT) (Wilmut et al., 1997). This study proved that a differentiated cell has the ability to produce exact copies of its source animals. SCNT has been successfully applied to clone 24 mammalian species, including mice, cows, pigs, cats, rats, dogs, and monkeys (Rodriguez-Osorio et al., 2012). However, SCNT was not successful in interspecies attempts. The process had been tested through electro-fusion using donor somatic cell nucleus replacement into a host's enucleated interspecies egg cytoplasm, but failed. The failure appears to be due to reprogramming elimination of the donor mitochondria by the host mitochondria, and inability to activate the donor embryogenesis program after fusion (Chang et al., 2003; Chen et al., 2003; St John and Lovell-Badge, 2007; Jiang et al., 2011). The interspecific SNCT studies imply that there are critical interspecies barriers at the subcellular level of totipotent zygotes, distinct from interspecies chimera that are at an intercellular level (Figure 1A). The study of interspecies SCNT, focusing on intracellular compartments, such as the interspecific reprogramming process, mitochondrial competition between donor and host, and genome-stability post-electrical fusion, may open new avenues to better understand subcellular interspecies barriers in SCNT.

4 Interspecies barriers in chimeras

The field of chimera research emerged nearly 50 years ago, with pioneering experiments using a mixture of pluripotent stem cells (PSCs) in an intra- or interspecies manner. Briefly, cells from the Ryukyu mouse (*Mus caroli*), when transplanted into blastocysts of the house mouse (*Mus musculus*), showed very high chimerism compared to cells derived from rat blastocysts (Stanny et al., 1980). On the other hand, cells derived from the bank vole (*Clethrionomys glareolus*), a more evolutionary distant rodent from mice, showed no detectable chimerism even during the late embryonic stages (Mystkowska, 1975). Similar studies were also performed within closely related mammalian species such as sheep and goats. Composite blastocysts from goats and

10.3389/fcell.2023.1070560

TABLE 1 Chimerism between various donor and host-derived organisms.

#	Donor	Host	Context	Context	% Chimerism	Remarks	Host stage	References	Year	Inter/ Intra	Donor cell pluripotency	Donor cell fate in chimera
1	Cattle	Cattle	Germ cells	*in-vivo*	Unknown	WT cattle blastomere derived germ cell in NANOS3-KO cattle	Blastocyst	Ideta et al. (2016)	2016	Intraspecies	naïve	GDF9, VASA, ESR1, NANOS3 positive primordial folicles
2	Chimpanzee	Rhesus macaque	Whole embryo	*ex-vivo*	Unknown	Bcl2 overexpressed chimpanzee ips cell injected into macaque embryo had chimeric contribution	Blastocyst	Roodgar et al. (2022)	2022	Interspecies	primed	Unknown
3	Human	Bovine	Whole animal	*ex-vivo*	8% *	Labelled Human naïve PSCs cultured in NHSM media into bovine blastocysts	Blastocyst	Wu et al. (2017)	2017	Interspecies	naïve/intermediate	SOX2 positive cell
4	Human	Chicken	Neural tube	*in-vivo*	Unknown	Injected hES cells contributed to ectopic nural tube formation in chick embryos	Pre-streak	Martyn et al. (2018)	2018	Interspecies	primed	T(BRACHURY), SOX17 positive cells
5	Human	Monkey	Whole embryo	*ex-vivo*	7% (EPI), 5% (HYP)	extended human ips cell contribute to both embryonic and extra-embryonic lineages in monkey embryos	Blastocyst	Tan et al. (2021)	2020	Interspecies	extended	Epiblast, hyphoblast, extra-embryonic mesenchyme, trophoectoderm lineage
6	Human	Mouse	Whole embryo	*ex-vivo*	<5% *	Region-specified hiPSCS injected into mice epiblast had low chimeric contribution	Epiblast	Wu et al. (2015)	2015	Interspecies	intermediate *	SOX2, FOXA2, T (BRACHURY) positive cells
7	Human	Mouse	Whole embryo	*in-vivo*	<4%	mTOR transient suppresion mediate high chmera of human iPSC in mice	Blastocyst	Hu et al. (2020)	2020	Interspecies	intermediate	AFP, BAND3, RE-COVERIN positive cells
8	Human	Mouse	Whole embryo	*in-vivo*	Unknown	Myd88 knockout human iPSC chimera formation in mice	Blastocyst	Zheng et al. (2021)	2021	Interspecies	primed	CNN1, PAX6, SOX17 positive cells
9	Human	Mouse	Whole embryo	*in-vivo*	Unknown	p53 knockout human iPSC chimera formation in mice	Blastocyst	Zheng et al. (2021)	2021	Interspecies	primed	CNN1, PAX6, SOX17 positive cells
10	Human	Mouse	Whole embryo	*in-vivo*	Unknown	p65 knockout human iPSC chimera formation in mice	Blastocyst	Zheng et al. (2021)	2021	Interspecies	primed	CNN1, PAX6, SOX17 positive cells
11	Human	Mouse	Whole embryo	*ex-vivo*	<5% *	hESCs and hiPSCS injected into mice epiblast had moderate chimeric contribution	Epiblast	Mascetti and Pedersen (2016)	2016	Interspecies	intermediate *	TBX6, SOX1, FOXA2,SOX2, SNAI, TNNT2, PDGFRB, TFAP2A positive cells
12	Human	Swine	Whole animal	*in-vivo*	<1% *	Labelled Human naïve PSCs into swine blastocysts	Blastocyst	Wu et al. (2017)	2017	Interspecies	naïve/intermediate	TUJ1. SMA, CK8, EpCAM, FOXA2 positive ells
13	Human	Swine	Endothelial and Hematopoteic cells	*in-vivo*	<5%	Bcl2 overexpressed hips cell injected into ETV-2-KO swine embryo had chimeric contribution	Blastocyst	Das et al. (2020)	2020	Interspecies	primed	E-CADHERIN, CONNEXIN-43 positive cells
14	Human	Swine	Skelton muscle	*in-vivo*	<5%	TP53-null hips cell injected into MYF5/MYOD/MYF6 -KO swine embryo had chimeric contribution	Blastocyst	Maeng et al. (2021)	2021	Interspecies	primed	MYOD positive cells

(Continued on following page)

TABLE 1 (*Continued*) Chimerism between various donor and host-derived organisms.

#	Donor	Host	Context	Context	% Chimerism	Remarks	Host stage	References	Year	Inter/ Intra	Donor cell pluripotency	Donor cell fate in chimera
15	Human	Swine	Whole animal	*ex-vivo*	6% *	Labelled Human naïve PSCs cultured in NHSM media into swine blastocysts	Blastocyst	Wu et al. (2017)	2017	Interspecies	naïve/intermediate	SOX2 positive cell
16	Monkey	Swine	Whole animal	*in-vivo*	<0.1%	Donor ESCs contributed to various organs of new-born swine-monkey chimera	Blastocyst	Fu et al. (2020)	2022	Interspecies	primed	TBX6, FOXA2, SOX1 positive cells
17	Mouse	Mouse	Immune system	*in-vivo*	100%	Donor mouse cell derived mature B and T cells in Rag2-KO mouse	Blastocyst	Chen et al. (1993)	1993	Intraspecies	naïve	B and T cell
18	Mouse	Mouse	Endothelial and Hematopoteic cells	*in-vivo*	100%	Mouse naïve iPSCs restored PECAM1+ endothelial cells in Flk1-mutant mice	Blastocyst	Hamanaka et al. (2018)	2018	Intraspecies	naïve	PECAM1, a-SMA positive cells
19	Mouse	Mouse	Heart	*in-vivo*	100%	Donor PSCs rescued heart fromation in Nkx2.5-Cre conditional DTA model	8-cell embryo	Coppiello et al. (2022)	2022	Intraspecies	naïve	CD31, CTNL positive cell
20	Mouse	Mouse	Vasculature	*in-vivo*	100%	Donor PSCs rescued heart fromation in Tie2-Cre conditional DTA model	8-cell embryo	Coppiello et al. (2022)	2022	Intraspecies	naïve	LECTIN, CD31 psotive cells
21	Mouse	Mouse	Heart and Vasculature	*in-vivo*	100%	Donor PSCs rescued heart fromation in Nkx2.5-Cre, Tie2-Cre conditional DTA model	8-cell embryo	Coppiello et al. (2022)	2022	Intraspecies	naïve	CTNL, Lectin positive cells
22	Mouse	Mouse	Lung	*in-vivo*	100%	Functional lung generation in Shh-driven Fgfr2 knockout mice	Blastocyst	Mori et al. (2019)	2019	Intraspecies	naïve	NKX2.1, PDPN, SFTPC, SOX2, SCGB1A1, BETA4TUBULIN positive cells
23	Mouse	Rat	Pancreas	*in-vivo*	100%	Mouse donor cell derived pancreas in Pdx1-KO Rat	Blastocyst	Yamaguchi et al. (2017)	2017	Interspecies	naïve	Pancreas
24	Mouse	Swine	Whole animal	*in-vivo*	0%	Labelled Mouse naïve iPSCs had no chimeric contribution in WT swine	Blastocyst	Wu et al. (2017)	2017	Interspecies	naïve	Not applicable
25	Rat	Mouse	Whole animal	*in-vivo*	20%	Labelled Rat naïve ESCs/iPSCs formed chimera in WT mouse	Blastocyst	Wu et al. (2017)	2017	Interspecies	naïve	Brain, heart, intestine, kidney, lung, pancreas, spleen, liver cells
26	Rat	Mouse	Pancreas	*in-vivo*	100%	Rat donor cell derived pancreas in Pdx1-KO mouse	Blastocyst	Kobayashi et al. (2010)	2010	Interspecies	naïve	Pancreas
27	Rat	Mouse	Heart and Vasculature	*in-vivo*	100%	Donor rat PSCs rescued heart fromation in Nkx2.5-Cre, conditional DTA model	8-cell embryo	Coppiello et al. (2022)	2022	Interspecies	naïve	NKX2.5 positive cells
28	Rat	Mouse	Pancreas	*in-vivo*	>20% *	Labelled Rat naïve ESCs/iPSCs formed pancreas in Pdx1-KO mouse	Blastocyst	Wu et al. (2017)	2017	Interspecies	naïve	a-AMYLASE positive cells

(Continued on following page)

10.3389/fcell.2023.1070560

TABLE 1 (*Continued*) Chimerism between various donor and host-derived organisms.

#	Donor	Host	Context	Context	% Chimerism	Remarks	Host stage	References	Year	Inter/ Intra	Donor cell pluripotency	Donor cell fate in chimera
29	Rat	Mouse	Heart	*in-vivo*	>20% *	Labelled Rat naïve ESCs/iPSCs formed heart in Nkx2.5-KO mouse	Blastocyst	Wu et al. (2017)	2017	Interspecies	naïve	NKX2.5 positive cells
30	Rat	Mouse	Eye	*in-vivo*	>20% *	Labelled Rat naïve ESCs/iPSCs formed eyes in Pax6-KO mouse	Blastocyst	Wu et al. (2017)	2017	Interspecies	naïve	PAX6 positive cells
31	Rat	Swine	Whole animal	*in-vivo*	0%	Labelled Rat naïve ESCs had no chimeric contribution in WT swine	Blastocyst	Wu et al. (2017)	2017	Interspecies	naïve	Not applicable
32	Swine	Swine	Pancreas	*in-vivo*	100%	WT Swine blastomere derived pancreas in Pdx1-KO swine	Blastocyst	Matsunari et al. (2013)	2013	Intraspecies	naïve	Pancreas
33	Swine	Swine	Endothelial and Hematopoteic cells	*in-vivo*	100%	WT Swine blastomere derived endothelium in ETV2-KO swine	Blastocyst	Das et al. (2020)	2020	Intraspecies	naïve	TIE-2 positive cells
34	Swine	Swine	skelton muscle	*in-vivo*	100%	WT Swine blastomere derived skelton muscle in MYF5/MYOD/ MYF6-KO swine	Blastocyst	Maeng et al. (2021)	2021	Intraspecies	naïve	MYF5, MYOD, ACTN2, DES, PAX7 positive cells
35	Swine	Swine	Eye	*in-vivo*	100%	WT Swine blastomere derived eye in MITF-KO swine	Blastocyst	Zhang et al. (2018)	2013	Intraspecies	naïve	PAX6, MITF, BESTROPHIN positive cells

"Host stage" refers to the timing of donor cell injection.

sheep could successfully generate goat-sheep chimeras (Fehilly et al., 1984). Likewise, chimeric calves produced from two closely related cow species—*Bos indicus* and *Bos taurus*, were also viable (Williams et al., 1990). These early experiments made a clear distinction between interspecies and intraspecies chimerism. In other words, the evolutionary distance between two species may be inversely correlated with the extent of chimerism (de Los Angeles and Wu, 2022).

This section reviews various interspecies chimera formation rates and chimerism during development. Chimera formation rate refers to the percentage of host animals with donor cells. Assessment of chimera formation requires checking the markers of donor cell survival, proliferation, and differentiation and proof that the donor cells are responsive to the host animal's developmental program. Chimerism, on the other hand, indicates the % of donor cell contribution to a particular developmental niche or organism. Overall, the efficacy of intraspecies chimerism and chimera formation is far superior to that of interspecies (Table 1). Elucidation of the interspecies barrier incompatibility between host animals and human cells during development is a breakthrough in the field of human organ generation in a host animal.

4.1 Human chimeras in chick

Chicken models offer significant advantages in the study of developmental biology and chimerism. The developmental stages can be accurately determined, and embryos can be manipulated for experiments such as tissue transplantation, resection, and genetic modification (Hamburger and Hamilton, 1951; Spurlin and Lwigale, 2013; Cloney and Franz-Odendaal, 2015). Early experiments with chick embryos used intraspecific chimeras to test the vertebrate "organizer" concept and its role in gastrulation, known as embryonic differentiation. When transplanted into another, a portion of the anterior streak cells from one embryo gave rise to an ectopic neural plate comprising a neural tube, notochord, and somites (Addington, 1932; Waddington and Schmidt, 1933; Waddington, 1934). Decades later, the first evidence of avian interspecies chimerism was demonstrated by Nicole le Douarin and colleagues by engrafting quail-derived neural crest cells into the neural plate boundary of chick embryos (Couly and le Douarin, 1985). Human embryonic stem cells (hESC) transplanted into the trunk of a chick embryo were also found to differentiate into β-III tubulin-positive neurons in the host microenvironment (Goldstein, 2010). Furthermore, the neurogenic potential of hESCs was tested in mutant chick models of open neural tube defects (ONTDs). ONTDs were significantly rescued in chick embryos by the transplanted hESCs, compared to control groups, as early as post-operative Day3 (Lee et al., 2004). In another study, inoculated donor hESCs adequately contributed to the hindbrain and regions of the spinal cord within host chick embryos (Boulland et al., 2010). Similar results were also observed when hESCs were injected intra-amnionically into neural-tube defective chick embryos after 24 h of lesion induction, miming a clinical situation of human ONTDs (Lee et al., 2006). Recently, in a pioneering effort, human RUES-GLR (germ layer reporter) cells treated with Wnt3a and Activin were transplanted into chick embryos to

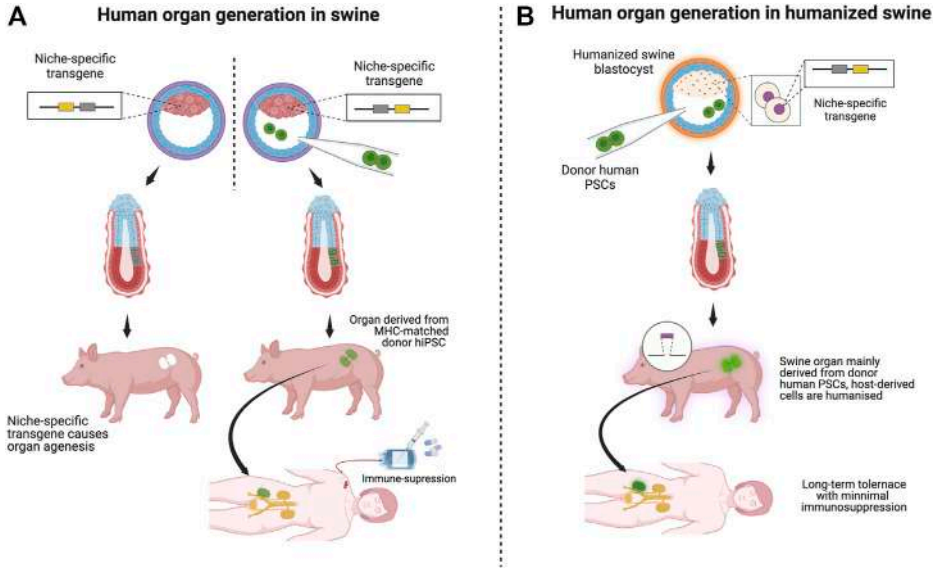

FIGURE 2
Scenarios of organ transplantation derived from various swine models: Schematic: [**(A)**, left] In BC, vacant organ niche formation by a niche-specific transgene depletion through genome editing is essential. [**(A)**, right] Injection of human patient-derived (or MHC-matched human) iPS cells (green) into a blastocyst of a host animal with an organ failure phenotype. [**(A)**, right, and **(B)**]. **(A)** Transplantation of human organs by BC is unlikely to fail because most cells are of human origin. Immunosuppression may be necessary if the porcine host origin remains in the graft component. **(B)** Organs transplanted from human-derived cells created in humanized pigs are assumed to function long-term in recipients with minimal or no immunosuppression because humanized pigs are designed to minimize immune rejection. Using humanized swine as host animals for the BC will work as a safety guard system for immune rejection.

assess their ability to serve as "organizers". This transplantation resulted in the generation of an ectopic secondary axis within the chick embryo capable of inducing neural tissue (marked by Sox2/Sox3 expression) in the adjacent regions (Martyn et al., 2018).

These chick studies showed relatively higher chimerism than rodent-human or pig-human chimera, although the exact extent of chimerism was not described. Although the injection timing differed from BC, host chicken embryos were rescued by human PSC-derived cells. They showed differentiation markers with high chimerism beyond the blastocyst stage at the donor cell injection site. Intriguingly, early embryos of humans are discoidal shaped, closely resembling that of chicken, while mouse embryos are more cylindrical (Akhlaghpour et al., 2021). It suggests that the molecular program of early embryos may be similar between humans and chickens, probably related to the polarity and the body plan, allowing human PSCs to differentiate into neuronal lineages. On the other hand, the evolutionary distance between birds and humans is more than 300 million years, while the differences between rodents and humans are about 96 million years old (Nanda et al., 1999; Nei et al., 2001). The implanted chicken niche may have a unique niche character that secretes or expresses proteins or other molecules to overcome interspecific barriers beyond evolution. Suppose these potential mechanisms of human cell compatibility are common in all bird species. In that case, the human chimera studies with giant birds, such as ostrich (*Struthio camelus*), are an intriguing option for studying organ generation. However, birds harbor completely distinct anatomy and circulation systems from humans, which must be considered well. A mouse-avian chimerism examination also would be fascinating to clarify the significance of such physical constraints toward interspecific incompatibility mechanisms in early embryogenesis.

4.2 Human chimeras in mice

Chimera efficiency depends on donor cell preparation and host genetic background. Various group attempts have made dramatic progress in maintaining the pluripotency of naïve, primed, intermediated, and extended PSCs under different cell culture conditions. A naïve pluripotent state can be best described by cells within the inner cell mass of a mouse blastocyst. Cells in the morulae or 16-cell stage are considered to have totipotency or expanded potential pluripotency because they can contribute to both embryonic and extra-embryonic lineages. The concept of primed-type pluripotency is typically associated with cells within the post-implantation epiblast of mouse embryos having very low chimeric potential when injected in a host blastocyst. Lastly, the newly established concept of intermediate pluripotency refers to many possible cell states that overlap between naïve-state markers and primed-state markers. In the following section, we discuss how the chimeric potential of PSCs in various pluripotent states varies within host mouse embryos.

4.2.1 Naïve type pluripotency

Regarding donor cell preparation, scientists successfully maintained embryonic stem (ES) cells from mouse blastocysts and recognized their ability to undergo various lineage differentiation over 4 decades ago (Evans and Kaufman, 1981; Martin, 1981; Martello and Smith, 2014). In subsequent years, with refinement in culture conditions, reagents, and specific inhibitors, using a "2i" medium, the combination of a MEK inhibitor and a GK3β inhibitor, mouse PSCs can be maintained and propagated in a state of naïve pluripotency (Ying et al., 2008). For the intraspecies blastocyst injection, a donor cell naïve pluripotent state is fundamentally

necessary to achieve a high degree of chimerism (Silva and Smith, 2008). Gene-targeted mouse ES cells have been successfully used in numerous studies for their ability to form germ-line chimeras (Mansour et al., 1990; Bradley, 1991; Robertson, 1991). However, the prolonged culture of PSCs in the 2i medium caused irreversible epigenetic changes leading to defects in developmental potential (Choi et al., 2017; Yagi et al., 2017). To overcome these problems, we have developed a defined media cocktail named a2i VPA LIF, which allows us to maintain PSCs with the highest chimera-forming capacity capable of forming functional lungs (Mori et al., 2019). To generate human naïve PSCs, 5iLAF, ReST, and t2iLGoY mediums have been developed (Theunissen et al., 2014; Pastor et al., 2016; Liu et al., 2017). Further comparative single-cell transcriptome analysis of the induced pluripotent stem cells (iPSCs) cultured in those media showed distinct naïve pluripotency.

4.2.2 Primed type pluripotency

There have been many efforts to generate and maintain various types of PSCs in human subjects. Human ES cells were first characterized as a primed state (Thomson et al., 1998). Unlike mice, human PSCs cannot be sustained in a naïve pluripotent state in the 2i-culture condition (Chan et al., 2013; Gafni et al., 2013; Takashima et al., 2014; Theunissen et al., 2014; Ware et al., 2014; Wu et al., 2015). This fundamental difference is likely a contributing factor behind the low chimerism of human ES in mouse embryos, examples of which are discussed below (Theunissen et al., 2014; Weinberger et al., 2016). The first evidence of human-mouse chimeras came from a study where RUES1 cells were transplanted into mouse blastocysts and examined for chimeric contribution *in-vivo*. Although the extent of chimerism was low, cells of human origin contributed to the prospective foregut epithelium and neuroepithelium at the E8.5 developmental stage (James et al., 2006). In a subsequent study, Hanna and colleagues reported a special 2i-LIF media supplemented with ligands FGF2 and TGFβ1, as well as inhibitors for p38 and JNK, that could confer naïve pluripotency in human ESCs and iPSCs. Additionally, they reported that cells grown in culture conditions robustly contributed to craniofacial tissues and embryonic neural folds within mouse-human chimeras (Gafni et al., 2013). Although this result was acclaimed to be a defining functional read-out for naive human pluripotency, other groups that tested this method failed to generate chimeras (Takashima et al., 2014; Theunissen et al., 2014).

4.2.3 Intermediate type pluripotency

During embryogenesis, cell competition is one of the significant interspecific incompatibility barriers that cause regional elimination of low-fitness cells, accounting for almost 35% of all cells produced *via* the balance between proliferation and apoptosis (Figure 1B) (Clavería and Torres, 2016; Merino et al., 2016; Bowling et al., 2019; Hashimoto and Sasaki, 2020). This mechanism, initially identified in *Drosophila*, involves relatively higher-MYC expressing "winner" cells to dominate the developing embryo by forcing adjacent, relatively lower-MYC "loser" cells to undergo apoptosis (de La Cova et al., 2004; Moreno and Basler, 2004; Clavería et al., 2013; Sancho et al., 2013; Díaz-Díaz et al., 2017). To avoid cell-competition-based elimination of donor cells in a chimeric epiblast, Belmonte and colleagues targeted E7.5 post-implantation mouse embryos for engrafting human PSCs and accessed chimeric efficiency (Figure 1C). By conditioning human ESCs into a region-selective primed state characterized by a transcriptome that closely matches that of a late-streak/no-bud stage mouse embryo, the authors reported efficient chimerism into endoderm, ectoderm, and mesoderm tissues (Wu et al., 2015). Mascetti and Pedersen further illustrated the idea of stage-matching hPSCs with the corresponding mouse embryonic state to enhance chimeric efficiency. However, in contrast to Belmonte's study, there was no requirement of special pre-treatment for human PSCs before their injection into early and late gastrulation-stage embryos. Yet, primed-type cells could differentiate very efficiently into tissues derived from all three germ layers (Mascetti and Pedersen, 2016). Such disparity in experimental results highlights the extent of technical challenges and the requirement of a reliable genetic or epigenetic landmark for evaluating human PSC lines that form chimera efficiently before injection.

The state of pluripotency can have a profound influence on chimeric efficiency. For instance, primed-type PSCs corresponding to epiblast stem cells cannot form chimeras even in intraspecies contexts (Nichols and Smith, 2009). On the other hand, naïve-type cells show gene expression profiles similar to a blastocyst's inner cell mass and can contribute to interspecies chimeras (Kobayashi et al., 2010). Although this distinction is well grounded for rodent models, the concept is not well defined in context of large animals (Rashid et al., 2014; Graham, 2017). Wu and colleagues examined all available culture conditions for primed and naïve states of human iPSCs (Wu et al., 2017). In addition to primed and naïve, human iPSCs were also characterized in an intermediate state of pluripotency, previously shown to have chimeric potential in mouse germline (Tsukiyama and Ohinata, 2014). Reporter human iPSCs were amenable to this state of pluripotency and showed significantly higher chimeric contribution in swine embryos compared to cells in other naïve or naïve-like pluripotent conditions (Wu et al., 2017). A recent study also showed that human iPSCs with intermediate pluripotency contribute to primordial germ cell specification in chimeric embryos (Yu et al., 2021).

4.2.4 Extended type pluripotency

In 2017, Deng and colleagues introduced the concept of extended pluripotency, a state of stemness that is transcriptionally distinct from conventional naïve and primed cells. An extended potential state exists between a totipotent 1-cell embryo and a blastocyst in a developing embryo. Both mouse and human extended pluripotent stem cells (EPSCs) were found to have very high chimeric potential, supported by the fact that a single mouse EPS cell could generate both embryonic and extraembryonic lineages *in vivo* (Yang Y. et al., 2017). Further developing this concept, human EPSCs were shown to be approximately 20 times more chimerically efficient than naïve hPSCs when injected into preimplantation mouse blastocysts (Yang Y. et al., 2017). The most recent evidence highlighted the importance of mTOR pathway inhibition in donor human PSCs enabling them to achieve a high degree of chimerism in mouse embryos (Hu et al., 2020; Zhang et al., 2021). In many of the examples discussed above, modified hPSCs were transplanted into a wild-type mouse host, and not surprisingly, the extent of chimerism was low (Freedman, 2018). Based on these results,

the human donor cell naïve pluripotency requirement for achieving high chimerism in the host organism is debatable in the human-mouse developmental chimera context. This is because it is difficult to maintain the chimera-competent naïve quality of human iPSCs for the long term even in naïve maintenance medium (5iLAF, ReST, and t2iLGoY) or 2i-medium and the naïve pluripotency is profoundly distinct across the species (Silva and Smith, 2008). Intermediate or extended-type PSCs are attractive; however, substantial efforts are required for efficient chimerism (Yang J. et al., 2017; Gao et al., 2019). How to maintain an organogenic competency in human iPSC, that is, the ability to form functional organs post-injection of cells in the host animals, remains a question, and it may depend on both pluripotency and the host animal developmental program.

4.3 Human chimeras in rats

Rats have also been used to study interspecies chimerism in various contexts for developing humanized rat models, although not to the same extent as mice. Early studies in the 1980s utilized the nude rat model to study the engraftment of human skin and immune cells (Vos et al., 1980). These rats exhibited moderate immunodeficiency characterized by loss of lymphocyte counts with age but sustained high counts for neutrophils, eosinophils, and monocytes. Therefore, this model could only support adult human skin grafts for a short time before host-mediated rejection (Brüngger et al., 1984; Gilhar et al., 1986; 1990). Human $CD45^+$ cells were detected in various rat tissues, such as the liver, thymus, kidney, spleen, etc., up to 6 months post-in-utero cord blood transplantation (Sun et al., 2007). The success of this model primarily relies on the permissive nature of the immune-deficient fetal state of rats. Recent studies have further perpetuated this concept by showing high engraftment efficiency of human iPSCs and human cancer cells in two rat models of severe combined immunodeficiency (Yang et al., 2018; He et al., 2019; Noto et al., 2020). The degree of immune surveillance for a given tissue also contributes to chimeric efficiency. Regions of the rat brain, such as the corpus striatum, when transplanted by human marrow stromal cells, show a remarkable 20% engraftment efficacy over 72 days with a lack of inflammatory responses (Azizi et al., 1998). In addition to immune aversion, various pathological conditions or tissue injury forms enhance chimerism's chances. Neural precursors cells derived from human ES cells differentiate into neurons and glial cells in the regions of adult rat brains and spinal cords (Tabar et al., 2005; Yan et al., 2007). Human neural stem cells exert neuroprotective function in rat models of Parkinson's disease and conditions of stroke-induced ischemia (Yasuhara et al., 2006; Bliss et al., 2007; Andres et al., 2011). Other human stem cell types, such as mesenchymal stem cells, also exhibit localized chimerism in rat organs such as the liver, heart, and pancreas (Grinnemo et al., 2004; Sato et al., 2005; Laporte et al., 2019). These studies primarily attempt to generate humanized rat models of various pathological conditions and tissue damage without using BC methods. With the emergence of new humanized rat models, the future of functional human-rat interspecies chimerism holds excellent promise, while the permissiveness of non-cancerous, normal human epithelial chimerism needs to be addressed well (Agarwal et al., 2020).

4.4 Human chimeras in monkeys

Close evolutionary relationships between monkeys and humans make them a suitable model for studying the long-term effects of interspecies organ chimerism (Gibbs et al., 2007; Stevens et al., 2013). Despite their relatively large size compared to small rodents, extended gestation period, and logistical difficulties such as labor and farming costs, monkeys can be valuable models for studying interspecies chimerism in various contexts. Takahashi and colleagues performed human ES stem cell-derived retinal tissue transplantation in two monkey models of injury-induced retinal degeneration (Shirai et al., 2016). It is well known that the odds of immune rejection decrease significantly in human-leucocyte antigen-matched iPSC transplantations (Sugita et al., 2016; Morizane et al., 2017). From this observation, Mandai and colleagues used human iPSCs to generate long-term functioning chimeric retinas in the same primate models of retinal degeneration with lower immunosuppression. In another pre-clinical study, human iPS cell-derived dopaminergic neurons showed functional engraftment in a neurotoxin-induced model of Parkinson's disease (Kikuchi et al., 2017).

Furthermore, when used in the order of billions, human ES cell-derived cardiomyocytes can regenerate hearts in a non-human primate model of myocardial ischemia (Chong et al., 2014). Despite such success, certain aspects of monkey-human chimerism remain poorly understood. For instance, human ES cell-derived cardiovascular progenitors failed to induce remuscularization in infracted primate hearts (Zhu et al., 2018). From the developmental standpoint, Belmonte and colleagues showed the ability of human EPSCs to differentiate into hypoblast and epiblast lineages in monkey-human chimeras *ex vivo* (Tan et al., 2021). Attempts have also been made to generate monkeys genetically predisposed to immunodeficiency (Niu et al., 2014). Such models can be beneficial in achieving a high chimeric success of engrafted donor cells. However, using monkey-human chimeras for studying complex human brain disorders will require more cautious exploration and robust ethical modalities for crossing the interspecies barrier (Greely and Farahany, 2021). The organ size distinction between humans and monkeys also can be another significant xenobarrier for monkey-human chimeric organ generation, particularly for the solid organs that require anatomically and physiologically functional size for transplantation, such as eyes, bones, kidneys, hearts, lungs, and gastrointestinal tracts.

4.5 Human chimeras in pigs

Previously, large animals such as cattle and pigs were mainly used for developing human/animal xenograft models. The main objective was to gain mechanistic insights into graft vs. host tissue interactions that could be leveraged to achieve long-term clinical success of organ transplantation. Modeling such events in smaller animals was not feasible owing to shorter life spans and anatomical disproportionalities. Flake and colleagues showed site-specific differentiation of engrafted human mesenchymal stem cells upon transplantation into sheep embryos (Liechty et al., 2000; Almeida-Porada et al., 2004). Among large animals, pigs have been proposed as an ideal host for studying interspecies chimerism, primarily due to very close anatomical and physiological similarities to humans

(Cooper et al., 2016; Nagashima and Matsunari, 2016). The following section summarizes currently available pig models and the prospects of using gene-modified pigs for xenotransplantation (Figure 1D).

5 Blastocyst complementation

"Blastocyst complementation (BC)" is a significant concept for organ generation as a regenerative approach. BC utilizes the host developmental program to incorporate donor PSCs. Donor PSCs, when injected into recipient morula or blastocysts lacking critical genes for organogenesis, can replace the defective organ niches and compensate for the functional defects of recipient cells.

Alt and colleagues first illustrated intraspecies BC when they injected wild-type mouse ES cells into RAG2-deficient blastocysts. Mature B and T cells derived from donor PSCs rescued adaptive immune responses in host mice that were niche depleted in terms of lymphocyte diversity (Chen et al., 1993). Approximately two decades later, Nakauchi and colleagues showed the first evidence of interspecies pancreatic organ generation in mice using rat PSCs (Kobayashi et al., 2010). Remarkably, they also showed that the rat pancreatic tissues generated in mice *via* BC were transplantable into a recipient rat disease model and rescued its phenotype (Yamaguchi et al., 2017).

Recently, this concept has been extended to large-animal interspecies, yet other barriers such as donor cell pluripotency, cell-cell competition, and other potential xenogeneic incompatibility barriers result in low chimeric efficacies (Wu et al., 2017; Garry and Garry, 2019; de Los Angeles and Wu, 2022; Roodgar et al., 2022). Chimerism during and beyond the post-implantation stage of development presents a separate set of challenges (Figure 1). Firstly, the stage-matching of donor cells into a particular tissue niche requires extensive optimization to ensure the proliferation of engrafted cells or tissues (Cohen et al., 2018; Thomas et al., 2021). Secondly, donor cells require well-fitness to survive cell competition (Wu and Barbaric, 2021). Finally, tissues derived from donor cells need to avoid immune rejection within transplant recipients even under treatment with immune-suppressive drugs (Lu et al., 2019). Critical barriers in interspecies chimerism corresponding to its developmental stage have been summarized in Figure 1.

5.1 Blastocyst complementation in pigs

BC to date has been performed mainly in mice. This is because it is relatively easy to create an organ niche in mice due to the well-established method of creating knockout mice and from the viewpoints of experimental time and cost efficiency. However, the clinical application of BC requires the generation of organs of a size that can be transplanted into humans. BC, with livestock, has attempted to overcome this problem. With newer developments in humanized animal models and an increasingly better understanding of pluripotency across various species, interspecies BC is one of the most promising bioengineering approaches for generating transplantable human organs (Figure 2A) (Garry and Garry, 2021).

Before the advent of CRISPR-Cas9 genome editing technology, pigs had been mass-edited over several decades by classical genome editing methods to accommodate immune systems similar to humans. With the success of CRISPR-Cas9 and its related genome editing technologies, pig-human chimera formation and intraspecies conditional BC approaches, the potential to grow human-size organs in swine is no longer a distant dream (Matsunari et al., 2013; Chang et al., 2018; Hamanaka et al., 2018; Mori et al., 2019; Kitahara A. et al., 2020; Kobayashi et al., 2021; Ruiz-Estevez et al., 2021; Wen et al., 2021). Yet, this will require a three-pronged approach—1) establishment of high chimera competent-donor human ESCs/iPSCs that can survive and propagate within the pig embryo, and 2) generation of a vacant organ niche in swine using CRISPR-Cas9 genome editing. When the pig embryo can genetically be engineered to form a defective organ niche in the targeted organs, cells of human origin can show localized and targeted chimerism to form the respective organ (Rashid et al., 2014; Kano et al., 2022).

Nakauchi and colleagues have successfully created donor-derived pancreas in *PDX1* knockout (KO) apancreatic pigs by BC (Matsunari et al., 2013). This article showed the generation of host pig embryos harboring apancreatic phenotype *via* SCNT, and Kusabira Orange^{+} pig blastomeres complemented the vacant niche. In another study, Nagashima and colleagues generated various organogenesis-disabled phenotypes in organs such as kidneys, liver, and blood vessels by targeting genes like KDR (FLK1), SALL1, and HHEX1, respectively (Matsunari et al., 2020). Recently, Zhou and colleagues successfully complemented the eye using wild-type blastomeres in pig eye deficiency by the mutation of the MITF gene in the host swine (Yao et al., 2021). Garry and colleagues injected human iPSCs into *ETV2* KO pig embryos (Das et al., 2020). Although human cells can incorporate into porcine host blastocysts, many embryos initially rejected human iPSCs. They overcame this issue by overexpressing BCL2, an anti-apoptotic gene, in donor human iPSCs. Remarkably, all TIE2+ endothelial cells were derived from human PSCs in chimeric pig embryos at gestation days 17–18 (Das et al., 2020). This group also reported efficient complementation of TP53 KO human iPSCs in skeletal muscles of MYF5, MYOD, and MYF6 KO pig embryos at two distinct developmental stages—Gestation days 20 and 27 (Maeng et al., 2021). However, the degree of chimerism in these embryos was highly variable, suggesting that interspecies BC needs further optimization and technical consistency.

5.2 Blastocyst complementation in large animals

BC methodology in large animals includes swine and cattle. Sendai, Aoyagi, and colleagues generated *NANOS3* KO Wagyu bovines that lack germ cells in ovaries using SCNT. They also succeeded in creating chimeric bovine ovaries capable of producing germ cells derived from donor (*NANOS3*$^{+/+}$) Holstein blastomeres (Ideta et al., 2016). The advantage of using cattle is the similar gestation period to humans and the potential lower xenogeneic incompatibility *via* interspecific cell competition. Cattle also intrinsically harbor unique tissues identical to humans. For example, limb bones and muscles have better size compatibility with humans than swine. Large internal organ size may also benefit transplantation. However, cattle have lower prolific features for robust applications worldwide than swine, and long-term high-cost performance is the central issue.

In *ex-vivo* culture experimental systems, Belmonte and colleagues reported that human EPSCs cultured in their original medium could contribute to both embryonic and extra-embryonic lineages in

ex-vivo-cultured monkey embryos. However, the contribution of human iPSCs is, at best, 7.08% for Epiblast and 4.96% for Hypoblast (Tan et al., 2021). Attempts have been made to form interspecies chimeras among large animals other than humans. Snyder and colleagues recently reported that over-expression of *BCL2* enhances the proliferation of chimpanzees and pig-tailed macaque iPSCs in host rhesus blastocysts. Two days post-injection, most control iPSCs that lacked *BCL2* overexpression did not survive (33.3%, chimpanzee; 54.5%, pig-tailed macaque).

In contrast, almost 100% of *BCL2* overexpressing pig-tailed macaque and chimpanzee iPSCs survived upon injection (Roodgar et al., 2022). These results demonstrate the feasibility of BC as a method to create human organs in large animal organ niches or non-human primates. In contrast, the efficiency of chimera formation with the versatility of genetic modifications in large animals remains low compared to attempts in rodents. Most current studies limit our understanding of chimerism to early developmental stages. Hence, it would be interesting to study interspecies chimerism over various developmental stages—from blastocysts to post-implantation- to validate the effectiveness of host models and donor cells.

Although very promising, successful BC doesn't guarantee functional organ generation. Until recently, only three organs—the brain, the lung, and the pancreas, have been successfully complemented in a way that has produced viable adult animals phenotypically indistinguishable from that of a WT littermate (Kobayashi et al., 2010; Chang et al., 2018; Mori et al., 2019). The barrier of functional organ generation is even higher in the case of interspecies chimeras. The only functional organs generated *via* interspecies chimerism are the pancreas and thymus (Kobayashi et al., 2010; Isotani et al., 2011). Generation of functional organs by intra- or interspecies BC requires not only compatible donor cells but also appropriate host models in which the function of each target organ can be assessed in live adult animals (Kobayashi et al., 2010; Chang et al., 2018; Mori et al., 2019).

6 Swine as a model for xenotransplantation

In 1964, Dr. James D. Hardy performed one of the first xenotransplantation surgeries in modern medicine by replacing a 68-year-old patient's heart with that of a chimpanzee. Although that first patient did not survive beyond 2 h and succumbed to a hyperacute immune response, there has been tremendous progress in the field of xenotransplantation over the last sixty years: earlier this year, the first porcine-to-human heart transplantation was performed in a patient who was not a candidate for conventional allogeneic heart transplantation, and the patient survived for 2 months (Griffith et al., 2022). Much progress may be attributed to a deeper understanding of the immune system and the relative ease of gene editing (Ekser et al., 2017; Niu et al., 2017). Although many large animals have been considered, pigs are more favored for xenotransplantation mainly because of ease of breeding (with large and frequent litters) and physiologic organ and size similarity to humans. The grafts of porcine origin survived for months and, in some cases, even years upon transplantation into non-human primates. However, xeno-organ transplantation to monkeys, such as lungs, islets, heart, and kidneys, requires systemic immune suppressive drugs for the long term, and most organs are ultimately rejected (Sykes and Sachs, 2019). Strikingly, the thymokidney approach can induce tolerance across allogeneic barriers, prolong the life of the xenograft when transplanted across xenogeneic barriers, and may ultimately be used to reduce the intensity of immunosuppression for xenotransplanted organs (Yamada et al., 1999; 2000; Shimizu et al., 2005; Rivard et al., 2018).

If an organ from a wild-type pig is transplanted directly into a human patient or a non-human primate, the organ will be rejected within minutes. This form of rejection, also known as a hyperacute immune reaction, results from interactions between host-preformed natural antibodies (Nabs) with the galactose-α1,3-galactose (Gal) antigens expressed on cells of pig grafts (Platt et al., 1991). Using antibody absorption techniques, acute rejection can be delayed to a few hours, but eventually, the graft is rejected (Kozlowski et al., 1997). To overcome innate responses and non-Gal preformed antibodies in addition to T Cell dependent responses against graft, researchers have continued to modify the pig genome to 1) target non-Gal natural antibodies and 2) correct species incompatibilities between swine and primate coagulation, phagocytosis and complement regulatory proteins. These include coagulation inhibition by overexpression of anti-coagulation factors hCD39 and hCD141, that express on the surface of endothelial cells, as well as the addition of complement regulatory protein human transgenes (Lee et al., 2018; Singh et al., 2019; Kemter et al., 2020). Using serial SCNT, additional mutations have been accommodated in pigs to avoid anti-inflammatory and anti-apoptotic responses (Fischer et al., 2016). For details on various engineering strategies of an ideal humanized pig, please refer to the latest reviews by Qin and colleagues (Lu et al., 2020).

If permissive, the humanized swine model would be an ideal background for generating niche-depleted host models using the BC approach (Figure 2B). Upon complementation by donor human PSCs, the resulting organ would be suitable for humanized organs, the mixture of human cells and humanized host cells, into MHC-matched patients awaiting organ transplantation. Suppose the entire targeted organ niche that involves endoderm, mesoderm, and ectoderm derivatives would be complemented by human iPSC-derived cells. It is an ideal treatment for MHC-compatible patients awaiting organ transplantation, with minimal or no immunosuppressive approaches.

Transplanted organs should theoretically be superior to humanized porcine-derived organs in function and means of evading short- and long-term immune responses since all cells are derived from each individual patient or MHC-matched donor (Figure 2B).

7 Other efforts for organ generation

With the introduction of iPSC cell technology, the field of organoid biology expanded to provide simple yet powerful insights underlying human tissue development and, more importantly, disease modeling of pathophysiological conditions (Rossi et al., 2018; Kim et al., 2020). Various organs, such as the liver, lung, kidney, brain, intestine, and even specialized tissues such as the endometrium, have been modeled using human iPSC-derived organoids, histologically similar to human organs (Lancaster et al., 2013; Takasato et al., 2015; Turco et al., 2017; Fujii et al., 2018; Hu et al., 2018; Sachs et al., 2019). With the increasing success of human iPSC-derived organoid grafting

studies, exploring organoid engraftment in a non-human host such as a mouse is exciting. Liver and kidney organoids derived from human iPSCs induced vascularization from host mouse tissue and support host tissue function (Takebe et al., 2013; van den Berg et al., 2018). Likewise, human intestinal organoids showed robust viability when implanted into mouse mesenteric tissues (Cortez et al., 2018). In another set of studies, human iPSC and ESC cell-derived brain organoids established subcortical projections and functionally integrated them into the mouse pre-existing neural (Dong et al., 2020). Human neural crest cells differentiate into melanocytes and produce pigmented hair in a c-kit mutant mouse background that lacks melanoblasts (Cohen et al., 2016). Engraftment of human iPSCs-derived neurospheres recover motor function characterized by synapse formation and increased local myelination in a nude mice model of spinal cord injury (Nori et al., 2011). In two models of acute liver failure, human liver organoids derived from hiPSCs rescued hepatic functions and improved survival rates in mice (Nagamoto et al., 2016; Nie et al., 2018). Human ES cell-derived cerebral organoids, when transplanted into injured mouse cerebral cortices, showed high survival efficiency, robust vascularization from host tissues, and recovery of axonal projections along corticospinal tracts (Daviaud et al., 2018; Kitahara T. et al., 2020). Transplantation of human iPSC-derived endothelial-like cells in a mouse model of hindlimb ischemia caused significant improvement in postnatal vascularization (Cho et al., 2007). The engineered human iPSC-derived organoid transplantation into the defective tissue niche, particularly in the immune-privilege niche such as subrenal regions, testes, eyes, liver, and brain, holds great promise for evaluating stemness and mouse disease modeling as a next-generation personalized medicine (Harrison et al., 2014; Paquet et al., 2016; Driehuis and Clevers, 2017; Artegiani et al., 2020). Overall, human iPSC-derived organoids are compelling disease models *in vitro* and *in vivo*. However, the main challenges of organoid.

-based approaches are the lack of transplantation methods, scalability to generate whole organs, and reproducibility to generate all cell types to replicate organ function. Unless these issues are resolved, the feasibility of organoids for organ transplantation is low and will depend largely on the stage of the disease; the earlier, the better, but not likely, at the terminal stage.

Tissue engineering is another approach to generating transplantable organs. In such an approach, the goal is to grow an entire or partial organ *in vitro*. If an engineered organ could be derived from autologous cells of the recipient, the chances of rejection would be close to zero. Creating mechanically, anatomically, physiologically, and biologically compatible organs similar to native organs is ideal. In this regard, decellularization of the extracellular matrix preserves the vascular network and structural framework (Crapo and Wang, 2011). In theory, a decellularized organ scaffold would function as a barcode of cellular repopulation. After an optimal number of cells have populated an organ scaffold, a bioreactor is used to facilitate organ generation. Bioreactors are devices where biological and/or biochemical processes develop under closely monitored and tightly controlled environmental conditions (Martin et al., 2004). Decellularized scaffolds have been made for various organs, including the lung, heart, kidney, liver, intestine, bladder, corneas, limbs, pancreas, and vasculature. (Ott et al., 2008; Hashimoto et al., 2010; Petersen et al., 2010; Yang et al., 2010; Quint et al., 2011; Totonelli et al., 2012; Song et al., 2013a; Gerli et al., 2018; Goh et al., 2019).

For lung tissue engineering, Niklason and colleagues repopulated acellular rat lung scaffolds with neonatal rat lung epithelial cells and microvascular endothelium. They generated viable lung tissue for up to 1 week under *in-vitro* conditions (Petersen et al., 2010). Ott and colleagues reported that perfusion decellularization of cadaveric lungs yield intact scaffolds seeded with cells to generate bioartificial lung grafts. Upon transplantation of such bioartificial lungs into rats, the grafts maintained respiratory function for up to 7 days (Song et al., 2011). Large animal trials have also been conducted with the hope of pre-clinical applications. Cortiella and colleagues generated porcine lung scaffolds with autologous cells from porcine recipients. Within 2 weeks of transplantation, the lung grafts generated alveolar tissues with supporting vasculature without any sign of immune rejection (Nichols et al., 2018). Ott and colleagues seeded porcine decellularized lung scaffolds with human airway epithelial progenitor cells derived from human donor lungs and banked human umbilical vein endothelial cells. By repopulating porcine extracellular matrix scaffolds with human endothelial cells, they generated pulmonary vasculature with mature endothelial lining supplemented with anti-thrombotic function to enable blood perfusion. They created a functioning gas exchange graft by repopulating the epithelial surface with human epithelial progenitor cells. This graft could withstand physiological blood flow from the recipient's pulmonary circulation and exchanged gases upon ventilation during the 1-h after transplantation (Zhou et al., 2018).

Initial studies on kidney tissue engineering focused on tissue decellularization methods. Soker and colleagues decellularized porcine kidney scaffolds using a technique that sustained blood pressure up to 2 weeks post-implantation into recipient swine (Orlando et al., 2012). Decellularized monkey kidneys were also functionally effective and biocompatible (Nakayama et al., 2010). Like the lung, kidney tissue engineering also requires the recellularization of decellularized scaffolds, as shown by various studies using swine, monkey, rat, and human organs. Upon transplantation, bioengineered kidney perfused well after orthotopic transplantation into anephric rats and showed urine production (Song et al., 2013b).

Taylor and colleagues reported perfusion decellularization of the whole rat heart, thus setting the stage for other groups to examine this for large animals such as swine (Ott et al., 2008; Wainwright et al., 2010; Weymann et al., 2011; Momtahan 2016). Human-sized decellularized porcine hearts were also developed and showed recellularization of coronary vasculature and myocardium with measurable electrical activity in the decellularized scaffold (Weymann et al., 2014). Shimizu and colleagues reported heterotopic transplantation of a decellularized porcine heart scaffold with mesenchymal stem cells into recipient pigs. The scaffolds could endure surgical procedures and perform short-term coronary artery perfusion by angiography (Kitahara et al., 2016).

Bioengineering techniques of organ generation involving decellularization-recellularization approaches can be challenging in many ways. For instance, existing protocols cannot guarantee the complete removal of residual toxic products within a decellularized tissue. Furthermore, upon transplanting bioengineered tissue into a recipient organism, the degradation rate of decellularized scaffolds should be synchronous with connective tissue remodeling to prevent transplantation failure. Yet, despite its limitations, bioengineering holds excellent promise for organ generation. Further efforts for optimizing recellularization coupled with drug-or genome-editing-mediated approaches for long-term organ maintenance, particularly endothelial components, are essential for organ transplantation into patients suffering from refractory diseases.

8 Future perspectives

Various chimeric, hybrid, and bioengineering studies are being attempted in many initiatives that could be applied to the generation of human organs. Still, most fields are immature, but the successful impact is enormous. Among them, BC is one of the most promising technologies, especially for generating whole organs for transplantation. One of the critical elements for successful entire organ generation using BC is a better understanding of the mechanism of interspecies chimerism between human and host cells during the host developmental program. However, the studies of human-animal chimeras are limited by a lack of resources and ethical concerns. In particular, the contribution of human PSCs to neurogenesis and reproductive tissues within chimeric animals can have profound ethical implications (Bourret et al., 2016; Kwisda et al., 2020). These concerns can be mitigated by engineering cells to be incompetent of ethical-related lineage differentiation.

Another essential step for BC's success is preparing human iPS cells with organogenic potential. Comparative genome-wide and epigenome-wide analysis of host animal pluripotency with human iPS cells can provide critical guidance. Besides human pluripotency maintenance in human iPSCs, ES cells have also recently been derived from large animals such as pigs, cows, and sheep (Bogliotti et al., 2018; Choi et al., 2020; Vilarino et al., 2020; Kumar et al., 2021). However, except for one study involving pig blastomeres, it has been technically challenging to accurately define naïve state pluripotency and germline competence of large-animal stem cells (Matsunari et al., 2013). To overcome the incompatibilities at the molecular level for efficient interspecies chimerism and subsequent xenotransplantation, humanized large-animal models need to be established, and attempts are already beginning to emerge (Yang et al., 2016; Boettcher et al., 2020). Most recently, Wu and colleagues showed further evidence for the involvement of interspecific cell competition during early embryogenesis. This paper demonstrated the inflammatory-like pathway activation of Myd88-p65-NFkB signaling in donor human iPS cells. The loss of function of Myd88 resulted in overcoming cell competition in early embryogenesis (Zheng et al., 2021). The common feature of outcompeting donor intra- and interspecies PSCs, including ES and iPSC cells that form functional organs in host large animals, is still an open question.

Bioengineered organ transplantation is another option to solve the shortage of donors. Toward human transplantation, the generation of scaffolds based on swine adapted to human organ sizes or human iPSC-derived organoids is promising. However, the fabrication of whole organs that can withstand clinical application has not been realized. Further conceptual and technological breakthroughs are needed beyond the scaffold barcodes of decellularized organs and the self-assembling function of organoids. In this regard, the BC method has perspective advantages over the organoid and decell-recell approaches in terms of scalability, livestock, and a surgical indication of organ transplantation applicable to most end-stage refractory diseases. The advantage of decell-recell-based or organoid systems over the BC approach is the potential for a xeno-free environment and less invasiveness during transplantation. In the future, depending on the recipient's refractory disease status, the advantages and disadvantages of each technology should complement each other to provide us with multiple beneficial options.

Author contributions

HS, AS, YH, AM, YS, JT, KY and MM conceived the study. HS, AS, KY, and MM, wrote the manuscript. YH, AM, YS, JT, KY, MM revised the manuscript. All authors contributed to the article and approved the submitted version.

Funding

This work was funded by NIH-NHLBI 1R01 HL148223-01, DoD PR190557, PR191133 to MM.

Acknowledgments

We sincerely appreciate the considerate support and scientific input from Dr. Wellington Cardoso and Dr. Jianwen Que at the Columbia Center for Human Development (CCHD). We thank Kathryn K. Kennedy for her grammatical checking of the manuscript.

Conflict of interest

The authors declare that the research was conducted in the absence of any commercial or financial relationships that could be construed as a potential conflict of interest.

Publisher's note

References

Addington, C. H. W. (1932). III. Experiments on the development of chick and duck embryos cultivated *in vitro*. *Philoso. Trans. Roy. Soc. Lond. Ser. B* 221, 179–230. doi:10.1098/RSTB.1932.0003

Agarwal, Y., Beatty, C., Ho, S., Thurlow, L., Das, A., Kelly, S., et al. (2020). Development of humanized mouse and rat models with full-thickness human skin and autologous immune cells. *Sci. Rep.* 10 (1), 14598–14611. doi:10.1038/s41598-020-71548-z

Akhlaghpour, A., Taei, A., Ghadami, S. A., Bahadori, Z., Yakhkeshi, S., Molamohammadi, S., et al. (2021). Chicken interspecies chimerism unveils human pluripotency. *Stem Cell Rep.* 16, 39–55. doi:10.1016/J.STEMCR.2020.11.014

Almeida-Porada, G., Porada, C., and Zanjani, E. D. (2004). The fetal sheep: A unique model system for assessing the full differentiative potential of human stem cells. *Yonsei Med. J.* 45, 7–14. doi:10.3349/YMJ.2004.45.SUPPL.7

Andres, R. H., Horie, N., Slikker, W., Keren-Gill, H., Zhan, K., Sun, G., et al. (2011). Human neural stem cells enhance structural plasticity and axonal transport in the ischaemic brain. *Brain* 134, 1777–1789. doi:10.1093/BRAIN/AWR094

Artegiani, B., Hendriks, D., Beumer, J., Kok, R., Zheng, X., Joore, I., et al. (2020). Fast and efficient generation of knock-in human organoids using homology-independent CRISPR–Cas9 precision genome editing. *Nat. Cell Biol.* 22 (3), 321–331. doi:10.1038/s41556-020-0472-5

Azizi, S. A., Stokes, D., Augelli, B. J., DiGirolamo, C., and Prockop, D. J. (1998). Engraftment and migration of human bone marrow stromal cells implanted in the brains of albino rats - similarities to astrocyte grafts. *Proc. Natl. Acad. Sci. U. S. A.* 95, 3908–3913. doi:10.1073/pnas.95.7.3908

Bliss, T., Guzman, R., Daadi, M., and Steinberg, G. K. (2007). Cell transplantation therapy for stroke. *Stroke* 38, 817–826. doi:10.1161/01.STR.0000247888.25985.62

Boettcher, A. N., Li, Y., Ahrens, A. P., Kiupel, M., Byrne, K. A., Loving, C. L., et al. (2020). Novel engraftment and T cell differentiation of human hematopoietic cells in ART−/−IL2RG−/Y SCID pigs. *Front. Immunol.* 11, 100. doi:10.3389/fimmu.2020.00100

Bogliotti, Y. S., Wu, J., Vilarino, M., Okamura, D., Soto, D. A., Zhong, C., et al. (2018). Efficient derivation of stable primed pluripotent embryonic stem cells from bovine blastocysts. *Proc. Natl. Acad. Sci. U. S. A.* 115, 2090–2095. doi:10.1073/pnas.1716161115

Boulland, J. L., Halasi, G., Kasumacic, N., and Glover, J. C. (2010). Xenotransplantation of human stem cells into the chicken embryo. *J. Vis. Exp.*, 2071. doi:10.3791/2071

Bourret, R., Martinez, E., Vialla, F., Giquel, C., Thonnat-Marin, A., and de Vos, J. (2016). Human–animal chimeras: Ethical issues about farming chimeric animals bearing human organs. *Stem Cell Res. Ther.* 7, 87. doi:10.1186/S13287-016-0345-9

Bowling, S., Lawlor, K., and Rodríguez, T. A. (2019). Cell competition: The winners and losers of fitness selection. *Dev. Camb.* 146, dev167486. doi:10.1242/dev.167486

Bradley, A. (1991). Modifying the mammalian genome by gene targeting. *Curr. Opin. Biotechnol.* 2, 823–829. doi:10.1016/S0958-1669(05)80114-4

Brüngger, A., Hubler, M., Rohr, H. P., and Brungger, A. (1984). Human skin grafts on athymic nude rats. An experimental model for dermatological research. *Exp. Cell Biol.* 52, 122–124. doi:10.1159/000163246

Chan, Y. S., Göke, J., Ng, J. H., Lu, X., Gonzales, K. A. U., Tan, C. P., et al. (2013). Induction of a human pluripotent state with distinct regulatory circuitry that resembles preimplantation epiblast. *Cell Stem Cell* 13, 663–675. doi:10.1016/j.stem.2013.11.015

Chang, A. N., Liang, Z., Dai, H. Q., Chapdelaine-Williams, A. M., Andrews, N., Bronson, R. T., et al. (2018). Neural blastocyst complementation enables mouse forebrain organogenesis. *Nature* 563, 126–130. doi:10.1038/S41586-018-0586-0

Chang, K. H., Lim, J. M., Kang, S. K., Lee, B. C., Moon, S. Y., and Hwang, W. S. (2003). Blastocyst formation, karyotype, and mitochondrial DNA of interspecies embryos derived from nuclear transfer of human cord fibroblasts into enucleated bovine oocytes. *Fertil. Steril.* 80, 1380–1387. doi:10.1016/j.fertnstert.2003.07.006

Chen, J., Lansford, R., Stewart, V., Young, F., and Alt, F. W. (1993). RAG-2-deficient blastocyst complementation: An assay of gene function in lymphocyte development. *Proc. Natl. Acad. Sci. U. S. A.* 90, 4528–4532. doi:10.1073/PNAS.90.10.4528

Chen, Y., He, Z. X., Liu, A., Wang, K., Mao, W. W., Chu, J. X., et al. (2003). Embryonic stem cells generated by nuclear transfer of human somatic nuclei into rabbit oocytes. *Cell Res.* 13 (4), 251–263. doi:10.1038/sj.cr.7290170

Cho, S. W., Moon, S. H., Lee, S. H., Kang, S. W., Kim, J., Lim, J. M., et al. (2007). Improvement of postnatal neovascularization by human embryonic stem cell–derived endothelial-like cell transplantation in a mouse model of hindlimb ischemia. *Circulation* 116, 2409–2419. doi:10.1161/CIRCULATIONAHA.106.687038

Choi, J., Huebner, A. J., Clement, K., Walsh, R. M., Savol, A., Lin, K., et al. (2017). Prolonged Mek1/2 suppression impairs the developmental potential of embryonic stem cells. *Nature* 548, 219–223. doi:10.1038/NATURE23274

Choi, K. H., Lee, D. K., Oh, J. N., Kim, S. H., Lee, M., Woo, S. H., et al. (2020). Pluripotent pig embryonic stem cell lines originating from *in vitro*-fertilized and parthenogenetic embryos. *Stem Cell Res.* 49, 102093. doi:10.1016/J.SCR.2020.102093

Chong, J. J. H., Yang, X., Don, C. W., Minami, E., Liu, Y. W., Weyers, J. J., et al. (2014). Human embryonic-stem-cell-derived cardiomyocytes regenerate non-human primate hearts. *Nature* 510, 7504273–7504277. doi:10.1038/nature13233

Clavería, C., Giovinazzo, G., Sierra, R., and Torres, M. (2013). Myc-driven endogenous cell competition in the early mammalian embryo. *Nature* 500, 746039–746044. doi:10.1038/nature12389

Clavería, C., and Torres, M. (2016). Cell competition: Mechanisms and physiological roles. *Annu. Rev. Cell Dev. Biol.* 32, 411–439. doi:10.1146/ANNUREV-CELLBIO-111315-125142

Cloney, K., and Franz-Odendaal, T. A. (2015). Optimized Ex-ovo culturing of chick embryos to advanced stages of development. *J. Vis. Exp.*, 52129. doi:10.3791/52129

Cohen, M. A., Markoulaki, S., and Jaenisch, R. (2018). Matched developmental timing of donor cells with the host is crucial for chimera formation. *Stem Cell Rep.* 10, 1445–1452. doi:10.1016/J.STEMCR.2018.03.004

Cohen, M. A., Wert, K. J., Goldmann, J., Markoulaki, S., Buganim, Y., Fu, D., et al. (2016). Human neural crest cells contribute to coat pigmentation in interspecies chimeras after *in utero* injection into mouse embryos. *Proc. Natl. Acad. Sci. U. S. A.* 113, 1570–1575. doi:10.1073/pnas.1525518113

Cooper, D. K. C., Ekser, B., Ramsoondar, J., Phelps, C., and Ayares, D. (2016). The role of genetically-engineered pigs in xenotransplantation research. *J. Pathol.* 238, 288–299. doi:10.1002/PATH.4635

Coppiello, G. P. B., Moya-Jodar, M., Abizanda, G., Barreda, C., Iglesias, E., Linares, J., et al. (2022). *In vivo* generation of heart and vascular system by blastocyst complementation. *BioRxiv*, 2022.10.04.510637. doi:10.1101/2022.10.04.510637

Cortez, A. R., Poling, H. M., Brown, N. E., Singh, A., Mahe, M. M., and Helmrath, M. A. (2018). Transplantation of human intestinal organoids into the mouse mesentery: A more physiologic and anatomic engraftment site. *Surgery* 164, 643–650. doi:10.1016/J.SURG.2018.04.048

Couly, G. F., and le Douarin, N. M. (1985). Mapping of the early neural primordium in quail-chick chimeras: I. Developmental relationships between placodes, facial ectoderm, and prosencephalon. *Dev. Biol.* 110, 422–439. doi:10.1016/0012-1606(85)90101-0

Crapo, P. M., and Wang, Y. (2011). Hydrostatic pressure independently increases elastin and collagen co-expression in small-diameter engineered arterial constructs. *J. Biomed. Mater Res. A* 96 A, 673–681. doi:10.1002/jbm.a.33019

Dahéron, L., Opitz, S. L., Zaehres, H., Lensch, W. M., Andrews, P. W., Itskovitz-Eldor, J., et al. (2004). LIF/STAT3 signaling fails to maintain self-renewal of human embryonic stem cells. *Stem Cells* 22, 770–778. doi:10.1634/STEMCELLS.22-5-770

Das, S., Koyano-Nakagawa, N., Gafni, O., Maeng, G., Singh, B. N., Rasmussen, T., et al. (2020). Generation of human endothelium in pig embryos deficient in ETV2. *Nat. Biotechnol.* 38, 297–302. doi:10.1038/s41587-019-0373-y

Daviaud, N., Friedel, R. H., and Zou, H. (2018). Vascularization and engraftment of transplanted human cerebral organoids in mouse cortex. *eNeuro* 5, ENEURO.0219–18.2018. doi:10.1523/ENEURO.0219-18.2018

de La Cova, C., Abril, M., Bellosta, P., Gallant, P., and Johnston, L. A. (2004). Drosophila myc regulates organ size by inducing cell competition. *Cell* 117, 107–116. doi:10.1016/S0092-8674(04)00214-4

de Los Angeles, A., and Wu, J. (2022). New concepts for generating interspecies chimeras using human pluripotent stem cells. *Protein Cell* 13, 234–238. doi:10.1007/s13238-021-00880-5

Díaz-Díaz, C., Fernandez de Manuel, L., Jimenez-Carretero, D., Montoya, M. C., Clavería, C., and Torres, M. (2017). Pluripotency surveillance by myc-driven competitive elimination of differentiating cells. *Dev. Cell* 42, 585–599.e4. doi:10.1016/J.DEVCEL.2017.08.011

Dong, X., Xu, S. B., Chen, X., Tao, M., Tang, X. Y., Fang, K. H., et al. (2020). Human cerebral organoids establish subcortical projections in the mouse brain after transplantation. *Mol. Psychiatry* 26, 2964–2976. doi:10.1038/s41380-020-00910-4

Driehuis, E., and Clevers, H. (2017). CRISPR/Cas 9 genome editing and its applications in organoids. *Am. J. Physiol. Gastrointest. Liver Physiol.* 312, G257–G265. doi:10.1152/ajpgi.00410.2016

Ekser, B., Li, P., and Cooper, D. K. C. (2017). Xenotransplantation: PAST, present, and future. *Curr. Opin. Organ Transpl.* 22, 513–521. doi:10.1097/MOT.0000000000000463

Evans, M. J., and Kaufman, M. H. (1981). Establishment in culture of pluripotential cells from mouse embryos. *Nature* 292, 154–156. doi:10.1038/292154A0

Fehilly, C. B., Willadsen, S. M., and Tucker, E. M. (1984). Interspecific chimaerism between sheep and goat. *Nature* 307, 634–636. doi:10.1038/307634a0

Fischer, K., Kraner-Scheiber, S., Petersen, B., Rieblinger, B., Buermann, A., Flisikowska, T., et al. (2016). Efficient production of multi-modified pigs for xenotransplantation by 'combineering', gene stacking and gene editing. *Sci. Rep.* 6, 29081. doi:10.1038/SREP29081

Freedman, B. S. (2018). Hopes and difficulties for blastocyst complementation. *Nephron* 138, 42–47. doi:10.1159/000480370

Fu, R., Yu, D., Ren, J., Li, C., Wang, J., Feng, G., et al. (2020). Domesticated cynomolgus monkey embryonic stem cells allow the generation of neonatal interspecies chimeric pigs. *Protein Cell* 11 (2), 97–107. doi:10.1007/S13238-019-00676-8/TABLES/2

Fujii, M., Matano, M., Toshimitsu, K., Takano, A., Mikami, Y., Nishikori, S., et al. (2018). Human intestinal organoids maintain self-renewal capacity and cellular diversity in niche-inspired culture condition. *Cell Stem Cell* 23, 787–793.e6. doi:10.1016/J.STEM.2018.11.016

Gafni, O., Weinberger, L., Mansour, A. A., Manor, Y. S., Chomsky, E., Ben-Yosef, D., et al. (2013). Derivation of novel human ground state naive pluripotent stem cells. *Nature* 504, 282–286. doi:10.1038/nature12745

Gao, X., Nowak-Imialek, M., Chen, X., Chen, D., Herrmann, D., Ruan, D., et al. (2019). Establishment of porcine and human expanded potential stem cells. *Nat. Cell Biol.* 21, 687–699. doi:10.1038/s41556-019-0333-2

Garry, D. J., and Garry, M. G. (2019). Interspecies chimeras and the generation of humanized organs. *Circ. Res.* 124, 23–25. doi:10.1161/CIRCRESAHA.118.314189

Garry, D. J., and Garry, M. G. (2021). Interspecies chimeras as a platform for exogenic organ production and transplantation. *Exp. Biol. Med.* 246, 1838–1844. doi:10.1177/15353702211024948

Gerli, M. F. M., Guyette, J. P., Evangelista-Leite, D., Ghoshhajra, B. B., and Ott, H. C. (2018). Perfusion decellularization of a human limb: A novel platform for composite tissue engineering and reconstructive surgery. *PLoS One* 13, e0191497. doi:10.1371/JOURNAL.PONE.0191497

Gibbs, R. A., Rogers, J., Katze, M. G., Bumgarner, R., Weinstock, G. M., Mardis, E. R., et al. (2007). Evolutionary and biomedical insights from the rhesus macaque genome. *Science* 316, 222–234. doi:10.1126/SCIENCE.1139247/SUPPL_FILE/GIBBS.SOM.PDF

Gilhar, A., Etzioni, A., and Krueger, G. G. (1990). Hair growth in human split-thickness skin grafts transplanted onto nude rats: The role of cyclosporin. *Dermatologica* 181, 117–121. doi:10.1159/000247898

Gilhar, A., Wojciechowski, Z. J., Piepkorn, M. W., Spangrude, G. J., Roberts, L. K., and Krueger, D. G. G. (1986). Description of and treatment to inhibit the rejection of human split-thickness skin grafts by congenitally athymic (nude) rats. *Exp. Cell Biol.* 54, 263–274. doi:10.1159/000163365

Giwa, S., Lewis, J. K., Alvarez, L., Langer, R., Roth, A. E., Church, G. M., et al. (2017). The promise of organ and tissue preservation to transform medicine. *Nat. Biotechnol.* 35 (6), 530–542. doi:10.1038/nbt.3889

Goh, S.-K., Bertera, S., Vaidya, V., Dumpe, S., Barner, S., Mathew, S., et al. (2019). Development of perfusion bioreactor for whole organ engineering — A culture system that enhances cellular engraftment, survival and phenotype of repopulated pancreas. *World Sci. Technol.* 6, 118–134. doi:10.1142/S2339547818500085.06

Goldstein, R. S. (2010). Transplantation of human embryonic stem cells and derivatives to the chick embryo. *Methods Mol. Biol.* 584, 367–385. doi:10.1007/978-1-60761-369-5_20

Graham, D. M. (2017). Beasts of burden: Large animal chimeras using human pluripotent stem cells. *Lab. Anim.* 46 (4), 77. doi:10.1038/laban.1241

Greely, H. T., and Farahany, N. A. (2021). Advancing the ethical dialogue about monkey/human chimeric embryos. *Cell* 184, 1962–1963. doi:10.1016/J.CELL.2021.03.044

Griffith, B. P., Goerlich, C. E., Singh, A. K., Rothblatt, M., Lau, C. L., Shah, A., et al. (2022). Genetically modified porcine-to-human cardiac xenotransplantation. *N. Engl. J. Med.* 387, 35–44. doi:10.1056/NEJMoa2201422

Grinnemo, K. H., Månsson, A., Dellgren, G., Klingberg, D., Wardell, E., Drvota, V., et al. (2004). Xenoreactivity and engraftment of human mesenchymal stem cells transplanted into infarcted rat myocardium. *J. Thorac. Cardiovasc. Surg.* 127, 1293–1300. doi:10.1016/j.jtcvs.2003.07.037

Hamanaka, S., Umino, A., Sato, H., Hayama, T., Yanagida, A., Mizuno, N., et al. (2018). Generation of vascular endothelial cells and hematopoietic cells by blastocyst complementation. *Stem Cell Rep.* 11, 988–997. doi:10.1016/J.STEMCR.2018.08.015

Hamburger, V., and Hamilton, H. L. (1951). A series of normal stages in the development of the chick embryo. *J. Morphol.* 88, 49–92. doi:10.1002/JMOR.1050880104

Harrison, M. M., Jenkins, B. v., O'Connor-Giles, K. M., and Wildonger, J. (2014). A CRISPR view of development. *Genes Dev.* 28, 1859–1872. doi:10.1101/GAD.248252.114

Hashimoto, M., and Sasaki, H. (2020). Cell competition controls differentiation in mouse embryos and stem cells. *Curr. Opin. Cell Biol.* 67, 1–8. doi:10.1016/J.CEB.2020.07.001

Hashimoto, Y., Funamoto, S., Sasaki, S., Honda, T., Hattori, S., Nam, K., et al. (2010). Preparation and characterization of decellularized cornea using high-hydrostatic pressurization for corneal tissue engineering. *Biomaterials* 31, 3941–3948. doi:10.1016/J.BIOMATERIALS.2010.01.122

He, D., Zhang, J., Wu, W., Yi, N., He, W., Lu, P., et al. (2019). A novel immunodeficient rat model supports human lung cancer xenografts. *FASEB J.* 33, 140–150. doi:10.1096/FJ.201800102RR

Hu, H., Gehart, H., Artegiani, B., Löpez-Iglesias, C., Dekkers, F., Basak, O., et al. (2018). Long-term expansion of functional mouse and human hepatocytes as 3D organoids. *Cell* 175, 1591–1606.e19. doi:10.1016/J.CELL.2018.11.013

Hu, Z., Li, H., Jiang, H., Ren, Y., Yu, X., Qiu, J., et al. (2020). Transient inhibition of mTOR in human pluripotent stem cells enables robust formation of mouse-human chimeric embryos. *Sci. Adv.* 6, eaaz0298–311. doi:10.1126/sciadv.aaz0298

Ideta, A., Yamashita, S., Seki-Soma, M., Yamaguchi, R., Chiba, S., Komaki, H., et al. (2016). Generation of exogenous germ cells in the ovaries of sterile NANOS3-null beef cattle. *Sci. Rep.* 6, 24983. doi:10.1038/srep24983

Isotani, A., Hatayama, H., Kaseda, K., Ikawa, M., and Okabe, M. (2011). Formation of a thymus from rat ES cells in xenogeneic nude mouse↔rat ES chimeras. *Genes Cells* 16, 397–405. doi:10.1111/J.1365-2443.2011.01495.X

James, D., Noggle, S. A., Swigut, T., and Brivanlou, A. H. (2006). Contribution of human embryonic stem cells to mouse blastocysts. *Dev. Biol.* 295, 90–102. doi:10.1016/J.YDBIO.2006.03.026

Jiang, Y., Kelly, R., Peters, A., Fulka, H., Dickinson, A., Mitchell, D. A., et al. (2011). Interspecies somatic cell nuclear transfer is dependent on compatible mitochondrial DNA and reprogramming factors. *PLoS One* 6, 14805. doi:10.1371/JOURNAL.PONE.0014805

Kano, M., Mizutani, E., Homma, S., Masaki, H., and Nakauchi, H. (2022). Xenotransplantation and interspecies organogenesis: Current status and issues. *Front. Endocrinol. (Lausanne)* 13, 963282. doi:10.3389/FENDO.2022.963282

Kemter, E., Schnieke, A., Fischer, K., Cowan, P. J., and Wolf, E. (2020). Xeno-organ donor pigs with multiple genetic modifications - the more the better? *Curr. Opin. Genet. Dev.* 64, 60–65. doi:10.1016/J.GDE.2020.05.034

Kikuchi, T., Morizane, A., Doi, D., Magotani, H., Onoe, H., Hayashi, T., et al. (2017). Human iPS cell-derived dopaminergic neurons function in a primate Parkinson's disease model. *Nature* 548 (548), 7669592–7669596. doi:10.1038/nature23664

Kim, J., Koo, B. K., and Knoblich, J. A. (2020). Human organoids: Model systems for human biology and medicine. *Nat. Rev. Mol. Cell Biol.* 21 (10 21), 571–584. doi:10.1038/s41580-020-0259-3

Kitahara, A., Ran, Q., Oda, K., Yasue, A., Abe, M., Ye, X., et al. (2020). Generation of lungs by blastocyst complementation in apneumic fgf10-deficient mice. *Cell Rep.* 31, 107626. doi:10.1016/J.CELREP.2020.107626

Kitahara, H., Yagi, H., Tajima, K., Okamoto, K., Yoshitake, A., Aeba, R., et al. (2016). Heterotopic transplantation of a decellularized and recellularized whole porcine heart. *Interact. Cardiovasc Thorac. Surg.* 22, 571–579. doi:10.1093/ICVTS/IVW022

Kitahara, T., Sakaguchi, H., Morizane, A., Kikuchi, T., Miyamoto, S., and Takahashi, J. (2020). Axonal extensions along corticospinal tracts from transplanted human cerebral organoids. *Stem Cell Rep.* 15, 467–481. doi:10.1016/J.STEMCR.2020.06.016

Kobayashi, T., Goto, T., Oikawa, M., Sanbo, M., Yoshida, F., Terada, R., et al. (2021). Blastocyst complementation using Prdm14-deficient rats enables efficient germline transmission and generation of functional mouse spermatids in rats. *Nat. Commun.* 12 (1), 1328. doi:10.1038/s41467-021-21557-x

Kobayashi, T., Yamaguchi, T., Hamanaka, S., Kato-Itoh, M., Yamazaki, Y., Ibata, M., et al. (2010). Generation of rat pancreas in mouse by interspecific blastocyst injection of pluripotent stem cells. *Cell* 142, 787–799. doi:10.1016/j.cell.2010.07.039

Kozlowski, T., Fuchimoto, Y., Monroy, R., Bailin, M., Martinez-Ruiz, R., Foley, A., et al. (1997). Apheresis and column absorption for specific removal of Gal-alpha-1,3 Gal natural antibodies in a pig-to-baboon model. *Transpl. Proc.* 29, 961. doi:10.1016/S0041-1345(96)00299-0

Kumar, D., Talluri, T. R., Selokar, N. L., Hyder, I., and Kues, W. A. (2021). Perspectives of pluripotent stem cells in livestock. *World J. Stem Cells* 13, 1–29. doi:10.4252/WJSC.V13.I1.1

Kwisda, K., White, L., and Hübner, D. (2020). Ethical arguments concerning human-animal chimera research: A systematic review. *BMC Med. Ethics* 21, 24–14. doi:10.1186/s12910-020-00465-7

Lancaster, M. A., Renner, M., Martin, C. A., Wenzel, D., Bicknell, L. S., Hurles, M. E., et al. (2013). Cerebral organoids model human brain development and microcephaly. *Nature* 501, 373–379. doi:10.1038/NATURE12517

Laporte, C., Tubbs, E., Cristante, J., Gauchez, A. S., Pesenti, S., Lamarche, F., et al. (2019). Human mesenchymal stem cells improve rat islet functionality under cytokine stress with combined upregulation of heme oxygenase-1 and ferritin. *Stem Cell Res. Ther.* 10, 85–12. doi:10.1186/s13287-019-1190-4

Lee, D. H., Eun, Y. K., Park, S., Ji, H. P., Kim, S. K., Cho, B. K., et al. (2006). Reclosure of surgically induced spinal open neural tube defects by the intraamniotic injection of human embryonic stem cells in chick embryos 24 hours after lesion induction. *J. Neurosurg.* 105, 127–133. doi:10.3171/PED.2006.105.2.127

Lee, D. H., Park, S., Kim, E. Y., Kim, S. K., Chung, Y. N., Cho, B. K., et al. (2004). Enhancement of re-closure capacity by the intra-amniotic injection of human embryonic stem cells in surgically induced spinal open neural tube defects in chick embryos. *Neurosci. Lett.* 364, 98–100. doi:10.1016/j.neulet.2004.04.033

Lee, S. J., Kim, J. S., Chee, H. K., Yun, I. J., Park, K. S., Yang, H. S., et al. (2018). Seven years of experiences of preclinical experiments of xeno-heart transplantation of pig to non-human primate (cynomolgus monkey). *Transpl. Proc.* 50, 1167–1171. doi:10.1016/J.TRANSPROCEED.2018.01.041

Liechty, K. W., Mackenzie, T. C., Shaaban, A. F., Radu, A., Moseley, A. M. B., Deans, R., et al. (2000). Human mesenchymal stem cells engraft and demonstrate site-specific differentiation after *in utero* transplantation in sheep. *Nat. Med.* 6, 1282–1286. doi:10.1038/81395

Liu, X., Nefzger, C. M., Rossello, F. J., Chen, J., Knaupp, A. S., Firas, J., et al. (2017). Comprehensive characterization of distinct states of human naive pluripotency generated by reprogramming. *Nat. Methods* 14, 1055–1062. doi:10.1038/nmeth.4436

Lu, T., Yang, B., Wang, R., and Qin, C. (2020). Xenotransplantation: Current status in preclinical research. *Front. Immunol.* 10, 3060. doi:10.3389/fimmu.2019.03060

Lu, Y., Zhou, Y., Ju, R., and Chen, J. (2019). Human-animal chimeras for autologous organ transplantation: Technological advances and future perspectives. *Ann. Transl. Med.* 7, 576. doi:10.21037/ATM.2019.10.13

Maeng, G., Das, S., Greising, S. M., Gong, W., Singh, B. N., Kren, S., et al. (2021). Humanized skeletal muscle in MYF5/MYOD/MYF6-null pig embryos. *Nat. Biomed. Eng.* 5, 805–814. doi:10.1038/s41551-021-00693-1

Mansour, S. L., Thomas, K. R., Deng, C., and Capecchi, M. R. (1990). Introduction of a lacZ reporter gene into the mouse int-2 locus by homologous recombination. *Proc. Natl. Acad. Sci. U. S. A.* 87, 7688–7692. doi:10.1073/PNAS.87.19.7688

Martello, G., and Smith, A. (2014). The nature of embryonic stem cells. *Annu. Rev. Cell Dev. Biol.* 30, 647–675. doi:10.1146/ANNUREV-CELLBIO-100913-013116

Martin, G. R. (1981). Isolation of a pluripotent cell line from early mouse embryos cultured in medium conditioned by teratocarcinoma stem cells. *Proc. Natl. Acad. Sci.* 78, 7634–7638. doi:10.1073/PNAS.78.12.7634

Martin, I., Wendt, D., and Heberer, M. (2004). The role of bioreactors in tissue engineering. *Trends Biotechnol.* 22, 80–86. doi:10.1016/j.tibtech.2003.12.001

Martyn, I., Kanno, T. Y., Ruzo, A., Siggia, E. D., and Brivanlou, A. H. (2018). Self-organization of a human organizer by combined Wnt and Nodal signalling. *Nature* 558, 132–135. doi:10.1038/s41586-018-0150-y

Mascetti, V. L., and Pedersen, R. A. (2016). Human-mouse chimerism validates human stem cell pluripotency. *Cell Stem Cell* 18, 67–72. doi:10.1016/J.STEM.2015.11.017

Matsunari, H., Nagashima, H., Watanabe, M., Umeyama, K., Nakano, K., Nagaya, M., et al. (2013). Blastocyst complementation generates exogenic pancreas *in vivo* in apancreatic cloned pigs. *Proc. Natl. Acad. Sci. U. S. A.* 110, 4557–4562. doi:10.1073/pnas.1222902110

Matsunari, H., Watanabe, M., Hasegawa, K., Uchikura, A., Nakano, K., Umeyama, K., et al. (2020). Compensation of disabled organogeneses in genetically modified pig fetuses by blastocyst complementation. *Stem Cell Rep.* 14, 21–33. doi:10.1016/j.stemcr.2019.11.008

Merino, M. M., Levayer, R., and Moreno, E. (2016). Survival of the fittest: Essential roles of cell competition in development, aging, and cancer. *Trends Cell Biol.* 26, 776–788. doi:10.1016/j.tcb.2016.05.009

Momtahan, N. (2016). Extracellular matrix from whole porcine heart decellularization for cardiac tissue engineering. Theses and Dissertations. Available at: https://scholarsarchive.byu.edu/etd/6225 (Accessed October 11, 2022).

Moreno, E., and Basler, K. (2004). dMyc transforms cells into super-competitors. *Cell* 117, 117–129. doi:10.1016/S0092-8674(04)00262-4

Mori, M., Furuhashi, K., Danielsson, J. A., Hirata, Y., Kakiuchi, M., Lin, C. S., et al. (2019). Generation of functional lungs via conditional blastocyst complementation using pluripotent stem cells. *Nat. Med.* 25 (11), 1691–1698. doi:10.1038/s41591-019-0635-8

Morizane, A., Kikuchi, T., Hayashi, T., Mizuma, H., Takara, S., Doi, H., et al. (2017). MHC matching improves engraftment of iPSC-derived neurons in non-human primates. *Nat. Commun.* 8 (1), 385–412. doi:10.1038/s41467-017-00926-5

Mystkowska, E. T. (1975). Development of mouse—Bank vole interspecific chimaeric embryos. *Development* 33, 731–744. doi:10.1242/DEV.33.3.731

Nagamoto, Y., Takayama, K., Ohashi, K., Okamoto, R., Sakurai, F., Tachibana, M., et al. (2016). Transplantation of a human iPSC-derived hepatocyte sheet increases survival in mice with acute liver failure. *J. Hepatol.* 64, 1068–1075. doi:10.1016/J.JHEP.2016.01.004

Nagashima, H., and Matsunari, H. (2016). Growing human organs in pigs-A dream or reality? *Theriogenology* 86, 422–426. doi:10.1016/J.THERIOGENOLOGY.2016.04.056

Nakayama, K. H., Batchelder, C. A., Lee, C. I., and Tarantal, A. F. (2010). Decellularized rhesus monkey kidney as a three-dimensional scaffold for renal tissue engineering. *Tissue Eng. Part A* 16, 2207–2216. doi:10.1089/TEN.TEA.2009.0602

Nanda, I., Shan, Z., Schartl, M., Burt, D. W., Koehler, M., Nothwang, G., et al. (1999). 300 million years of conserved synteny between chicken Z and human chromosome 9. *Nat. Genet.* 21 (3), 258–259. doi:10.1038/6769

Nei, M., Xu, P., and Glazko, G. (2001). Estimation of divergence times from multiprotein sequences for a few mammalian species and several distantly related organisms. *Proc. Natl. Acad. Sci. U. S. A.* 98, 2497–2502. doi:10.1073/pnas.051611498

Nichols, J. E., la Francesca, S., Niles, J. A., Vega, S. P., Argueta, L. B., Frank, L., et al. (2018). Production and transplantation of bioengineered lung into a large-animal model. *Sci. Transl. Med.* 10, eaao3926. doi:10.1126/SCITRANSLMED.AAO3926

Nichols, J., and Smith, A. (2009). Naive and primed pluripotent states. *Cell Stem Cell* 4, 487–492. doi:10.1016/j.stem.2009.05.015

Nie, Y. Z., Zheng, Y. W., Ogawa, M., Miyagi, E., and Taniguchi, H. (2018). Human liver organoids generated with single donor-derived multiple cells rescue mice from acute liver failure. *Stem Cell Res. Ther.* 9, 5–12. doi:10.1186/s13287-017-0749-1

Niu, D., Wei, H. J., Lin, L., George, H., Wang, T., Lee, I. H., et al. (2017). Inactivation of porcine endogenous retrovirus in pigs using CRISPR-Cas9. *Science* 357, 1303–1307. doi:10.1126/science.aan4187

Niu, Y., Shen, B., Cui, Y., Chen, Y., Wang, J., Wang, L., et al. (2014). Generation of gene-modified cynomolgus monkey via Cas9/RNA-mediated gene targeting in one-cell embryos. *Cell* 156, 836–843. doi:10.1016/j.cell.2014.01.027

Nori, S., Okada, Y., Yasuda, A., Tsuji, O., Takahashi, Y., Kobayashi, Y., et al. (2011). Grafted human-induced pluripotent stem-cell-derived neurospheres promote motor functional recovery after spinal cord injury in mice. *Proc. Natl. Acad. Sci. U. S. A.* 108, 16825–16830. doi:10.1073/pnas.1108077108

Noto, F. K., Sangodkar, J., Adedeji, B. T., Moody, S., McClain, C. B., Tong, M., et al. (2020). The SRG rat, a Sprague-Dawley Rag2/Il2rg double-knockout validated for human tumor oncology studies. *PLoS One* 15, e0240169. doi:10.1371/JOURNAL.PONE.0240169

Orlando, G., Farney, A. C., Iskandar, S. S., Mirmalek-Sani, S. H., Sullivan, D. C., Moran, E., et al. (2012). Production and implantation of renal extracellular matrix scaffolds from porcine kidneys as a platform for renal bioengineering investigations. *Ann. Surg.* 256, 363–370. doi:10.1097/SLA.0B013E31825A02AB

Ott, H. C., Matthiesen, T. S., Goh, S. K., Black, L. D., Kren, S. M., Netoff, T. I., et al. (2008). Perfusion-decellularized matrix: Using nature's platform to engineer a bioartificial heart. *Nat. Med.* 14, 213–221. doi:10.1038/nm1684

Paquet, D., Kwart, D., Chen, A., Sproul, A., Jacob, S., Teo, S., et al. (2016). Efficient introduction of specific homozygous and heterozygous mutations using CRISPR/Cas9. *Nature* 533, 125–129. doi:10.1038/NATURE17664

Pastor, W. A., Chen, D., Liu, W., Kim, R., Sahakyan, A., Lukianchikov, A., et al. (2016). Naïve human pluripotent cells feature a methylation landscape devoid of blastocyst or germline memory. *Cell Stem Cell* 18, 323–329. doi:10.1016/J.STEM.2016.01.019

Petersen, T. H., Calle, E. A., Zhao, L., Lee, E. J., Gui, L., Raredon, M. S. B., et al. (2010). Tissue-engineered lungs for *in vivo* implantation. *Science* 329, 538–541. doi:10.1126/SCIENCE.1189345

Platt, J. L., Lindman, B. J., Geller, R. L., Noreen, H. J., Swanson, J. L., Dalmasso, A. P., et al. (1991). The role of natural antibodies in the activation of xenogenic endothelial cells. *Transplantation* 52, 1037–1043. doi:10.1097/00007890-199112000-00019

Quint, C., Kondo, Y., Manson, R. J., Lawson, J. H., Dardik, A., and Niklason, L. E. (2011). Decellularized tissue-engineered blood vessel as an arterial conduit. *Proc. Natl. Acad. Sci. U. S. A.* 108, 9214–9219. doi:10.1073/pnas.1019506108

Rashid, T., Kobayashi, T., and Nakauchi, H. (2014). Revisiting the flight of icarus: Making human organs from PSCs with large animal chimeras. *Cell Stem Cell* 15, 406–409. doi:10.1016/J.STEM.2014.09.013

Rivard, C. J., Tanabe, T., Lanaspa, M. A., Watanabe, H., Nomura, S., Andres-Hernando, A., et al. (2018). Upregulation of CD80 on glomerular podocytes plays an important role in development of proteinuria following pig-to-baboon xeno-renal transplantation - an experimental study. *Transpl. Int.* 31, 1164–1177. doi:10.1111/TRI.13273

Robertson, E. J. (1991). Using embryonic stem cells to introduce mutations into the mouse germ line. *Biol. Reprod.* 44, 238–245. doi:10.1095/BIOLREPROD44.2.238

Rodriguez-Osorio, N., Urrego, R., Cibelli, J. B., Eilertsen, K., and Memili, E. (2012). Reprogramming mammalian somatic cells. *Theriogenology* 78, 1869–1886. doi:10.1016/J.THERIOGENOLOGY.2012.05.030

Roodgar, M., Suchy, F. P., Nguyen, L. H., Bajpai, V. K., Sinha, R., Vilches-Moure, J. G., et al. (2022). Chimpanzee and pig-tailed macaque iPSCs: Improved culture and generation of primate cross-species embryos. *Cell Rep.* 40, 111264. doi:10.1016/J.CELREP.2022.111264

Rossi, G., Manfrin, A., and Lutolf, M. P. (2018). Progress and potential in organoid research. *Nat. Rev. Genet.* 19, 671–687. doi:10.1038/S41576-018-0051-9

Ruiz-Estevez, M., Crane, A. T., Rodriguez-Villamil, P., Ongaratto, F. L., You, Y., Steevens, A. R., et al. (2021). Liver development is restored by blastocyst complementation of HHEX knockout in mice and pigs. *Stem Cell Res. Ther.* 12, 292–313. doi:10.1186/s13287-021-02348-z

Sachs, N., Papaspyropoulos, A., Ommen, D. D. Z., Heo, I., Böttinger, L., Klay, D., et al. (2019). Long-term expanding human airway organoids for disease modeling. *EMBO J.* 38, e100300. doi:10.15252/EMBJ.2018100300

Sancho, M., Di-Gregorio, A., George, N., Pozzi, S., Sánchez, J. M., Pernaute, B., et al. (2013). Competitive interactions eliminate unfit embryonic stem cells at the onset of differentiation. *Dev. Cell* 26, 19–30. doi:10.1016/J.DEVCEL.2013.06.012

Sato, Y., Araki, H., Kato, J., Nakamura, K., Kawano, Y., Kobune, M., et al. (2005). Human mesenchymal stem cells xenografted directly to rat liver are differentiated into human hepatocytes without fusion. *Blood* 106, 756–763. doi:10.1182/BLOOD-2005-02-0572

Shimizu, A., Yamada, K., Yamamoto, S., Lavelle, J. M., Barth, R. N., Robson, S. C., et al. (2005). Thrombotic microangiopathic glomerulopathy in human decay accelerating factor-transgenic swine-to-baboon kidney xenografts. *J. Am. Soc. Nephrol.* 16, 2732–2745. doi:10.1681/ASN.2004121148

Shirai, H., Mandai, M., Matsushita, K., Kuwahara, A., Yonemura, S., Nakano, T., et al. (2016). Transplantation of human embryonic stem cell-derived retinal tissue in two primate models of retinal degeneration. *Proc. Natl. Acad. Sci. U. S. A.* 113, E81–E90. doi:10.1073/pnas.1512590113

Silva, J., and Smith, A. (2008). Capturing pluripotency. *Cell* 132, 532–536. doi:10.1016/j.cell.2008.02.006

Singh, A. K., Chan, J. L., DiChiacchio, L., Hardy, N. L., Corcoran, P. C., Lewis, B. G. T., et al. (2019). Cardiac xenografts show reduced survival in the absence of transgenic human thrombomodulin expression in donor pigs. *Xenotransplantation* 26, e12465. doi:10.1111/XEN.12465

Song, J. J., Guyette, J. P., Gilpin, S. E., Gonzalez, G., Vacanti, J. P., and Ott, H. C. (2013a). Regeneration and experimental orthotopic transplantation of a bioengineered kidney. *Nat. Med.* 19, 646–651. doi:10.1038/nm.3154

Song, J. J., Guyette, J. P., Gilpin, S. E., Gonzalez, G., Vacanti, J. P., and Ott, H. C. (2013b). Regeneration and experimental orthotopic transplantation of a bioengineered kidney. *Nat. Med.* 19, 646–651. doi:10.1038/NM.3154

Song, J. J., Kim, S. S., Liu, Z., Madsen, J. C., Mathisen, D. J., Vacanti, J. P., et al. (2011). Enhanced *in vivo* function of bioartificial lungs in rats. *Ann. Thorac. Surg.* 92, 998–1005. doi:10.1016/J.ATHORACSUR.2011.05.018

Spurlin, J., and Lwigale, P. (2013). A technique to increase accessibility to late-stage chick embryos for in ovo manipulations. *Dev. Dyn.* 242, 148–154. doi:10.1002/DVDY.23907

St John, J., and Lovell-Badge, R. (2007). Human-animal cytoplasmic hybrid embryos, mitochondria, and an energetic debate. *Nat. Cell Biol.* 9, 988–992. doi:10.1038/NCB436

Stanny, L. F., Elfner, R. R., Zwicker, E., Terhardt, E., and Springer-, E. (1980). Interspecific chimeras in mammals: Successful production of live chimeras between *Mus musculus* and *Mus caroli*. *Science* 208, 419–421. doi:10.1126/SCIENCE.7367871

Stevens, N. J., Seiffert, E. R., O'Connor, P. M., Roberts, E. M., Schmitz, M. D., Krause, C., et al. (2013). Palaeontological evidence for an Oligocene divergence between Old World monkeys and apes. *Nature* 497, 611–614. doi:10.1038/nature12161

Sugita, S., Iwasaki, Y., Makabe, K., Kimura, T., Futagami, T., Suegami, S., et al. (2016). Lack of T Cell response to iPSC-derived retinal pigment epithelial cells from

HLA homozygous donors. *Stem Cell Rep.* 7, 619–634. doi:10.1016/J.STEMCR.2016.08.011

Sun, Y., Xiao, D., Pan, X. H., Zhang, R. S., Cui, G. H., and Chen, X. G. (2007). Generation of human/rat xenograft animal model for the study of human donor stem cell behaviors *in vivo*. *World J. Gastroenterology WJG* 13, 2707–2716. doi:10.3748/WJG.V13.I19.2707

Sykes, M., and Sachs, D. H. (2019). Transplanting organs from pigs to humans. *Sci. Immunol.* 4, eaau6298. doi:10.1126/SCIIMMUNOL.AAU6298

Tabar, V., Panagiotakos, G., Greenberg, E. D., Chan, B. K., Sadelain, M., Gutin, P. H., et al. (2005). Migration and differentiation of neural precursors derived from human embryonic stem cells in the rat brain. *Nat. Biotechnol.* 23, 601–606. doi:10.1038/nbt1088

Takasato, M., Er, P. X., Chiu, H. S., Maier, B., Baillie, G. J., Ferguson, C., et al. (2015). Kidney organoids from human iPS cells contain multiple lineages and model human nephrogenesis. *Nature* 526, 564–568. doi:10.1038/NATURE15695

Takashima, Y., Guo, G., Loos, R., Nichols, J., Ficz, G., Krueger, F., et al. (2014). Resetting transcription factor control circuitry toward ground-state pluripotency in human. *Cell* 158, 1254–1269. doi:10.1016/j.cell.2014.08.029

Takebe, T., Sekine, K., Enomura, M., Koike, H., Kimura, M., Ogaeri, T., et al. (2013). Vascularized and functional human liver from an iPSC-derived organ bud transplant. *Nature* 499, 481–484. doi:10.1038/nature12271

Tan, T., Wu, J., Si, C., Dai, S., Zhang, Y., Sun, N., et al. (2021). Chimeric contribution of human extended pluripotent stem cells to monkey embryos *ex vivo*. *Cell* 184, 2020–2032.e14. doi:10.1016/j.cell.2021.03.020

Theunissen, T. W., Powell, B. E., Wang, H., Mitalipova, M., Faddah, D. A., Reddy, J., et al. (2014). Systematic identification of culture conditions for induction and maintenance of naive human pluripotency. *Cell Stem Cell* 15, 471–487. doi:10.1016/j.stem.2014.07.002

Thomas, J., Zimmerlin, L., Huo, J. S., Considine, M., Cope, L., and Zambidis, E. T. (2021). Running the full human developmental clock in interspecies chimeras using alternative human stem cells with expanded embryonic potential. *npj Regen. Med.* 6, 25–13. doi:10.1038/s41536-021-00135-1

Thomson, J. A., Itskovitz-Eldor, J., Shapiro, S. S., Waknitz, M. A., Swiergiel, J. J., Marshall, V. S., et al. (1998). Embryonic stem cell lines derived from human blastocysts. *Science* 282, 1145–1147. doi:10.1126/SCIENCE.282.5391.1145

Totonelli, G., Maghsoudlou, P., Garriboli, M., Riegler, J., Orlando, G., Burns, A. J., et al. (2012). A rat decellularized small bowel scaffold that preserves villus-crypt architecture for intestinal regeneration. *Biomaterials* 33, 3401–3410. doi:10.1016/j.biomaterials.2012.01.012

Tsukiyama, T., and Ohinata, Y. (2014). A modified EpiSC culture condition containing a GSK3 inhibitor can support germline-competent pluripotency in mice. *PLoS One* 9, e95329. doi:10.1371/JOURNAL.PONE.0095329

Turco, M. Y., Gardner, L., Hughes, J., Cindrova-Davies, T., Gomez, M. J., Farrell, L., et al. (2017). Long-term, hormone-responsive organoid cultures of human endometrium in a chemically defined medium. *Nat. Cell Biol.* 19, 568–577. doi:10.1038/NCB3516

van den Berg, C. W., Ritsma, L., Avramut, M. C., Wiersma, L. E., van den Berg, B. M., Leuning, D. G., et al. (2018). Renal subcapsular transplantation of PSC-derived kidney organoids induces neo-vasculogenesis and significant glomerular and tubular maturation *in vivo*. *Stem Cell Rep.* 10, 751–765. doi:10.1016/J.STEMCR.2018.01.041

Vilarino, M., Soto, D. A., Bogliotti, Y. S., Yu, L., Zhang, Y., Wang, C., et al. (2020). Derivation of sheep embryonic stem cells under optimized conditions. *Reproduction* 160, 761–772. doi:10.1530/REP-19-0606

Vos, J. G., Kreeftenberg, J. G., Kruijt, B. C., Kruizinga, W., and Steerenberg, P. (1980). The athymic nude rat: II. Immunological characteristics. *Clin. Immunol. Immunopathol.* 15, 229–237. doi:10.1016/0090-1229(80)90033-1

Waddington, C. H. (1934). Experiments on embryonic induction. *J. Exp. Biol.* 11, 224–227. doi:10.1242/JEB.11.3.224

Waddington, C. H., and Schmidt, G. A. (1933). Induction by heteroplastic grafts of the primitive streak in birds. *Wilhelm Roux' Arch. für Entwicklungsmechanik Org.* 128, 522–563. doi:10.1007/BF00649863

Wainwright, J. M., Czajka, C. A., Patel, U. B., Freytes, D. O., Tobita, K., Gilbert, T. W., et al. (2010). Preparation of cardiac extracellular matrix from an intact porcine heart. *Tissue Eng. Part C Methods* 16, 525–532. doi:10.1089/TEN.TEC.2009.0392

Ware, C. B., Nelson, A. M., Mecham, B., Hesson, J., Zhou, W., Jonlin, E. C., et al. (2014). Derivation of naïve human embryonic stem cells. *Proc. Natl. Acad. Sci. U. S. A.* 111, 4484–4489. doi:10.1073/pnas.1319738111

Weinberger, L., Ayyash, M., Novershtern, N., and Hanna, J. H. (2016). Dynamic stem cell states: Naive to primed pluripotency in rodents and humans. *Nat. Rev. Mol. Cell Biol.* 17, 155–169. doi:10.1038/nrm.2015.28

Wen, B., Li, E., Ustiyan, V., Wang, G., Guo, M., Na, C. L., et al. (2021). *In vivo* generation of lung and thyroid tissues from embryonic stem cells using blastocyst complementation. *Am. J. Respir. Crit. Care Med.* 203, 471–483. doi:10.1164/rccm.201909-1836OC

Weymann, A., Loganathan, S., Takahashi, H., Schies, C., Claus, B., Hirschberg, K., et al. (2011). Development and evaluation of a perfusion decellularization porcine heart model--generation of 3-dimensional myocardial neoscaffolds. *Circ. J.* 75, 852–860. doi:10.1253/CIRCJ.CJ-10-0717

Weymann, A., Patil, N. P., Sabashnikov, A., Jungebluth, P., Korkmaz, S., Li, S., et al. (2014). Bioartificial heart: A human-sized porcine model--the way ahead. *PLoS One* 9, e111591. doi:10.1371/JOURNAL.PONE.0111591

Williams, T. J., Munro, R. K., and Shelton, J. N. (1990). Production of interspecies chimeric calves by aggregation of *Bos indicus* and *Bos taurus* demi-embryos. *Reprod. Fertil. Dev.* 2, 385–394. doi:10.1071/RD9900385

Wilmut, I., Schnieke, A. E., McWhir, J., Kind, A. J., and Campbell, K. H. S. (1997). Viable offspring derived from fetal and adult mammalian cells. *Nature* 385, 6619810–6619813. doi:10.1038/385810a0

Wu, J., and Barbaric, I. (2021). Fitness selection in human pluripotent stem cells and interspecies chimeras: Implications for human development and regenerative medicine. *Dev. Biol.* 476, 209–217. doi:10.1016/J.YDBIO.2021.03.025

Wu, J., Okamura, D., Li, M., Suzuki, K., Luo, C., Ma, L., et al. (2015). An alternative pluripotent state confers interspecies chimaeric competency. *Nature* 521, 316–321. doi:10.1038/nature14413

Wu, J., Platero-Luengo, A., Sakurai, M., Sugawara, A., Gil, M. A., Yamauchi, T., et al. (2017). Interspecies chimerism with mammalian pluripotent stem cells. *Cell* 168, 473–486.e15. doi:10.1016/j.cell.2016.12.036

Yagi, M., Kishigami, S., Tanaka, A., Semi, K., Mizutani, E., Wakayama, S., et al. (2017). Derivation of ground-state female ES cells maintaining gamete-derived DNA methylation. *Nature* 548, 224–227. doi:10.1038/nature23286

Yamada, K., Shimizu, A., Ierino, F. L., Utsugi, R., Barth, R. N., Esnaola, N., et al. (1999). Thymic transplantation in miniature swine. I. Development and function of the "thymokidney. *Transplantation* 68, 1684–1692. doi:10.1097/00007890-199912150-00011

Yamada, K., Shimizu, A., Utsugi, R., Ierino, F. L., Gargollo, P., Haller, G. W., et al. (2000). Thymic transplantation in miniature swine. II. Induction of tolerance by transplantation of composite thymokidneys to thymectomized recipients. *J. Immunol.* 164, 3079–3086. doi:10.4049/JIMMUNOL.164.6.3079

Yamaguchi, T., Sato, H., Kato-Itoh, M., Goto, T., Hara, H., Sanbo, M., et al. (2017). Interspecies organogenesis generates autologous functional islets. *Nature* 542, 191–196. doi:10.1038/nature21070

Yan, J., Xu, L., Welsh, A. M., Hatfield, G., Hazel, T., Johe, K., et al. (2007). Extensive neuronal differentiation of human neural stem cell grafts in adult rat spinal cord. *PLoS Med.* 4, e39. doi:10.1371/JOURNAL.PMED.0040039

Yang, B., Zhang, Y., Zhou, L., Sun, Z., Zheng, J., Chen, Y., et al. (2010). Development of a porcine bladder acellular matrix with well-preserved extracellular bioactive factors for tissue engineering. *Tissue Eng. Part C Methods* 16, 1201–1211. doi:10.1089/TEN.TEC.2009.0311

Yang, J., Ryan, D. J., Wang, W., Tsang, J. C. H., Lan, G., Masaki, H., et al. (2017). Establishment of mouse expanded potential stem cells. *Nature* 550, 393–397. doi:10.1038/nature24052

Yang, X., Zhou, J., He, J., Liu, J., Wang, H., Liu, Y., et al. (2018). An immune system-modified rat model for human stem cell transplantation research. *Stem Cell Rep.* 11, 514–521. doi:10.1016/J.STEMCR.2018.06.004

Yang, Y., Liu, B., Xu, J., Wang, J., Wu, J., Shi, C., et al. (2017). Derivation of pluripotent stem cells with *in vivo* embryonic and extraembryonic potency. *Cell* 169, 243–257.e25. doi:10.1016/j.cell.2017.02.005

Yang, Y., Wang, K., Wu, H., Jin, Q., Ruan, D., Ouyang, Z., et al. (2016). Genetically humanized pigs exclusively expressing human insulin are generated through custom endonuclease-mediated seamless engineering. *J. Mol. Cell Biol.* 8, 174–177. doi:10.1093/JMCB/MJW008

Yao, J., Wang, Y., Cao, C., Song, R., Bi, D., Zhang, H., et al. (2021). CRISPR/Cas9-mediated correction of MITF homozygous point mutation in a Waardenburg syndrome 2A pig model. *Mol. Ther. Nucleic Acids* 24, 986–999. doi:10.1016/J.OMTN.2021.04.009

Yasuhara, T., Matsukawa, N., Hara, K., Yu, G., Xu, L., Maki, M., et al. (2006). Transplantation of human neural stem cells exerts neuroprotection in a rat model of Parkinson's disease. *J. Neurosci.* 26, 12497–12511. doi:10.1523/JNEUROSCI.3719-06.2006

Ying, Q. L., Wray, J., Nichols, J., Batlle-Morera, L., Doble, B., Woodgett, J., et al. (2008). The ground state of embryonic stem cell self-renewal. *Nature* 453, 519–523. doi:10.1038/nature06968

Yu, L., Wei, Y., Sun, H. X., Mahdi, A. K., Pinzon Arteaga, C. A., Sakurai, M., et al. (2021). Derivation of intermediate pluripotent stem cells amenable to primordial germ cell specification. *Cell Stem Cell* 28, 550–567.e12. doi:10.1016/j.stem.2020.11.003

Zhang, B., Li, H., Hu, Z., Jiang, H., Stablewski, A. B., Marzullo, B. J., et al. (2021). Generation of mouse–human chimeric embryos. *Nat. Protoc.* 16 (8), 3954–3980. doi:10.1038/s41596-021-00565-7

Zhang, H., Huang, J., Li, Z., Qin, G., Zhang, N., Hai, T., et al. (2018). Rescuing ocular development in an anophthalmic pig by blastocyst complementation. *EMBO Mol. Med.* 10 (12). doi:10.15252/emmm.201808861

Zheng, C., Hu, Y., Sakurai, M., Pinzon-Arteaga, C. A., Li, J., Wei, Y., et al. (2021). Cell competition constitutes a barrier for interspecies chimerism. *Nature* 592, 272–276. doi:10.1038/S41586-021-03273-0

Zhou, H., Kitano, K., Ren, X., Rajab, T. K., Wu, M., Gilpin, S. E., et al. (2018). Bioengineering human lung grafts on porcine matrix. *Ann. Surg.* 267, 590–598. doi:10.1097/SLA.0000000000002129

Zhu, K., Wu, Q., Ni, C., Zhang, P., Zhong, Z., Wu, Y., et al. (2018). Lack of remuscularization following transplantation of human embryonic stem cell-derived cardiovascular progenitor cells in infarcted nonhuman primates. *Circ. Res.* 122, 958–969. doi:10.1161/CIRCRESAHA.117.311578

A developmental program that regulates mammalian organ size offsets evolutionary distance

One Sentence Summary:

A cross-species developmental molecular atlas identified the indicator of lung and animal size beyond evolution

Authors: Yuko Shimamura[1]*, Junichi Tanaka[1]*, Miwako Kakiuchi[2], Hemanta Sarmah[1], Akihiro Miura[1], Youngming Hwang[1], Anri Sawada[1], Zurab Ninish[1], Kazuhiko Yamada[3], James J. Cai[4†], Munemasa Mori[1†]

Affiliations:

1 Columbia Center for Human Development and Division of Pulmonary, Allergy, Critical Care, Department of Medicine, Columbia University Medical Center, New York, NY, USA.

2 Department of Preventive Medicine, Graduate School of Medicine, the University of Tokyo

3 Department of Surgery, Johns Hopkins University, Baltimore, MD, USA

4 Department of Veterinary Integrative Biosciences, Department of Electrical & Computer Engineering Interdisciplinary Graduate Program in Genetics Center for Statistical Bioinformatics, Texas A&M University, TX, USA

* † Equal contribution, respectively

† To whom correspondence should be addressed:

Munemasa Mori†, MD, Ph.D.
Assistant Professor of Medicine,
Columbia Center for Human Development (CCHD),
Pulmonary Allergy & Critical Care Medicine, Department of Medicine,
Columbia University Irving Medical Center
Email: mm4452@cumc.columbia.edu
Tel: 212-305-1731

James J. Cai†, Ph.D.
Associate Professor,
Department of Veterinary Integrative Biosciences,
Department of Electrical & Computer Engineering,
Texas A&M University
Email: jcai@tamu.edu
Tel: 979-458-5482

Abstract:

Pigs are evolutionarily more distant from humans than are mice, but their physiological organs are closest to humans. The molecular program leading to a 1,000-fold increase in organ size in pigs and humans over that of mice during evolution has not been elucidated. We discovered a core organ-size regulation program (COSRP), well-conserved in swine and human lungs but less so in mice using large-scale single-cell transcriptome analysis during swine lung development. Strikingly, human COSRP promoters showed a higher homology to evolutionary-distant pigs and large animals than evolutionary-close small rodents. Our cross-species analysis provides a molecular foundation of swine lung development and unveiled previously unknown animal size regulation encoded in COSRP promoter, independent of global genome-wide evolution, relevant to various fields such as evolution, development, cancer, zoology, and biotechnology.

Main Text:

Evolution changes the size of animals to adapt to the environment(*1*, *2*). Organ size regulation is a fundamental program of the developmental process, however, the molecular program that regulates organ size during evolution remains a mystery(*3–5*). Exploring the organ size regulators in specific organogenesis programs by cross-species analyses may unlock the hidden mechanism of organ size diversification. This could prove significant in advancing regenerative medicine and organ bioengineering that requires the replication of full organ size for sustaining organ functionality, such as the lungs and other internal organs (*3–5*). However, there has been a considerable knowledge gap in how the development of large lung sizes is controlled.

The lungs are one of the most diversified organs during evolution. The need for life-sustaining gas exchange through the lungs facilitated environmental adaptation by evolving the lung's developmental program over billions of years, allowing species-specific physiological morphologies, surfactant protein production, and unique circulatory systems(*6*, *7*). Conversely, species such as the plethodontid salamander, which breaths through skins, lost the lungs by evolutionary design(*8*). Mice and swine have been used as essential model organisms for decades, and both harbor life-sustaining, well-lobulated, branched lungs(*9–13*). Multiple studies of comparative genomic evolution show that pigs primitively separated around 97 million years ago from mice and humans(*14–17*). Mice and humans were divided about six million years later. Thus, swine genome-wide sequences are evolutionarily apart from humans as compared to mice(*14–17*). Contradictorily, pigs harbor physiological organs similar to humans, distinct from small rodents by more than 1,000-fold in size(*17*, *18*). Given the prolific feature and the physiological similarities to humans, pigs are considered an ideal resort for xenogeneic organ transplantation and the host animals for human organ bioengineering by blastocyst complementation for the ultimate cure for various refractory diseases(*19*, *20*). Although many signaling pathways, including Hippo-Yap, JNK, and IGF-1(*3*), are involved in organ size regulation, their signaling alone does not explain the regulatory mechanism for more than 1,000-fold difference in organ size between small animals and animals of comparable size to humans. To address this question, we performed comparative cross-species bioinformatic analyses in pig, mouse, and human lung development.

Results

Pig embryonic lungs develop exponentially along with their body size.

The mouse lung developmental stage has been molecularly well-characterized, whereas swine lung development rarely(*10*, *13*). To fill the huge knowledge gap on the molecular program on how and when swine lung organ size change is initiated, we harvested developing lungs from miniature pigs harboring human-compatible organ size(*19*) (**Fig. 1A**). We identified embryonic gestation day18 and 19 (hereafter, E18 and E19) as the primary lung bud formation stage (**Fig. 1B**). After secondary buds appear on E20~E23, sequential pseudostratified epithelial branching occurs (**Fig. 1B**). Through the pseudoglandular stage, the lungs expanded their size exponentially from E40 to E70, along with body weight changes (**Fig. 1C**).

Pigs and humans share unique organ size regulator programs, distinct from mice.

Although swine are evolutionarily more distant from humans than mice(*14–17*), the molecular program required for the acquisition of a human-compatible lung organ size phenotype remains elusive (**Fig. 1D**). We isolated RNA from miniature swine lung tissues at E26, E40, and E70 for bulk RNA-seq analysis (**Fig. 1A**) and defined swine developmental stages by gross lung morphology, histology, and cross-species transcriptome (**Fig. 1A, S1A, Data S1**). To extract latent variables underlying phenotypic divergence across species, we performed a principal component (PC) analysis. Using PC1 (39% variance) and PC2 (28% variance), the most extensive variant sets in PC analyses confirmed a relatively uniform sampling without significant batch variance (**Fig. S2A**). Importantly, PC3 (13% variance) indicates the developmental time course over the species (**Fig. 2A**). With the combination of PC1 and PC3, the most prominent variance among all PCs, we realized that swine developing lungs have a closer transcriptome variance to humans than mice do (**Fig. 2A**). To identify the genes involved in the human and swine transcriptome variance proximity, apart from mice, we ranked genes based on their contribution to the PC1 minus axis. We performed GO term analysis on the top 10% of genes. Of note, we found the program of anatomical structure size regulation (ASSR) (GO: 0090066) (**Fig. 2B, S2B**). Unexpectedly, the neuronal-like developmental program (GO:0007409, 0099536, 0051960, 0010975, 0051963) highly overlays ASSR. We defined the neuronal and ASSR programs as the **c**ore of the **o**rgan **s**ize **r**egulation **p**rogram (COSRP) that includes 230 genes (**Fig. 2B**, red circled area). Further, the Venn chart illustrated that the COSRP neuronal-like program overlapped with 57.1% of the ASSR program (80 out of 140 ASSR genes) (**Fig. 2C, S2C**).

To map which cell type acquires the unique COSRP features conserved in swine and humans but not in mice, we harvested swine-developing lungs (a total of 83,433 cells from 11 independent samples, 7 distinct time points for lung mesenchyme, and 4 particular time points for $EPCAM^+$ FACS-sorted lung epithelium). We utilized SCGEATOOL(*21*) to perform subclustering annotation with combined datasets across time points, as well as data-driven analyses of gene expression patterns, gene-regulatory networks, and trajectory inference. For cross-species comparison, we combined datasets of swine, human, and mouse-developing lungs and analyzed them in an integrated manner (**Fig. 2D**). The UMAP analyses revealed that the transcriptome profile of swine lung epithelium across the developmental time point showed relatively closer progenitor identity with that of human lung epithelium than mice (**Fig. 2D**). In the transcriptome profile of the lung mesenchyme, mice were still far apart from humans overall (**Fig. 2D**). Among 230 COSRP genes in the Venn chart (**Fig. S2C**), we discovered that 45 genes were expressed in human and swine lung development but rarely in mice by the cross-species 3D-tSNE scRNA-seq analyses (**Fig. 2E**, **Data S**). Unexpectedly, we also discovered that 17 COSRP genes, including the neuronal-like program and ASSR, were ubiquitously conserved in both $EPCAM^+$ pig and human lung epithelium or mesenchyme but not well in mice (**Fig. 2E, F, G, Data S2**). These ubiquitous

gene expression patterns during swine and human lung development but rarely in mice showed three distinct distributions: first, 3 COSRP genes were exclusively enriched in the $EPCAM^+$ epithelium (*SEMA3C, B3GNT2,* and *B4GALT5*); second, 4 genes exclusively enriched in $EPCAM^-$ mesenchyme (*COL5A2*, *ENAH*, *PRKG1,* and *NR2F1*); third, 10 genes were enriched in both, such as (*SRP54, EFNA5, ANTXR1, ADNP, ID4, TERF2LP, ADAMTS7, CCDC85B, TET1,* and *ZFP36L2*) (**Fig. 2E, F, G, S2C, Data S2**). These results suggested that 45 COSRP genes are the responsible organ size regulator conserved in swine and human lung development but rarely in mice over time.

Unique expression pattern of COSRP genes in swine developing lung epithelium

To uncover which cells express COSRP genes in developing lung epithelium and systematically characterize early lung epithelial progenitor molecular identities, we analyzed scRNA-seq data of swine lung epithelium across four-time points from E18, E19, E40, and E70 (27,287 genes for a total of 9,240 live cells) (**Fig. 3A**). Human lung epithelial progenitors exhibit $SOX2^+SOX9^+$ double-positive distal lung bud progenitors, never seen in the mice at the pseudoglandular stage(*22*). On E18 and E19 of the primary lung bud formation stage, *SOX2* and *SOX9* were indeed co-expressed almost entirely in the lung epithelium (**Fig. 3B,** asterisks), and confocal immunofluorescent (IF) protein expression analyses further confirmed their distribution and SPB and SPC protein expression in the distal lung bud regions (**Fig. 3C,** asterisks, **S3A-D**). In contrast, at the beginning of the sacculation stage on E70, SOX2 and SOX9 rarely overlapped (**Fig. 3B, C, D,** arrow). On the other hand, SOX2 and SOX9 coincided with E40 lung buds, but the SOX2 expression level was relatively decreased compared to the $SOX2^+$ proximal domain (**Fig. 3B, C, D,** arrowhead).

ScRNA-seq analysis further identified 10 epithelial clusters (**Fig. 3E**). E18 and E19, the primary lung bud formation stage, showed similar profiles but were utterly different from E40 and E70, pseudoglandular and canalicular lung bud stages, respectively. Using classical mouse lung epithelial markers(*23*), the dot plot and feature plot visualized airway and alveolar epithelial cells during swine lung development (**Fig. S3A, B**). We also discovered novel stage-specific markers such as *NES, SLC16A3, FABP3*, and *SLC2A3* explicitly in the $SOX2^+SOX9^+$ double-positive swine primary lung bud epithelial cells, while *Slc16a3, Fabp3*, and *Slc2a3* were partially expressed in E9, the mouse primordial lung stage (**Fig. S4A, B**). *SLC22A3*, *GPLD1*, *SHISA2*, and *KCNJ15*, were the markers of pseudoglandular~canalicular specific $SOX9^+$ swine lung bud epithelial cells, in which *SLC22A3*, *SHISA2*, and *KCNJ15* were well-preserved in human lung development but not in mice (**Fig. S4A-C**). Among the 45 COSRP genes, we found 12 genes *(SRP54, B4GALT5, B3GNT2, EFNA5, ANTXR1, ADNP, ID4, TERF2IP, SEMA3, ADAMTS7, CCDC85B, TET1,* and *ZFP36L2*) were moderately or highly expressed in most lung epithelium throughout swine lung development (**Fig. 3F, G, Data S2**). The dot plot analyses showed the spatially distinct expression pattern of COSRP genes in the subclusters (**Fig. 3F**). Briefly, *NR2F1* and *ENAH* were exclusively expressed at the primary lung bud epithelium but rarely later. Interestingly, *B4GALT5, SOCS1, and COL5A2* were highly enriched in the $SOX9^+$ distal lung bud. In contrast, *SEMA3C or B3GNT2 was* relatively increased in the proximal epithelial domain on day40 or day70, respectively. *ID4* was enriched in neuroendocrine cells (NEC) (**Fig. 3F, G, Data S2**).

Unique expression pattern of COSRP genes in swine developing lung mesenchyme

To reveal the COSRP gene expression in the lineage trajectory and diversification of developing pig lung mesenchyme, scRNA-seq datasets of whole lungs on E18, 19, 23, and 25 and peripheral lung tissues on E35, E40, and E70 were analyzed using Seurat (**Fig. S5A**). We demonstrated that chondrocyte progenitors emerged at the swine primary lung bud stage, marked by *SOX9*. At the E35 and 40 middle pseudoglandular stage, matrix fibroblast and smooth muscle cell (SMC) clusters appeared (**Fig. S5A**). At E70, late pseudoglandular~canalicular stage, SMC, pericyte, and matrix fibroblast clusters were found

(**Fig. S5A**). A dot plot and feature plot analysis of swine lung mesenchymal cells showed stage-specific subclusters and their gene expression profiles well-known in mouse studies (**Fig. S5B, C**). For example, *NOTCH3* and *EBF1* were enriched in the vascular pericyte clusters at the canalicular stage. At the swine lung bud stage, a part of proliferative mesenchyme or matrix fibroblast expressed *FGF10*, a critical mitogen for primary lung bud formation and branching morphogenesis(*24*), *WNT2,* a marker for the lung mesenchyme specifier(*25*), *RSPON2*, a feature of lung bud-specific mesenchyme in human lung development(*26*)(**Fig. S5B, C**). *ACTA2, TAGLN, MYH11,* and *HHIP* were highly expressed in the smooth muscle cell (SMC) clusters at the canalicular stage and myofibroblasts at the pseudoglandular stage(*27*). *ACTA2* and *IGF1-positive* myofibroblasts emerged from E23 and differentiated into *ACTA2*- and *FGF18*-positive smooth muscle cells at E70 **(Fig. S5B, C**). Pseudotime analysis revealed stage-specific genes enriched in the primary lung bud fibroblast-specific stage (*CXADR* and *DSP*), primary to pseudoglandular stage (*HMGA1* and *NASP*) (**Fig. S5D, E)**. A matrix fibroblast (MF) labeled by *MFAP4, ELN, MEOX2, TCF21,* and *DCN* has been abundantly enriched in swine and human lung development but rare in mice(*28*). We found *MFAP4*, *ELN*, and *TCF21* gradually increased their expression levels during swine lung development and peaked at E70, most likely by its maturation (**Fig. S6A, B**). *TCF21* and *DCN* expressions were conserved across swine and humans but not in mice (**Fig. S6B**). We identified novel MF markers through scRNA-seq of swine developing lung mesenchyme. *CAV2*, *RGCC*, and *INMT* were highly expressed in swine MFs. These genes were expressed in human lung mesenchymal tissue but were not abundant in mice (**Fig. S6C**). These results suggest that the mesenchymal subcluster of peripheral lung tissue reported in humans is highly conserved in pigs. Among the 45 COSRP genes, 7 *(ERF2IP, COL5A2, ZFP36L2, ENAH, PRKG1, NR2F1,* and *ADNP)* were ubiquitously expressed in the lung mesenchyme throughout swine lung development (**Fig. S5C**, **Data S2**).

COSRP gene regulatory networks are conserved in swine and humans but not in mice

To elucidate the significant network of cellular functional programs governing the organ size regulators during lung development over mRNA and protein expression patterns, we performed gene regulatory network (GRN) analyses for the 45 COSRP genes. We used swine, human, and mouse lung developmental scRNA-seq databases at each time point by SCGEATOOL(*21*). Based on the scRNA-seq GRN analysis (scGRN), swine lung developmental scGRN showed multiple highly interacting nodes with connected networks similar to humans (**Fig. S7A, B**). The highly-dense scGRN network is conserved in swine and human lung development but sparse in mice.

Together, our analyses showed that swine developmental lung's phenotypic similarity of organ size, cellular phenotype, and scGRN with humans is regulated by COSRP that is not well-conserved in mice. However, it was unclear how organ size regulators represented by COSRP offset the evolutionary distance to humans, in contrast to the mice, which is calculated by each species' overall genomic sequences(*14–17*).

COSRP genomic promoters are better conserved in large animals than in small animals

Since COSRP mRNA expression depends on its promoter activation, we speculated that swine and humans' lung organ size phenotypes might rely on the COSRP promoter genomic sequence homologies against the entire genomic evolution. to explore this possibility, we investigated 15 COSRP gene promoter regions ($pCOSRP_{15}$) and 11 HK gene promoter regions (pHK_{11}) as controls. To keep the evolutionary significance and avoid the complexity of differential length of promoter analyses across the various species, we analyzed 2kb upstream of TSS: transcription starting site for a human COSRP promoter (pCOSRP) (**Fig. 4A**) (*29*).

Strikingly, we discovered that $pCOSRP_{15}$ aligned sequences showed a significantly higher level of homology between humans and pigs (69.7% ±7.01%) than the homologies between mice and humans

(59.1%±7.29%) (P<0.001***). Conversely, pHK_{11} did not significantly (ns: non-significant) differ between the homology comparison with pigs (59.4%±8.16%) and mice (57.9% ±8.35%) (**Fig. 4A**). We also checked the COSRP gene coding sequence (CDS) alignments ($_{CDS}COSRP_{15}$). However, $_{CDS}COSRP_{15}$ did not show a significant homology difference in humans between mice (85.3%±9.57%) and pigs (89.1%±8.41%) nor in HK genes (mouse: 91.9%±2.95%, pigs 93.2%±5.23%). Those results indicate that lung organ size regulation depends on the 2kb upstream of TSS of 15 COSRP genes most likely to activate the COSRP program.

COSRP was found by the cross-species bulk RNA-seq analyses when the lung size exponentially increased along with the organismal size's drastic change (**Fig. 1, 2**). Thus, we hypothesized that pCOSRP homology might be an indicator of lung size but also the organismal size itself among mammalian organisms. Since some organisms were not known the genomic sequence of COSRP or HK promoter homologous regions in the Ensemble, we selected 8 animals (Lion, Pig, Horse, Guinea pig, Golden hamster, Mouse, and Shrew mouse) and used 14 COSRP gene's promoter regions $pCOSRP_{14}$ and 10 HK genes (pHK_{10}) for the homology comparisons (**Fig. 4B**). Strikingly the $pCOSRP_{14}$ genomic homology was well-conserved in mammalian large animals compared to small creatures (**Fig. 4B**). The Pigs (*Sus Scrofa*)'s $pCOSRP_{14}$ homologies (% identity and % Gap) to the humans showed significance to all small animals such as Shrew (*Mus phahari*) (% identity*: p=0.0013,* % Gap: *p=0.0017, respectively*), Mouse (*Mus Musculus*) (*p=0.0006, p=0.005*), and hamster (*Mesocricetus auratus*) (*p=0.0040, p=0.034*), but not to the large animals such as Lion (*Panthera Leo*) (*p>0.05, p>0.05*) or Horse (*Equus Caballus*) (*p>0.05, p>0.05*) (**Fig. 4B**). The pHK_{10} homologies to the humans vary and no significant change between pigs and the other animals (*ns*: non-significant), suggesting $pCOSRP_{14}$ is the unique genomic region highly conserved in large animals but less in small animals.

Our analyses unlocked previously unknown COSRP regulatory mechanisms for lung size along with the body plan that contradicts the species' entire genomic sequence-based evolutionary distance. Since small rodents did not show high $pCOSRP_{14}$ homology to humans, even though they are evolutionarily closer to humans than swine, they most likely needed to lose the $pCOSRP_{14}$ to adapt to the environment billions of years ago as a survival strategy during evolution. Our results suggest that large organismal size development requires COSRP in epithelial and mesenchymal cells. Further detailed analyses for the COSRP promoters will be required to elucidate which signaling pathways, such as Hippo-Yap, and JNK, coordinate to activate the $pCOSRP_{14}$. Our results indicate that "species" various phenotypic divergence relies more on the responsible promoter element than an entire genomic sequence that determines genome-wide evolutionary distances (*14–17*). Thus, our findings provide a novel paradigm for cross-species analysis, organismal size regulations, and lung organ size across the species, distinct from the classical evolutionary phylogenic tree studies. The discovery of COSRP and pCOSRP will lead to a better understanding of zoology, evolution, pulmonary medicine, regeneration, development, cancer biology, and bioengineering, particularly organ bioengineering compatible with humans.

Reference:

1. G. Horiguchi, H. Tsukaya, Organ size regulation in plants: Insights from compensation. *Front. Plant Sci.* **2**, 1–6 (2011).
2. B. L. M. Hogan, P. a Kolodziej, Organogenesis: molecular mechanisms of tubulogenesis. *Nat. Rev. Genet.* **3**, 513–23 (2002).
3. A. I. Penzo-Mendez, B. Z. Stanger, Organ-size regulation in mammals. *Cold Spring Harb. Perspect. Biol.* **7** (2015), doi:10.1101/cshperspect.a019240.
4. F. Marongiu, M. Serra, E. Laconi, Development versus Evolution in Cancer Biology. *Trends in Cancer*. **4**, 342–348 (2018).
5. D. M. Bryant, K. E. Mostov, From cells to organs: building polarized tissue. *Nat. Rev. Mol. Cell Biol.* **9**, 887–901 (2008).
6. M. Lambertz, K. Grommes, T. Kohlsdorf, S. F. Perry, Lungs of the first amniotes: Why simple if they can be complex? *Biol. Lett.* **11**, 1–5 (2015).
7. C. B. Daniels, S. Orgeig, Pulmonary surfactant: The key to the evolution of air breathing. *News Physiol. Sci.* **18**, 151–157 (2003).
8. Z. R. Lewis, R. Kerney, J. Hanken, Developmental basis of evolutionary lung loss in plethodontid salamanders. *Sci. Adv.* **8**, eabo6108 (2022).
9. J. M. Flint, The development of the lungs. *Am. J. Anat.* **VI.** (1906), doi:https://doi.org/10.1002/aja.1000060102.
10. D. N. Kotton, E. E. Morrisey, Lung regeneration: Mechanisms, applications and emerging stem cell populations. *Nat. Med.* **20**, 822–832 (2014).
11. J. R. Rock, B. L. M. Hogan, Epithelial progenitor cells in lung development, maintenance, repair, and disease. *Annu. Rev. Cell Dev. Biol.* **27**, 493–512 (2011).
12. M. Mori, W. V Cardoso, "Chapter 1 - Lung Progenitor Cell Specification and Morphogenesis" in *The Lung: Development, Aging and the Environment*, R. H. E. B. T.-T. L. (Second E. Pinkerton, Ed. (Academic Press, Boston, 2014; http://www.sciencedirect.com/science/article/pii/B9780127999418000018), pp. 3–9.
13. W. V Cardoso, J. Lü, Regulation of early lung morphogenesis: questions, facts and controversies. *Development*. **133**, 1611–24 (2006).
14. M. A. M. Groenen, A. L. Archibald, H. Uenishi, C. K. Tuggle, Y. Takeuchi, M. F. Rothschild, C. Rogel-Gaillard, C. Park, D. Milan, H. J. Megens, S. Li, D. M. Larkin, H. Kim, L. A. F. Frantz, M. Caccamo, H. Ahn, B. L. Aken, A. Anselmo, C. Anthon, L. Auvil, B. Badaoui, C. W. Beattie, C. Bendixen, D. Berman, F. Blecha, J. Blomberg, L. Bolund, M. Bosse, S. Botti, Z. Bujie, M. Bystrom, B. Capitanu, D. Carvalho-Silva, P. Chardon, C. Chen, R. Cheng, S. H. Choi, W. Chow, R. C. Clark, C. Clee, R. P. M. A. Crooijmans, H. D. Dawson, P. Dehais, F. De Sapio, B. Dibbits, N. Drou, Z. Q. Du, K. Eversole, J. Fadista, S. Fairley, T. Faraut, G. J. Faulkner, K. E. Fowler, M. Fredholm, E. Fritz, J. G. R. Gilbert, E. Giuffra, J. Gorodkin, D. K. Griffin, J. L. Harrow, A. Hayward, K. Howe, Z. L. Hu, S. J. Humphray, T. Hunt, H. Hornshøj, J. T. Jeon, P. Jern, M. Jones, J. Jurka, H. Kanamori, R. Kapetanovic, J. Kim, J. H. Kim, K. W. Kim, T. H. Kim, G. Larson, K. Lee, K. T. Lee, R. Leggett, H. A. Lewin, Y. Li, W. Liu, J. E. Loveland, Y. Lu, J. K. Lunney, J. Ma, O. Madsen, K. Mann, L. Matthews, S. McLaren, T. Morozumi, M. P. Murtaugh, J. Narayan, D. T. Nguyen, P. Ni, S. J. Oh, S. Onteru, F. Panitz, E. W. Park, H. S. Park, G. Pascal, Y. Paudel, M. Perez-Enciso, R. Ramirez-Gonzalez, J. M. Reecy, S. Rodriguez-Zas, G. A. Rohrer, L. Rund, Y. Sang, K. Schachtschneider, J. G. Schraiber, J. Schwartz, L. Scobie, C. Scott, S. Searle,

B. Servin, B. R. Southey, G. Sperber, P. Stadler, J. V. Sweedler, H. Tafer, B. Thomsen, R. Wali, J. Wang, J. Wang, S. White, X. Xu, M. Yerle, G. Zhang, J. Zhang, J. Zhang, S. Zhao, J. Rogers, C. Churcher, L. B. Schook, Analyses of pig genomes provide insight into porcine demography and evolution. *Nature*. **491**, 393–398 (2012).

15. J. Zhu, F. Chen, L. Luo, W. Wu, J. Dai, J. Zhong, X. Lin, C. Chai, P. Ding, L. Liang, S. Wang, X. Ding, Y. Chen, H. Wang, J. Qiu, F. Wang, C. Sun, Y. Zeng, J. Fang, X. Jiang, P. Liu, G. Tang, X. Qiu, X. Zhang, Y. Ruan, S. Jiang, J. Li, S. Zhu, X. Xu, F. Li, Z. Liu, G. Cao, D. Chen, Single-cell atlas of domestic pig cerebral cortex and hypothalamus. *Sci. Bull.* **66**, 1448–1461 (2021).

16. A. D. Foote, Y. Liu, G. W. C. Thomas, T. Vinař, J. Alföldi, J. Deng, S. Dugan, C. E. Van Elk, M. E. Hunter, V. Joshi, Z. Khan, C. Kovar, S. L. Lee, K. Lindblad-Toh, A. Mancia, R. Nielsen, X. Qin, J. Qu, B. J. Raney, N. Vijay, J. B. W. Wolf, M. W. Hahn, D. M. Muzny, K. C. Worley, M. T. P. Gilbert, R. A. Gibbs, Convergent evolution of the genomes of marine mammals. *Nat. Genet.* **47**, 272–275 (2015).

17. L. Jin, Q. Tang, S. Hu, Z. Chen, X. Zhou, B. Zeng, Y. Wang, M. He, Y. Li, L. Gui, L. Shen, K. Long, J. Ma, X. Wang, Z. Chen, Y. Jiang, G. Tang, L. Zhu, F. Liu, B. Zhang, Z. Huang, G. Li, D. Li, V. N. Gladyshev, J. Yin, Y. Gu, X. Li, M. Li, A pig BodyMap transcriptome reveals diverse tissue physiologies and evolutionary dynamics of transcription. *Nat. Commun.* **12** (2021), doi:10.1038/s41467-021-23560-8.

18. E. Sjöstedt, W. Zhong, L. Fagerberg, M. Karlsson, N. Mitsios, C. Adori, P. Oksvold, F. Edfors, A. Limiszewska, F. Hikmet, J. Huang, Y. Du, L. Lin, Z. Dong, L. Yang, X. Liu, H. Jiang, X. Xu, J. Wang, H. Yang, L. Bolund, A. Mardinoglu, C. Zhang, K. von Feilitzen, C. Lindskog, R. Pontén, Y. Luo, T. Hökfelt, M. Uhlén, J. Mulder, An atlas of the protein-coding genes in the human, pig, and mouse brain. *Science (80-.).* **367**, eaay5947 (2020).

19. M. Sykes, D. H. Sachs, Transplanting organs from pigs to humans. *Sci. Immunol.* **4** (2019), doi:10.1126/sciimmunol.aau6298.

20. J. Wu, H. T. Greely, R. Jaenisch, H. Nakauchi, J. Rossant, J. C. I. Belmonte, Stem cells and interspecies chimaeras. *Nature*. **540**, 51–59 (2016).

21. J. J. Cai, scGEAToolbox: A matlab toolbox for single-cell RNA sequencing data analysis. *Bioinformatics*. **36**, 1948–1949 (2020).

22. M. Z. Nikolić, O. Caritg, Q. Jeng, J. A. Johnson, D. Sun, K. J. Howell, J. L. Brady, U. Laresgoiti, G. Allen, R. Butler, M. Zilbauer, A. Giangreco, E. L. Rawlins, Human embryonic lung epithelial tips are multipotent progenitors that can be expanded in vitro as long-term self-renewing organoids. *Elife*. **Jun 30**, e26575 (2017).

23. M. E. Ardini-Poleske, R. F. Clark, C. Ansong, J. P. Carson, R. A. Corley, G. H. Deutsch, J. S. Hagood, N. Kaminski, T. J. Mariani, S. S. Potter, G. S. Pryhuber, D. Warburton, J. A. Whitsett, S. M. Palmer, N. Ambalavanan, S. Lin, C. Ljungberg, Z. Bar-Joseph, D. Al Alam, R. Figueroa, S. Fraser, D. Koos, R. Lansford, R. Moats, H. Pollack, W. Shi, A. Shirtz, C. Wigfall, M. Adam, B. Aronow, Y. Du, M. Guo, J. Kitzmiller, A. Perl, A. Potter, J. Snowball, S. Wert, K. Wikenheiser-Brokamp, J. Woods, Y. Xu, C. Chan, C. Hill, J. Kirchner, G. C. Clair, J. Laskin, J. E. McDermott, M. Duparc, N. Gaddis, J. Levy, G. Page, H. Pan, T. Nicola, M. Chan, D. Chhabra, C. Espinoza, G. Bandyopadhyay, T. Bushnell, J. Holden-Wiltse, P. Katzman, R. Misra, C. Frevert, S. Gharib, F. Ahangari, LungMAP: The molecular atlas of lung development program. *Am. J. Physiol. - Lung Cell. Mol. Physiol.* **313**, L733–L740 (2017).

24. F. Chen, T. J. Desai, J. Qian, K. Niederreither, J. Lü, W. V Cardoso, Inhibition of Tgf beta signaling by endogenous retinoic acid is essential for primary lung bud induction. *Development*. **134**, 2969–79 (2007).

25. A. M. Goss, Y. Tian, T. Tsukiyama, E. D. Cohen, D. Zhou, M. M. Lu, T. P. Yamaguchi, E. E. Morrisey, Wnt2/2b and beta-catenin signaling are necessary and sufficient to specify lung progenitors in the foregut. *Dev. Cell*. **17**, 290–8 (2009).

26. R. F. C. Hein, J. H. Wu, Y. Tsai, A. Wu, A. J. Miller, E. M. Holloway, T. Frum, A. S. Conchola, E. Szenker-ravi, B. Reversade, K. S. Yan, C. J. Kuo, J. R. Spence, R-SPONDIN2+ Mesenchymal Cells Form the Bud Tip Progenitor Niche During Human Lung Development. *bioRxiv* (2021).

27. S. Ghosh, J. R. Paez-Cortez, K. Boppidi, M. Vasconcelos, M. Roy, W. Cardoso, X. Ai, A. Fine, Activation dynamics and signaling properties of Notch3 receptor in the developing pulmonary artery. *J. Biol. Chem.* **286**, 22678–87 (2011).

28. S. Danopoulos, S. Bhattacharya, T. J. Mariani, D. Al Alam, Transcriptional characterisation of human lung cells identifies novel mesenchymal lineage markers. *Eur. Respir. J.* **55** (2020), doi:10.1183/13993003.00746-2019.

29. S. Lee, I. Kohane, S. Kasif, Genes involved in complex adaptive processes tend to have highly conserved upstream regions in mammalian genomes. *BMC Genomics*. **6** (2005), doi:10.1186/1471-2164-6-168.

30. M. J. L. de Hoon, S. Imoto, J. Nolan, S. Miyano, Open source clustering software. *Bioinformatics*. **20**, 1453–1454 (2004).

31. A. J. Saldanha, Java Treeview—extensible visualization of microarray data. *Bioinformatics*. **20**, 3246–3248 (2004).

32. A. Vienna, R: A language and environment for statistical computing. R Foundation for Statistical Computing, . *R Core Team* (2022).

33. P. Bardou, J. Mariette, F. Escudié, C. Djemiel, C. Klopp, Jvenn: An interactive Venn diagram viewer. *BMC Bioinformatics*. **15**, 1–7 (2014).

34. P. Meylan, R. Dreos, G. Ambrosini, R. Groux, P. Bucher, EPD in 2020: enhanced data visualization and extension to ncRNA promoters. *Nucleic Acids Res.* **48**, 65–69 (2019).

35. G. O. C. Cory, R. Garg, R. Cramer, A. J. Ridley, Phosphorylation of tyrosine 291 enhances the ability of WASp to stimulate actin polymerization and filopodium formation. Wiskott-Aldrich Syndrome protein. *J. Biol. Chem.* **277**, 45115–21 (2002).

Acknowledgments:

We thank the members of the Columbia Center for Human Development for the scientific input, members of the Columbia Genome Center for the transcriptional analysis for RNA-seq, the CCTI flow cytometry core (LSRII: NIH S10RR027050), and Columbia Stem Cell Initiative (CSCI) Flow Cytometry core (FACS Area) for FACS and sorting.

Funding:

NIH-NHLBI 1R01 HL148223-01, DoD PR190557, PR191133 to M. M.

DoD GW190096 to J.J.C.

Author contributions:

Conceptualization: M.M.

Methodology: M.M., Y.S., J.T., J.J.C., M.K.

Investigation: Y.S., J.T., H.S., A.M., Y.H., A.S., Z.N., K.Y., M.M.

Visualization: Y.S., J.T., M.K., J.J.C., M.K.

Funding acquisition: M.M.

Project administration: M.M.

Supervision: J.J.C., M.M.

Writing – original draft: Y.S., J.T., J.J.C., M.M.

Competing interests: Authors declare that we have no competing interests.

Data and materials availability: Data available upon request

Supplementary Materials

Materials and Methods

Figs. S1 to S7

Data S1 to S2

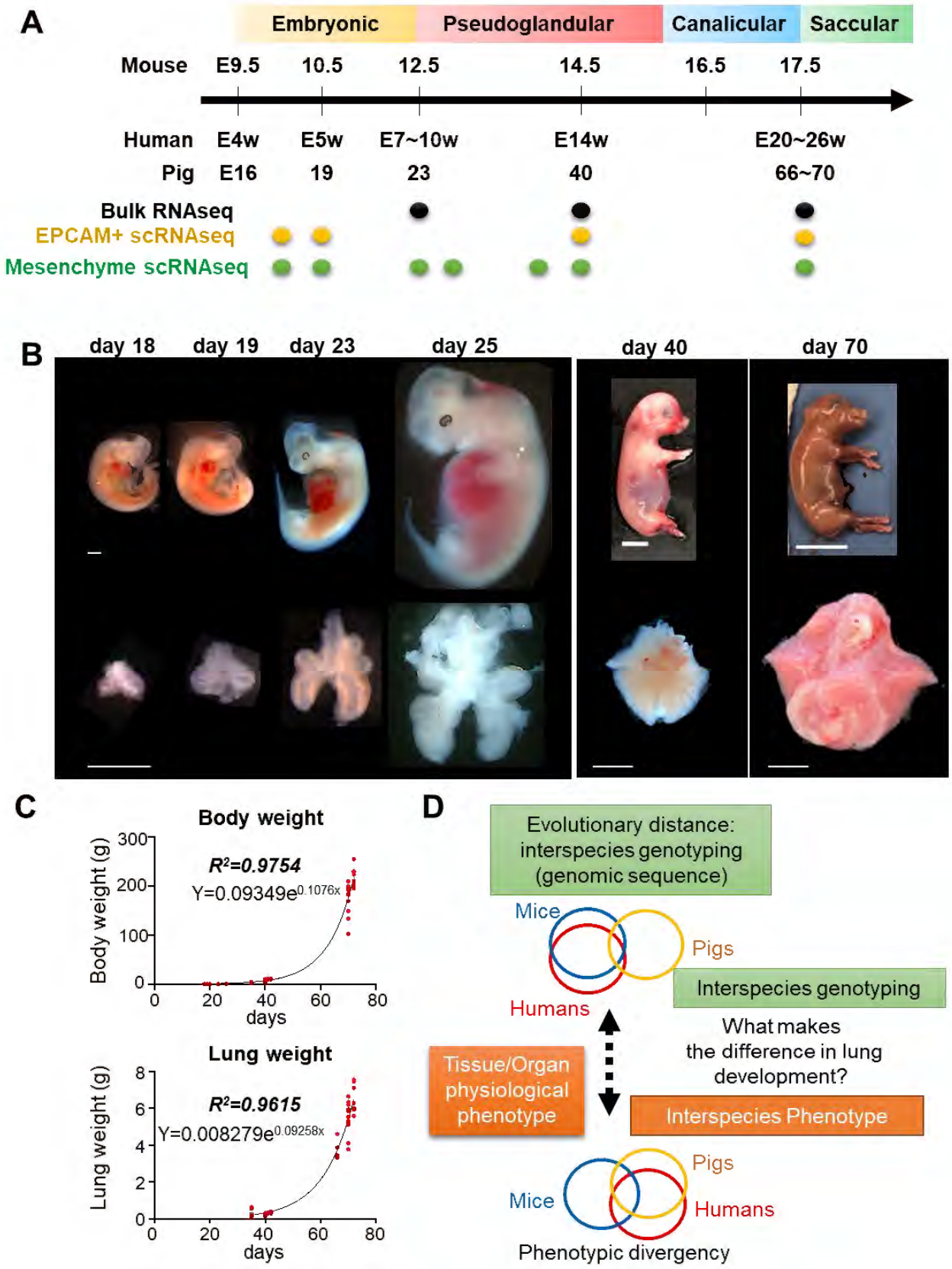
A
Embryonic
Pseudoglandular
Canalicular
Saccular
Mouse
E9.5
10.5
12.5
14.5
16.5
17.5
Human
E4w
E5w
E7~10w
E14w
E20~26w
Pig
E16
19
23
40
66~70
Bulk RNAseq
EPCAM+ scRNAseq
Mesenchyme scRNAseq
B
day 18
day 19
day 23
day 25
day 40
day 70
C
Body weight
Body weight (g)
R²=0.9754
Y=0.09349e^0.1076x
days
Lung weight
Lung weight (g)
R²=0.9615
Y=0.008279e^0.09258x
days
D
Evolutionary distance:
interspecies genotyping
(genomic sequence)
Mice
Pigs
Humans
Interspecies genotyping
What makes
the difference in lung
development?
Tissue/Organ
physiological
phenotype
Interspecies Phenotype
Pigs
Mice
Humans
Phenotypic divergency

Figure 1. The dramatic change of organismal and lung size during swine development (A) Schematic diagram: Developmental stages and sampling of pig lungs compared to mice and humans. Each experiment is indicated by a dot (Black: bulk RNA-seq, Yellow: EPCAM-sorted epithelial scRNA-seq, Green: mesenchyme scRNA-seq). **(B)** The representative gross morphology of pig embryos at each embryonic gestation period (E) 18, 19, 23, 25, 42, 70. **(C)** Graphs: Exponential change of the weight of pig embryos and lungs. Each red dot indicates each embryonic pig specimen. **(D)** The schematic model depicting the discrepancy between interspecies genotyping and phenotype. The human organ size phenotype is closer to a pig than a mouse, while the human genomic sequence is evolutionarily closer to a mouse than a pig. **Scale Bar:** 1mm (E18-25), 1cm (E40 embryo and lung, and E70 lung), 5cm (E70 lung)

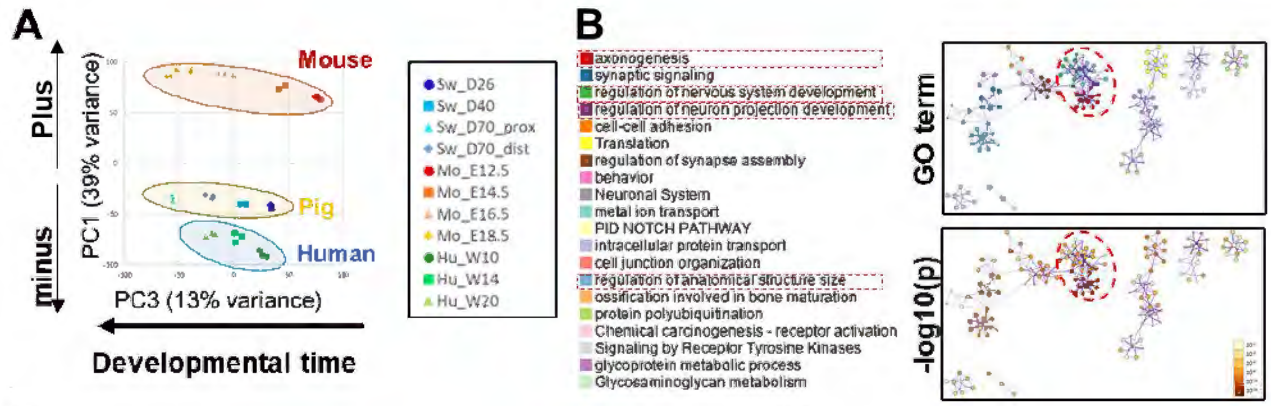
A
Plus
minus
PC1 (39% variance)
PC3 (13% variance)
Developmental time
Mouse
Pig
Human
Sw_D26
Sw_D40
Sw_D70_prox
Sw_D70_dist
Mo_E12.5
Mo_E14.5
Mo_E16.5
Mo_E18.5
Hu_W10
Hu_W14
Hu_W20
B
axonogenesis
synaptic signaling
regulation of nervous system development
regulation of neuron projection development
cell-cell adhesion
Translation
regulation of synapse assembly
behavior
Neuronal System
metal ion transport
PID NOTCH PATHWAY
intracellular protein transport
cell junction organization
regulation of anatomical structure size
ossification involved in bone maturation
protein polyubiquitination
Chemical carcinogenesis - receptor activation
Signaling by Receptor Tyrosine Kinases
glycoprotein metabolic process
Glycosaminoglycan metabolism
GO term
-log10(p)

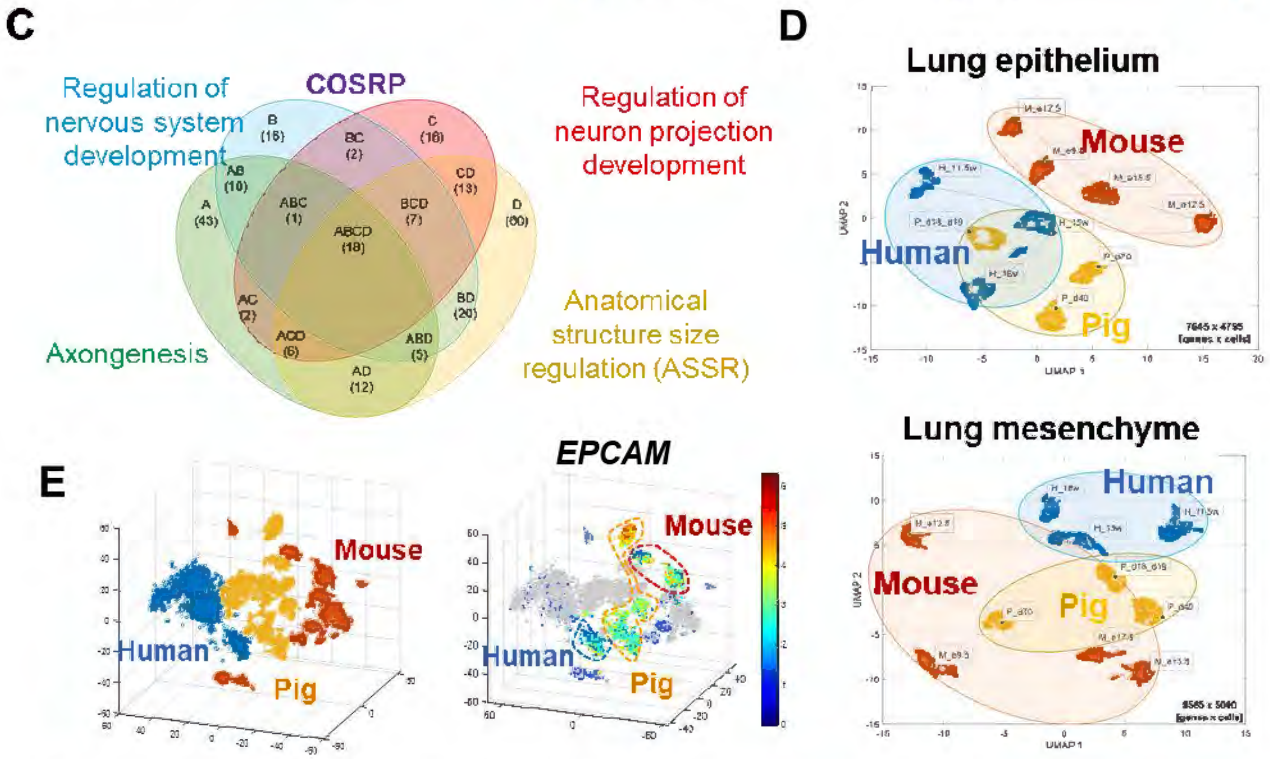
C
Regulation of nervous system development
COSRP
Regulation of neuron projection development
Axongenesis
Anatomical structure size regulation (ASSR)
A (43)
B (18)
C (16)
D (60)
AB (10)
BC (2)
CD (13)
ABC (1)
BCD (7)
ABCD (18)
AC (2)
BD (20)
ACD (6)
ABD (5)
AD (12)
D
Lung epithelium
Mouse
Human
Pig
UMAP 1
UMAP 2

E
Mouse
Human
Pig
EPCAM
Mouse
Human
Pig
Lung mesenchyme
Human
Mouse
Pig
UMAP 1
UMAP 2

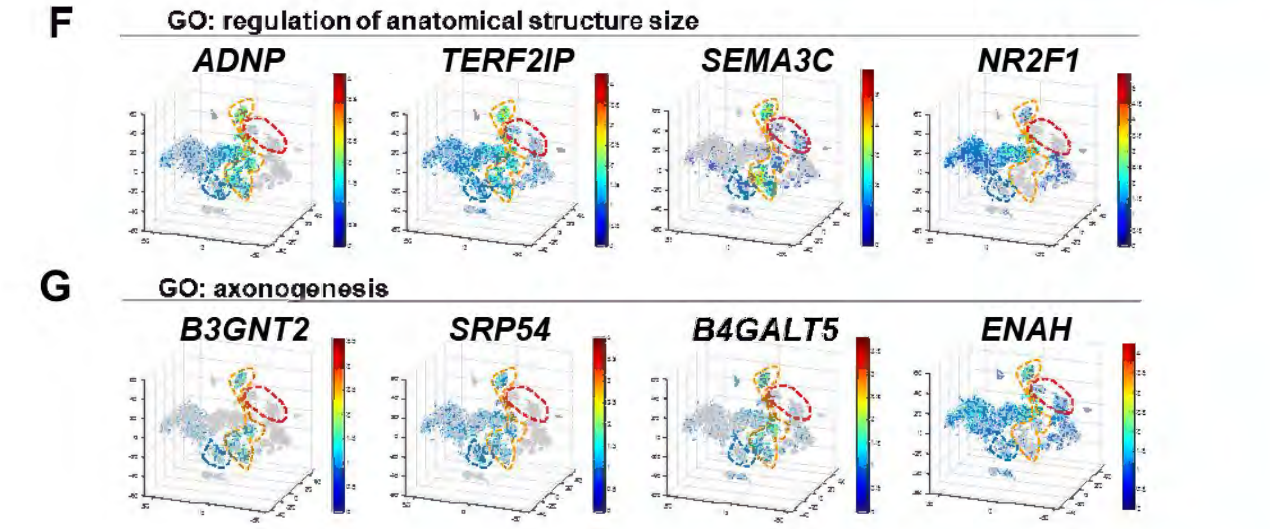
F
GO: regulation of anatomical structure size
ADNP
TERF2IP
SEMA3C
NR2F1
G
GO: axonogenesis
B3GNT2
SRP54
B4GALT5
ENAH

Figure 2. Cross-species transcriptome analyses identify the core of the organ size regulation program (COSRP) during swine lung development. (A) PCA analyses showing human, mouse, and pig embryonic lung transcriptional variance. PC3: the developmental time of each species. PC1 minus in the Y axis: the human and swine had similar variance over time, distinct from mice. **(B)** Gene ontology (GO) terms network analysis visualizing the top 10% genes contributing to PC1 minus axis and GO-term associated network: top: Each color indicates GO term category in the left panel. Bottom: colored by significance (P-value: 10^{-2}~10^{-20}). Red dotted circle: COSRP. (**C**) Venn chart plot visualizing 45 COSRP genes composed of four GO terms; Axonogenesis, Regulation of nervous system development, Regulation of neuron projection development, and Anatomical structure size regulation (ASSR). **(D)** Cross-species scRNA-seq UMAP: swine transcriptome closer to humans than mice in developing lung epithelium (top) and mesenchyme (bottom) over time. **(E)** 3D tSNE plot: human, mouse, and swine $EPCAM^+$ lung epithelium and $EPCAM^-$ mesenchyme scRNA-seq combined data. 3D tSNE feature plot for representative COSRP genes: **(F)** *ADNP, TERF2IP, SEMA3C,* and *NR2F1.* **(G)** *B3GNT2, SRP54, B4GALT5,* and *ENAH* were highly enriched in swing and human epithelium or mesenchyme but rarely in mice.

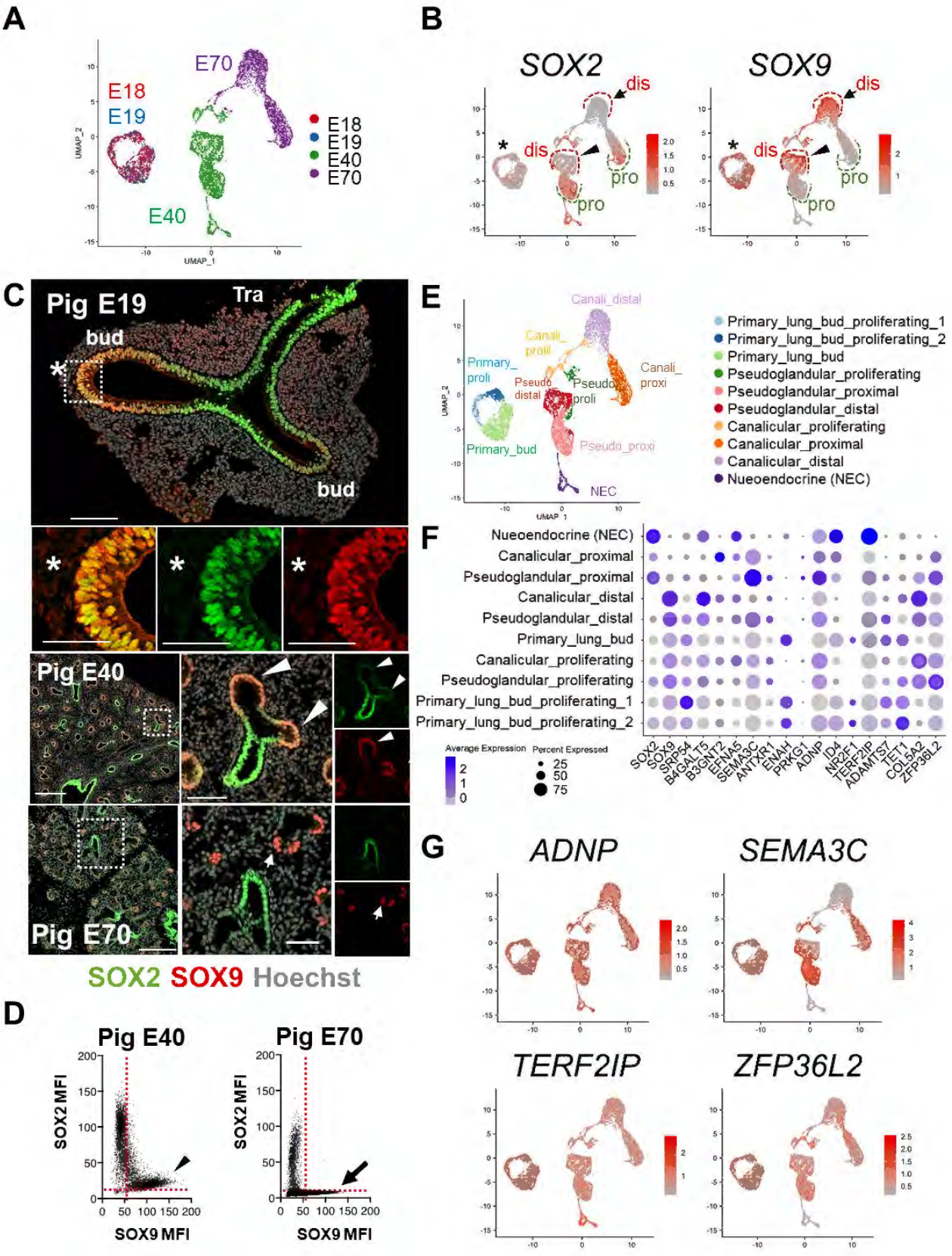
A
E70
E18
E19
E40
E18
E19
E40
E70
UMAP_2
UMAP_1
B
SOX2
SOX9
dis
dis
pro
pro
C
Pig E19
Tra
bud
bud
Pig E40
Pig E70
SOX2 SOX9 Hoechst
D
Pig E40
Pig E70
SOX2 MFI
SOX9 MFI
E
Canali_distal
Canali_ proli
Primary_ proli
Pseudo distal
Pseudo proli
Canali_ proxi
Primary_bud
Pseudo_proxi
NEC
Primary_lung_bud_proliferating_1
Primary_lung_bud_proliferating_2
Primary_lung_bud
Pseudoglandular_proliferating
Pseudoglandular_proximal
Pseudoglandular_distal
Canalicular_proliferating
Canalicular_proximal
Canalicular_distal
Nueoendocrine (NEC)
F
Nueoendocrine (NEC)
Canalicular_proximal
Pseudoglandular_proximal
Canalicular_distal
Pseudoglandular_distal
Primary_lung_bud
Canalicular_proliferating
Pseudoglandular_proliferating
Primary_lung_bud_proliferating_1
Primary_lung_bud_proliferating_2
Average Expression
Percent Expressed
SOX2
SOX9
SRP54
B4GALT5
B3GNT2
EFNA5
SEMA3C
ANTXR1
ENAH
PRKG1
ADNP
ID4
NR2F1
TERF2IP
ADAMTS7
TET1
COL5A2
ZFP36L2
G
ADNP
SEMA3C
TERF2IP
ZFP36L2

Figure 3. A unique human-like embryonic porcine lung epithelial program. UMAP feature plot for scRNA-seq depicting the samplings from embryonic lung epithelial cells from pig E18, E19, E40, and E70 **(A)**, *SOX2* and *SOX9* gene expression patterns (**B**), ten clusters in swine developing epithelial cells (**E**), and a ubiquitous expression of COSRP genes (ADNP, SEMA3C, *TERF2IP,* and *ZFP36L2)* in swine developing epithelial cells throughout lung development (**G**). **(C)** confocal IF imaging: embryonic pig lungs at E19, E40, and E70: SOX2 (green) and SOX9 (red) were co-expressed on the primary lung buds (asterisks*) and day40 distal lung buds (arrowheads), while only SOX9 were present on the day70 distal lung buds (arrows). **(D)** Graphs: qualitative morphometric analysis for SOX2 and SOX9 protein expression in the nucleus of pig E40 and E70 epithelial cells. Each dot: mean fluorescent intensity (MFI) of Sox2 or Sox9 in a cell nucleus. Arrow; day70 distal epithelial cells, arrowhead: day40 distal epithelial cells. **(F)** Dot plot showing the expression levels of *SOX2, SOX9*, and representative COSRP genes. Dis: distal (red dot lines), Pro: proximal (green dot lines) lung epithelial compartment. Scale bars: top: 100μm, enlarged: 50μm, middle 500μm, enlarged: 100μm, Bottom: 200μm, enlarged: 50μm

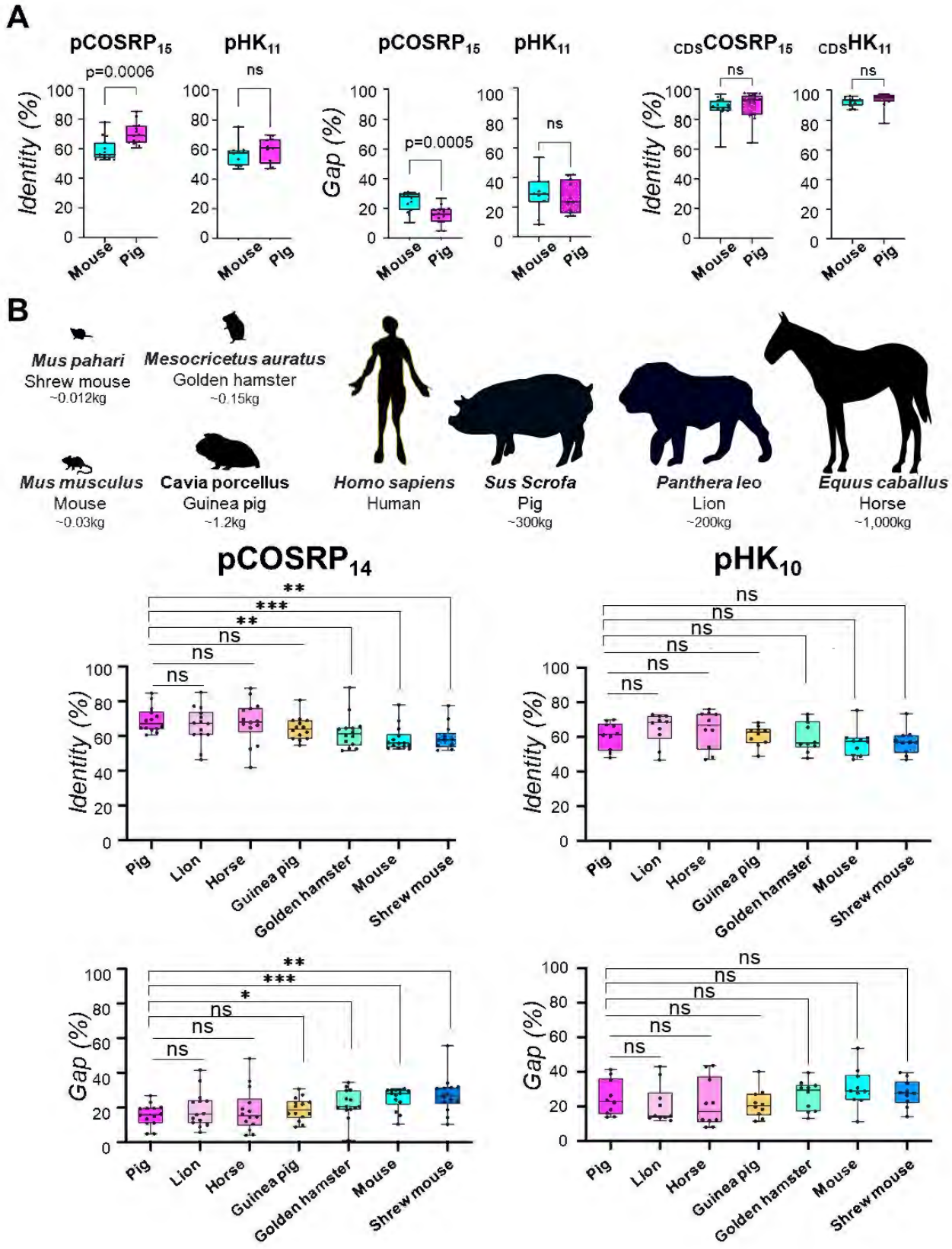
A
pCOSRP15
pHK11
pCOSRP15
pHK11
CDSCOSRP15
CDSHK11
Identity (%)
Gap (%)
p=0.0006
ns
p=0.0005
Mouse
Pig
B
Mus pahari
Shrew mouse
~0.012kg
Mesocricetus auratus
Golden hamster
~0.15kg
Mus musculus
Mouse
~0.03kg
Cavia porcellus
Guinea pig
~1.2kg
Homo sapiens
Human
Sus Scrofa
Pig
~300kg
Panthera leo
Lion
~200kg
Equus caballus
Horse
~1,000kg
pCOSRP14
pHK10
Pig
Lion
Horse
Guinea pig
Golden hamster
Mouse
Shrew mouse

Figure 4. COSRP promoter region encodes a relative organismal size. (A) graphs: A box and whisker plot: COSRP or housekeeping (HK) gene promoter homologies (left: % identity, middle: % gap) of mice and pigs to humans. Right: The Coding sequence (CDS) homologies (% identity) of mice and pigs to humans. The homology of the human COSRP promoter region was significantly lower in mice than in swine ($p=0.0006$, ***$P<0.001$) while not significant in HK promoter regions or CDS or HK regions. (COSRP gene; n=15, HK genes; n=11) **(B)** top: Schematic diagram of large and small animals with representative body weight. Bottom: Graphs: Homologies (% identity, % gap) of each species COSRP, housekeeping (HK) gene promoters to humans. A dot in each graph (**A, B**) represents each COSRP or HK gene in each species. mean±s.e.m. in 14 COSRP genes or 10 HK genes per group. two-tails Student's t-test, *$P<0.05$, **$P<0.01$, ***$P<0.001$, ****$P<0.0001$, ns: statistically non-significant.

Science
AAAS

Supplementary Materials for

A developmental program that regulates mammalian organ size offsets evolutionary distance

Yuko Shimamura *et al*.

Corresponding authors: Munemasa Mori, mm4452@cumc.columbia.edu; James J, Cai, jcai@tamu.edu

This PDF file includes:

Materials and Methods
Figs. S1 to S7
Captions for Data S1to S2

Other Supplementary Materials for this manuscript include the following:

Data S1 to S2

Materials and Methods

Animals

Timed-pregnant Yucatan miniature sows were obtained from Sinclair BioResources. We surgically harvested the embryos from E18 to E70 and euthanized the pregnant sows right after the surgery. The body weight of swine embryos and their lungs were measured right after sampling the specimens. The gross morphology images were taken by a digital camera and dissection microscopy (Leica TL5000 elgo, Nikon Labophot 2 microscope). All surgical procedures were performed under the approval of the Columbia University Institutional Animal Care and Use Committee and the USAMRMC Animal Care and Use Review Office (ACURO).

Tissue preparation for bulk RNA-Seq

For bulk RNA-seq analyses, we collected the peripheral lungs from E66 and E40 pig embryos, the proximal lungs (around the main bronchus) from E66, and half of the whole lungs from E26. Biological triplicates were prepared from independent embryos (*n=3,* at each time point). Total RNA from those samples was extracted with ReliaPrep RNA Miniprep Systems (Z6111, Promega) according to the manufacturer's protocol. Libraries for RNA-Seq were prepared using Illumina TruSeq chemistry that were sequenced with paired-end sequencing using Illumina NovaSeq 6000. The sequencing reads were performed pseudo alignment to a Kallisto index created from Pig transcriptomes Sscrofa11.1 using Kallisto (0.44.0).

Tissue dissociation for scRNA-Seq

Lung buds from E41 and E70 embryos are dissociated with the accutase and stained with DAPI to detect dead cells by FACS analyzer. Live cells were sorted out using FACSAria II (BD). Whole lungs from E18, 19, 23, and 25 embryos and lung buds from E35 embryos were dissociated using *Bacillus licheniformis* protease (P5380, Millipore Sigma) with DNaseI. The live cells or $EPCAM^+$ cells were sorted using the following staining: rabbit anti-pig EPCAM antibody (MyBioSource, MBS2053510) and Donkey anti-rabbit IgG Alexa Fluor 647 (A-31573, Thermo Fisher Scientific); live or dead staining: SYTOX Green Nucleic Acid Stain (S7020, Thermo Fisher Scientific), and Vybrant DycycleRuby Stain (V10309, Thermo Fisher Scientific). Cells were loaded on a 10x Genomics Chromium controller, aiming for 5,000 cell recoveries. For swine epithelium analyses, 4,464, 1,372, 5,528, and 5852 cells from E18, 19, 40, and 70 were recovered. For swine mesenchyme analyses, 12,288, 8,547, 11,006, 11, 851, 8, 478, and 7,596 cells from E18, 19, 23, 25, 35, 40, 70 were recovered.

Bulk RNA-seq analysis

For the cross-species bulk RNA-seq analyses, we input identifiers of a mouse (GSE122919; E12, 14, 16, 18, *n=3 each*), human (GSE121238; E10, 14, 20 weeks, *n=3 each*), and the swine lung development database (E26, 40, E70 distal, proximal, *n=3 each*). We annotated and mapped 12,424 common orthologues genes in mouse, human, and swine lung development using EggNOG and Homologene databases. To decide the swine lung stage, we generated a heatmap based on the normalized TPM value by comparing the human lung development database

(GSE121238). Briefly, we selected significant differentially-expressed genes (DEGs; Fold Change >1.5, FDR < 0.1) at each time point of human lung development using DESeq2 and applied the DEGs to the swine lung database. The normalization and unsupervised clustering of swine data were performed using Cluster3.0(*30*), and heatmaps were visualized using Java Treeview(*31*).

For the cross-species PCA, we used the TPM value of 12,424 common genes from mouse, human, and swine datasets in R ver 4.2.1(*32*). Among 12,424 common genes, PC1 minus-contributing genes were ranked by rotation of PC1, and the top 10% genes (1,242 genes) were further extracted to apply to gene ontology (GO) term enrichment analyses. GO enrichment analysis was used for each MCODE network to extract "biological meanings" from the network component. The top three best p-value terms were retained compared to all samples. We first identified all statistically enriched GO terms based on the default choices under Express Analysis using metascape. For generating the GO term network in Figure 2B, we selected a subset of representative terms from the full cluster and converted them into a network layout. Specifically, each term is represented by a circle node whose size is proportional to the number of input genes that fall under that term. Its color represents its cluster identity (i.e., nodes of the same color belong to the same cluster). Terms with a similarity score > 0.3 are linked by an edge (the thickness of the edge represents the similarity score). The network is visualized with Cytoscape with a "force-directed" layout and edge bundled for clarity. The same enrichment network has its nodes colored by p-value, as shown in the legend. Venn charts were drawn for 230 COSRP genes using the jvenn software(*33*).

Cross-species scRNA-seq data analysis

For the cross-species analyses, we used SCGEATOOL to combine datasets of the mouse (E9.5; GSE136689, E12.5; GSM4504959, E15.5; GSM4504960, E17.5; GSM4504961), human (E-MTAB-8221), and our swine lung development (E18, 19, 35, 40, 70 epithelium and E18, 19, 23, 26, 35, 40, 70 mesenchyme). Subsequently, UMAP and 3D tSNE analyses were unbiasedly calculated. We manually selected 45 genes highly expressed in humans and swine but not mice among the 230 COSRP genes in the 3D-tSNE plot. Among 45 genes, we identified 15 genes ubiquitously enriched either in swine and human lung mesenchyme or epithelium across the time, but not mice. For scGRN analyses, we applied 45 COSRP genes across the species at each developmental time point.

scRNA-seq data analysis

All scRNA-seq assays were performed with Illumina NovaSeq 6000. Reads alignment to Sscrofa11.1 pig reference genome and generation of gene expression matrix were processed using 10x genomics cellranger software version 6.1.2. For processing, integration, and downstream analysis, the Seurat package and SCGEATOOL were used. Cells were selected in the range of 2,000 to 9,000 mapped genes. Feature data were scaled using the Seurat ScaleData function. Non-linear dimension reduction was performed using uniform manifold projection (UMAP) using the Seurat RunUMAP process. The clustering was performed using the Louvain algorithm, and parameters were set empirically by detecting marker genes in each cluster. Pseudotime analysis was performed using Monocle 3 with the default parameter. The clusters

associated with leukocyte, erythroid, endothelial, and neuronal cells were excluded from mesenchyme analysis. Differential expression for clusters was performed using the Seurat FindAllMarkers function using the Wilcoxon rank test. Marker genes were calculated for each cluster against the cells within all the other clusters.

Genomic sequence alignment analysis

By the GO network analysis using cross-species bulk RNA-seq datasets, we found the condensed four GO nodes (ASSR, Regulation of neuron projection development, Regulation of nervous system development, and Axongenesis) with highly enriched networks. We defined those four GO term networks as COSRP, containing overlapping 230 genes. Within those 230 COSRP genes, 45 genes were enriched in human and pig lung development but not in mice, analyzed by cross-species 3D tSNE plot using SCSEGATOOL. Among 45 COSRP genes, 17 showed ubiquitous expression patterns with moderate or high levels in swine scRNA-seq Seurat analysis (**Data S2**). Since mouse *PRKG1* CDS and *human CCDC85B* TSS were not annotated in the Ensemble, we selected human CDS (coding sequence) or promoters (2,000 bp upstream of TSS) of 15 COSRP (*SEMA3C, NR2F1, B3GNT2, ENAH, EFNA5, ADNP, ADAMTS7, ANTXR1, B4GALT5, COL5A2, ID4, SRP54, TERF2IP, TET1,* and *ZFP36L2*) and 11 HK genes (*EIF4G2, HNRNPA2B1, HNRNPC, RBX1, SEC62, SON, YBX1, EIF3H, PFDN5, SNRPE,* and *YWHAE*) in the Ensemble. For comparing eight animals, *NR2F1* and *SNRPE* were excluded from the analysis because the homologous sequence was not annotated in shrew mouse and golden hamster. Human TSS information was identified from Eukaryotic Promotor Database. In the case of multiple promoters, the primary promoter for each gene was used for the following analysis(*34*). The homology (% identity: percentage of nucleotide sequence identity, and % Gaps) was calculated using a pair-wise comparison program with the Smith-Waterman algorism(*35*) by Snapgene (ver. 6.1.1) software(Gap open penalty: 10.0, Gap extend penalty: 1.0). For the interspecies promoter or CDS analysis, we compared the human CDS or promoter (2,000 bp upstream of TSS) sequence of COSRP genes or HK genes with the homologous region of each species, identified through comparative genomics alignment (text) or Nucleotide program in the Ensemble. The graphs were visualized, and statistical analyses were performed using Prism (ver. 9).

Immunostainings

Tissue samples were fixed in 4% paraformaldehyde and embedded in OCT compound, reacted with the primary antibodies (SOX2 (Invitrogen, 14-9811-82, 1:200), SOX9(R & D, AF3075, 1:200), NKX2-1(Abcam, ab76013, 1:100), Pro-SPC(Seven hills, WRAB-9337, 1:1000), Pro-SPB (Seven hills, WRAB-55522, 1:1000) overnight at 4 degrees in PBS, and washed in PBS, then incubated with the secondary antibodies conjugated with Alexa488 (Invitrogen, A21208, A21202, each 1:300), 568 (Invitrogen, A10042, A11057, each 1:300), or 647 (Invitrogen, A31573, 1:300), and Hoechst 33342 (Invitrogen, R37605, 1 drop in 500ul PBS) for 2 hours. Samples were mounted with PloLong Gold antifade reagent (Invitrogen, P37606). All images were captured with a 10x or 20x objective lens using confocal microscopy (Zeiss LSM 710).

Morphometric analysis for immunostainings

To determine the mean fluorescent intensity (MFI) of the SOX2 and SOX9 of the pig epithelial cells, all images were captured with the same settings captured by confocal microscopy (Leica LSM 710) (*n=3*). More than two thousand NKX2-1 positive cells from each sample were randomly selected, and each cell's nuclear MFI for SOX2-A488 and SOX9-A568 channels were calculated with the algorithm of Nuclei Count using Aivia software(Ver 10.5.1). The graphs were visualized using Prism (ver. 9).

Study approval: All experiments involving animals were performed according to the protocol approved by Columbia University Institutional Animal Care and Use Committee and USAMRMC Animal Care and Use Review Office (ACURO).

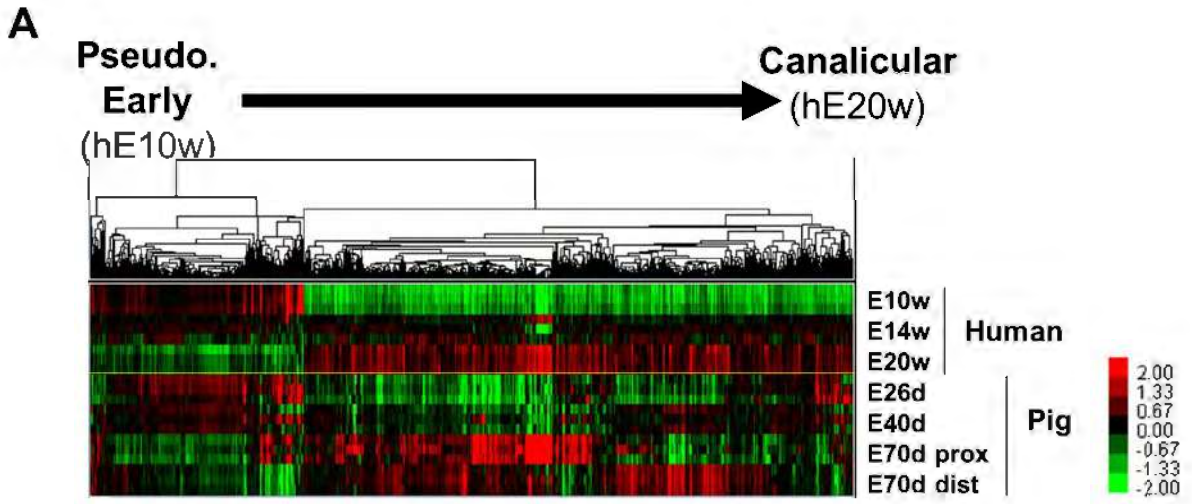

Figure S1. Swine lung developmental stage analysis by cross-species bulk RNA-seq (A) Heatmap of swine lung development at E26, E40 lungs, and E70 proximal or distal lungs depicting the top10% differentially expressed gene (DEG) found in human E10w, E14w, and E20w (gestation weeks 10, 14 and 20) during human lung development (data from GSE121238). The gene lists are in Data S1. The hE10w-einrched genes were expressed at E26 and E40 swine lungs but low at E70, while the hE20w-enriched genes were enriched at both E70 proximal and distal regions.

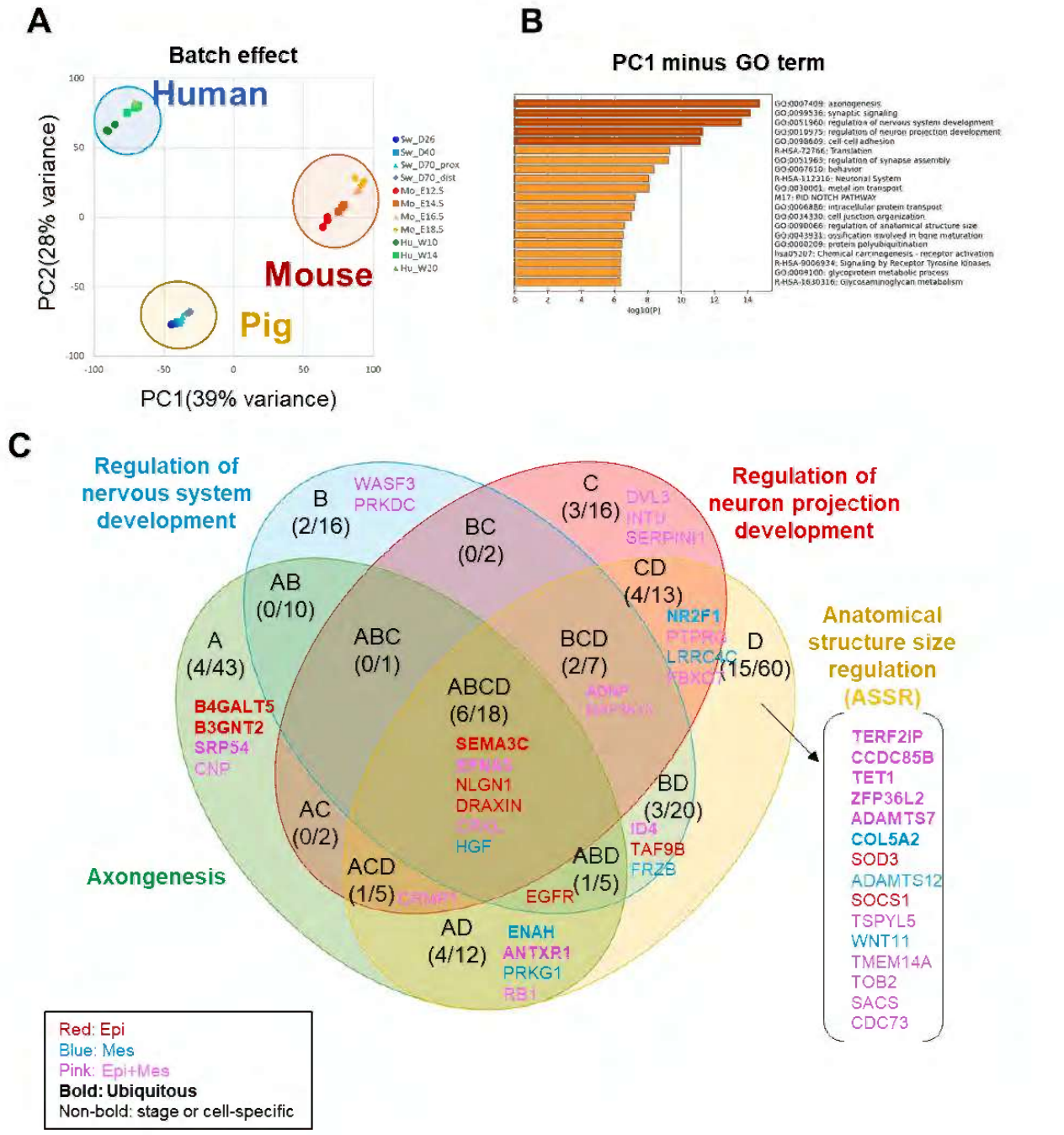

Figure S2. COSRP gene expression patterns during swine lung development (A) PCA analysis of human, mouse, and pig embryonic lung samples showed batch effect. **(B)** Bar graph depicting GO terms contributing to PC1 minus axis (colored by p-values). **(C)** Venn diagrams: each COSRP gene classification to 4 GO terms (axonogenesis, regulation of nervous system development, regulation of neuron projection development, and ASSR). Gene names were colored by their expression pattern in pig scRNA-seq Seurat analysis. COSRP genes expressed in epithelial (red), mesenchymal (blue), or both epithelial and mesenchymal cells (pink). Bold font: ubiquitous expression throughout swine lung development. Non-bold font: stage-specific or cell

type-specific expression pattern. The number in the Venn diagrams: the genes expressed in humans and pigs specifically but rarely in mice by the cross-species 3D-tSNE plot (left)/ the number of COSRP genes picked up by the cross-species bulk RNA-seq (right).

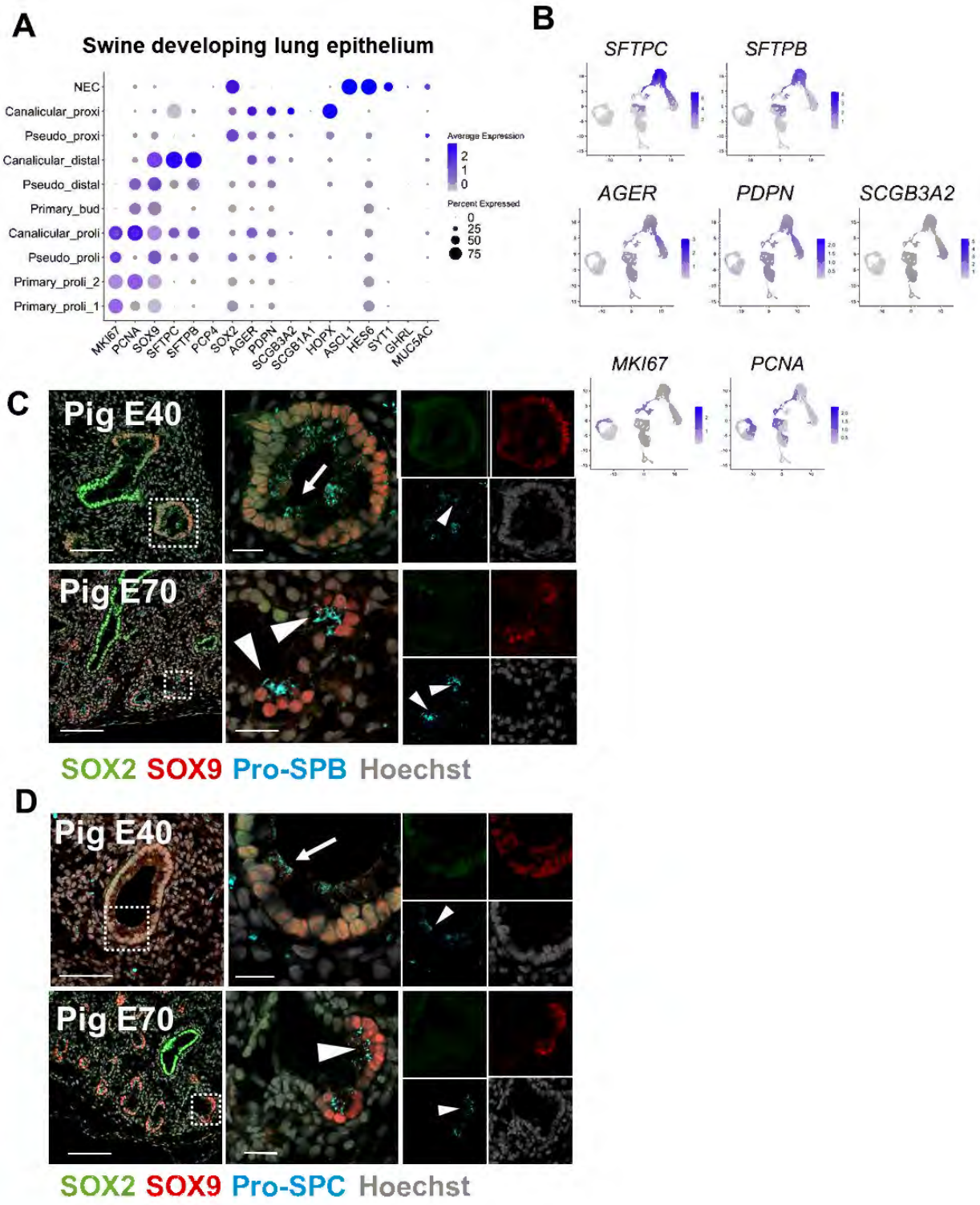

Figure S3. Expression patterns of mouse lung epithelial markers during pig lung development. Dot plot (**A**) and UMAP feature plot (**B**) depicting the airway (*SCGB3A2*: secretory cells, *MUC5AC*: goblet cells), alveolar (*SFTPC*, *SFTPB*: type2 cells, *PDPN*, *HOPX*: type1 cells, bipotential progenitors), and proliferating cell markers (*MKI67*, *PCNA*) during pig

lung development. Confocal IF imaging: SOX2 (green), SOX9 (red), and pro-SPB (cyan) (**C**) or pro-SPC (cyan) (**D**). Dense pro-SPB-positive or pro-SPC granules were present at E70 $SOX9^{+}SOX2^{-}$ sacculating cells (arrowheads) but less on the E40 $SOX9^{+}SOX2^{+}$ cells. Scale: left: 100μm, right: 20μm

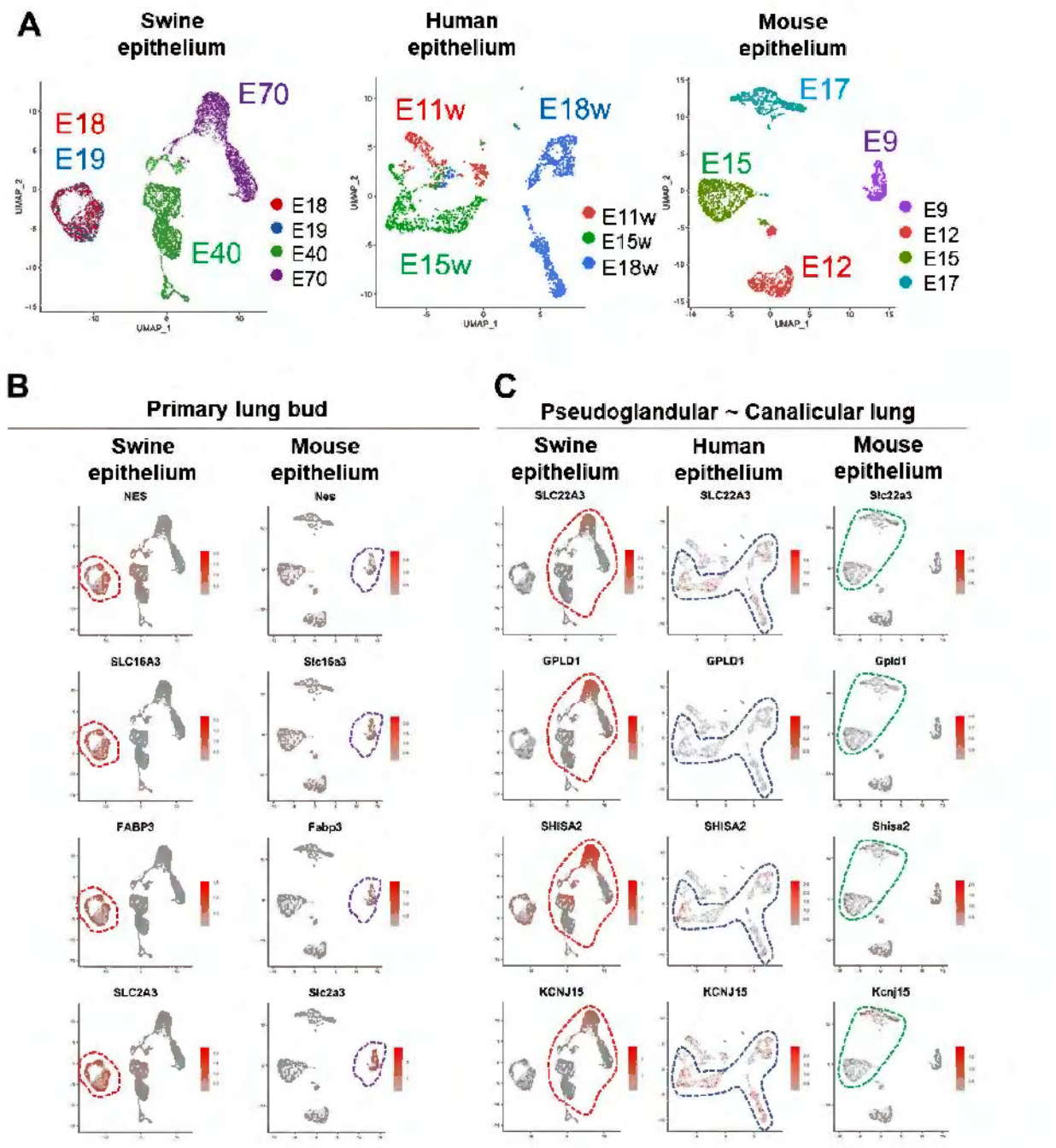

Figure S4. Identification of stage-specific lung bud markers during swine lung development **(A)** UMAP visualization of each developmental time point in the swine, human, and mouse epithelial cells during lung development. **(B)** UMAP feature plot showing genes highly expressed at the pig primary lung bud stage (*NES*, *SLC16A3*, *FABP3,* and *SLC2A3*) compared to mouse lung development. **(C)** UMAP feature plot of genes highly expressed from pseudoglandular to the canalicular stage in pigs (*SLC22A3, GPLD1, SHISA2, KCNJ15*).

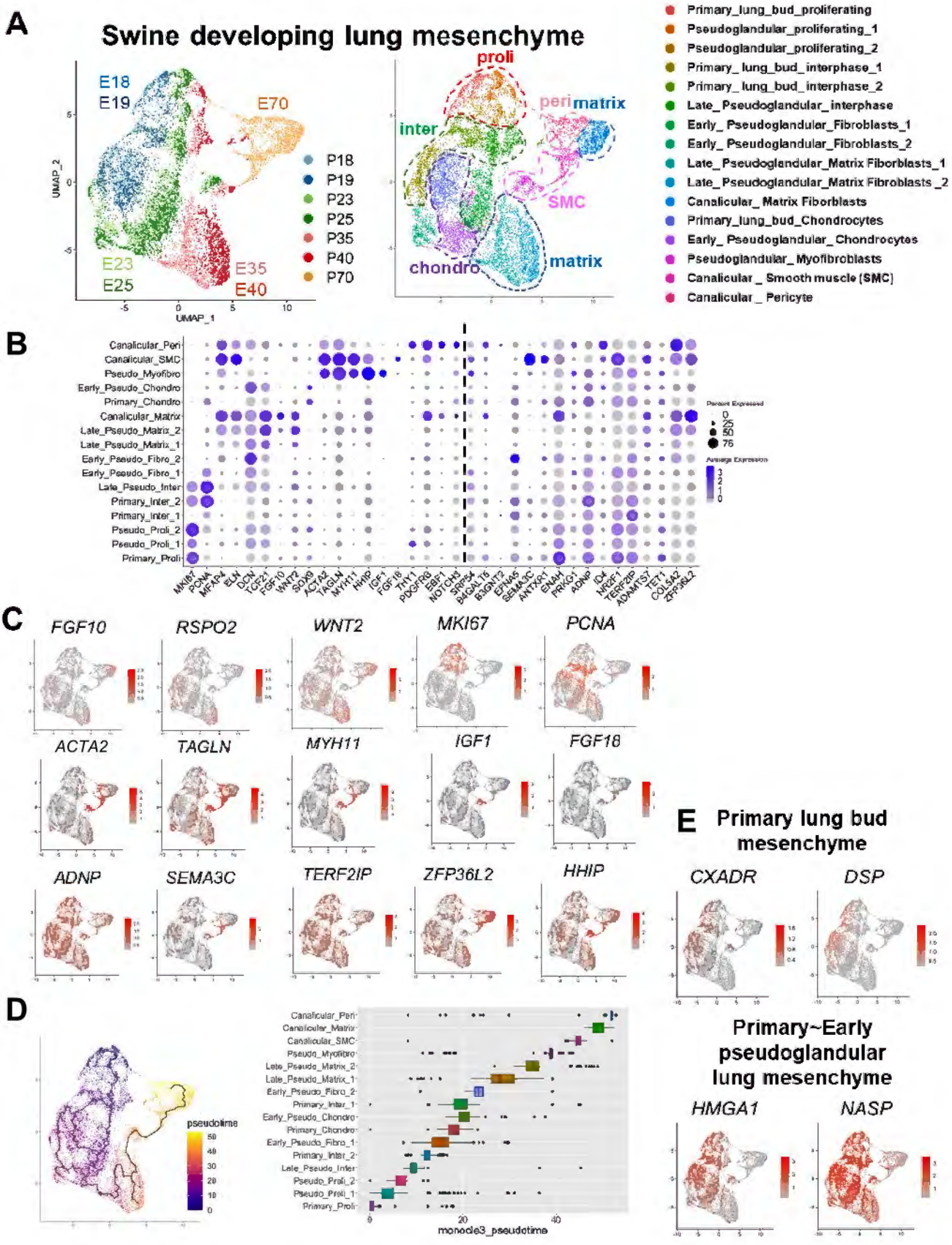
A
Swine developing lung mesenchyme
E18
E19
E70
E23
E25
E35
E40
P18
P19
P23
P25
P35
P40
P70
UMAP_1
UMAP_2
proli
peri
matrix
inter
SMC
chondro
matrix
Primary_lung_bud_proliferating
Pseudoglandular_proliferating_1
Pseudoglandular_proliferating_2
Primary_ lung_bud_ interphase_1
Primary_ lung_bud_ interphase_2
Late_ Pseudoglandular_ interphase
Early_ Pseudoglandular_Fibroblasts_1
Early_ Pseudoglandular_Fibroblasts_2
Late_ Pseudoglandular_Matrix Fiborblasts_1
Late_ Pseudoglandular_Matrix Fibroblasts _2
Canalicular_ Matrix Fiborblasts
Primary_lung_bud_Chondrocytes
Early_ Pseudoglandular_ Chondrocytes
Pseudoglandular_ Myofibroblasts
Canalicular _ Smooth muscle (SMC)
Canalicular _ Pericyte
B
Canalicular_Peri
Canalicular_SMC
Pseudo_Myofibro
Early_Pseudo_Chondro
Primary_Chondro
Canalicular_Matrix
Late_Pseudo_Matrix_2
Late_Pseudo_Matrix_1
Early_Pseudo_Fibro_2
Early_Pseudo_Fibro_1
Late_Pseudo_Inter
Primary_Inter_2
Primary_Inter_1
Pseudo_Proli_2
Pseudo_Proli_1
Primary_Proli
MKI67 PCNA MFAP4 ELN DCN TCF21 FGF10 WNT2 SOX9 ACTA2 TAGLN MYH11 HHIP IGF1 FGF18 THY1 PDGFRB EBF1 NOTCH3 SRPX4 B4GALT6 B3GNT2 EFNA5 SEMA3C ANTXR1 ENAH PRKG1 ADNP ID4 MYZF1 TERF2IP ADAMTS7 TET1 COL5A2 ZFP36L2
Percent Expressed
0
25
50
75
Average Expression
3
2
1
0
C
FGF10
RSPO2
WNT2
MKI67
PCNA
ACTA2
TAGLN
MYH11
IGF1
FGF18
ADNP
SEMA3C
TERF2IP
ZFP36L2
HHIP
D
pseudotime
50
40
30
20
10
0
monocle3_pseudotime
E
Primary lung bud mesenchyme
CXADR
DSP
Primary~Early pseudoglandular lung mesenchyme
HMGA1
NASP

Figure S5. COSRP gene transcriptional profiling of embryonic porcine lung mesenchymal cells. (A) UMAP visualization of lung mesenchymal cells from pig E18, E19, E23, E25, E35, E40, and E70. A dot blot (**B**) and UMAP feature plot (**C, E**) for COSRP genes (*ADNP, ENAH, NR2F1, TERF2IP, COL5A2, SEMA3C, and ZFP36L2*) and representative classical lung mesenchymal markers (distal lung bud markers: *FGF10, RSPO2,* lung mesenchyme specifier*: WNT2,* pericyte: *NOTCH3, EBF1, THY1,* smooth muscle cells (SMC) and myofibroblasts*: ACTA2, TAGLN, MYH11, HHIP, FGF18, IGF1,* chondrocyte: *DCN, SOX9, PDGFRB,* Matrix fibroblast*: MFAP4, ELN, TCF21*, proliferating cells (*MKI67, PCNA*))(**C),** and the stage-specific markers: primary lung bud stage (*CXADR* and *DSP*) and primary to pseudoglandular stage (*HMGA1* and *NASP*) (**E**). **(D)** Monocle pseudotime analysis of embryonic porcine lung mesenchymal cells. Cells are labeled by pseudotime. Boxplot showing the distribution of pseudotime within each cell group.

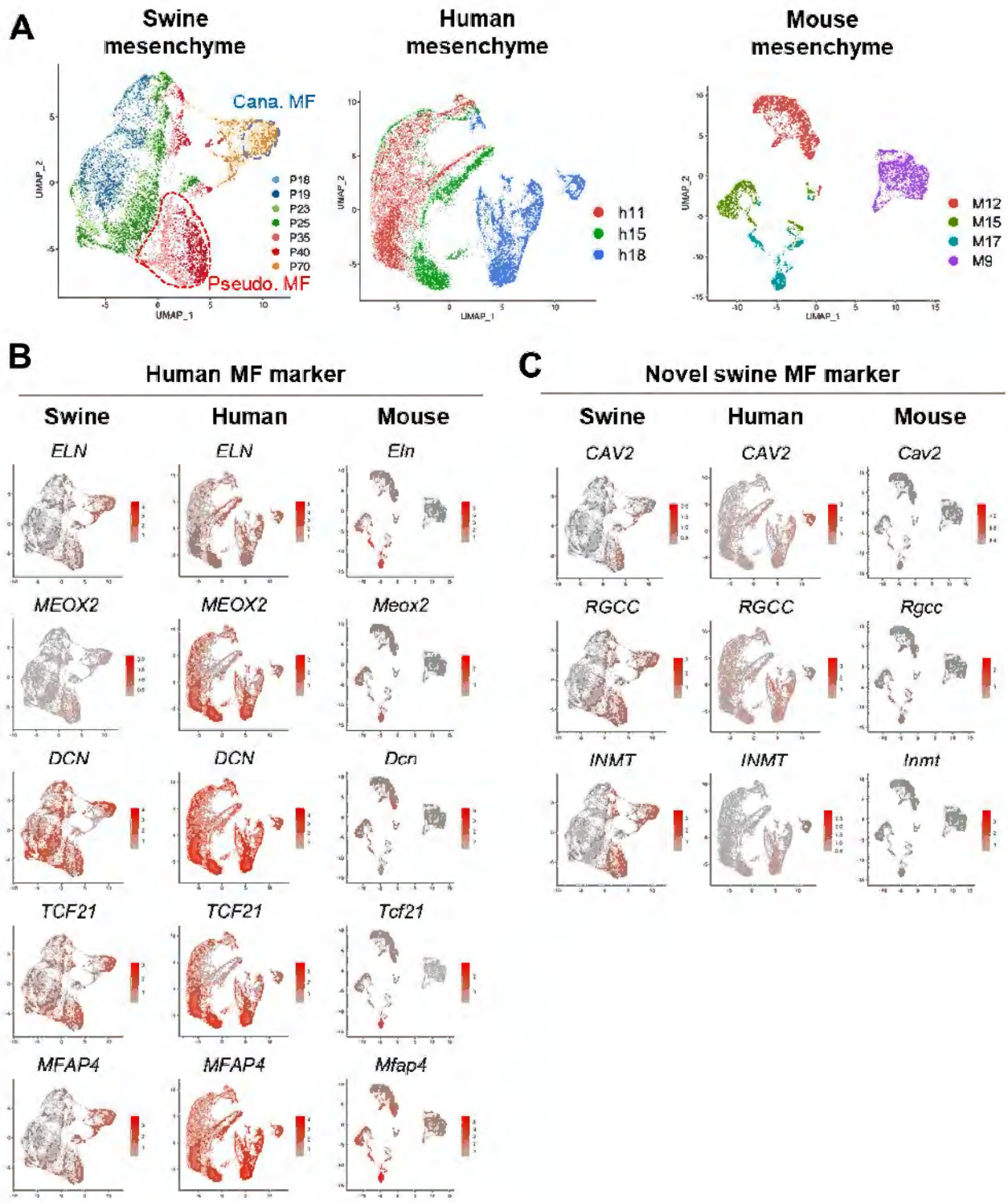

Figure S6. Expression patterns of matrix fibroblast (MF) associated genes in pig, human, and mouse lung development (A) UMAP visualization of mesenchymal cells at each stage of lung development of pigs (pig gestation days: P18, P19, P23, P25, P35, P40, and P70), humans (human gestation weeks: h11, h15, and h18), and mice (mouse gestation days: M9, M12, M15, and M17). **(B)** Feature plots for human matrix fibroblast (MF) markers; *ELN, MEOX2, DCN,*

TCF21, and *MFAP4*. During swine lung development, *ELN* and *MEOX2* enriched exclusively in MF. *ELN* was also expressed in SMC. During swine lung development, *DCN* and *TCF21* were not specific for MF but expressed in most lung mesenchyme over time except canalicular SMC. *MFAP4* was enriched in MF but also present in SMC, pericyte, and in a part of early pseudoglandular fibroblasts. (**C**) UMAP feature plots: novel MF genes enriched in swine and humans but not in mice: *CAV2, INMT,* and *RGCC* were enriched in MF, pericyte, proliferating pseudoglandular fibroblasts, and SMC. *RGCC* was also expressed in the early pseudoglandular fibroblast or chondrocyte.

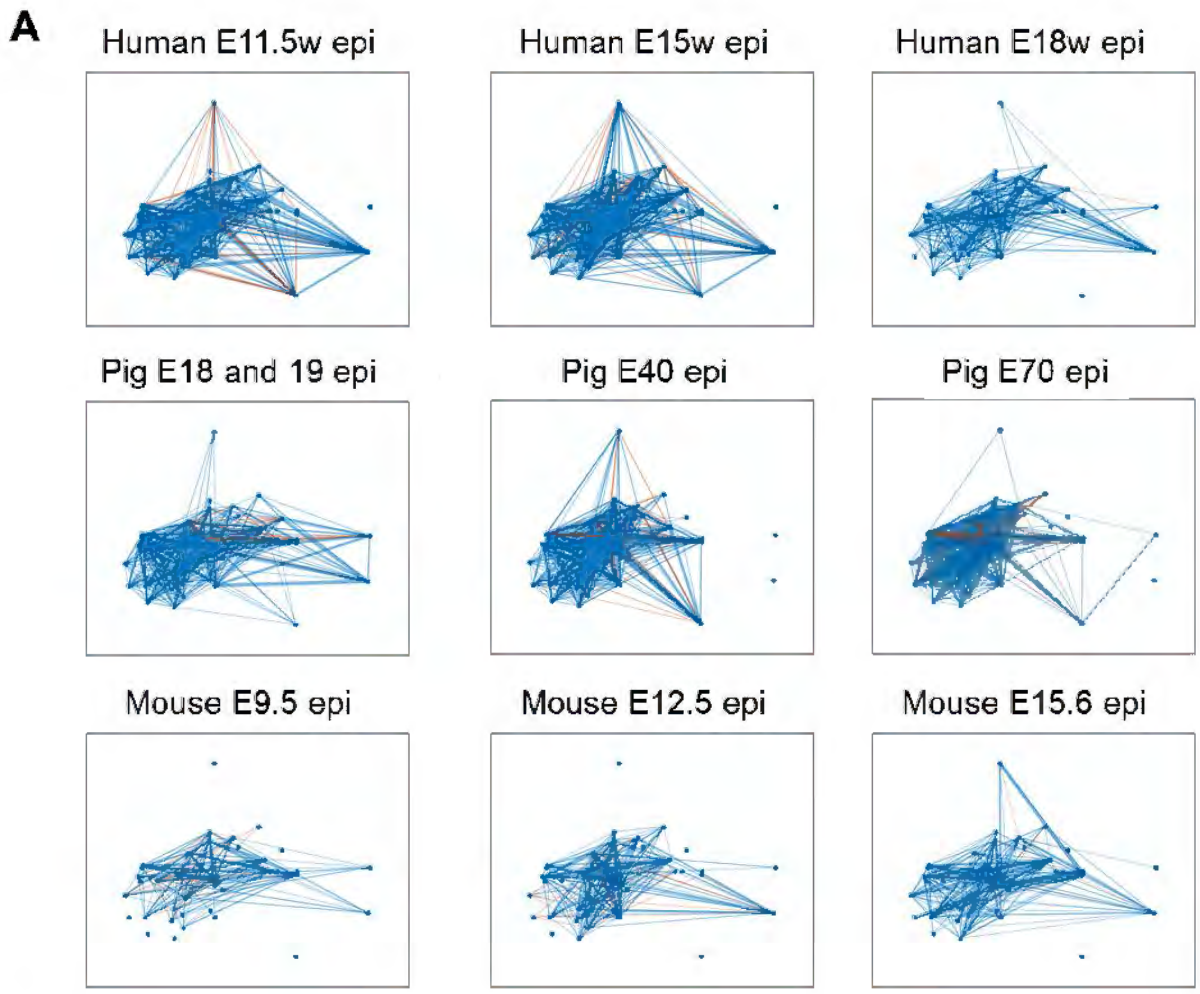
A
Human E11.5w epi
Human E15w epi
Human E18w epi
Pig E18 and 19 epi
Pig E40 epi
Pig E70 epi
Mouse E9.5 epi
Mouse E12.5 epi
Mouse E15.6 epi

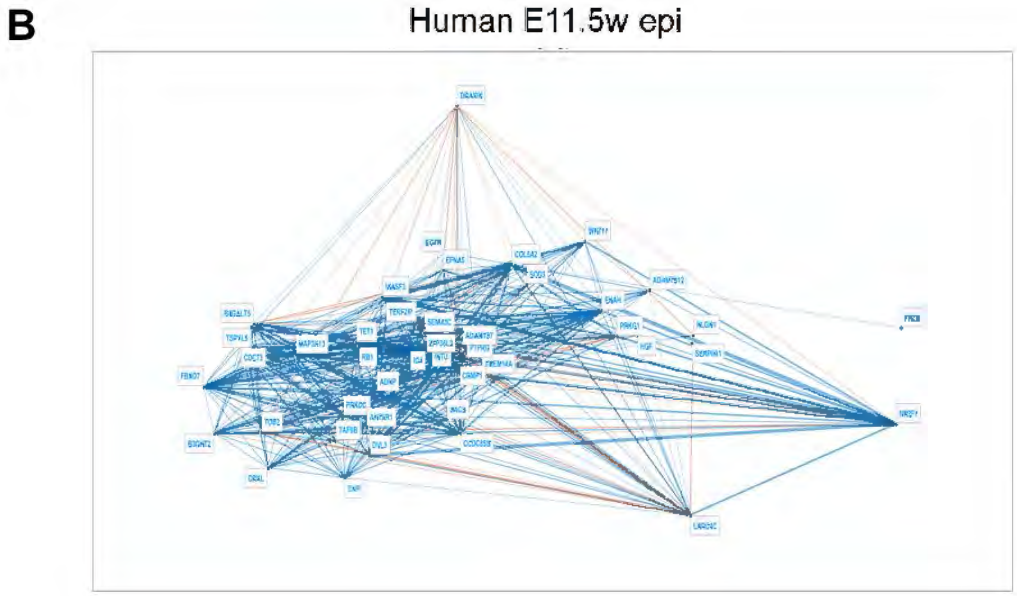
B
Human E11.5w epi

Figure S7. Conserved COSRP Gene regulatory network (GRN) during human and swine lung development (**A**) GRN visualization for COSRP genes in the epithelial cells at each stage of lung development of pigs (pig gestation days: P18, P19, P40, and P70), humans (human gestation weeks: h11, h15, and h18), and mice (mouse gestation days: M9, M12, M15). Over time, pig and human scGRN showed a highly dense network connected to the GRN nodule but sparse in mouse scGRN. (**B**) scGRN with gene annotation: *ZEP36L2, SEMA3C, TERF2IP, and ADNP* formed a central nodule in the scGRN of developing lung epithelium.

Data S1. (Separate file) List of DEGs in the human embryonic lung at 10w and 20w (GSE121238)
Data S2. (Separate file) List of COSRP genes with their expression levels in developing swine lung epithelium and mesenchyme analyzed by Seurat feature map.